Intrusion, wall fountain and stratification of homogeneous fluid in confined space filling with fountains

Liqiang Dong

for the degree of *Doctor of Philosophy*

in the *College of Science and Engineering*

James Cook University

Australia

To my parents

Statement of access

I, the undersigned, author of this work, understand that James Cook University will make this thesis available for use within the University Library and, via the Australian Digital Theses network, for use elsewhere.

I, understand that, as an unpublished work, a thesis has significant protection under the Copyright Act and;

I do not wish to place any further restriction on access to this work.

Liqiang Dong

July 2019

Statement of sources declaration

I declare that this thesis is my own work and has not been submitted in any form for another degree or diploma at any other university or other institution of tertiary education.Information derived from the published or unpublished work of others has been acknowledged in the text and a list of references is given.

Liqiang Dong

July 2019

Electronic copy

I, the undersigned, the author of this work, declare that the electronic copy of this provided to the James Cook University Library is an accurate copy of the print thesis submitted, within the limits of the technology available.

Liqiang Dong

July 2019

Acknowledgments

I would like to express my sincere gratitude to my supervisor Prof. Wenxian Lin, whose outstanding guidance and continuous assistance enabled me to complete this thesis. His patience and encouragement helped me through the confusions and difficulties in my Ph.D study. I am truly grateful that he provided me the opportunity to be a part of his research group. Under his supervision, I not only gained invaluable skills and knowledge, but also saw his enthusiasm for research and professional ethic, which has become an inspiration that will surely benefit my future career.

I would like to thank my co-supervisor Prof. Steven W. Armfield, A/Prof. Michael Kirkpatrick and Dr. Madoc Sheehan for their comments and assistance in my thesis project and the publications. Every meeting with Prof. Steven W. Armfield is a great opportunity to improve my research with his considerable insight, great erudition and professional competence.

I would also like to thank all the staff of the College of Science and Engineering, in particular Ms Melissa Norton, Mr Troy Poole, Dr. Rong Situ for their assistance in my Ph.D study. I would like to include a special note of thanks to Dr. Mehdi Kahatamifar for his selfless assistance in my research work as a group member and his encouragement as a good friend.

I am grateful to A/Prof. Dan Zhao from Harbin Engineering University for her considerable help in my study. There are several friends I would like to mention and to whom I am indebted: Ms Meihui Dong, Mr Binbin Xie, among many others.

Financial supports from the Australian Research Council and James Cook University for this work are also gratefully acknowledged.

Finally, my warmest thanks to my parents, my brother and my grandparents for their love and support throughout my student years and indeed my whole life. Special thanks go to Tiange for her patience, understanding and encouragement. Without her, I would not be where I am today.

Nomenclature

Alphabet

B	buoyancy flux
$B-I$	buoyancy-inertial
$B-V$	buoyancy-viscosity
C	constant of proportionality
C'	constant of proportionality
C^*	constant of proportionality
DNS	direct numerical simulation
Fr	Froude number
Fr_c	confined Froude number
Fr_i	Froude number at the density interface
g	acceleration due to gravity
H	height of rectangular box or cylindrical container
h	dimensionless height of rectangular box or cylindrical container
h_i	intrusion thickness
L	rectangular box half-width
M	momentum flux
n_i	component of outward normal surface vector
P	pressure
p	dimensionless pressure
P_0	reference pressure
Pr	Prandtl number
Q	volume flux
Q_0	volume flux at the source
Q_E	volume flux of the entrainment
Q_i	volume flux of the upflow at interface

Q_s	volume flux of stratified fluid
Q_{out}	volume flux of the fountain downflow
R	cylindrical container radius
r	dimensionless radial coordinate
R^{ϕ}	residual
R_0	nozzle radius
Re	Reynolds number
Ri	Richardson number at the density interface
S_{ϕ}	source term
T	temperature
t	time
T_0	fountain fluid temperature
T_a	ambient fluid temperature
U	velocity in X direction
u	dimensionless velocity in x direction
u_{φ}	dimensionless velocity in φ direction
u_e	mean inflow velocity of the entrained fluid
u_r	dimensionless velocity in r direction
u_z	dimensionless velocity in z direction
V	velocity in Y direction
v	dimensionless velocity in y direction
v_i	intrusion front velocity
v_s	stratification development rate
W	gap width
w	vertical velocity
$W-J$	wall jet
W_0	fountain fluid uniform velocity at the source
X	horizontal coordinate

x	dimensionless horizontal coordinate
X_0	slot half-width or orifice radius
Y	vertical coordinate
y	dimensionless vertical coordinate
y_m	dimensionless maximum penetration height
z	dimensionless vertical coordinate
Z_m	maximum penetration height
z_m	dimensionless maximum penetration height

Greek symbol

α	factor
α_e	entrainment coefficient for plume
β	coefficient of volumetric expansion
$\Delta\tau$	dimensionless time difference
Δt	time difference
Δx	dimensionless distance between volumes in x direction
ΔX_i	distance between volumes
Δy	dimensionless distance between volumes in y direction
Γ_ϕ	diffusion coefficient for ϕ
κ	thermal diffusivity
λ	dimensionless parameter of confinement extent
λ_i	confinement parameter
ν	kinematic viscosity
ϕ	quantity in the general transport equation
$\rho(P_0, T_0)$	reference density
$\rho(T)$	density
ρ_0	fountain fluid density
ρ_a	ambient fluid density
τ	dimensionless time

τ_m	dimensionless time-scale for the wall fountain to attain its maximum penetration height
τ_w	dimensionless time-scale for the intrusion to impinge with the wall
θ	dimensionless temperature
φ	dimensionless angular coordinate

Subscript

E	control volume E
e	edge e
N	control volume N
n	edge n
nb	neighboring cells
P	control volume P
S	control volume S
s	edge s
W	control volume W
w	edge w

Abstract

Fountains, also known as negatively buoyant jet, widely exist in both natural and industrial settings. Extensive attentions have been attracted since 1950s, with numerous theoretical, experimental and numerical investigations on the transient behavior of the planar and round fountains from weak to forced turbulent. However, most of the existing studies are about free fountains. While the understanding of the behavior of the fountain in a confined space, which is more realistic for practical applications, is currently lacking. This motivates the work of this thesis.

The confined fountain flow considered in this project is formed by the ejection of dense fluid upward into a confined space with a homogeneous ambient fluid of less density. The evolution of a typical confined fountain flow includes five stages; at first, the dense jet penetrates to a finite height and then a reversal flow falls back towards the source, creating a fountain flow; subsequently, a secondary intrusion flow results from the impingement of the fountain downflow with the bottom and spreads outwards horizontally as a gravity current, which may experience three regimes, *i.e.*, 'wall-jet' regime, 'buoyancy-inertial' regime and 'buoyancy-viscosity' regime in terms of the governing forces; after impinging with the sidewall, the intrusion is turned up and develops along the sidewall, and, since the flow is still denser than the environment, its front falls down after reaching its maximum penetration height, creating a wall fountain flow whose flow behavior is not continuous; a reversed flow is subsequently created and moves from the sidewall to the fountain source due to the stagnation pressure from the sidewall; with the reversed flow approaching the fountain flow, the interactions among the fountain flow, the intrusion, the reversed flow and the ambient fluid are strengthened, resulting in a 'two-layer' structure in the confined region and a density stratified structure is eventually formed over a long run of the fountain flow. The whole evolution of the confined fountain flow can be described as a 'fountain filling box model'. The strong secondary flows in turn will significantly affect the fountain flow behavior.

The behavior of the confined fountain flow is mainly dependent on the Froude number Fr, the Reynolds number Re, the Prandtl number Pr and the dimensionless confinement size parameter λ. In this thesis, the direct numerical simulation (DNS) and high-speed camera (HSC) experimental techniques are used to study the flow behavior of confined fountain flows and to illustrate the influence of these governing parameters on the behavior.

Two-dimensional (2D) DNS are carried out to simulate the transient flow behavior of confined weak planar fountains over the ranges of $0.1 \leq Fr \leq 3.0$, $5 \leq Re \leq 800$, $0.7 \leq Pr \leq 100$ and $10 \leq \lambda \leq 35$, by assuming the flow behavior remains as 2D and laminar over the whole evolution. It is found that the behavior of the secondary intrusion flow for the confined planar fountain considered here can be approximately quantified with the scaling relation for the planar gravity current obtained by Chen [1]. However, a two-constant speed stage is observed for the 'buoyancy-inertial' regime and the influence of Re on the intrusion speed v_i cannot be ignored, which are different from the previous studies. Additionally,

the intrusion flow regimes are determined by the strength of the governing forces that not all the intrusion flow in this thesis experiences all the three regimes; for example, only the intrusion for the fountain of $Re = 200$ with $Fr \leq 0.25$ experiences the 'wall-jet' regime. The characteristic time-scale τ_w is determined for the intrusion to impinge with the sidewall. τ_w is found to increase with the increase of Fr and the decrease of Re. Three mechanisms are identified for the secondary wall fountain behavior for the planar fountain, *i.e.*, no-falling for $Re \leq 20$, slumping down for $50 \leq Re \leq 100$ and rolling down for $200 \leq Re$, except for a slumping down mechanism observed for the case of $Re = 200$ and $\lambda = 10$. The maximum penetration height of the wall fountain on the sidewall, y_m, and the corresponding time, τ_m, increase with increasing Fr and λ, or decreasing Pr. Convection, mixing, thermal conduction and filling all contribute the formation of the stratified structure, but their effects at individual stages are at different extents. For the initial stages, convection and mixing play a key role which is corresponding to an increasing bulk entrainment rate. While thermal conduction and filling dominate the development of the stratification after a quasi-steady stratification is created, with a decreasing bulk entrainment rate.

A series of three-dimensional (3D) DNS are carried out to investigate the behavior of confined weak round fountains over the ranges of $0.25 \leq Fr \leq 3.0$, $5 \leq Re \leq 800$, $0.7 \leq Pr \leq 100$ and $10 \leq \lambda \leq 35$. Similarly, the secondary intrusion for the round fountain can be treated as radial gravity current. However, the correlations for the intrusion speed v_i of $v_i \sim Fr^{-1/5}Re^{1/5}\tau^{-1/2}$ and $v_i \sim Fr^{-1/2}Re^{1/10}\tau^{-1/4}$ obtained with the numerical results are again different from the results of the scaling study on gravity current [1]. The increase of Fr or the decrease of Re results in a larger τ_w, where τ_w is the time scale for the intrusion to reach the sidewall. When Pr is very small, *e.g.*, $Pr = 0.7$ or 1, τ_w is noticeably reduced, while the influence of Pr is minor when $Pr \geq 7$. This is because the thermal conduction effect is significant for very small Pr values. There is no rolling down observed for the wall fountain in the DNS of confined weak round fountains in this thesis. z_m is re-defined as the maximum penetration height of the wall fountain in the sidewall region for the round fountain. It is observed that z_m and τ_m increase with the increase of Fr for $Fr \leq 1.75$, but decrease with the increasing Re. Similar to the planar case, the influence of Pr is significant when Pr is small. During the evolution of a confined weak round fountain, the bulk entrainment rate experiences three stages. Initially, the entrainment rate meets a monotonic increase, which mainly results from the entrainment of ambient fluid by the intrusion head. Then the entrainment rate reaches a peaking value with the intrusion flow impinging on the sidewall. A relatively high entrainment rate is subsequently remained, due to the convection and mixing created by the interactions among the fountain flow, the secondary flows and the ambient fluid, until the formation of a quasi-steady stratification. After that, the entrainment rate gradually decreases, with filling and thermal conduction becoming dominant.

The behavior of confined round fountains with Fr, Re and λ over the range of $1.0 \leq Fr \leq 20.0$, $102 \leq Re \leq 1502$ and $27.9 \leq \lambda \leq 48.75$ is studied experimentally by using High-speed Camera techniques and dye visualization. The round fountain is formed by ejecting saline water of various densities upward into a cylindrical container filled with quiescent fresh water at specific constant flow rates. A

system of two Photron FASTCAM Mini UX100 High-Speed Cameras and a SONY HDR-PJ810 video camera is used to record the transient behavior of the confined fountains. The experimental results of several typical confined round weak fountain are compared against the results of the corresponding DNS results, which are in good agreement both qualitatively and quantitatively, indicating the DNS runs predict the flow behavior with sufficient accuracy. The influence of Fr, Re and λ on τ_w is analyzed quantitatively. For intermediate (*e.g.*, $Fr = 3.0$) and forced turbulent fountain (*e.g.*, $Fr = 5.0, 8.0$) with fixed λ, τ_w is nearly constant for $500 \lesssim Re$. Since the 'wall-jet' and 'buoyancy-inertial' regime dominate the secondary intrusion flow where the location of the intrusion front gets less influenced by Re (after [1]). However, τ_w for the fountains of $Re \lesssim 204$ is significantly different, which may results from the change in the dominant regime for the intrusion flow or the interaction among the upflow, downflow of the fountain and the ambient fluid. $Re = 204$ is identified as a critical value for different behavior of the turbulent fountains. The correlations between Fr and τ_w is different at specific values of Re. For $Re = 204$ and $Re = 511$ with $\lambda = 27.9$, $Fr = 2.0$ is found to distinguish the influence of Fr ($1.0 \leq Fr \leq 5.0$) into two ranges, and linear correlations $\tau_w \sim Fr$ are determined. For $Re = 1002$ and $Re = 1502$ with $\lambda = 48.75$, a power law $\tau_w \sim Fr^{1.23}$ is determined for $8.0 \leq Fr \leq 20.0$. The influence of the confinement size λ on τ_w follows a power law, *i.e.*, $\tau_w \sim \lambda^{1.35}$. The turbulent secondary flows created by the confined intermediate and forced turbulent fountain result in a more significant influence of convection on the development of the stratification.

List of Associated Publications

Refereed Conference Papers

1. Liqiang Dong, Wenxian Lin, S. W. Armfield, M. P. Kirkpatrick, N. Williamson, and Dan Zhao. Direct numerical simulation of the thermal stratification produced byweak plane fountains in confined regions, *In Proceedings of the* 11^{th} *Australasian Heat and Mass Transfer Conference*, Australasian Fluid and Thermal Engineering Society, Melbourne, Australia, 2018.

2. Liqiang Dong, Wenxian Lin, S. W. Armfield, M. P. Kirkpatrick, N. Williamson, and Dan Zhao. Direct numerical simulation of the long-term behavior of weak fountains in a homogeneous fluid. *In Proceedings of the* 16^{th} *International Heat Transfer Conference*, The Assembly for International Heat Transfer Conferences, Beijing, China, 2018.

3. Liqiang Dong, Wenxian Lin, S. W. Armfield, M. P. Kirkpatrick, N. Williamson, and Dan Zhao. Filling box flow with weak plane fountain: The effect of Reynolds and Prandtl number. *In Proceedings of the* 21^{th} *Australasian Fluid Mechanics Conference*, Australasian Fluid Mechanics Society, Adelaide, Australia, 2018.

Papers In Preparation

1. Liqiang Dong, Wenxian Lin, S. W. Armfield, M. P. Kirkpatrick and N. Williamson, Confined buoyant flows: a literature review.

2. Liqiang Dong, Wenxian Lin, S. W. Armfield, M. P. Kirkpatrick and N. Williamson, Filling box with a weak plane fountain I: the intrusion flow.

3. Liqiang Dong, Wenxian Lin, S. W. Armfield, M. P. Kirkpatrick and N. Williamson, Filling box with a weak plane fountain II: the secondary wall fountain and stratification.

4. Liqiang Dong, Wenxian Lin, S. W. Armfield, M. P. Kirkpatrick and N. Williamson, Direct numerical simulation of confined weak round fountains.

5. Liqiang Dong, Wenxian Lin, S. W. Armfield, M. P. Kirkpatrick, N. Williamson and M. Khatamifar, Experimental study on confined turbulent round fountains.

Contents

List of Figures

List of Tables

Chapter 1

Introduction

1.1 Background

Fountain is known as a jet with buoyancy acting in the opposite direction of its momentum at the source, which may result from either the upward ejection of a heavier jet or the downward discharge of a lighter jet into the ambient fluid. For an upward ejected fountain, as shown in Figure 1.1, the vertical velocity of the upflow is gradually decelerated due to the negative buoyancy until zero when the fountain flow reaches its maximum penetration height. After that, a downflow is present, which falls back toward the fountain source and subsequently forms an intrusion which spreads outward along the base.

Fountains are abundant in nature, industry, agriculture and our daily life, thus it is of fundamental significance and practical importance to understand the behavior of various fountains under a wide range of conditions. This has led to extensive research on the topic.

Some typical examples include lava flows in magma chambers, explosive volcanic eruptions, discharge of brine from desalination plants into the sea, replenishing the

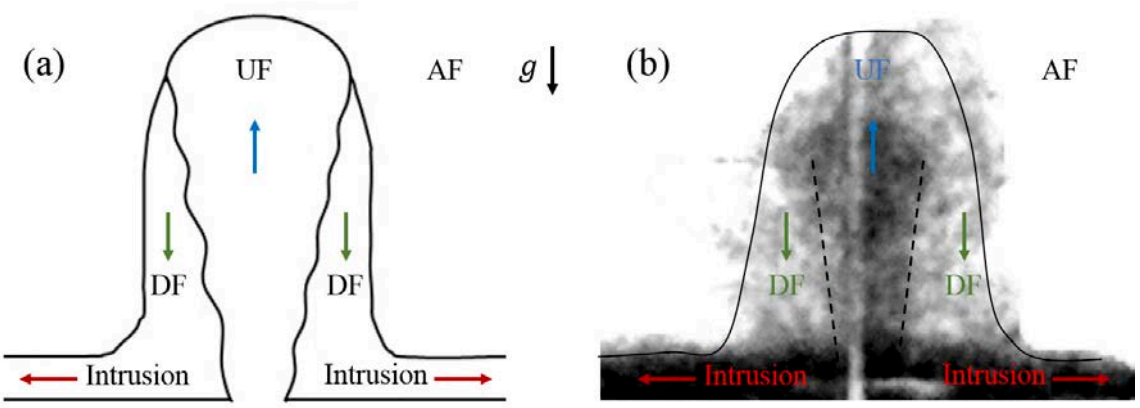

FIGURE 1.1: (a) Schematic illustration and (b) an image from experiment of a turbulent fountain, where AF, UF and DF denote the ambient fluid, upflow, and downflow, respectively.

cold saline water in solar ponds, eliminating the damage in agriculture due to radiation frost, and reverse cycle air-conditioning systems in the building, to name just a few.

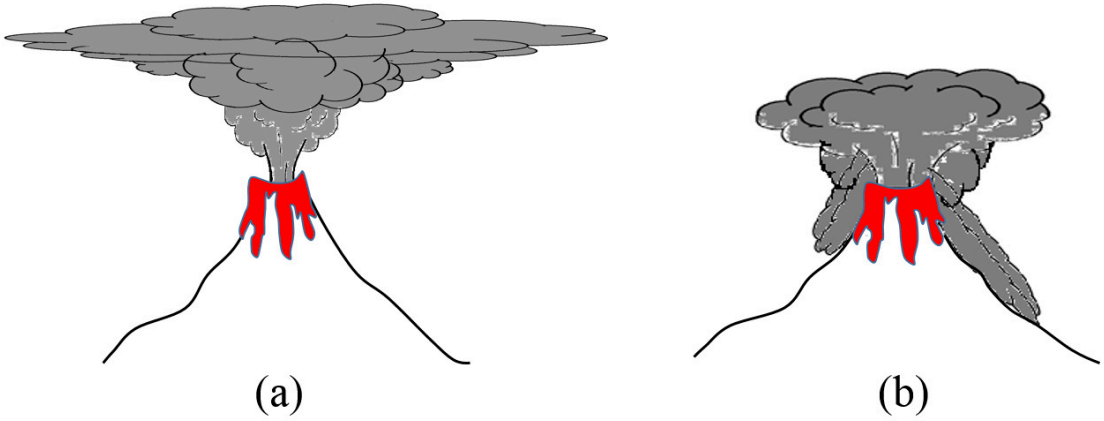

FIGURE 1.2: Schematic illustration of explosive volcanic eruptions: (a) Plinian plume and (b) Pyroclastic flow.

In an explosive volcanic eruption, a large amount of the mixture of gas and pyroclasts is propelled into the atmosphere, resulting in the most energetic and dangerous turbulent flow on earth [12]. The high-velocity hot and dense jet is initially with negative buoyancy, but later the flow develops within two regimes. When enough air entrains into the jet, the jet becomes neutral or positively buoyant and keeps rising, forming a high Plinian plume as shown in Figure 1.2(a). Otherwise,

the jet collapses with depleting initial momentum, creating dense pyroclastic flows as shown in Figure 1.2(b). The ash and pumice of the eruption columns not only present potential severe hazards to the human surrounding, but also influence the volcanic climate. Hence the realistic prediction of the behavior of explosive volcanic eruption columns and assessing the consequence is necessary. This has led to numerous studies on explosive volcanic eruption (see, *e.g.*, [13–15]). The entrainment rate has been identified as the key factor for the transition between different regimes. Additionally, the results can also be applied for the safe forecasting of the accident leaks of hazardous gases [16].

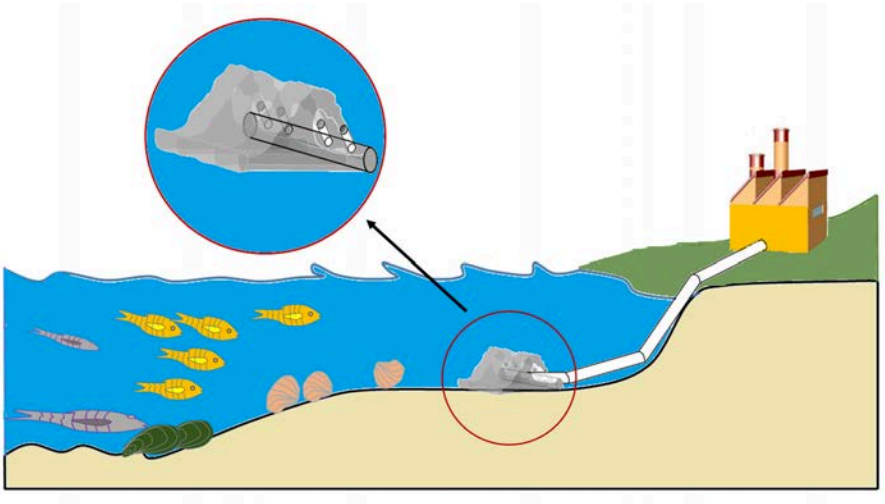

FIGURE 1.3: Schematic illustration of the fountain formed by discharging brine water from desalination plants into the sea.

The fountain is a major means for the disposal of effluents into water bodies, as commonly used to discharge brine from desalination plants into the ocean. The hypersaline water has a significant influence on the offshore environment, since the high salinity can be toxic to marine organisms. To reduce the influence, the brine is usually inclined upward to be discharged from a diffuser at a high velocity as shown in Figure 1.3, resulting in an inclined turbulent fountain. The entrainment of seawater then reduces both the salinity and the concentration of the pollution to a safe level. Identifying key physical processes governing the characteristics of the brine flow, particularly the dilution when the jet impinges on the bottom, is

central to the design of the diffuser [17, 18]. Similarly, when the cooling water from power plants is discharged downward into lake or river bodies, a downward fountain occurs [19, 20].

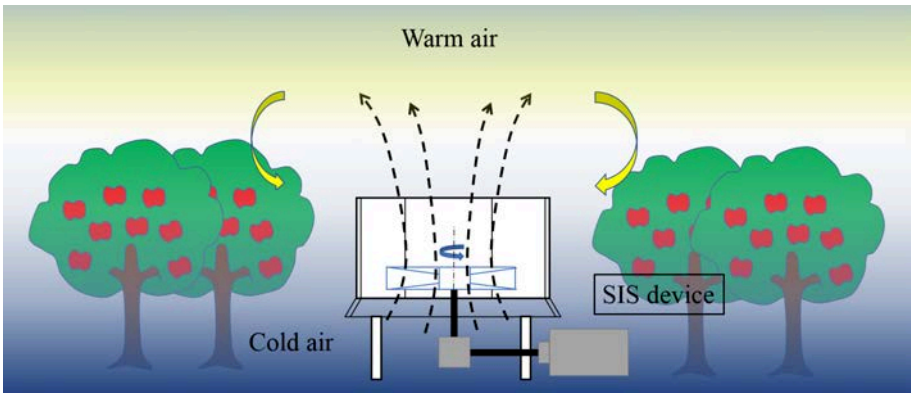

FIGURE 1.4: Schematic illustration of the Selective Inverted Sink (SIS) device.

Fountains also have important applications in agricultural production. For example. the Selective Inverted Sink (SIS) device is developed to mitigate the damage of radiation frost in agriculture, which is a problem that can cause significant annual losses in food production worldwide [21]. In the presence of a radiation frost, air temperature increases with altitude where the coldest air is deposited near the soil, potentially damaging crops particularly when it is below a critical temperature. Therefore, the effective control of temperature in cultivated areas is crucial. As illustrated in Figure 1.4, the SIS device selectively drains and expels the coldest air upwards out of the plantation area by means of mechanical power, preventing the onset of radiation frost. The upward cold flow here behaves as a turbulent fountain in a stratified environment. An experimental work supported by CONICYT (National Council of Scientific and Technological Research) reported that the averaged frost damage at the orchard with SIS protection was 14%, against the 42% observed at the counterpart unprotected orchard [22].

Fountains also widely exist in our daily life. Figure 1.5(a) shows a warm air curtain on the store entrance in the cold time, formed by the downward ejection of heated air from a thin horizontal slot at the top of the doorway, which is a downward

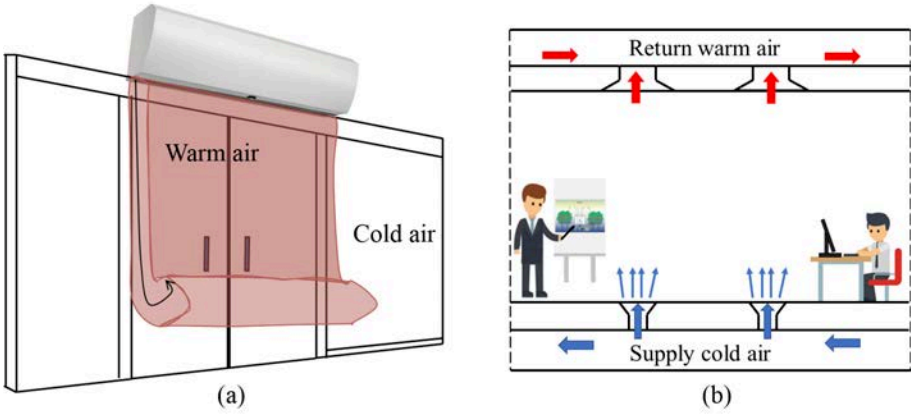

FIGURE 1.5: (a) Warm air curtain above the entrance of buildings in winter and (b) underfloor air-conditioning system in buildings.

fountain [23]. The similar technique is also used for forced heating of big structures, *e.g.*, aircraft hangars [24], and the energy efficient underfloor air distribution system as shown in Figure 1.5b which ejects upward cool air from vents on the floor to achieve localized cooling of the room, instead of cooling the whole room [25, 26].

All the application examples above require a full understanding of the behavior of fountains. There have been numerous studies on fountains since the 1950s. Depending on the shape of the source, a fountain can be either a round fountain or a plane fountain; when the source is an orifice, the resultant fountain will be a round one whereas for a slot source, the fountain will be a planar fountain (also named as line fountain or plane fountain). Fountains can also be classified as forced fountains or weak fountains based on the physical conditions at the source.

The early research had been mainly focused on turbulent fountains (see, *e.g.*, [27–29]). More recently, weak fountains have also received considerable attentions (see, *e.g.*, [4, 30–32]). Most of the existing studies are primarily about free fountain cases where fountains freely penetrate and mix with the ambient fluid without a confinement from boundaries, as will be summarized in Chapter 2. However, in many applications, fountains occur in the environment of limited extent (see, *e.g.*, accident leaks of hazardous gas or localized cooling are usually confined in buildings as shown in Figure 1.6).

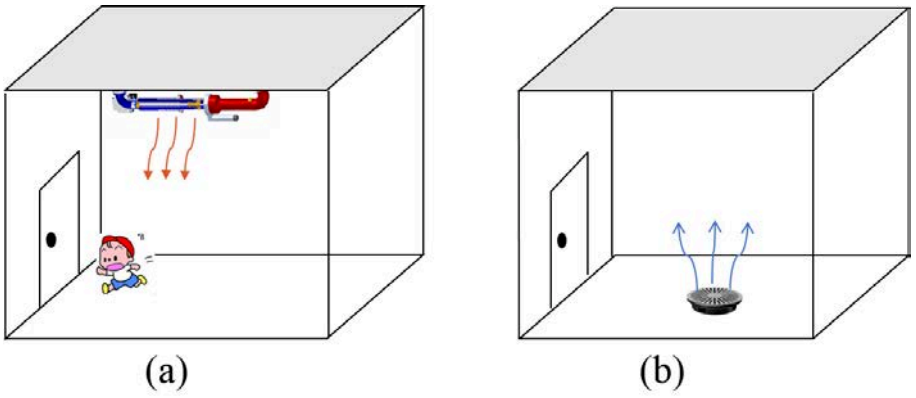

FIGURE 1.6: Confined fountain applications: (a) hazardous gas leakage and (b) localized cooling system.

In such a confined situation the transient behavior of the fountain flow is inherently different from that of fountain flow freely spreading in an infinite space. Figure 1.7 presents the numerically simulated evolution of a weak plane fountain in an open channel. The initial behavior of the confined fountain is similar to that for the free fountain case, that is, an intrusion resulted from the impingement of the downflow on the floor spreads outward as gravity current (Figure 1.7(a)-(b). Subsequently, the gravity current impinges with and is turned up by the sidewall (Figure 1.7(c)). Due to the negative buoyancy, the flow on the vertical wall falls back after it reaches a finite distance, resulting in a wall fountain (Figure 1.7(d)). With the continuous supply of the dense fluid, the intrusion deepens and a reversed fluid moves from the side-wall and approaches the fountain core (Figure 1.7(e)). During the course, the reversed flow interacts with the intrusion, the fountain source and the ambient fluid. A density stratification is gradually formed in the confined space (Figure 1.7(f)). Conversely, the change in the ambient fluid also affects the behavior of the fountain flow, which makes the fountain flow even more complicated.

Quantitative prediction of the behavior of confined fountains highlights the potential for energy saving design, safe forecasting of hazardous gas leakage, *etc.*To this end,the factors affecting the confined fountains need to be fully understood. These include the physical conditions at the source, the length scales of the confinement,

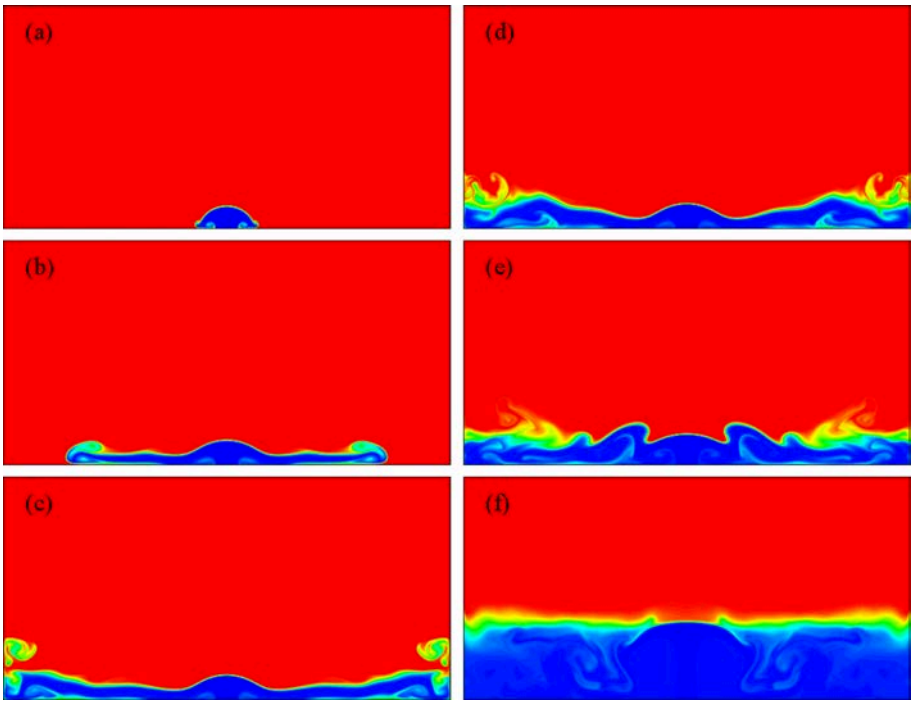

FIGURE 1.7: Numerically simulated evolution of a weak plane fountain: (a) formation of the fountain, (b) intrusion, (c) maximum penetration height of wall fountain, (d) falling down of wall fountain, (e) reversed flow, and (f) density stratification.

the geometry of the source and confinement, *etc.*Although there have been some investigations on the behavior of buoyant flow released in confined spaces, such as plume filling box, impinging fountains or fountain in stratified environment, *etc.*, as will be reviewed in Chapter 2, the understanding of fountain in confined space filled with homogeneous fluid is still scarce, particularly of the confined weak fountain, which is the motivation of this study.

1.2 Problem addressed and objectives

The problem addressed in this thesis is the behavior of fountain in confined space with a homogeneous ambient fluid, including the intrusion, wall fountain, reversed flow and stratification. Both round and planar fountains are considered. Two-dimensional and three-dimensional direct numerical simulation (DNS) are employed to simulate the transient behavior of confined weak planar and round fountains

respectively. In addition, high-speed camera techniques are used for the experiments of forced round fountains in confined cylindrical containers.

In the case of planar fountains, the physical system under consideration is a two-dimensional rectangular box of height H and half-width L, whereas in the case of round fountains, it is a three-dimensional cylindrical container of height H and radius R, as sketched in Figure 1.8. The vertical sidewalls of the containers are no-slip and insulated, and the top of the container is a free surface. On the bottom center, a slot of half-width X_0 or an orifice of radius X_0 is used as the fountain source for planar fountains or round fountains respectively. The remaining bottom region is a rigid non-slip and insulated boundary. In both cases, the containers are initially filled with a homogeneous Newtonian fluid at rest and with uniform temperature T_a. At time $t = 0$, a dense jet at temperature T_0 ($T_0 < T_a$) is ejected upward into the container with a uniform velocity W_0 and this discharge is maintained thereafter.

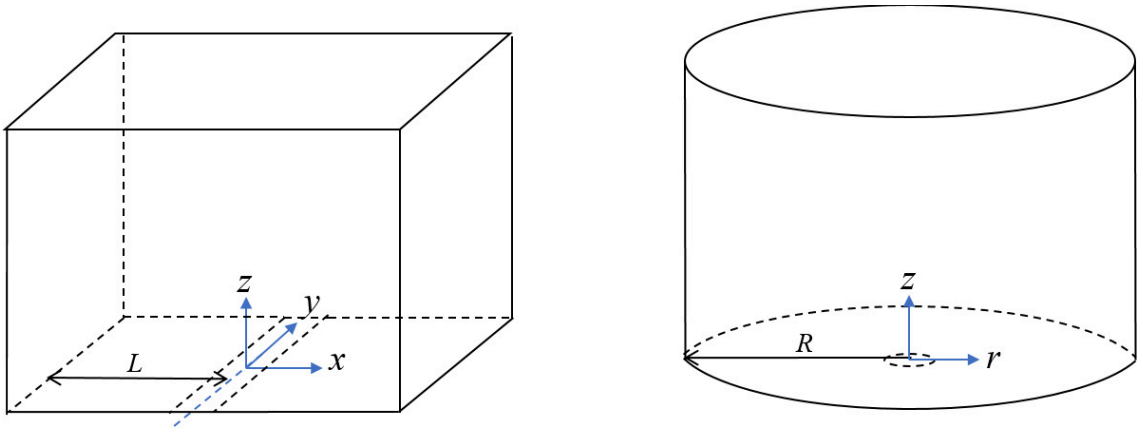

FIGURE 1.8: Schematic illustration of the physical systems for a fountain in a confined space with a homogeneous fluid: (a) planar fountain and (b) round fountain.

For either type, the transient behavior of free fountains in a homogeneous ambient fluid is mainly governed by the Reynolds number, Re, and the Froude number, Fr, defined as follows,

$$Re = \frac{W_0 X_0}{\nu} \tag{1.1}$$

$$Fr = \frac{W_0}{\sqrt{gX_0(\rho_0 - \rho_a)/\rho_a}} = \frac{W_0}{\sqrt{g\beta X_0(T_a - T_0)}} \tag{1.2}$$

where g is the acceleration due to gravity, ρ_0 and ρ_a are the densities of the jet fluid and the ambient fluid at the source, ν and β are the kinematic viscosity and the coefficient of volumetric expansion of the ambient fluid, respectively. For fountains with the density difference due to the temperature difference between the jet and ambient fluid, Fr can also be calculated with the temperature difference using the Oberbeck-Boussinesq approximation, which requires the density ratio of $(\rho_0 - \rho_a)/\rho_a$ to be significantly less than unity. For such a case, the influence of thermal conduction is quantified by the Prandtl number, Pr, which is defined as,

$$Pr = \frac{\nu}{\kappa} \tag{1.3}$$

where κ is the thermal diffusivity.

When a fountain is confined, its behavior will also be influenced by the size of the space, which can be scaled by a dimensionless number λ defined as,

$$\lambda = \frac{L}{X_0} = \frac{R}{X_0} \tag{1.4}$$

for rectangular boxes and cylindrical containers, respectively.

To the best knowledge of the author, all the existing research on 'fountain filling box' flows are conducted experimentally to illustrate the forced fountain bulk behavior, *e.g.*, the penetration height and the bulk entrainment. However, it is difficult to obtain the detailed internal dynamics of the flow by experiments. Numerical method overcomes this shortage, particularly DNS, which can capture all the internal dynamics of the flow, including the internal density distribution and the couplings between the fountain and the secondary flows. Nevertheless, the DNS of the flows with high Re is still challenging due to the computational consumption.

Based on the dynamic behavior of the fountain with different Fr, round fountains are classified as 'very weak' ($0.3 \lesssim Fr \lesssim 1.0$), 'weak' ($1.0 \lesssim Fr \lesssim 2.0$), 'intermediate' ($2.0 \lesssim Fr \lesssim 4.0$) and 'forced/highly forced' fountains ($4.0 \lesssim Fr$) by Hunt &

Burridge [2]. Similarly, Hunt & Coffey [33] distinguished the planar fountains into 'very weak' ($Fr \lesssim 2.3$), 'weak' ($2.3 \lesssim Fr \lesssim 5.7$) and 'forced' ($5.7 \lesssim Fr$), which are reviewed in detail in Chapter 2. The aim of this thesis is to investigate the long-term transient behavior of confined fountains (from weak to forced) by experiments, direct numerical simulations and scaling analysis. Therefore, DNS is employed to simulate the behavior of confined weak plane and round fountain (with low Fr and Re), whereas experiments are carried out for fountains from weak to forced, with covering a wider range of Fr and Re. More specifically, the objectives of this thesis are as follows:

- To understand the transient flow behavior of confined weak planar fountains over the ranges of $0.1 \leq Fr \leq 3$, $5 \leq Re \leq 800$, $0.7 \leq Pr \leq 100$ and $10 \leq \lambda \leq 35$.
- To understand the transient flow behavior of confined round fountains over the ranges of $0.25 \leq Fr \leq 15$, $5 \leq Re \leq 1502$, $0.7 \leq Pr \leq 100$ and $10 \leq \lambda \leq 35$.
- To investigate the influence of Fr, Re, Pr, and λ on the transient behavior of both the confined planar fountains and round fountains, and to determine the scaling correlations to quantify the influence.

1.3 Significance and innovation

As mentioned in § 1.1, there are extensive practical applications involving the confined fountain flow. Hence, it is of fundamental significance and practical importance to investigate the behavior of the 'filling box flow' with the confined fountain. The innovations of this project are summarized as follows:

- Establishment of a two-dimensional numerical model for confined weak plane fountain.

- Establishment of a three-dimensional numerical model for confined round fountain.
- Numerical and experimental investigation on the influence of Fr, Re and Pr on the behavior of the fountain flow and its secondary flows.
- Numerical and experimental illustration of the influence of confinement on the behavior of the fountain flow and its secondary flows in terms of the dimensionless confinement parameter λ.

1.4 Thesis outline

The rest of this thesis is outlined as follows,

- In Chapter 2, a literature review is presented to briefly review and discuss previous research on fountains, including planar and round fountains, both free and confined.
- Chapter 3 introduces the numerical method and experimental method used in this study. A detailed description of the governing equations for the fountain flow and the appropriate initial and boundary conditions is given first, followed by a brief introduction of the Finite Volume Method and the discretization schemes used to solve the differential equations. The procedure to set up numerical simulations in ANSYS Fluent is also briefly described, along with the experimental system for the study of round fountains confined in cylindrical containers. The use of the high-speed camera technique is also briefly described.
- In Chapter 4, the transient behavior of confined planar fountains over the ranges of $0.1 \leq Fr \leq 3$, $5 \leq Re \leq 800$, $0.7 \leq Pr \leq 100$ and $10 \leq \lambda \leq 35$ is studied through a series of two-dimensional direct numerical simulations. The evolution of confined planar fountains is presented and the effects of Fr,

Re, Pr and λ on the behavior of the intrusion, the wall fountain, the thermal stratification are discussed and determined using the DNS results.

- Chapter 5 presents the three-dimensional direct numerical simulation of confined round fountains over the range of $0.25 \leq Fr \leq 3$, $5 \leq Re \leq 800$, $0.7 \leq Pr \leq 100$ and $10 \leq \lambda \leq 35$. The effects of Fr, Re, Pr and λ on the behavior of the intrusion, the wall fountain, the thermal stratification are discussed and quantified by the DNS results.

- Chapter 6 presents the experimental study on the behavior of confined round fountains over the ranges of $1 \leq Fr \leq 20$, $102 \leq Re \leq 1502$, and $27.9 \leq \lambda \leq 48.75$. The behavior of confined turbulent round fountains is studied by qualitative observation of the time evolution of the experimental food dyed contours. The experimental data are compared with the DNS results and analytical predictions to benchmark the accuracy of the numerical code.

- In Chapter 7, a summary of the major findings of this study and the suggestions for future work are given.

Chapter 2

Literature review

2.1 Introduction

As mentioned in the previous chapter, a fountain is the jet with opposing buoyancy resulted from the density difference between the source fluid and the ambient fluid. The broad applications of fountains have motivated extensive studies on the behavior of fountains from different aspects in the past 60 years and the related work is continuously developing. By using various methods (*i.e.*, experimental, theoretical and numerical method), the behavior of fountains is found to be significantly influenced by numerous factors [2]. These factors include the nature of the jet (*e.g.*, laminar or turbulent); the geometry of the source (*e.g.*, orifice or slot); the direction of jet ejection (vertical or inclined); and the physical properties of the fluids. In addition, the effect of the ambient fluid is also important, *e.g.*, whether the ambient is quiescent, in motion, homogeneous, stratified, and whether it can mix with the ejected fluid from the source.

When the jet fluid is ejected from the source into the ambient fluid at an angle smaller than 90 degrees, an inclined fountain is formed. Inclined fountains arise in a number of applications, particularly in the disposal of brine and sewerage into the marine environment as shown in Figure 1.3. There have been numerous studies

on inclined fountains, most of which are about inclined turbulent fountain (see, *e.g.*, [34–39]). As this thesis focuses on vertical fountains, the inclined fountains are beyond the scope of this thesis and therefore will not be discussed in details here. Similarly, there are numerous studies on other types of fountains, such as multiple interacting fountains (see, *e.g.*, [40–44]), fountains in crossflow (see, *e.g.*, [45–48]) and fountains which are immiscible with the ambient fluid (see, *e.g.*, [49–52]), which are also beyond the scope of this thesis and hence are not dealt with here as well. The readers are referred to, *e.g.*, [48, 53, 54], for the details of some of these studies.

In this literature review, only the works closely related to the current study are reviewed and discussed. These include the studies on vertical round and planar fountains in both free and confined environment, where the fountain fluid is miscible with the ambient fluid and the density difference is small.

2.2 Fountain classification

In terms of the fountain source geometry, fountains are distinguished as round fountains or planar fountains, with round fountains from an orifice source and a planar fountain from a slot source, which have been extensively investigated in the past decades, as reviewed in [2]. For either type, the behavior of the fountain flow in the homogeneous environment differs from that in the stratified environment [55]. It has also been found that the behavior of both the round fountain and planar fountain varies significantly under different source conditions (represented by the Froude number, Fr, and the Reynolds number, Re, at the source), due to the change of the dominant physics of the flow. Therefore, the classifications need to be considered for the fountain research [56].

Different classifications of fountains have been reported, particularly for the round fountain (see, *e.g.*, [6, 32, 57]). The most complete classification was given

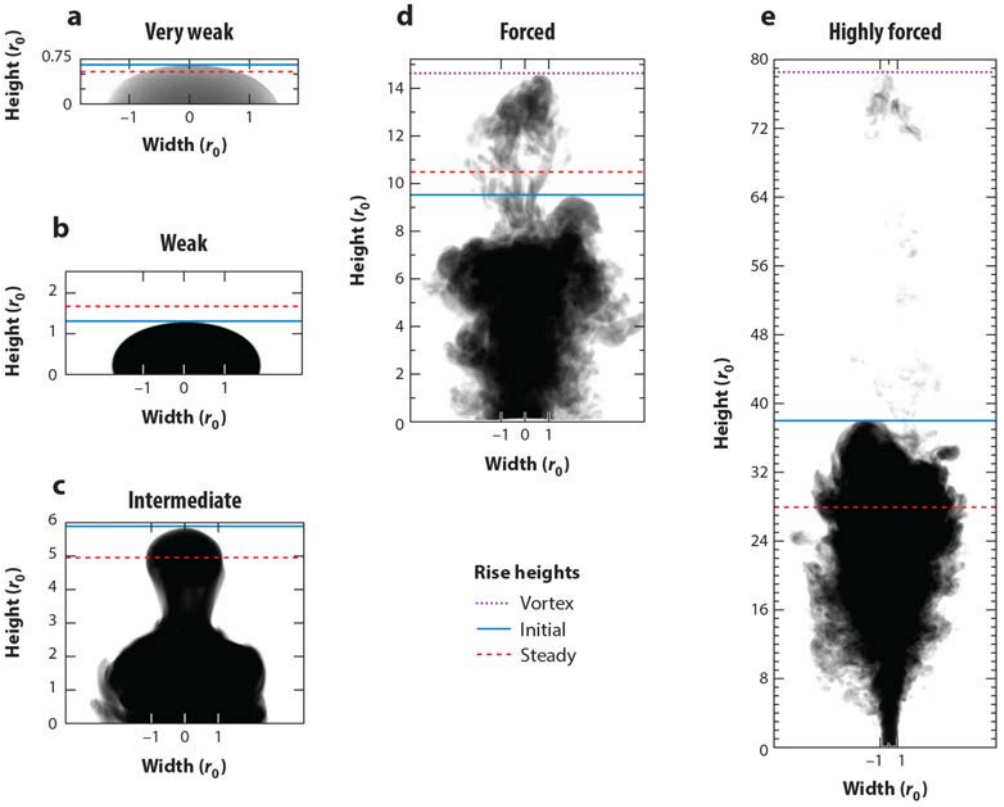

FIGURE 2.1: Experimental images of round fountains presenting their typical shape and characteristic penetration heights: (a) very weak fountain, (b) weak fountain, (c) intermediate fountain, (d) forced fountain, and (e) highly forced fountain [2].

by Hunt & Burridge [2], which distinguishes the round fountain in a homogeneous ambient fluid into the following classes in terms of Fr, namely,

- Very weak fountains ($0.3 \lesssim Fr \lesssim 1.0$)
- Weak fountains ($1.0 \lesssim Fr \lesssim 2.0$)
- Intermediate fountains ($2.0 \lesssim Fr \lesssim 4.0$)
- Forced and highly fountains ($4.0 \lesssim Fr$)

Fr, as defined in Eq.(1.2), represents the ratio of the inertial force to the buoyant force at the source. The dominate physics at the source varies with different Fr

values, resulting in a considerable change in the behavior of the fountain. Experimental images shown in Figure 2.1 presents the features including the shape and the characteristic heights of a round fountain, indicating the reason for the classification.

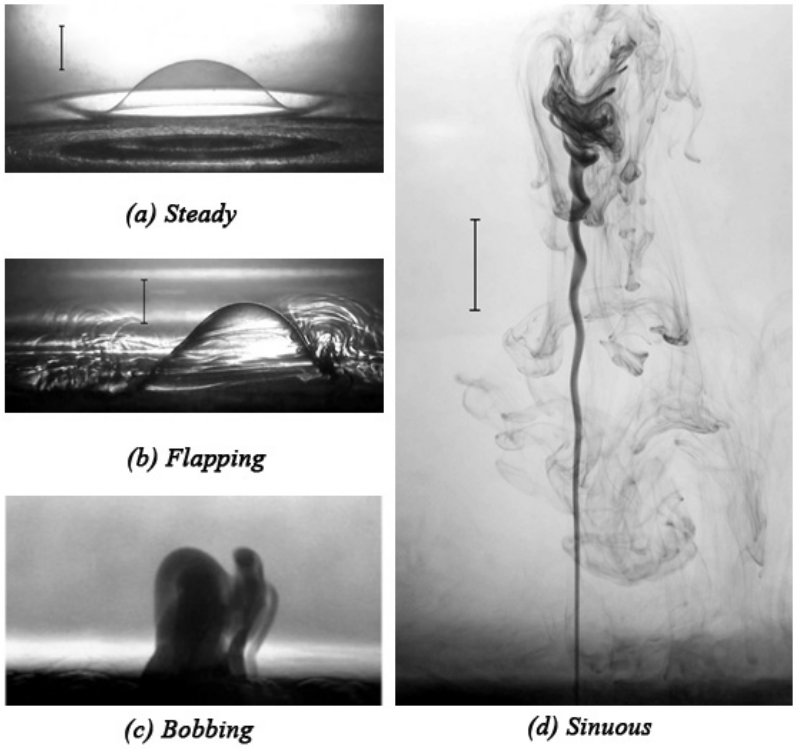

FIGURE 2.2: Experimental images demonstrating the effect Re on the behavior of round fountain: (a) steady, (b) flapping, (c) laminar bobbing and (d) sinuous [3].

What should be noted is that the classification presented above is solely based on Fr, whereas the influence of Re was not taken into account. Re, as defined in Eq.(1.1), characterizes the inertial force relative to the viscous force at the source. The experiments by Williamson *et al.* [3] show that Re has significant influence on the behavior of fountains. They identified a laminar flapping as the first unstable model of a round fountain, and the fountain behavior becomes more disorderly, with the appearance of a laminar bobbing motion or sinuous motions when Fr and Re are increased, as shown in Figure 2.2. For the range of $0.7 < Fr < 10$ and $10 < Re < 120$, a function of $C = FrRe^{2/3}$ is identified to approximately describe the transition between the steady behavior, the laminar flapping and the laminar bobbing, where C is a constant. The flow is steady and axisymmetric with

no fluctuation in the fountain height as shown in Figure 2.2(a) for $0 < C < 16$. When C falls into the range of $16 < C < 27$, the flows become unstable, with several oscillation modes as shown in Figure 2.2(b), including a two-dimensional flapping motion that the peak of the fountain moves from one side to the other and a circling or multimodal flapping that the top of the fountain circles around the fountain axis. When $35 < C$, the fountain behavior becomes highly unsteady and three-dimensional, with a bobbing motion that the fountain front continuously rises, stagnates and then collapses around the next rising front as presented in Figure 2.2(c). The fountain front always attains a maximum in the center of the fountain axis for the bobbing motion, whereas the location of the maximum fountain height for flapping motion is usually off-axis. Moreover, they found that the behavior of a round fountain remains laminar for $Re \leq 120$ and turns into fully turbulent for $2000 \lesssim Re$, independent of Fr. They classified fountains over the range of $120 < Re < 2000$ as the transiti onal fountain [3].

By taking into account the Re influence, Hunt & Burridge [2] presented an overview of the fountain studies with low Re and high Re, and discussed the major features of the behaviors of these fountains, as shown in Figure 2.3.

Although the studies on planar fountains are not as extensive as those for the round fountain, Hunt & Coffey [33] was still able to classify the behavior of planar fountain. In terms of the penetration height, a planar fountain is distinguished as either a very weak fountain for $Fr \lesssim 2.3$, or a weak fountain for $2.3 \lesssim Fr \lesssim 5.7$, or a forced fountain for $5.7 \lesssim Fr$. Again, in this classification, Hunt & Coffey [33] only considered the effect of Fr and did not take into account the effect of Re. The experimental study by Srinarayana *et al.* [58] demonstrates the influence of Re on the behavior of planar fountains and four regimes of the behavior of planar fountains was identified by them in terms of Re, *i.e.*, steady, flapping, laminar mixing and jet-type mixing behavior. They also found that the critical values of Fr for the planar fountain to change from a steady behavior to an unsteady behavior depend on Re. The transition does not depend on Re when $Re \gtrsim 60$ and the critical value

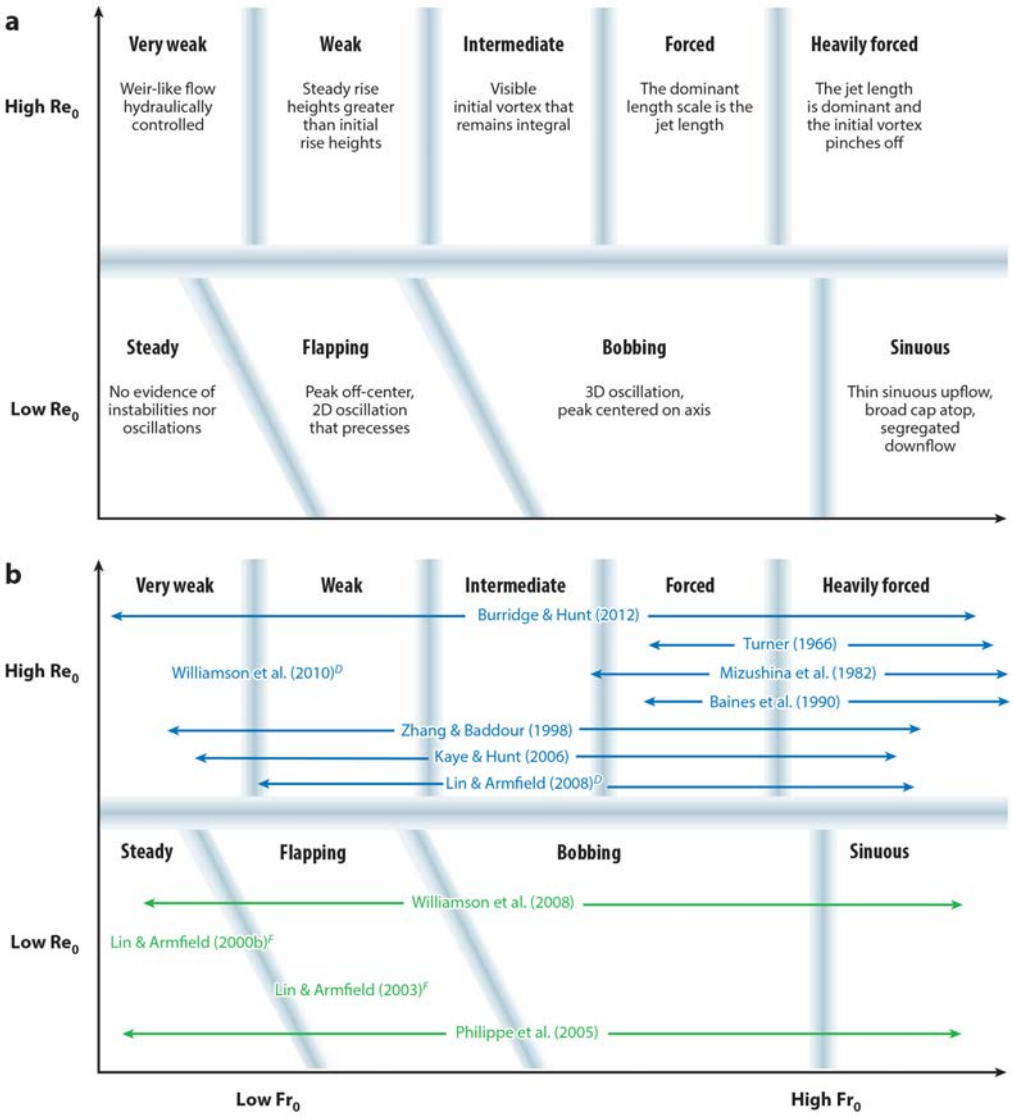

FIGURE 2.3: Fountain classification at low and high Re, and the major fountain features under different categories [2].

is $Fr = 1.0$. However, for $10 < Re \lesssim 50$, the transition depends on Re and the critical values can be approximated by a constant $FrRe^{-2/3}$ line. When Re is further reduced ($Re \lesssim 10$), the dependence of the transition on Re becomes stronger and the demarcation line can be approximated by $Fr \sim Re^n$ (where $n \approx 2 - 4$).

2.3 Free fountains

In large open bodies of fluid, the fountain fluid released from the source is not restricted by physical boundaries, that is, the fountain flow propagates freely through the ambient fluid. Such free fountain can be seen, *e.g.*, in the brine effluent discharged into the ocean or the explosive volcanic eruption into the atmosphere, as mentioned earlier. The majority of the existing studies are on free fountains, as reviewed in [2]. In a free fountain case, the scale of the fountain flow is usually much smaller than that of the ambient, implying that the fountain flow does not significantly modify or influence the nature of the ambient fluid, *e.g.*, the density distribution. Hence, most of the research on free fountain have focused only on the behavior of fountains themselves, with the principal parameters of interest including the maximum penetration heights, entrainment, the onset of asymmetry, *etc.*

2.3.1 Round fountain

2.3.1.1 Maximum penetration height

When the momentum flux at the source is much larger than the negative buoyancy flux ($Fr \gg 1.0$), the fountain flow presents a 'double plume' structure where the inner upflow behaves more like a turbulent jet around by the downflow falling as a dense plume, as shown in Figure 1.1. The maximum penetration height, Z_m, reached by the fountain flow is generally the focus of most early studies on turbulent fountains. Morton [27] pioneered the research on a turbulent round fountain in both homogeneous and stratified environment based on the entrainment assumption proposed by him and his co-workers [59]. Using the integral method, he successfully obtained an analytic solution for the maximum penetration height in terms of the source conditions, which is $z_m = 2.05Fr$, where z_m is the dimensionless maximum penetration height non-dimensionalized by X_0 (*i.e.*, $z_m = Z_m/X_0$) [27]. However, Morton assumed that the vertical flux of the tracer contained in the jet is constant

from the source to the top, which is not realistic. In consideration of the decrease of the vertical flux close to the fountain top, Abraham [60] developed an analytic prediction as $z_m = 2.74Fr$. However, the analysis from both studies is only applicable for the start-up flow at the initial developing stage prior to the creation of the downflow, since the entrainment from the downflow is ignored.

To overcome this shortage, Turner [28] proposed a 'double plume' structure theory for forced round fountains and his dimensional analysis provided the scaling $z_m = C^*Fr$, where C^* is a constant of proportionality. Through a series of experiments on turbulent round fountains for $2 \lesssim Fr \lesssim 30$, C^* was determined as 2.46 [28]. Later, new entrainment equations to quantify the mixing between the upflow and downflow, and between the downflow and ambient fluid permitted McDougall [61] to develop a theoretical model of turbulent round fountains, which gives $z_m = 2.56Fr$. Based on the same idea, Bloomfield & Kerr [29] employed an alternative entrainment formulation between the upflow and downflow to give a theoretical prediction, $z_m = 2.26Fr$, which is in good agreement with their experimental data for $10 \leq Fr \leq 70$. Similar scalings for turbulent fountain were also obtained by some other experimental studies (see, *e.g.*, [32, 62–64]), as listed in Table 2.1. Although considerable discrepancies exist in the values of C^* for these studies, the scalings show that the maximum penetration height of turbulent round fountain only linearly depends on Fr at the source, which may be regarded as robust.

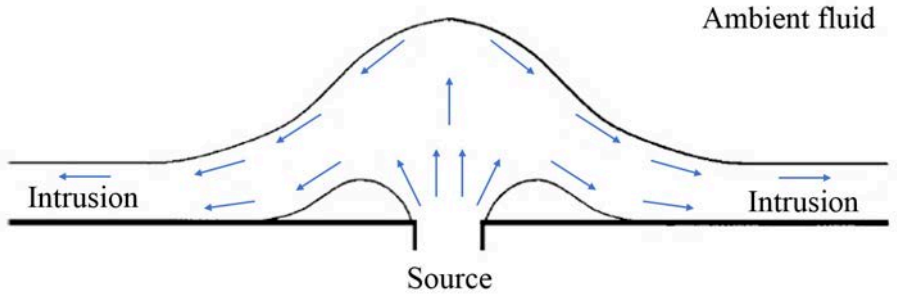

FIGURE 2.4: Sketch of the weak round fountain (after [4]).

For the case with the momentum flux playing the same or less important role than the negative buoyancy flux, the fountain usually remains laminar without distinguishable upward or downward flow. Instead, the streamlines curve and spread from the source as shown in Figure 2.4 [4]. These fountains are classified as weak fountains ($Fr \sim 1$) or very weak fountains ($Fr \ll 1$), which behave considerably different from the turbulent fountains, since the effect of viscosity cannot be ignored (via Re), in addition to the momentum flux and buoyancy flux influence. More recently, weak and very weak round fountains have been investigated through a series of experimental, analytic, and numerical research. For example, Zhang & Baddour [56] found experimentally $z_m = 1.7Fr^{1.3}$ for the round fountain over $1.0 \lesssim Fr < 7.0$. Based on a plume entrainment model, Kaye & Hunt [32] obtained $z_m \sim Fr^2$ and $z_m \sim Fr^{2/3}$ for the round fountain over $1.0 \lesssim Fr \lesssim 3.0$ and $0 < Fr \lesssim 1.0$, respectively. However, these studies did not include the influence of Re. Lin & Armfield [4, 30, 31] carried out a series of numerical simulations to investigate the behavior of round fountains with small Fr and Re values. Their numerical results showed a linear scaling $z_m \sim Fr$ for fountains over the range of $0.2 \leq Fr \leq 1.0$ and $200 \leq Re \leq 800$ [4]. For the fountains with $0.2 \leq Fr \leq 1.0$ and $5 \leq Re \leq 200$, the scaling $z_m \sim FrRe^{-1/2}$ was obtained [30]. The experimental and theoretical study by Philippe *et al.* [52] on round fountains with $Re < 100$ and $Fr \approx 10$ suggested a different scaling, $z_m \sim FrRe^{1/2}$. The reason for the difference of the scalings is due to the different ranges of Fr and Re used for the two studies.

For the round fountain with $0.0025 \leq Fr \leq 0.2$ and $5 \leq Re \leq 800$, the momentum flux is negligible compared to the buoyancy flux and the flow is dominated by the balance between the buoyancy and the viscosity [31]. The dimensional analysis, numerical and experimental studies all identified the scalings $z_m \sim Fr^{2/3}Re^{-2/3}$ [31, 32, 57, 65, 66].

Table 2.1 presents the scaling relations of the maximum penetration height z_m in terms of Fr and Re at the source for both the forced and weak round fountains obtained by the above mentioned studies. A more recent experimental study on

TABLE 2.1: Summary of the scalings obtained for the maximum penetration height of round fountains, after [10].

Authors	**Method**	**Scaling**	Fr **and** Re	**Class**
Morton [27]	Analytic	$z_m = 2.05Fr$	-	Forced
Abraham [60]	Experimental	$z_m = 2.07Fr$	-	Forced
Turner [28]	Analytic	$z_m = 2.46Fr$	$2 \lesssim Fr \lesssim 30$	Forced
McDougall [61]	Analytic	$z_m = 2.56Fr$	-	Forced
Mizushina *et al.* [63]	Experimental	$z_m = 2.35Fr$	$5 \lesssim Fr \lesssim 250$ $1100 \lesssim Re \lesssim 2700$	Forced
Campbell & Turner [62]	Experimental	$z_m = 2.07Fr$	$20 \lesssim Fr \lesssim 90$	Forced
Baines *et al.* [64]	Experimental Analytic	$z_m = 2.46Fr$	$10 \lesssim Fr \lesssim 250$	Forced
Zhang & Baddour [56]	Experimental	$z_m = 1.73Fr^{1.3}$ $z_m = 3.06Fr$	$0.37 \lesssim Fr < 7$ $7 < Fr \lesssim 36.2$	Transition Forced
Bloomfield & Kerr [29]	Analytic	$z_m = 2.26Fr$	$2 \lesssim Fr \lesssim 30$	Forced
Kaye & Hunt [32]	Analytic	$z_m = 0.94Fr^{2/3}$ $z_m = 0.9Fr^2$ $z_m = 2.46Fr$	$0 < Fr \lesssim 1.0$ $1.0 \lesssim Fr \lesssim 3.0$ $3.0 \lesssim Fr$	Laminar Transition Forced
Lin & Armfield [4]	Numerical Dimensional	$z_m \sim Fr$	$0.2 \leq Fr \leq 1.0$ $Re = 200$	Laminar
Lin & Armfield [30]	Numerical Dimensional	$z_m \sim FrRe^{-1/2}$	$0.2 \leq Fr \leq 1.0$ $5 \leq Re \leq 200$	Laminar
Lin & Armfield [31]	Numerical Dimensional	$z_m \sim Fr^{2/3}Re^{-2/3}$	$0.0025 \leq Fr \leq 0.2$ $5 \leq Re \leq 800$	Laminar
Philippe *et al.* [52]	Experimental Analytic	$z_m \sim FrRe^{1/2}$	$1 \lesssim Fr \lesssim 200$ $0 < Re \lesssim 80$	Laminar

round fountain explored the influence of Re and determined the threshold value for Re, *i.e.*, the value beyond which z_m may be regarded as independent of Re [65]. It is observed that when Re is very small, z_m increases with the Re; however, it decreases with Re when Re is large enough, and eventually becomes independent of

Re when Re is very large. The threshold value of Re was identified to depend on Fr at the source, *e.g.*, z_m can be treated as independent of Re when $Re > 1000$ for $Fr \geq 2.0$, or $Re > 500$ for $Fr \leq 1.0$, but for $1.0 \leq Fr \leq 2.0$, no threshold Re was identified. A prevailing summary of the scaling relation for z_m for round fountains in different categories is given by Hunt & Burridge [2], as shown in Section 2.2.

2.3.1.2 Entrainment

The penetrative entrainment is a common feature of all turbulent free-shear flows including jets, plumes and fountains. In the process of entrainment, the surrounding fluid is turbulently engulfed into the plume. This process plays an important role in the development of fountains, since the mass flux entrained from the ambient fluid into the fountain flow controls the dilution rate, resulting in the modification of the opposing buoyancy flux. Additionally, the entrainment also significantly determines the appearance of a fountain, which includes its volume and physical shape [6]. Therefore, it is important to get a comprehensive understanding of the entrainment process and to obtain the entrainment rate. However, the entrainment process by a fountain does not only engulfs fluid from its surrounding environment (including at its top) but also exchanges fluids between its upflow and downflow, which makes it considerably complex.

Previous theoretical and experimental studies of the entrainment for jets and plumes usually focused on determining an entrainment coefficient to achieve turbulence closure. For example, in the closure model proposed by Morton, Taylor & Turner [59], the mean inflow velocity of the entrained fluid u_e across the interface between the flume and the surrounding environment is proportional to the vertical velocity at the same level w, *i.e.*,

$$u_e = \alpha_e w \tag{2.1}$$

where α_e is the entrainment coefficient for the plume. This elegant parameterisation is called as the entrainment hypothesis, which is the cornerstone of the classic plume theory. Moreover, the entrainment hypothesis has also been successfully applied to a variety of other turbulent flows, *e.g.*, buoyant jets in a steady environment [67] and gravity currents [68]. However, experimentally measuring the entrainment coefficient, particularly determining its variation with height, or with the local Froude number is challenging and related work is still continuing [69].

Significant efforts have been made to build simplified theoretical models to describe the dynamics of fountains, from the early studies only on the start-up flow stage (see, *e.g.*, [27, 60]), to the study about the quasi-steady behavior (see, *e.g.*, [29, 61, 70, 71]). The plume theory can be successfully applied for the initial rising-up behavior of fountains. However, to describe the quasi-steady behavior (including both upflow and downflow) by plume theory ideally needs to parameterize the fluid exchange between the upflow and downflow, and between the downflow and the surroundings. To date, the mechanism of these fluid exchanges has not been extensively studied and clearly understood, with no firm conclusions reached yet [72, 73].

However, the bulk entrainment of the ambient fluid (*i.e.*. the entrainment over the fountain as a whole,) can be measured with reasonable accuracy [6]. The measurement of the bulk entrainment estimates the mean dilution of the buoyancy scalar over the fountain as a whole instead of resolving the local entrainment rate. Therefore, no assumptions are required for the interactions between the upflow and downflow, or the entrainment process between the fountains and the surroundings. However, the relevant reported results are still rare, as only two studies have found so far which explicitly explore the bulk entrainment by fountains, that is, the early work of Baines, Corriveau & Reedman [5] and the more recent work by Burridge & Hunt [6].

In the study of Baines *et al.* [5], a fountain was formed by the upward ejection

of dense saline solution into an initially uniform environment of freshwater. The intrusion created by the impingement of the downflow with the floor laterally spread, resulting in a saline layer. The volume flux in the downflow of the fountain at the level of the saline-freshwater interface was inferred by the increasing rate of the saline layer depth, whereas the entrainment above the interface was calculated by estimating the volume flux in the jet-like upflow at the interface height, where the width of the upflow was assumed to linearly increase with the interface level and the source height. Based on the similarity between fountains and plumes, the local Froude number at the density interface Fr_i is assumed to determine the entrainment of a fountain. The main conclusion of their study is that $Q_E/Q_i \propto {Fr_i}^3$ for $Fr_i \leq 3.0$ and $Q_E/Q_i \propto Fr_i$ for $Fr_i \geq 3.0$, where Q_E/Q_i is a dimensionless entrainment volume flux, Q_E and Q_i denoting the volume flux of the entrainment and the upflow at interface height respectively, as shown in Figure 2.5(a).

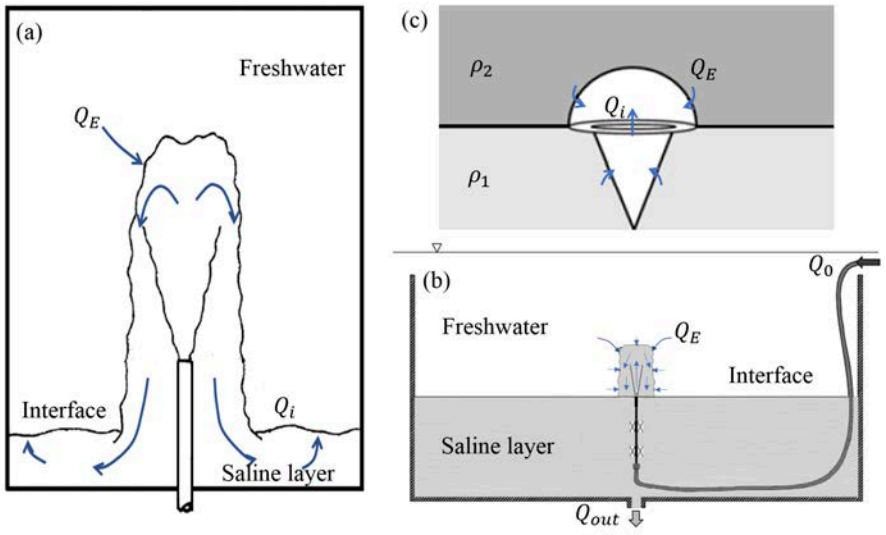

FIGURE 2.5: Sketch of the turbulent entrainment into fountain or fountain-like flows, after [5–7].

Similarly, in the experiments of Burridge & Hunt [6], a saline layer was resulted from the downflow of a round saline fountain in a cylinder initially filled uniform freshwater, as shown in Figure 2.5(b). By modifying the experimental technique proposed by Baines [74], Burridge & Hunt [6] sought for directly quantifying the total volume flux of the entrainment by fountains. In their experiment, the density

interface with a fixed height of the source was achieved for the first time by equaling the volume flux of the downflow to the flow rate of the extract pump. This enabled to directly describe the behavior of fountains in the upper light environment without any theoretical estimation of its evolution, and to deduce the entrainment by measuring the stationary height of the interface rather than the local rate. The bulk entrainment by the fountain was then calculated directly via $Q_E = Q_{out} - Q_0$, where Q_{out} is the volume flux of the fountain downflow (equal to the extract pump flow rate) and Q_0 is the source volume flux as shown in Figure 2.5(b). The fountains in the experiment covered a wide range of the Froude number and the Reynolds number at the source, over $0.004 \leq Fr_0 \leq 25$ and $350 \leq Re_0 \leq 3460$. However, no significant correlation was observed between entrainment and Re_0 after a series of tests, where Re_0 always exceeded the threshold value reported by Burridge, Mistry & Hunt [65]. The results showed the scalings for the dimensionless entrainment volume flux Q_E/Q_0 in terms of Fr, the Froude number at the source, that is,

$$Q_E/Q_0 = \begin{cases} 1.08 \pm 0.025, & Fr \lesssim 0.1, \\ 0.37Fr^{2/3}, & 0.1 \lesssim Fr \lesssim 1.0, \\ 0.38Fr^2, & 1.0 \lesssim Fr \lesssim 2.0, \\ 0.71Fr, & 2.0 \lesssim Fr \lesssim 8.0, \\ 0.77Fr - 1, & Fr \gtrsim 8.0. \end{cases} \tag{2.2}$$

These results have been consistent with the volume flux scalings for fountains on dimensional grounds at low and high Froude numbers [64, 75].

A significant number of studies have focused on determining the entrainment rate across a density interface due to localized forcing by a fountain-like flow. A typical fountain-like flow above the density interface is formed by the upward ejection of the fluid from a localized source within a stratified (usually two-layer) environment as shown in Figure 2.5(c), where the impinging flow can be a buoyant plume (*e.g.*, [76–78]) or turbulent jet (*e.g.*, [79–81]). Although the behavior of these flows is indeed

fountain-like, the entrainment process is influenced by the stratification.

The pioneering work by Turner [82] hypothesized that the entrainment rate can be quantified in terms of the Richardson number at the interface, Ri (notably Ri and Fr_i are interchangeable, as $Fr_i = Ri^{-1/2}$), which has laid the foundation for the research on entrainment across the interface. Based on this hypothesis, Banies [76] carried out experiments on round turbulent plumes or jets impinging on a density interface and identified the following scaling for the dimensionless entrainment rate, Q_E/Q_i, and the Froude number at the interface, Fr_i,

$$Q_E/Q_i \propto {Fr_i}^n \tag{2.3}$$

with $n = 3$ for $0.25 < Fr_i < 1.8$. Regarding the same problem, Kumagai [77] presented the same scaling for $Fr_i \ll 1$, but Q_E/Q_i tends to approaches a constant value (0.56) for $Fr_i \gg 1$. Coffey & Hunt [83] studied the interfacial mixing induced by the impingement of a turbulent freshwater jet in a confined box, whose results also supported that $Q_E/Q_i \propto {Fr_i}^3$ for $Fr_i < 1$ and a constant Q_E/Q_i for $Fr_i > 1$. In another experiment conducted by Cardoso & Woods [78], the entrainment is formed by releasing a rising round plume from a stratified upper layer across an interface into a uniform lower layer. Cardoso & Woods [78] converted the energy for turbulent entrainment into the potential energy of the stratification by assuming the fraction of the kinetic energy supplied at the interface by the plume as constant. Both of their theoretical model and experimental results identified a scaling as $Q_E/Q_i \propto {Fr_i}^2$ for $0.4 \leq Fr_i \leq 1.3$. Moreover, this scaling even fits the Kumagai's [77] data better than that of $Q_E/Q_i \propto {Fr_i}^3$ for the range of $Fr_i \lesssim 1$.

Some other entrainment scalings have also been reported, as reviewed in [85] and [86]. Lin & Linden [84] identified the entrainment coefficient by turbulent fountains impinging on a steady interface to be around 0.65 for $0.9 \lesssim Fr_i \lesssim 2.2$. Shrinvas & Hunt [7] theoretically described the volume flux entrained by a forced

TABLE 2.2: Summary of some scaling relations for entrainment law, after [2, 7].

Authors	**Scaling**	Fr_i/Fr	**Flow type**
Baines [76]	$Q_E/Q_i \propto {Fr_i}^3$	$0.25 \lesssim Fr \lesssim 1.8$	Impinging plume
Kumagai [77]	$Q_E/Q_i \propto {Fr_i}^3$ $Q_E/Q_i \propto Const$	$Fr \ll 1.0$ $1.0 \ll Fr$	Impinging plume
Cardoso & Woods [78]	$Q_E/Q_i \propto {Fr_i}^2$	$0.4 \lesssim Fr \lesssim 1.3$	Impinging plume
Baines *et al.* [5]	$Q_E/Q_i \propto {Fr_i}^3$ $Q_E/Q_i \propto Fr$	$Fr \lesssim 3.0$ $3.0 \lesssim Fr$	Impinging fountain
Lin & Linden [84]	$Q_E/Q_i \propto Fr$	$0.9 < Fr < 2.2$	Impinging fountain
Coffey & Hunt [83]	$Q_E/Q_i \propto {Fr_i}^3$ $Q_E/Q_i \propto Const$	$Fr < 1.0$ $1.0 < Fr$	Impinging plume
Shrinivas & Hunt [7]	$Q_E/Q_i \propto {Fr_i}^2$ $Q_E/Q_i \propto Fr$	$Fr < 1.4$ $3.8 < Fr$	Impinging plume
Burridge & Hunt [6]	$Q_E/Q_0 \propto Const$ $Q_E/Q_0 \propto {Fr_i}^{2/3}$ $Q_E/Q_0 \propto {Fr_i}^2$ $Q_E/Q_0 \propto Fr$	$Fr \lesssim 0.1$ $0.1 \lesssim Fr \lesssim 1.0$ $1.0 \lesssim Fr \lesssim 2.0$ $2.0 \lesssim Fr$	Confined fountain

round jet across a stable density interface in two-layer ambient fluids. They identified $Q_E/Q_i \propto {Fr_i}^2$ for a low-Fr_i regime (*i.e.*, $Fr_i < 1.4$) characterized by an axisymmetric semi-ellipsoidal impingement dome, whereas $Q_E/Q_i \propto Fr_i$ for a high-Fr_i regime (*i.e.*, $3.8 < Fr_i$) characterized by a fully penetrating turbulent fountain. More recently, a phenomenological model was proposed by Debugne & Hunt [87] to quantify the entrainment into the fountain-top, which shows that the volume flux of fountain-top entrainment is proportional to the incoming volume flux.

A summary of the scaling ($Q_E/Q_i \propto {Fr_i}^n$) for entrainment by both fountain and fountain-like flow (by impingement of plumes on density interface) is presented in

Table 2.2. These large discrepancies may be caused by a variety of reasons, including the uncertainties in estimating Q_E, Q_i and Fr_i, and different experiment setups [2]. Additionally, despite box confinement is an innate characteristic of all laboratory experiments, the effect of the confinement on the entrainment behavior has not been taken into account by the studies cited above. To the knowledge of the author, the only study seeking to investigate the confinement influence on entrainment is that of Shrinivas & Hunt [88]. Nevertheless, the entrainment in the study is by a turbulent fountain and a turbulent pure plume in a two-layer environment. The significant discrepancies in fountain entrainment laws and the lack of knowledge about the influence of confinement on the entrainment by fountains (from weak to highly forced) also motivates this thesis. A bulk thermal entrainment or dilution rate of weak planar and round fountains will be defined in this thesis, and will be studied under different source conditions (Fr, Re, Pr) and confinement (λ).

2.3.2 Planar fountain

As mentioned above, a planar fountain results from the ejection of a jet with opposing buoyancy flux from a two-dimensional source (*i.e.*, slot), which widely occurs in engineering applications, such as the downward warm air curtain above tunnels and shop entrances [89]. Additionally, the flow formed by releasing a row of closely spaced round fountains may be regarded as an approximately planar fountain [64], *e.g.*, the underfloor air distribution systems to replenish cooling air in buildings [41]. Although planar fountains have not attracted the same attention like round fountains, some studies have been conducted to investigate the behavior of planar fountains from the early research on turbulent planar fountains (see, *e.g.*, [33, 62, 64, 70]) to recent research on laminar planar fountains (see, *e.g.*, [30, 58, 90–92]). Here only the related studies are summarized. The readers are referred to [2, 33, 86, 93] for a detailed review.

Similar to turbulent round fountains, the dimensionless maximum penetration height of turbulent planar fountain z_m (non-dimensionalized by slot half-width X_0) only depends on the Source Froude number Fr. By extending the research on turbulent round fountain of Turner [28] to turbulent planar fountains, Campbell & Turner [62] and Baines *et al.* [64] analytically obtained a scaling of $z_m = C'Fr^{4/3}$, where $C'$is a constant of proportionality. The experiment conducted by Campell & Turner [62] gave $C' = 1.64 - 1.97$ for $5.6 \lesssim Fr \lesssim 51$. But Baines *et al.* [64] obtained $C' = 0.65$ for $5 \lesssim Fr \lesssim 1000$, which was pointed out as an error in the presentation of the data by Hunt & Coffey [33]. The true value of C' should be 1.64 which have been supported by the experimental result of [70] using the same experimental rig as [64]. The 4/3 power law for the turbulent plane fountain height was also supported by the experimental data of Zhang & Baddour [94], showing a scaling of $z_m = 2.0Fr^{4/3}$ for the range of $10 \lesssim Fr \lesssim 113$. Hunt & Coffey [33] argued the influence of the source geometry used by the studies cited above and developed an analytic solution as $z_m = 0.84Fr^{4/3}$ for the fountain of $Fr \gtrsim 5.7$, which is characterized as turbulent planar fountains. Recently, the numerical studies of Srinarayana *et al.* [58, 91] identified the scaling relation $z_m \propto Fr^{4/3}$ for planar fountains with uniform inlet-velocity profile over $4.0 \leq Fr \leq 10$ and with a parabolic inlet-velocity profile of $2.1 \leq Fr \leq 10$.

Zhang & Baddour [94] proposed two models for weak plane fountains with smaller Fr at which buoyancy flux dominates near these fountain sources. In the first model, the fountain was assumed to develop from a virtual source of momentum flux and buoyancy flux only, and a following empirical scaling relation was identified by dimensional analysis and their experimental results,

$$z_m = (2.0 - 1.12Fr^{-2/3})Fr^{4/3} \tag{2.4}$$

for $0.62 \lesssim Fr \lesssim 6.5$. While the second model was established by assuming z_m proportional to the product of the characteristic vertical velocity W_0 and the time

for a fountain to reach the maximum penetration height which can be scaled with the ratio of the momentum flux and buoyancy flux. The corresponding scaling of the second model for the same Fr range is as follows,

$$z_m = 0.71Fr^2 \tag{2.5}$$

Recently, this scaling relation was modified by Hunt & Coffey [33] using their experimental data as

$$z_m = 0.5Fr^2 \tag{2.6}$$

for $2.3 \lesssim Fr \lesssim 5.7$. The power law $z_m \propto Fr^2$ is also confirmed by the experimental and numerical studies of Srinarayana *et al.* [58, 91], where the scaling was quantified as

$$z_m = 1.05Fr^2 + 2.73 \tag{2.7}$$

A series of dimensional analysis and numerical studies conducted by Lin & Armfield [31, 90] have focused on weak planar fountains and they identified distinct scaling relations for planar fountains of $Fr \sim 1.0$ and $Fr \ll 1.0$. They also took into account the influence of Re at the source [30]. For $0.2 \leq Fr \leq 1.0$ and $5 \leq Re \leq 200$, they gave the following scaling,

$$z_m \sim FrRe^{-1/2} \tag{2.8}$$

whereas for the same Fr, but with sufficiently large Re ($200 \leq Re$), the relation becomes

$$z_m \sim Fr^{4/3} \tag{2.9}$$

which is independent of Re. A similar conclusion has been made for the influence of Re, however, the scaling was quantified as $z_m \sim Fr$ based the DNS results by Lin & Armfield [90]. The experiments conducted by Srinarayana *et al.* [58] confirmed the scaling relation $z_m \sim FrRe^{-1/2}$ for $0.47 \lesssim Fr \lesssim 11.5$ and $2.1 \lesssim Re \lesssim 121$. Similarly, for fountains over $Fr \ll 1.0$, Lin & Armfield [31] determined the following scaling

through dimensional analysis,

$$z_m \sim Fr^{2/3} Re^{-2/3} \tag{2.10}$$

The numerical results for $0.0025 \leq Fr \leq 0.2$ at $Re = 200$ quantified the scaling as follows,

$$z_m = 1.88 Fr^{2/3} \tag{2.11}$$

Notably, the rise height scaling relations $z_m \sim FrRe^{-1/2}$ and $z_m \sim Fr^{2/3}Re^{-2/3}$ for planar fountains are the same as for their counterpart for round fountains [4, 30, 31].

A summary of the scaling relations rise height in planar fountains has been listed in Table 2.3. Hunt & Coffey [33] compared their analytical and experimental results to previous studies, and distinguished the planar fountains into 'very weak', 'weak' and 'forced' depending on the rise height scaling as follows,

- Very weak planar fountains ($Fr \lesssim 2.3$)
- Weak planar fountains ($2.3 \lesssim Fr \lesssim 5.7$)
- Forced planar fountains ($5.7 \lesssim Fr$)

which is currently the prevailing classification of planar fountains in terms of Fr [2].

TABLE 2.3: Summary of the scaling obtained for the maximum penetration height of planar fountains, after [10]

Authors	**Method**	**Scaling**	Fr **and** Re	**Classes**
Campbell & Turner [62]	Experimental	$z_m = C' Fr^{4/3}$ $C' = 1.64 - 1.79$	$5.6 \lesssim Fr \lesssim 51$	Forced
Baines *et al.* [64]	Experimental Analytic	$z_m = 0.65 Fr^{4/3}$	$5 \lesssim Fr \lesssim 1000$	Forced
Zhang & Baddour [94]	Experimental Analytic	$z_m = 2.0 Fr^{4/3}$ -1.12Fr$^{2/3}$ $z_m = 0.71 Fr^2$ $z_m = 2.0 Fr^{4/3}$	$0.62 \lesssim Fr < 6.5$ $0.62 \lesssim Fr < 6.5$ $10 \lesssim Fr \lesssim 113$ $325 \lesssim Re \lesssim 2700$	Transition Forced
Bloomfield & Kerr [70]	Experimental Analytic	$z_m = 1.64 Fr^{4/3}$	$5 \lesssim Fr \lesssim 1000$	Forced
Hunt & Coffey [33]	Analytic	$z_m = 1.5 Fr^{2/3}$ $z_m = 0.5 Fr^2$ $z_m = 0.84 Fr^{4/3}$	$Fr \lesssim 2.3$ $2.3 \lesssim Fr \lesssim 5.7$ $5.7 \lesssim Fr$	Laminar Transition Forced
Srinarayana et al [92]	Numerical	$z_m \sim Fr$ $z_m \sim Fr^{1.15}$ $z_m \sim Fr^{4/3}$	$0.25 \leq Fr \leq 2.0$ $2.25 \leq Fr \leq 3.0$ $4.0 \leq Fr \leq 10.0$ $Re = 100$	Laminar Transition Forced
Srinarayana *et al.* [91]	Numerical	$z_m \sim Fr$ $z_m \sim Fr^2$ $z_m \sim Fr^{4/3}$	$0.25 \leq Fr \leq 1.0$ $1.25 \leq Fr \leq 2.25$ $2.5 \leq Fr \leq 10.0$ $Re = 100$	Laminar Transition Forced
Srinarayana *et al.* [58]	Experimental	$z_m \sim Fr Re^{-1/2}$	$0.47 \lesssim Fr \lesssim 11.57$ $2.1 \lesssim Re \lesssim 121$	Laminar
Lin & Armfield [90]	Numerical Dimensional	$z_m \sim Fr$	$0.2 \leq Fr \leq 1.0$ $200 \leq Re \leq 800$	Laminar
Lin & Armfield [30]	Numerical Dimensional	$z_m \sim Fr Re^{-1/2}$ $z_m \sim Fr^{4/3}$	$5 \leq Re \leq 200$ $200 \leq Re \leq 800$ $0.2 \leq Fr \leq 1.0$	Laminar
Lin & Armfield [31]	Numerical Dimensional	$z_m \sim Fr^{2/3} Re^{-2/3}$	$0.0025 \leq Fr \leq 0.2$ $5 \leq Re \leq 800$	Laminar

2.4 Confined fountain

Most of the existing fountain studies have focused on free fountains, although the box confinement is an innate characteristic of all laboratory experiments. Furthermore, confined fountains widely exist in natural and engineering applications, such as the

replenishment of magma chambers, the cold salt water replenishment in solar ponds, localized cooling air conditioning system in low-energy buildings and the accident leakage of hazardous gases in or between buildings, as mentioned before. Fountain confined with boundaries has received much less attention [2, 88] than free fountains.

As mentioned in Chapter 1, in the case of releasing a fountain in a box initially filled with homogeneous fluid, the impingement of the fountain downflow on the base creates a horizontally spreading gravity current, subsequently resulting in a lower dense layer. Continuing the injection of the fountain fluid, the dense layer gradually deepens, creating a time-dependent density stratification in the box. Obviously, the behavior of the fountain in such a confined environment is more complicated, due to a complex coupling between the time-dependent density stratification and the fountain flow. This kind of confined fountain was first proposed as 'fountain filling box' by Baines *et al.* [64] as a complement to the 'plume filling box' which was named by Turner [95] to the theory of Baines & Turner [96] describing the flow produced by convection (jet or plume) from a source in a confined region.

In the past decades, 'plume filling box' has received extensive attention because of its fundamental and application significance (*e.g.*, a fire plume in buildings) [97], where the focus is on two facets *i.e.*, the dynamics behavior of the plume and the time evolution of density stratification. It has been found that the turbulent jets and plumes in confined space can cause strong secondary flows in the environment, including the strong shear flow (*i.e.*, intrusion) resulted from the plume outflow and the overturning structure (*i.e.*, wall fountain) created by the impingement of the intrusion on side boundaries, in the early development stage [97]. Kaye & Hunt [97] developed theoretical models for a confined pure plume, in which the outflow from the plume was treated as a forced gravity current with constant buoyancy flux, whereas the flow developing along sidewall is modeled as a wall fountain. Two regimes are identified in terms of the box aspect ratio R/H, where R is the radius and H is the height. For a room with large aspect $0.66 < R/H$, the intrusion is pure gravity current when impinging on the sidewall, and the rise height of the wall

fountain only depends on H. However, for $0.2.5 < R/H < 0.66$, the intrusion is not fully developed into pure gravity before the impingement, resulting in the wall fountain height proportional to $(R/H)^{-1/3}$. Their experimental results also agreed with these scalings [97]. Notably, for $R/H < 0.25$, Barnett [98] found that the plume was prevented from impinging with the ceiling due to the downflow in the ambient, which is named as 'blocked' regimes. Apparently, the secondary flows can in turn affect the behavior of the plumes and jets. In another experimental study, Jaluria & Kapoor [99] found that the wall fountain penetration depth only depends on the Froude number of the outflowing buoyant jet. Therefore, the secondary flows (*i.e.*, intrusion and wall fountains) and the development of stratification are significantly influenced by the source conditions and the geometry of the confinement. For more studies on 'plume filling box', the readers are referred to [97] for a review.

Based on the similarity to 'plume filling box', it is reasonable to expect that the intrusion, wall fountain and time-dependent density stratification resulted from 'fountain filling box' are also influenced by the source condition (via Fr and Re) and the confinement conditions. However, only few studies have been reported, from the early work by Baines *et al.* [64] to the latest study about the spanwise confined round fountain [100]. Baines *et al.* [64] developed a confined fountain to infer the entrainment into the fountain, while the effect of confinement has not been addressed. A similar shortage is also found for the experimental research to obtain the entrainment for fountains by plumes impinging with density interface. To the knowledge of the author, only Shrinivas & Hunt [88] took into account of the confinement influence on the entrainment for fountain. In their study, the confinement parameter λ_i is characterized by the ratio of the interfacial turbulence length scale to the depth of the upper layer of the ambient (two-layer). For small λ_i, a weak secondary flow influences the entrainment not significantly, with the scaling relation of $Q_i/Q_0 \propto {Fr_i}^2$. While for large λ_i, a strong secondary flow significantly influences the entrainment, with the scaling relation of $Q_i/Q_0 \propto {Fr_i}^3$ [88]. More recently, Debugne & Hunt [100] experimentally studied the influence of spanwise confinement

on turbulent round fountains. Four flow regimes have been identified by them for the fountain with $0.5 \leq Fr \leq 96$ and the confinement ratio $2 < W/R_0 < 24$, where W is the gap width and R_0 is the source radius. To encompasses the effects of confinement, a 'confined' Froude number $Fr_c \equiv Fr(W/R_0)^{-5/4}$ was introduced as the governing parameter for confined fountains. Notably, the fountain is only spanwise confined, with no confinement in lateral wise. Lippert & Woods [101] theoretically and experimentally examined a particle fountain in a confined environment recently, identifying four regimes for the flow with different source conditions, which is beyond the scope of this study.

Additionally, a fountain may impinge with, or develop along a boundary. When a fountain impinges with a flat solid ceiling/floor, an outward intrusion flow is created and then detaches from the ceiling/floor under the influence of buoyancy. The spreading distance of the intrusion along the horizontal surface before the detachment has been studied numerically and experimentally (see, *e.g.*, [10, 93, 102]). In some circumstances, the impinging surface may be replaced by the interface of phase or density, see, *e.g.*, [84, 103, 104]. A detailed summary has been given by Srinarayana *et al.* [10], and the readers are referred to it for a review.

2.5 Summary

Fountains have received extensive attention from researchers in the past six decades and the related research continues to be reported nowadays. Most of the existing studies have focused on the fountains freely propagating and mixing with the ambient fluid. While the impinging fountain, wall fountain and confined fountain have received relatively little attention, particularly confined fountains. Additionally, the previous studies about the confined fountain or fountain-like flow are all about the turbulent fountain, whereas studies on the weak fountain filling box (no mater planar or round) are not reported, to the best knowledge of the author.

The maximum penetration height is the main parameter to represent the behavior of fountain in the previous studies on fountains. With distinct scaling relations for the penetration height in terms of Fr, the classification from 'very weak' to 'forced' fountains has been made for both round and planar fountains. Although a few studies (*e.g.*, [3, 30, 58]) have examined the effects of Re on the maximum penetration height, no firm conclusion has been obtained for the role of Re in the fountain classification. In a confined space, the outflow of the fountain can cause strong secondary shear flows in the environment, such as the intrusion and overturning. Similar to the study of 'plume filling box', the intrusion and overturning can be modeled as purely gravity current and wall fountain [97], which are significantly influenced by the confinement. At the early development stage, the behavior of intrusion for a confined fountain is the same as for a free fountain [105]. Another important characteristic of a confined fountain is the time-dependent density stratification due to the continuous filling by fountain. The existing confined fountain or fountain-like studies have mainly focused on the entrainment process for the fountain. No clear understanding of the secondary flows (*i.e.*, intrusion and wall fountain), time-dependent stratification and their coupling in fountain filling box has been obtained.

Up to date, all the confined fountain (fountain filling box) studies are conducted experimentally, which allows the researcher to measure the bulk behavior of the fountain, *e.g.*, the penetration distance and the bulk entrainment into the fountain. However, the detailed internal dynamics of fountains are difficult to explore by experiments. Numerical simulations, particularly direct numerical simulation (DNS), enable researchers to reveal the internal structure (density distribution) and the couplings between the fountain, the secondary flows and the time-dependent stratification. Another advantage offered by numerical simulation is that any values of the governing parameters (Fr, Re and Pr) can be achieved accurately, although the computational consumption is still challenging for DNS of high Re.

All of these motivate the current study.

Chapter 3

Methodologies

3.1 Introduction

In this thesis, the behavior of round and planar fountains (from weak to forced) in a confined space with a homogeneous fluid is studied by a combination of methodologies, including direct numerical simulation (DNS), scaling analysis and experiments with high-speed cameras techniques to record the flow visualization (by food dye). A brief description of the major methodologies and techniques is given in this chapter. To be more specific, the numerical methods will be presented in § 3.2, while the experimental methods will be described in § 3.3. The technique for the scaling analysis will be presented in subsequent chapters when it is used for pertinent situations.

3.2 Numerical methods

The physical systems under consideration here are illustrated in Figure 1.8 and the corresponding computational domain used for the numerical simulations will be presented introduced in § 4.2 and § 5.2 respectively. For the unsteady confined

weak/transitional fountains considered in this study, the governing equations are the Navier-Stokes equations and the temperature equation, which are presented in § 3.2.1, along with the appropriate boundary and initial conditions, for both planar and round fountains. In § 3.2.2, the Finite Volume Method (FVM) to solve the governing equations is introduced and a brief description of the commercial computational fluid dynamics (CFD) software package ANSYS Fluent 17 is also given. The discretization of governing equations and solution strategy in the CFD modelling are detailed in § 3.2.3 and § 3.2.4, respectively. In § 3.2.5, the setup of Fluent to carry out the simulation is briefly presented.

3.2.1 Governing equations, initial and boundary conditions

The governing equations for fountains considered in this thesis are Navier-Stokes equations and temperature equation with the Oberbeck-Boussinesq approximation, which assumes that density $\rho(T)$ has a linear relation with temperature T solely in the buoyancy term, as follows,

$$\rho(T) = \rho(P_0, T_0)[1 - \beta(T - T_0)]. \tag{3.1}$$

where P_0 denotes the reference pressure at the reference temperature T_0. The approximation also assumes that the changes of other properties of the fluid with temperature are negligible, under the condition that the relative density ratio $(\rho(T) - \rho(P_0, T_0))/\rho(P_0, T_0)$ is trivial. Under such a condition, a fountain is called a Boussinesq fountain. Otherwise it is a non-Boussinesq fountain. However, a considerable discrepancy exists in the previous studies to determine the critical value for the relative density ratio. For positively buoyant jet, Crapper & Baines [106] identified the Oberbeck-Boussinesq assumption valid up to $(\rho(T) - \rho(P_0, T_0))/\rho(P_0, T_0) \approx 0.05$, which is confirmed by the forced plume study conducted by Ai *et al.* [107]. Whereas for fountain flow, Baddour & Zhang [108] suggested $(\rho(T) - \rho(P_0, T_0))/\rho(P_0, T_0) \approx$

0.003 as the critical value for distinguishing Boussinesq and non-Boussinesq fountains. To ensure the Oberbeck-Boussinesq approximation is valid for this study, the relative density ratio smaller than 0.0009 is used.

3.2.1.1 Confined planar fountains

For a two-dimensional planar fountain in a confined homogeneous environment, the two-dimensional incompressible Navier-Stokes and temperature equations are written in the Cartesian coordinates (X, Y) as follows,

$$\frac{\partial U}{\partial X} + \frac{\partial V}{\partial Y} = 0, \tag{3.2}$$

$$\frac{\partial U}{\partial t} + \frac{\partial (UU)}{\partial X} + \frac{\partial (VU)}{\partial Y} = -\frac{1}{\rho}\frac{\partial P}{\partial X} + \nu \left(\frac{\partial^2 U}{\partial X^2} + \frac{\partial^2 U}{\partial Y^2} \right), \tag{3.3}$$

$$\frac{\partial V}{\partial t} + \frac{\partial (UV)}{\partial X} + \frac{\partial (VV)}{\partial Y} = -\frac{1}{\rho}\frac{\partial P}{\partial Y} + \nu \left(\frac{\partial^2 V}{\partial X^2} + \frac{\partial^2 V}{\partial Y^2} \right) + g\beta(T - T_0), \tag{3.4}$$

$$\frac{\partial T}{\partial t} + \frac{\partial (UT)}{\partial X} + \frac{\partial (VT)}{\partial Y} = \kappa \left(\frac{\partial^2 T}{\partial X^2} + \frac{\partial^2 T}{\partial Y^2} \right). \tag{3.5}$$

where U and V are velocity components in the X and Y directions, T is temperature, P is pressure, t is time, and κ and ν are the thermal diffusivity and the kinematic viscosity of the fluid, respectively. These governing equations can be further written in the following dimensionless form,

$$\frac{\partial u}{\partial x} + \frac{\partial v}{\partial y} = 0, \tag{3.6}$$

$$\frac{\partial u}{\partial \tau} + \frac{\partial (uu)}{\partial x} + \frac{\partial (vu)}{\partial y} = -\frac{\partial p}{\partial x} + \frac{1}{Re} \left(\frac{\partial^2 u}{\partial x^2} + \frac{\partial^2 u}{\partial y^2} \right), \tag{3.7}$$

$$\frac{\partial v}{\partial \tau} + \frac{\partial (uv)}{\partial x} + \frac{\partial (vv)}{\partial y} = -\frac{\partial p}{\partial y} + \frac{1}{Re} \left(\frac{\partial^2 v}{\partial x^2} + \frac{\partial^2 v}{\partial y^2} \right) + \frac{1}{Fr^2}\theta, \tag{3.8}$$

$$\frac{\partial \theta}{\partial \tau} + \frac{\partial (u\theta)}{\partial x} + \frac{\partial (v\theta)}{\partial y} = \frac{1}{RePr} \left(\frac{\partial^2 \theta}{\partial x^2} + \frac{\partial^2 \theta}{\partial y^2} \right), \tag{3.9}$$

where x and y are the dimensionless coordinates, u and v are the dimensionless velocity components in the x and y directions, and τ, p and θ are the dimensionless time, pressure and temperature, respectively, which are made dimensionless by their respective scales as follows,

$$\left.\begin{aligned} x = \frac{X}{X_0}, \quad y = \frac{Y}{X_0}, \quad u = \frac{U}{W_0}, \quad v = \frac{V}{W_0}, \\ \tau = \frac{t}{X_0/W_0}, \quad p = \frac{P}{\rho W_0^2}, \quad \theta = \frac{T - T_a}{T_a - T_0}. \end{aligned}\right\} \tag{3.10}$$

in which X_0, W_0, and T_0 are the half-width, the average vertical velocity and the temperature of the ejected fountain fluid at the source slot, respectively, whereas T_a is the temperature of the ambient fluid at the before the commencement of the fountain flow. With using X_0 and W_0 as the reference length and velocity, a reference time is determined as X_0/W_0, which is used for the non-dimensionalization of τ as above. Re, Fr and Pr are the Reynolds, Froude and Prandtl numbers as expressed in Eqs.(1.1), (1.2) and (1.3).

The appropriate initial and boundary conditions, as presented in Figure 1.8, are as follows,

$$u = v = 0, \quad \theta = 0, \quad \text{at all} \quad x, y \quad \text{and} \quad \tau < 0 \tag{3.11}$$

and at $\tau \geq 0$,

$$\left.\begin{aligned} &u = 0, \quad \frac{\partial v}{\partial x} = 0, \quad \frac{\partial \theta}{\partial x} = 0 \quad \text{on} \quad x = \pm L/X_0, \quad 0 \leq y \leq H/X_0; \\ &u = 0, \quad v = 1, \quad \theta = -1, \quad \text{on} \quad -1 \leq x \leq 1, \quad y = 0; \\ &u = 0, \quad v = 0, \quad \frac{\partial \theta}{\partial y} = 0, \quad \text{on} \quad 1 < x \leq L/X_0, \quad y = 0; \\ &u = 0, \quad v = 0, \quad \frac{\partial \theta}{\partial y} = 0, \quad \text{on} \quad -L/X_0 \leq x < -1, \quad y = 0; \\ &\frac{\partial u}{\partial y} = \frac{\partial v}{\partial y} = \frac{\partial \theta}{\partial y} = 0, \quad \text{on} \quad -L/X_0 \leq x \leq L/X_0, \quad y = H/X_0. \end{aligned}\right\} \tag{3.12}$$

3.2.1.2 Confined round fountains

For a three-dimensional round fountain in a confined homogeneous ambient fluid, the Navier-Stokes and temperature equations with the Oberbeck-Boussinesq assumption can be written in dimensionless form in cylindrical coordinates (r, φ, z) as follows,

$$\frac{1}{r}\frac{\partial(ru_r)}{\partial r} + \frac{1}{r}\frac{\partial u_\varphi}{\partial \varphi} + \frac{\partial u_z}{\partial z} = 0, \tag{3.13}$$

$$\begin{aligned}\frac{\partial u_r}{\partial \tau} + u_r\frac{\partial u_r}{\partial r} + \frac{u_\varphi}{r}\frac{\partial u_r}{\partial \varphi} - \frac{u_\varphi^2}{r} + u_z\frac{\partial u_r}{\partial z} = \\ -\frac{\partial p}{\partial r} + \frac{1}{Re}\left[\frac{1}{r}\frac{\partial}{\partial r}\left(r\frac{\partial u_r}{\partial r}\right) - \frac{u_r}{r^2} + \frac{1}{r^2}\frac{\partial^2 u_r}{\partial \varphi^2} - \frac{2}{r^2}\frac{\partial u_\varphi}{\partial \varphi} + \frac{\partial^2 u_r}{\partial z^2}\right],\end{aligned} \tag{3.14}$$

$$\begin{aligned}\frac{\partial u_\varphi}{\partial \tau} + u_r\frac{\partial u_\varphi}{\partial r} + \frac{u_\varphi}{r}\frac{\partial u_\varphi}{\partial \varphi} + \frac{u_r u_\varphi}{r} + u_z\frac{\partial u_\varphi}{\partial z} = \\ -\frac{1}{r}\frac{\partial p}{\partial \varphi} + \frac{1}{Re}\left[\frac{1}{r}\frac{\partial}{\partial r}\left(r\frac{\partial u_\varphi}{\partial r}\right) - \frac{u_\varphi}{r^2} + \frac{1}{r^2}\frac{\partial^2 u_\varphi}{\partial \varphi^2} - \frac{2}{r^2}\frac{\partial u_r}{\partial \varphi} + \frac{\partial^2 u_\varphi}{\partial z^2}\right],\end{aligned} \tag{3.15}$$

$$\begin{aligned}\frac{\partial u_z}{\partial \tau} + u_r\frac{\partial u_z}{\partial r} + \frac{u_\varphi}{r}\frac{\partial u_z}{\partial \varphi} + u_z\frac{\partial u_z}{\partial z} = \\ -\frac{\partial p}{\partial z} + \frac{1}{Re}\left[\frac{1}{r}\frac{\partial}{\partial r}\left(r\frac{\partial u_z}{\partial r}\right) + \frac{1}{r^2}\frac{\partial^2 u_z}{\partial \varphi^2} + \frac{\partial^2 u_z}{\partial z^2}\right] + \frac{1}{Fr^2}\phi,\end{aligned} \tag{3.16}$$

$$\frac{\partial \theta}{\partial \tau} + u_r\frac{\partial \theta}{\partial r} + \frac{u_\varphi}{r}\frac{\partial \theta}{\partial \varphi} + u_z\frac{\partial \theta}{\partial z} = \frac{1}{RePr}\left[\frac{1}{r}\frac{\partial}{\partial r}\left(r\frac{\partial \theta}{\partial r}\right) + \frac{1}{r^2}\frac{\partial^2 \theta}{\partial \varphi^2} + \frac{\partial^2 \theta}{\partial z^2}\right], \tag{3.17}$$

where r and z are made dimensionless by X_0 and u_r and u_z, which are the dimensionless velocity components in the r and and z directions, which are made dimensionless by W_0, respectively. φ (in radiant) is itself dimensionless. For two-dimensional round fountain cases, the flow is axisymmetric and u_φ is zero.

The following initial and boundary conditions are for round fountains, as also presented in Figure 1.8,

$$u = v = 0, \quad \theta = 0, \quad \text{at all} \quad r, \varphi, z \quad \text{and} \quad \tau < 0 \tag{3.18}$$

and at $\tau \geq 0$,

$$\left.\begin{aligned}
&u_r = u_\varphi = u_z = 0, \quad \text{on} \quad r = 1, \quad 0 \leq \varphi \leq 2\pi, \quad 0 \leq z \leq H/X_0; \\
&u_r = u_\varphi = 0, \quad u_z = 1, \quad \theta = -1, \quad \text{on} \quad 0 \leq r \leq 1, 0 \leq \varphi \leq 2\pi, \quad z = 0; \\
&u_r = u_\varphi = u_z = 0, \quad \frac{\partial \theta}{\partial z} = 0, \quad \text{on} \quad 1 < r \leq R/X_0, 0 \leq \varphi \leq 2\pi, \quad z = 0; \\
&\frac{\partial u_r}{\partial z} = \frac{\partial u_\varphi}{\partial z} = \frac{\partial u_z}{\partial z} = \frac{\partial \theta}{\partial z} = 0, \quad \text{on} \quad 0 \leq r \leq R/X_0, 0 \leq \varphi \leq 2\pi, \quad z = H/X_0.
\end{aligned}\right\} \tag{3.19}$$

For all direction numerical simulations in this study, the heights of both the rectangular box for planar fountains and the cylinder container for round fountains are set high enough to eliminate the influence of the top boundary on the fountain behavior.

3.2.2 Numeral techniques

The above governing equations must be solved numerically to obtain approximate solutions. There are a number of commercial CFD packages available to do so, such as, ANSYS Fluent, ANSYS CFX, COMSOL Multiphysics, OPENFOAM, STAR CCM+, FLOW3D and PHOENICS etc. Currently ANSYS Fluent is the most popular. In this thesis, all numerical simulations are carried out by using ANSYS Fluent 17.

There are two solvers available in ANSYS Fluent for the simulation, namely the pressure-based solver, originally developed for low-speed incompressible flows, and density-based solver, originally developed for high-speed compressible flows. However, both solvers have experienced significant modifications and been extended to solve a wider range of flows than their traditional or original intent. For the pressure-based solver, the velocity filed is obtained from the momentum equations and the pressure field is determined by solving a pressure or pressure correction equation which is derived from the continuity equation. This solver is selected in this thesis.

In ANSYS Fluent, the finite volume method is employed to solve the governing equations. The general procedure for the finite volume method consists of the following steps: firstly, the whole computational domain is divided into numerous discrete control volumes to form a computational mesh, the governing equations are then discretized on each control volume using different schemes to convert the partial differential equations into algebraic equations, and subsequently these discretized equations are solved using solvers to give the solutions, which generally require numerous iterations to ensure the accuracy of the solutions. A more specific description of the procedure is shown in Figure 3.1 where the solution algorithm is presented (see ANSYS Fluent Theory Guide [9] for details).

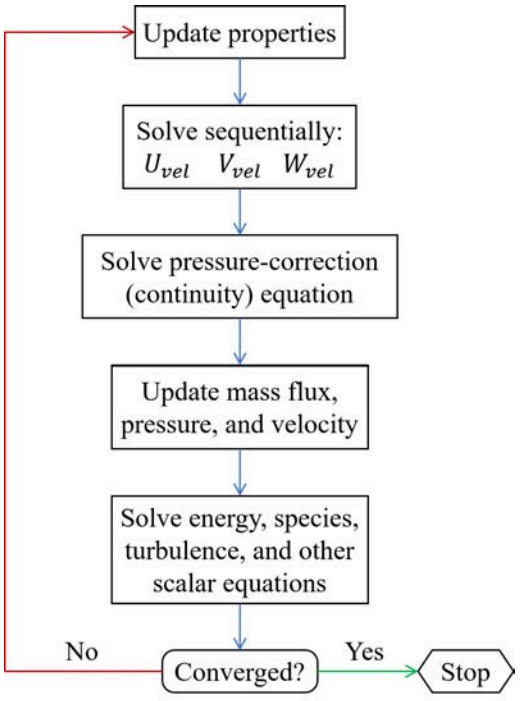

FIGURE 3.1: The flow chart of the pressure-based solution method with Segregated algorithm

3.2.3 Discretization of governing equations

The governing equations are discretized on finite control volumes. The discretization is demonstrated here using the two-dimensional governing equations Eqs.(3.2)-(3.5)

for plane fountains. These governing equations can be represented by the following equation for a general parameter ϕ,

$$\frac{\partial(\rho\phi)}{\partial t} + \frac{\partial(\rho U_i\phi)}{\partial X_i} = \Gamma_\phi \frac{\partial^2\phi}{\partial {X_i}^2} + S_\phi, \tag{3.20}$$

where Γ_ϕ denotes diffusion coefficient for ϕ and S_ϕ is the source term and $i = 1$ for X and $i = 2$ for Y. In the above equation, the first term $(\partial(\rho\phi)/\partial t)$ and the second term $(\partial(\rho U_i\phi)/\partial X)$ on the left side are the transient term and the convection term, and the first term on the right side $(\Gamma_\phi \partial^2\phi/\partial {X_i}^2)$ is the diffusion term. By assigning different values to ϕ, Γ_ϕ and S_ϕ, this general equation can represent any of Eqs.(3.2)-(3.5). The equation reduces to the continuity equation (Eq.(3.2)) when $\phi = 1$, $\Gamma_\phi = 0$ and $S_\phi = 0$. Eq.(3.3) is obtained by assigning $\phi = U$, $\Gamma_\phi = \nu$ and $S_\phi = 0$, Eq.(3.4) is obtained by assigning $\phi = V$, $\Gamma_\phi = \nu$ and $S_\phi = g\beta(T - T_0)$, and Eq.(3.5) is obtained by assigning $\phi = T$, $\Gamma_\phi = \kappa$ and $S_\phi = 0$.

As illustrated in Figure 3.2, a two-dimensional staggered mesh consists of numerous control volumes represented by a box, with 'e', 's', 'w' and 'n' denoting the east, south, west and north sides, respectively. The control volume is represented by 'P' which is located at its center, while its four neighboring control volumes are denoted by 'E' (for east), 'S' (for south), 'W' (for west), and 'N' (for north), all of them are also located their individual center.

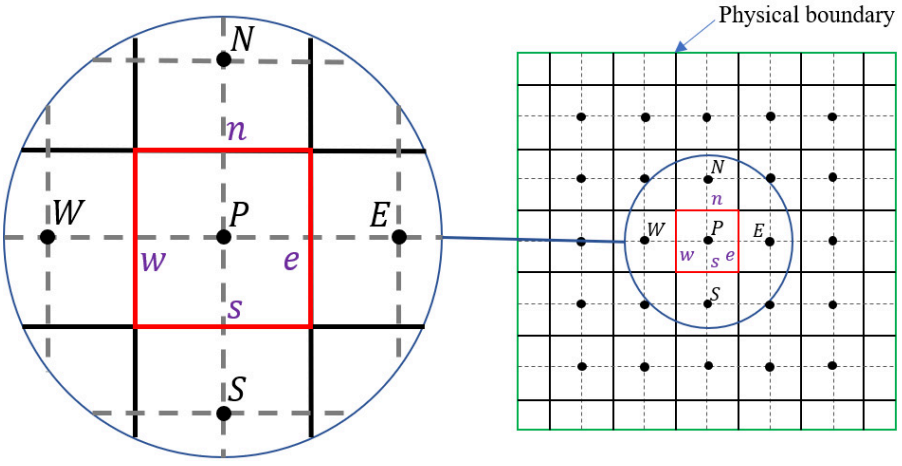

FIGURE 3.2: The sketch of a two-dimensional mesh and control volumes (after [8]).

With finite volume method, the general equation Eq.(3.20) is integrated over each control volume as follows,

$$\int_V \frac{\partial(\rho\phi)}{\partial t}dV + \int_V \frac{\partial(\rho U_i\phi)}{\partial X_i}dV = \int_V \Gamma\frac{\partial^2\phi}{\partial {X_i}^2}dV + \int_V SdV. \tag{3.21}$$

By using the Gauss Divergence Theorem, the above equation can be converted into the following expression,

$$\int_V \frac{\partial(\rho\phi)}{\partial t}dV + \int_S \rho U_i\phi n_i dS = \int_S \Gamma\frac{\partial\phi}{\partial X_i}n_i dS + \int_V SdV. \tag{3.22}$$

where n_i represents the Cartesian component of the outward normal surface vector. In this thesis, the 3rd-order QUICK scheme and the 2nd-order central difference scheme are selected for the discretization of the convection and diffusion terms, respectively, while the 2nd-order backward scheme is used for the time integration.

By using the 2nd-order central difference scheme, the discretization of the diffusion term can be written as follows:

$$\int_S \Gamma\frac{\partial\phi}{\partial X_i}n_i dS = \frac{\Gamma A_e}{\Delta X_{PE}}(\phi_E-\phi_P)-\frac{\Gamma A_w}{\Delta X_{PW}}(\phi_P-\phi_W)+\frac{\Gamma A_n}{\Delta X_{PN}}(\phi_N-\phi_P)-\frac{\Gamma A_s}{\Delta X_{PS}}(\phi_P-\phi_S). \tag{3.23}$$

where ΔX_{PE}, ΔX_{PW}, ΔX_{PN}, and ΔX_{PS} are the distances between 'P' and 'E', 'W', 'N' and 'S', respectively.

The convection term is the integration of the fluxes through the four cell faces surrounding the control volume, which can be represented as,

$$\int_S \rho U_i\phi n_i dS = \rho u_e A_e\phi_e - \rho u_w A_w\phi_w + \rho u_n A_n\phi_n - \rho u_s A_s\phi_s. \tag{3.24}$$

This equation integrates the values of ϕ at the cell faces of the control volume. However, the solutions for variables store at the centre of the control volume (*i.e.*, at P, E, W, N, and S) in ANSYS Fluent. Therefore, the values of ϕ at the faces need to be approximated by the values at the center of the control volume by using

an 'advection scheme'. Due to the highly nonlinear nature of this term, a high order discretization scheme must be used to ensure accuracy. The most popular one is the third-order QUICK scheme, which is thus selected in this thesis to discretize the convection term.

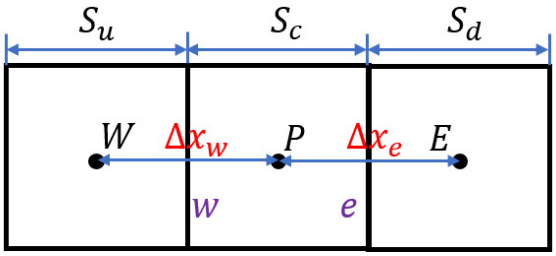

FIGURE 3.3: The sketch of three neighbouring control volumes to illustrate the QUICK scheme for convection term (after [9]).

The QUICK scheme using a three-point upwind weighted quadratic interpolation to determine the face vales. As shown in Figure 3.3, the variable value at face e can be determined by the following equation,

$$\phi_e = \alpha[\frac{S_d}{S_c+S_d}\phi_P + \frac{S_c}{S_c+S_d}\phi_E] + (1-\alpha)[\frac{S_u+2S_c}{S_u+S_c}\phi_P - \frac{S_c}{S_u+S_c}\phi_W]. \quad (3.25)$$

where α is factor depending on the scheme. The traditional QUICK scheme is corresponding to $\alpha = 1/8$.

The discretization process above only considers the steady terms in the governing equations, which is for steady simulations. However, in this thesis the simulation is for transient flow behavior. Therefore, the governing equations must be discretized in both space and time. The spatial discretization for transient governing equations is identical to the process for steady-state equations above. While the temporal discretization involves the integration of every term in the differential equations over a time step Δt. The integration of the transient terms is straight forward. A generic expression of the time progression of the quantity ϕ is assumed by,

$$\frac{\phi}{t} = F(\phi). \quad (3.26)$$

By using a backward difference scheme with second-order discretization and implicit time integration, the discretization of the transient equation is given as

$$\frac{3\phi^{n+1} - 4\phi^{n} + \phi^{n-1}}{2\Delta t} = F(\phi^{n+1}). \tag{3.27}$$

where $n+1$, n and $n-1$ denote the next time level $(t+\Delta t)$, current time level (t) and the previous time level $(t-\Delta t)$, respectively.

In this section, only the basic formulation of the finite volume method used in ANSYS Fluent 17.0 is briefly presented. The reader is referred to the user manual of ANSYS Fluent 17, or in some related CFD books, *e.g.*, [109–111], for more detailed information.

3.2.4 Solution Strategies

3.2.4.1 Solving the Linear Equations

As illustrated above, the discretization converts the non-linear partial differential equations into linear ordinary differential equations. The discretized transport equation contains the unknown scalar variable ϕ_P at the centre of the control volume and the unknown values at the cell faces between the surrounding cells, which can be written as follows,

$$a_P\phi = \sum_{nb} a_{nb}\phi_{nb} + b. \tag{3.28}$$

where the subscript nb refers to neighboring cells, and a_P and a_{nb} represent the linearized coefficients for ϕ_P and ϕ_{nb}, respectively. The number of neighbors for each cell is decided by the mesh topoloy, which is typically equal to the number of faces enclosing the cell except for the boundary cells. The discretization for each cell is therefore produces a set of algebraic linear equations with a sparse coefficient matrix, which will be solved through a point implicit (Gauss-Seidel) linear equation

solver in conjunction with an algebraic multigrid (AMG) method in ANSYS Fluent. The reader can find detailed information from the ANSYS Fluent User's Guide [9].

3.2.4.2 Controlling the iterative process

It is essential to control the change of the scalar variable ϕ during the iterative solution process by ANSYS Fluent to ensure the solution converges. This is usually done by the under-relaxation of variables (also named as explicit relaxation), through which the change of variables ϕ produced during each iteration is reduced. The new value of variable ϕ in a cell can be determined through the following simple form in terms of the old value ϕ_{old} and the computed change in the variable $\Delta\phi$,

$$\phi = \phi_{old} + a\Delta\phi. \tag{3.29}$$

where a is the under-relaxation factor.

3.2.4.3 Convergence

The success and efficiency of the iterative calculation depend on an appropriate convergence criterion. Since the errors from the previous time step will transfer to the next step in a numerical simulation of unsteady flows, without appropriate convergence criterion setting, the solution may not converge, even resulting in a failure in simulating the real physical flow.

However, there is no universal criterion for judging convergence. For most types of flows, examining the residual levels can be used for the convergence judgment. The residual R^{ϕ} computed by a pressure-based solver in ANSYS Fluent is defined as the imbalance in Eq.(3.28) summed over all control volumes, which can be written as

$$R^{\phi} = \sum_{cells P} \mid \sum_{nb} a_{nb}\phi_{nb} + b - a_P\phi_P \mid . \tag{3.30}$$

where the subscripts denote the same parameters as those of Eq.(3.28). However, using the residuals defined by Eq.(3.30) is difficult, since no scaling is employed, for example, there is no inlet flow rate of ϕ for natural convection in a room to compare the residual. Therefore, ANSYS Fluent uses a scaling factor representative of the flow rate of ϕ to scale the residual, which is defined as follows,

$$R^{\phi} = \frac{\sum_{cells P} \mid \sum_{nb} a_{nb}\phi_{nb} + b - a_P\phi_P \mid}{\sum_{cells P} \mid a_P\phi_P \mid}. \tag{3.31}$$

While for the momentum equations, the scaling factor is changed by replacing the denominator term $a_P\phi_P$ with $a_P v_P$, where v_P is the magnitude of the velocity at cell P. In this thesis, residual levels are selected as the indicator of convergence. Notably, in some conditions residuals may be not appropriate to be the criterion. In such cases, monitoring relevant integrated quantities (*e.g.*, drag or heat transfer coefficient) as a complement to examining residual levels is useful to judge convergence. Details about the convergence criterion selection can be found in the ANSYS Fluent User's Guide [9].

3.2.5 Fluent setup

Again the two-dimensional planar fountain is used here as an example to illustrate the procedure for the setup in Fluent. A new fluent fluid flow analysis system can be created from the ANSYS Workbench by selecting **Fluid Flow (FLUENT)** under **Analysis Systems** listed on the left as shown in Figure 3.4. The project consists of five cells, *i.e.*, **Geometry**, **Mesh**, **Setup**, **Solution** and **Results**. In this example, a non-uniform mesh document created by ICEM CFD software is directly imported into the **Mesh** cell. The detailed information of the non-uniform mesh will be presented in Chapter 4. By double-clicking the **Setup** cell in the Project Schematic, ANSYS Fluent 17 will be started with displaying Fluent Launcher, as shown in Figure 3.5.

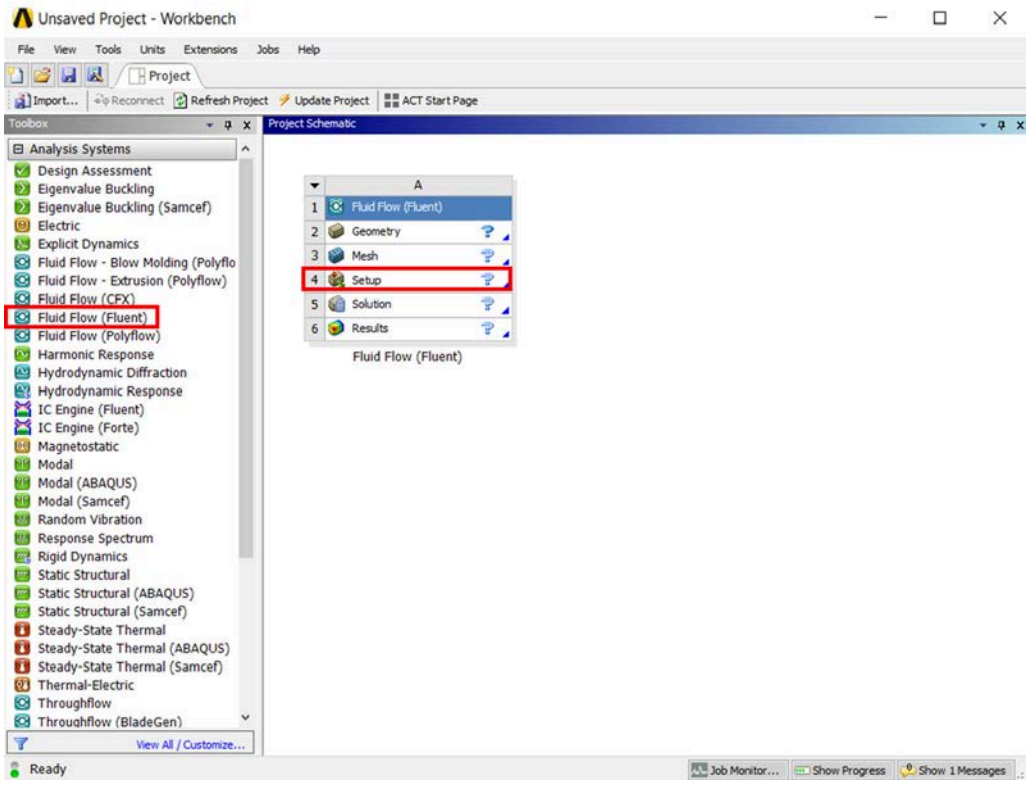

FIGURE 3.4: Starting the Fluid Flow (FLUENT) analysis system in the ANSYS Workbench.

The Fluent Launcher allows users to decide the version of ANSYS Fluent to use, based the geometry and the processing capabilities of the computational source. Here ANSYS Fluent automatically set the **Dimension** as 2D based on the mesh for the current system. To achieve high accuracy calculation, **Double Precision** is selected under **Options** . **Parallel** is selected with setting **Number of Processes** as 8 for **Processing Options** to enhance the calculation efficiency for the computers used in the numerical simulation in this thesis. Then click the **OK** button, a graphical user interface (GUI) of Fluent is launched, as shown in Figure 3.6. A navigation pane is on the left part of the GUI, including a list of items *i.e.*, **Problem Setup**, **Solution** and **Results**. The setup of these items can be achieved through an individual task page which will be shown by double-clicking the corresponding item. The functions of the region of GUI are as shown in Figure 3.6. The Fluent Launcher can also be directly started from the Windows **Start** menu.

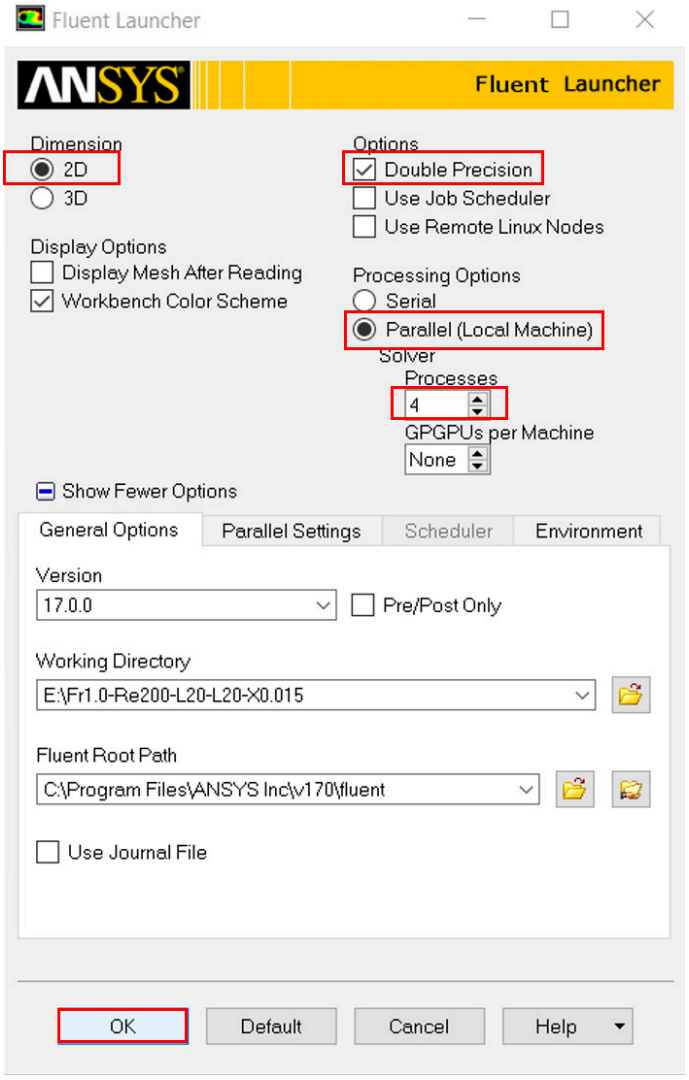

FIGURE 3.5: Setting up of the Fluent Launcher.

3.2.5.1 Problem setup

General

A task pane appears by clicking **General** in the navigation pane as shown in Figure 3.6, where the mesh-related activities and solver options are listed. **Check** is used to report the results of the mesh as shown in the console, where the minimum volume should not be negative, otherwise ANSYS Fluent cannot begin the calculation. Additionally, the quality of the mesh plays a considerable role in the calculation accuracy and stability of the numerical simulation, which can be checked

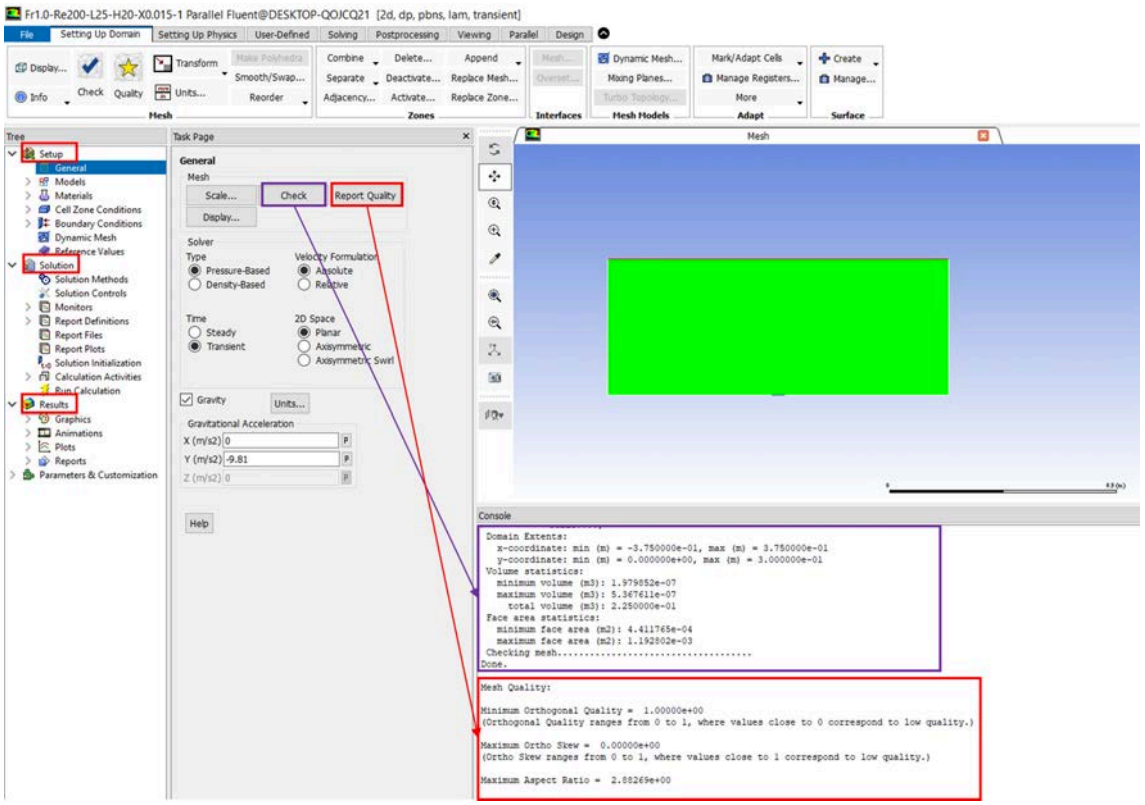

FIGURE 3.6: The graphical user interface (GUI) of Fluent and General setup.

through **Report Quality**. The result of the mesh quality is shown in the console as shown in Figure 3.6. **Pressured-Based** is selected for **Solver** in this thesis, while **Absolute** and **Transient** are filled under **Velocity Formulation** and **Time**, respectively. **Gravity** option is activated with the gravitational acceleration set as -9.81.

Models

There are a series of modelling options available in ANSYS Fluent 17. By clicking **Models** in the navigation pane, a list of models is shown in the task page (Figure 3.7). In this thesis, **Energy** is turned on by double-clicking the **Energy** item and enabling the **Energy Equation**. Additionally, **Laminar** is selected as **Viscous** model for the DNS simulation.

Materials

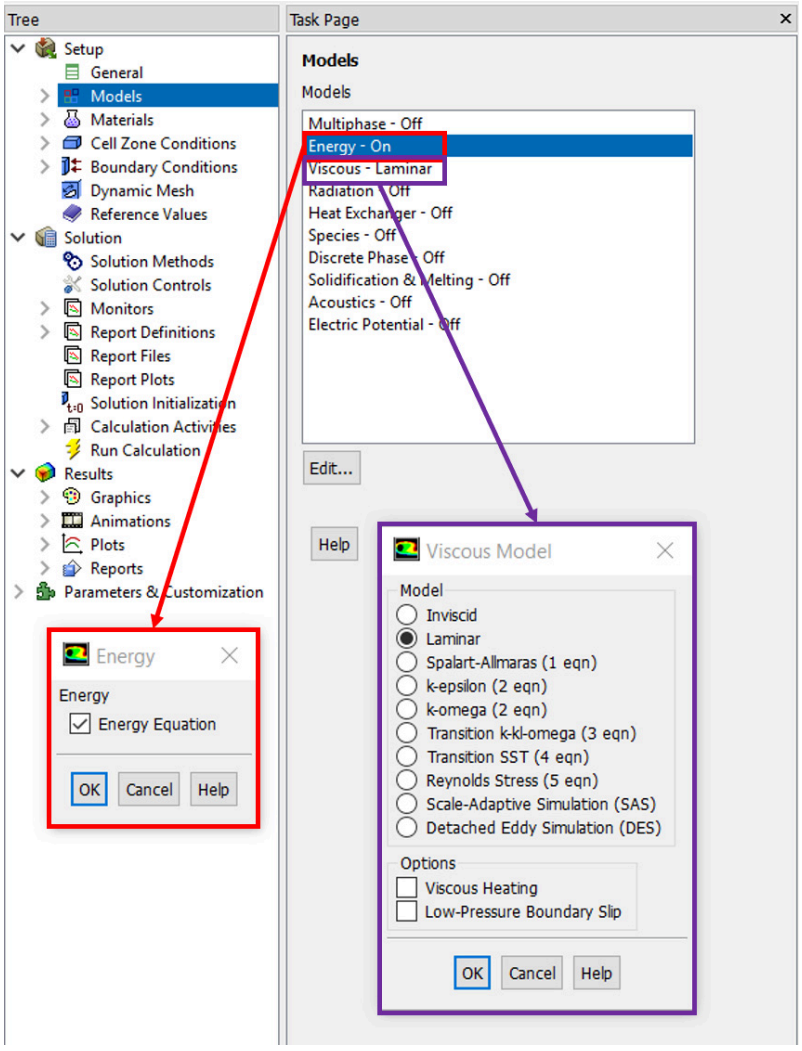

FIGURE 3.7: The models setup in ANSYS Fluent.

The properties of the fluid for the simulation is quantified by the **Materials** task pane. In this thesis, the fountain is created by using water. By clicking the **Create/Edit** button, a dialog box appears as illustrated in Figure 3.8. The name of the fluid is filled as water, and the detailed properties including the **Density**, **Specific Heat**, **Thermal Conductivity**, **Viscosity** and **Thermal Expansion** are filled as shown in the Figure 3.8. Then the **Change/Create** button is clicked to add the defined water in **Materials** options. For some fluid, it can be directly imported from **Fluent Database**, however, some modifications may be needed to satisfy the requirement of the simulation.

Cell Zone Conditions

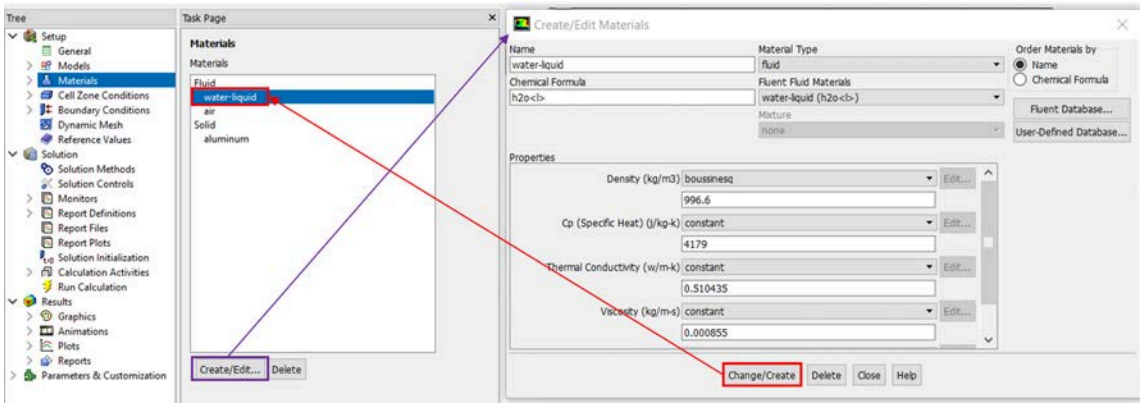

FIGURE 3.8: The materials setup in ANSYS Fluent.

To set up the cell zone conditions for the simulation, **Fluid** in the zone list in the **Cell Zone Conditions** task page is selected and then the **Fluid** dialog box is opened by clicking the **Edit** button. In the **Fluid** dialog box, the material is changed to **Water** which is created by material setting as shown in Figure 3.9. Then in the **Operating Conditions** dialog, by clicking **Operating Conditions** in the **Cell Zone Conditions** task page, the **Operating Temperature** is filled as 300, while other parameters remain as default value.

Boundary Conditions

The boundary conditions described above are implemented with the **Boundary Conditions** task pane. In the task pane, a list of boundaries is listed under the **Zone**, which is defined during the creation of the mesh. To set a specific boundary condition, the boundary name should be selected under the **Zone** first, and then the boundary condition desired is chosen in the **Type** list and the parameter values are edited through clicking the **Edit** button. For example, the fountain source boundary is set as **velocity-inlet** and the parameters are filled as shown in Figure 3.10. Similarly, the remaining bottom and sidewall are set as **wall** with **no-slip** condition, while **outflow** is selected for the top surface boundary.

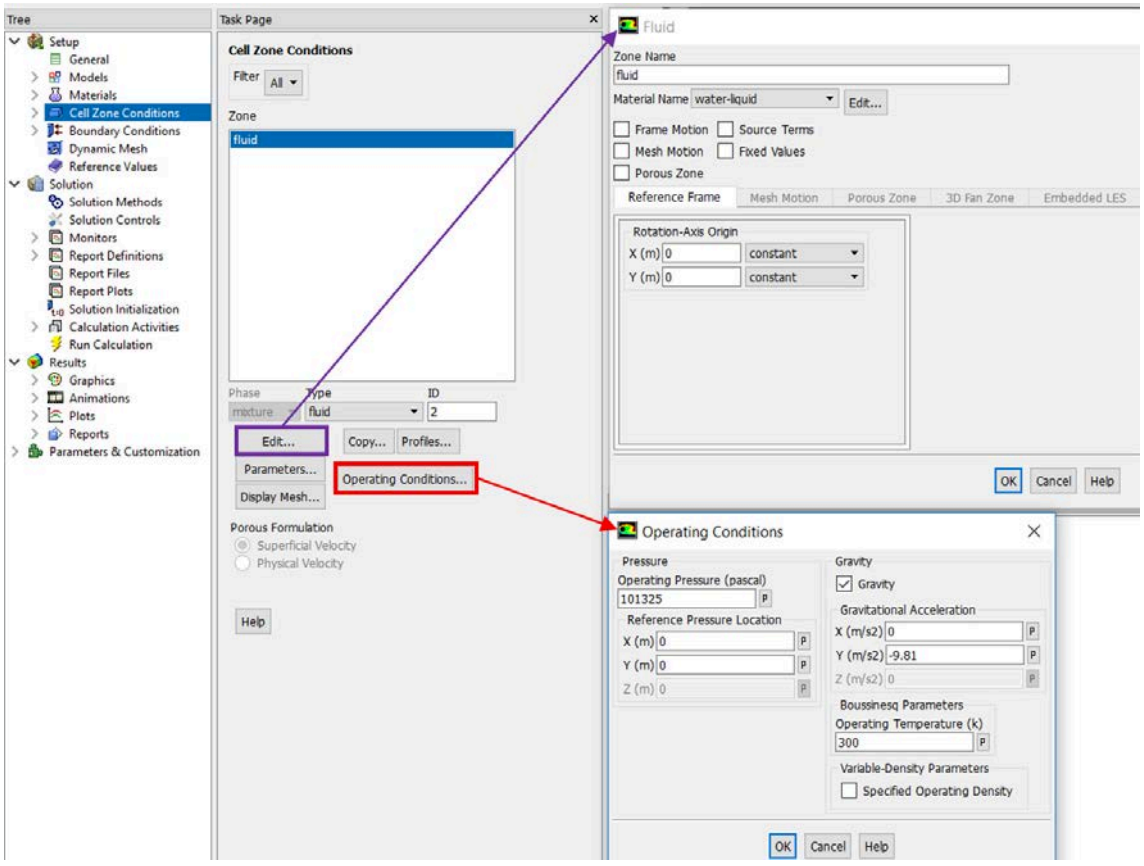

FIGURE 3.9: The cell zone conditions setup in ANSYS Fluent.

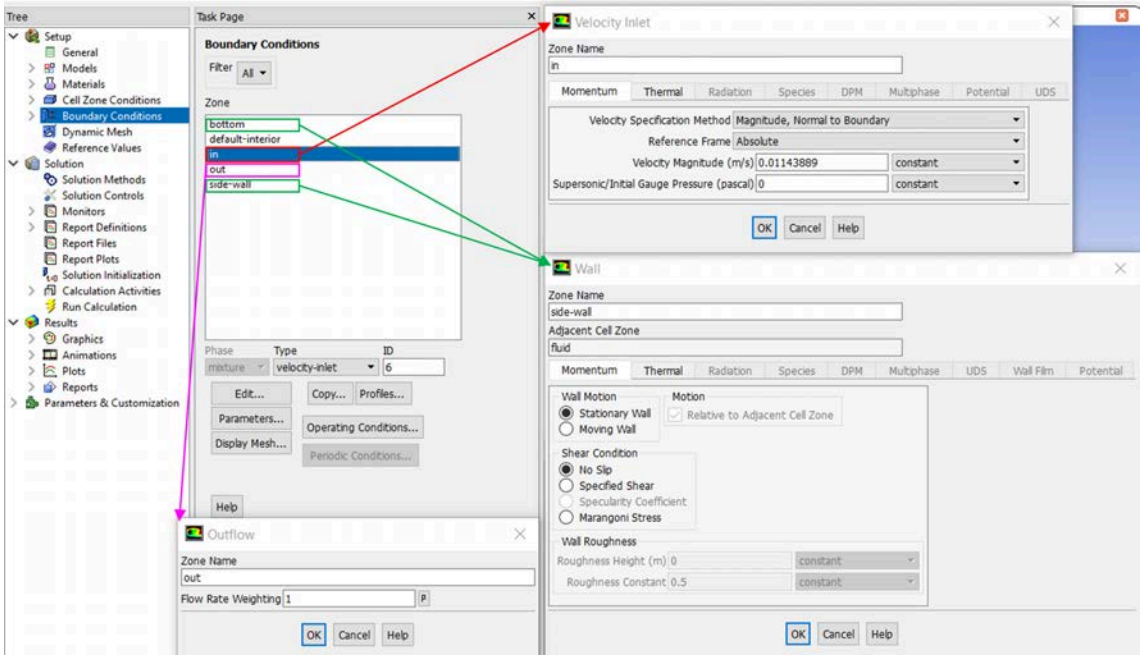

FIGURE 3.10: Boundary conditions setup in ANSYS Fluent.

3.2.5.2 Solution control

The solution parameters are set up using the the task pages listed under the **Solution** in the navigation pane.

Solution Methods

The task pane is opened by clicking **Solution Method** under the **Solution** in the navigation pane. In this task pane, **SIMPLE** scheme is selected for **Pressure-Velocity Coupling**, while **Green-Gauss Cell Based**, **PRESTO!** and **QUICK** methods are chosen for the spatial discretization of **Gradient**, **Pressure**, and **Momentum** and **Energy**. **Second Order Implicit** method is used for **Transient Formulation**, as shown in Figure 3.11.

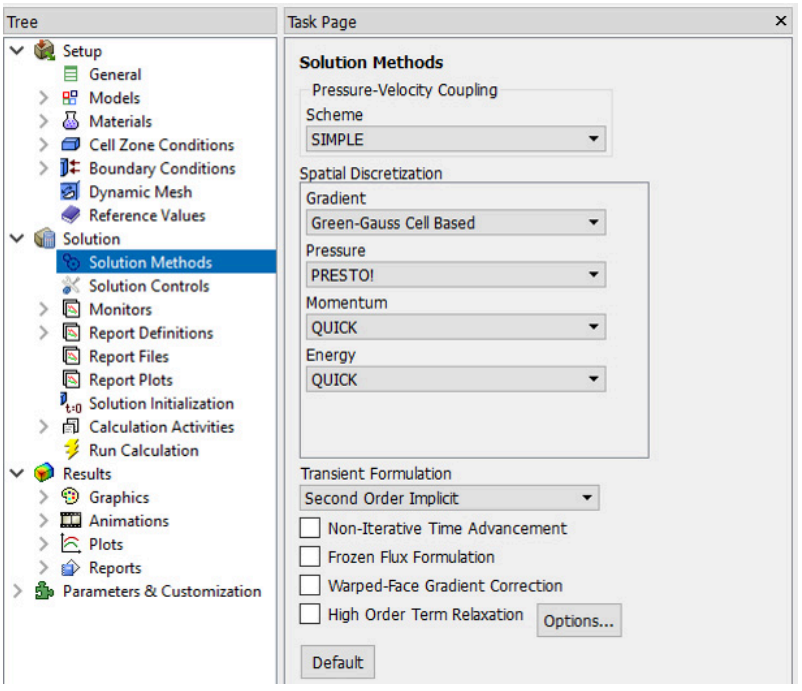

FIGURE 3.11: Solution methods setup in ANSYS Fluent.

Solution Control

As mentioned above, the under relaxation factor is used to control the variation of scalar quantity in equations set during the iteration process. The **Under-Relaxation Factors** are set in the **Solution Controls** task pane, which remain the default values in this thesis as shown in Figure 3.12.

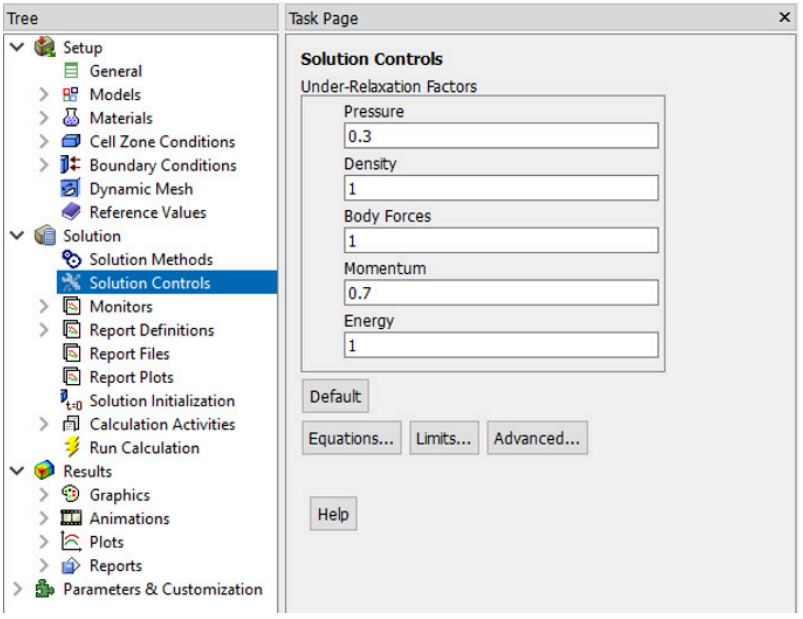

FIGURE 3.12: Solution controls setup in ANSYS Fluent.

Monitors

There are four types of monitors under the **Monitors** task page, including **Residuals, Statistic and Force Monitors**, **Surface Monitors**, **Volume Monitors** and **Convergence Monitors**. As discussed above, the residual levels play an important role to judge the convergence of the iterative calculation. Here, the residual values as the convergence criterion are set in **Residual Monitors** dialog pane, as shown in Figure 3.13.

Surface Monitors can be used to save any desired data in every time step or each iteration. In this thesis, a number of variables, such as the fountain penetration height, the intrusion front, the wall fountain height, need to be recorded for every step for the analysis of the fountain behavior. Figure 3.13 demonstrates how to use **Surface Monitors** to create a new monitor the intrusion front. The **Surface**

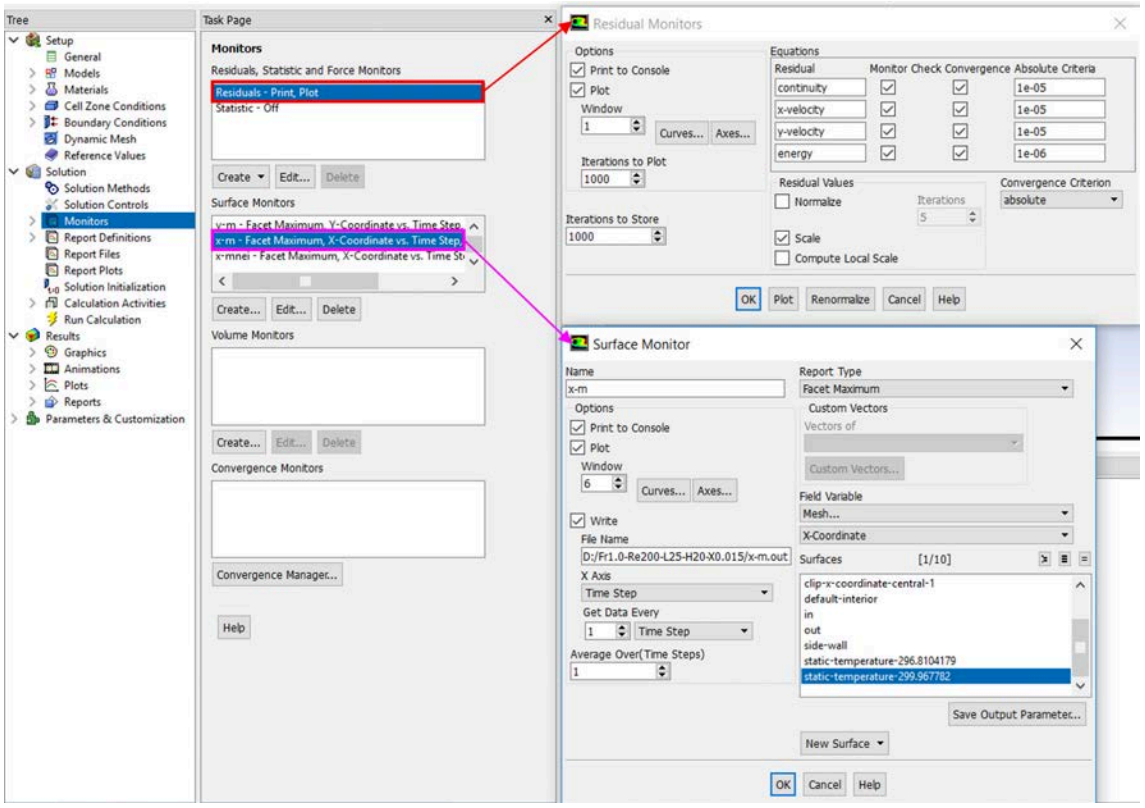

FIGURE 3.13: Monitors setup in ANSYS Fluent.

Monitors dialog box is activated by click **Create** button under the task pane. Then the **Name** is filled with x-m and the **Options** is set as illustrated in the Figure 3.13. The maximum intrusion front defined by specific temperature is the variable desired to be monitored, resulting in the setting of **Report Type**, **Field Variable** and **Surfaces**. The data will be written in the computer following the specific route in **File Name**.

Solution Initialization

The solution needs to be initialized before the simulation starts and set up the **Surface Monitors**. In this thesis, the ambient fluid is initially homogeneous with a specific temperature. Hence, it can be initialized by the clicking the **Initialize** button under the **Initialization Methods** task pane with keeping the default setting for **Standard Initialization** as shown in Figure 3.14.

Calculation Activities

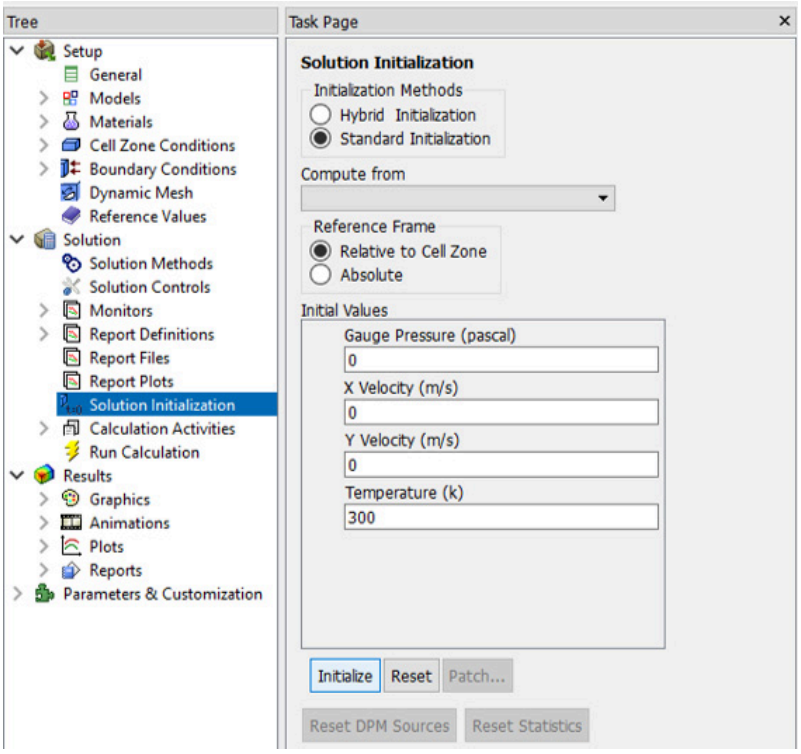

FIGURE 3.14: Solution initialization setup in ANSYS Fluent.

Calculation Activities enable ANSYS Fluent to save the simulation data automatically, which is important for the data post process and reduce the risks threatening the data safety, such as unexpected power outage or crash of the software. The setup of **Calculation Activities** can be shown by using filling 500 in the dialog of **Autosave Every (Time steps)** as shown in Figure 3.15 as an example, which commands ANSYS Fluent to save the data document every 500 time steps. Similarly, the task pane of **Automatic Export** and **Solution Animations** can be used for automatically exporting data and making simulation animation.

Run Calculation

Run Calculation task pane as shown in Figure 3.16 controls the setting of the **Time Step Size** and the **Number of Time Steps**. Additionally, the **Max Iterations/Time Step** decides the maximum number of the iterations for each time step. The setting for the example is illustrated in Figure 3.16. Then the simulation can start with clicking the **Calculate** button.

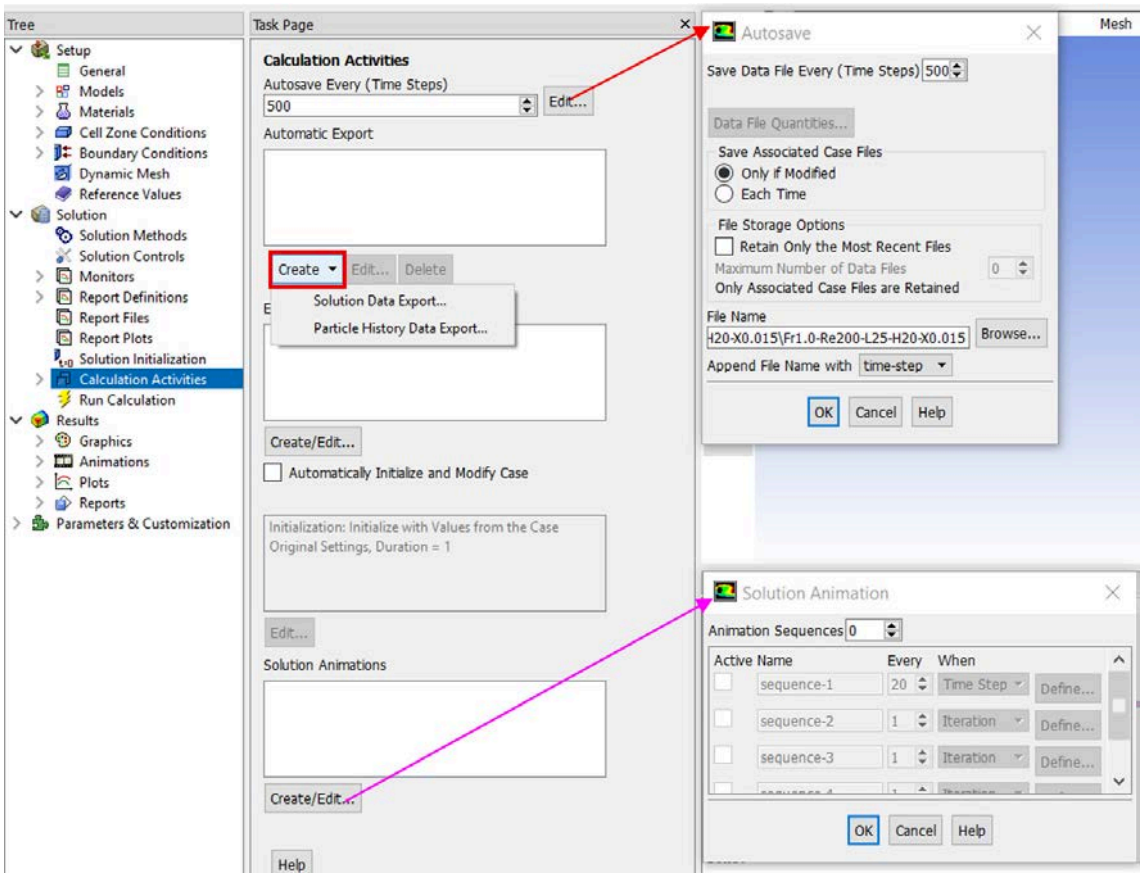

FIGURE 3.15: Calculation Activities setup in ANSYS Fluent.

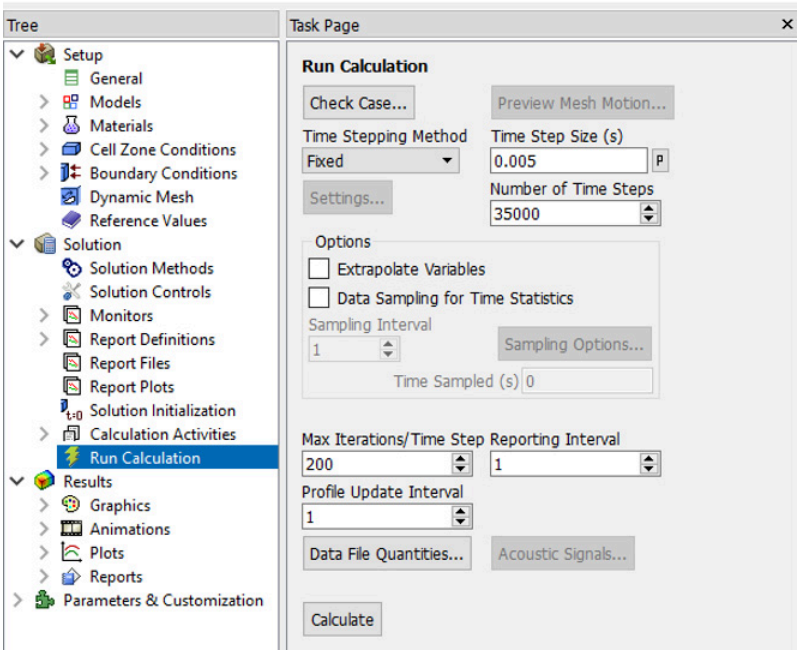

FIGURE 3.16: Run calculation setup in ANSYS Fluent.

3.2.5.3 Results

After the simulation has been finished, the numerical results can be processed and analyzed by the tools under **Results** in the navigation pane. **Graphics**, **Animations**, **Plots** and **Reports** can be used to create different contours, animations, plots, etc. Figure 3.17 illustrates the procedure to create a temperature contour of the two-dimensional calculation domain. Double-clicking the **Contours** under the **Graphics and Animations** task pane, the **Contours** dialog box appears where **Static Temperature** is selected as the contour, **Levels** is filled with 60, while other parameters remain their individual default setting. Then, clicking the **Display** button will show the temperature contour. The **Colormap** button can be used for the modification of the contour display as shown in Figure 3.17.

In this section, only a brief description of the procedure used in ANSYS Fluent is given. For more detailed information about the setup and data post process, the readers are referred to ANSYS Fluent User's Guide [112].

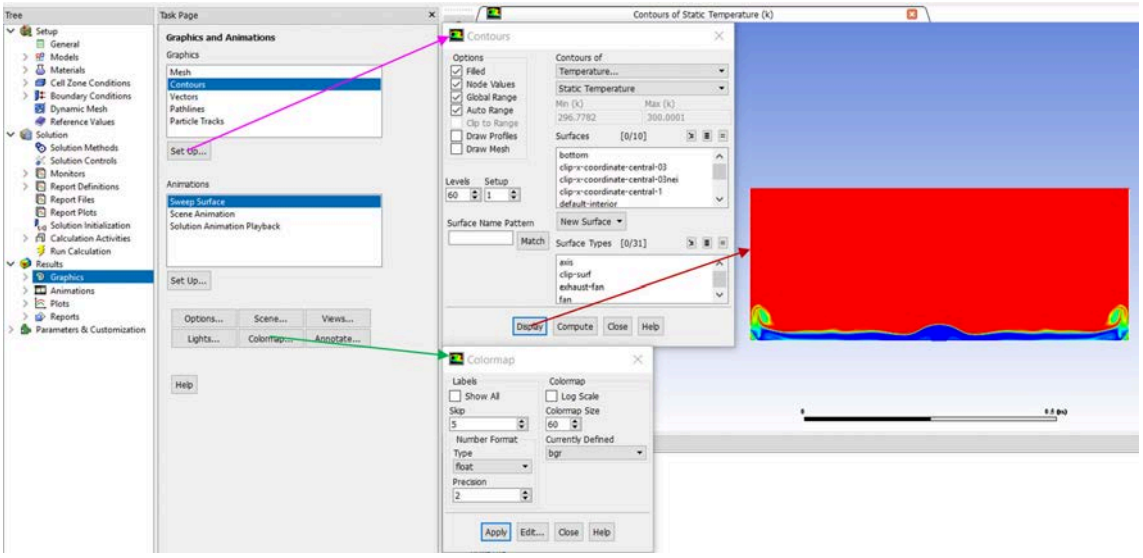

FIGURE 3.17: Results setup in ANSYS Fluent.

3.2.5.4 Example of numerical simulation setup

The following Table 3.1 shows the set up of the numerical model using the planar fountain of $Fr = 1.0$, $Re = 200$, $Pr = 7$ and $\lambda = 20$ as an example, with other parameters are set as default.

TABLE 3.1: The setup of the two-dimensional numerical simulation for the planar fountain of $Fr = 1.0$, $Re = 200$, $Pr = 7$ and $\lambda = 20$

General	Solver type	Pressure-Based
	Velocity Formulation	Absolute
	Time	Transient
	2D space	Planar
	Gravity (m/s^2)	9.81
Models	Energy	On
	Viscous	Laminar
Materials	Density (kg/m^3)	996.6
	Specific Heat (J/kgK)	4179
	Thermal Conductivity (w/mK)	0.510435
	Viscosity (kg/ms)	0.000855
	Thermal Expansion Coefficient (1/K)	0.000276
Cell Zone Conditions	Operating Temperature (K)	300
Boundary Conditions	velocity-inlet: Velocity mangnitude (m/s)	0.011438892
	velocity-inlet: Temperature (K)	296.7781999
	outflow	
	wall	no-slip
Solution Methods	Scheme	SIMPLE
	Gradient	Green-Gauss Cell Based
	Pressure	PRESTO!
	Momentum	QUICK
	Energy	QUICK
	Transient Formulation	Second Order Implicit
Monitors (Residual)	continuity	1e−5
	x-velocity	1e−6
	y-velocity	1e−6
	energy	1e−6
Solution Initialization	Standard Initialization	Standard Initialization
Run Calculation	Time Step Size (s)	0.005
	Max Iteration/Time Step	200

3.3 Experimental methods

In this thesis, the high-speed camera technique is used in the experiments to investigate the bulk dynamics behaviour of confined round fountains (from weak to forced) in a homogeneous fluid. Through the experiments, the parameters such as the intrusion front, the stratification surface level and the fountain penetration height are obtained. This section provides a brief description of the general design of the experiment and the major experimental apparatus. Additionally, the technique to process and analyze the data and error is also introduced.

3.3.1 Design of experiment

Experiments were conducted to investigate the bulk behavior of the round fountain filling box flow. Figure 3.18 schematically illustrates the design of the experimental system which consists of (1) a saline reservoir tank containing the colored saline of specific density, (2) a submersible pump, (3) a pipe system with a series of valves for flow control, (4) a needle valve and flow meter unit, (5) a round nozzle, (6) a testing cylindrical Perspex tank initially filled with fresh water, (7) the fountain flow to be recorded, (8) back lights, (9) cameras including two high-speed cameras and a video camera. The saline water is transported by the pump to the testing tank through the pipe system and the round nozzle, creating a round fountain flow visualized by food dye. The initial behavior of the fountain is then recorded by high-speed cameras, while a relatively long-term behavior is recorded by the video camera. A detailed description of the apparatus will be given in the next section.

The experiments cover a range of Fr and Re with $1.0 \lesssim Fr \lesssim 15.0$ and $100 \lesssim Re \lesssim 2000$, where the Re and Fr are determined by adjusting the injection flow rate (via the needle valve and flow meter unit), changing the density difference between the source and ambient fluid through adjusting the salt content in the saline solution and using nozzles with different diameters. The range of Fr covers round fountains

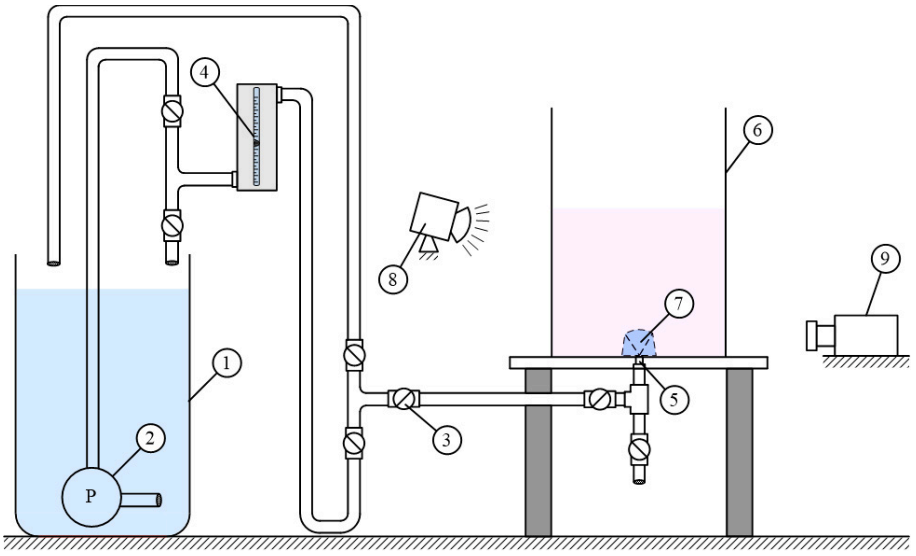

FIGURE 3.18: Schematic illustration of the experiment system.

from 'weak' to 'highly forced' according to the classification mentioned in Chapter 1, which can not only be compared with the numerical results, but also allow for a complete analysis of confined round fountains.

3.3.2 Experimental apparatus

Figure 3.19 is the picture of the current experimental setup used in this thesis, which shows the main apparatus for the experiments.

Saline water reservoir

A 600 Liters black polyethylene container as shown in Figure 3.20 is used as the saline water reservoir. In the tank, a Davey D15A submersible sump pump (maximum total head, 12 meters) is installed to fully mix freshwater and salt to produce uniform saline water and pump the saline to the fresh water tank through the pipe to create an upward fountain flow. In addition, the saline tank is mounted on a pre-fabricated frame and fastened tightly to avoid vibration during the pump operations.

Flow meter

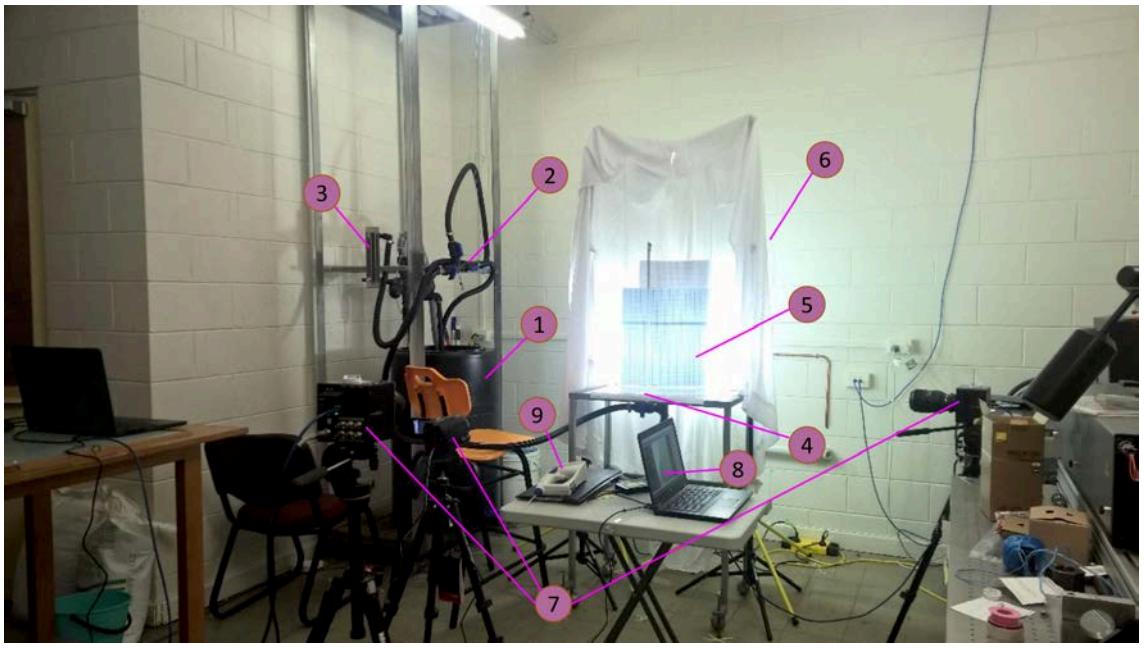

FIGURE 3.19: Picture of the testing experiment system used, including (1) a saline reservoir, (2) a pipe system, (3) a needle valve and flow meter unit, (4) a round nozzle, (5) a Perspex testing tank, (6) back lightting, (7) cameras, (8) laptops, and (9) density meter.

As shown in Figure 3.21, a Dwyer needle valve and flow meter (RMB-83D-SSV) is used to adjust and measure flow rate to achieve the specific Froude and Reynolds numbers. The flow meter allows for flow control and measurement and is capable of measuring up to $1.2L \cdot min^{-1}$.

Round nozzle

The round nozzles were 3D printed with the diameter from 1.0 mm to 7.0 mm in 0.5 mm increments. As an example, Figure 3.22 shows three 3D round nozzles, where a black rubber O-ring is with the nozzle for sealing when fitted on the testing tank. In this study, the nozzles of 4mm, 5mm, 6mm and 7mm are selected to achieve the range of the Froude number, Reynolds number and confinement scale.

Perspex cylindrical testing tank

As shown in Figure 3.23, a transparent cylindrical container of perspex is selected as the testing tank to allow a full view of the fountain behavior. The container is of 390 mm inner radius, 400 mm outer radius and 1000 mm length.

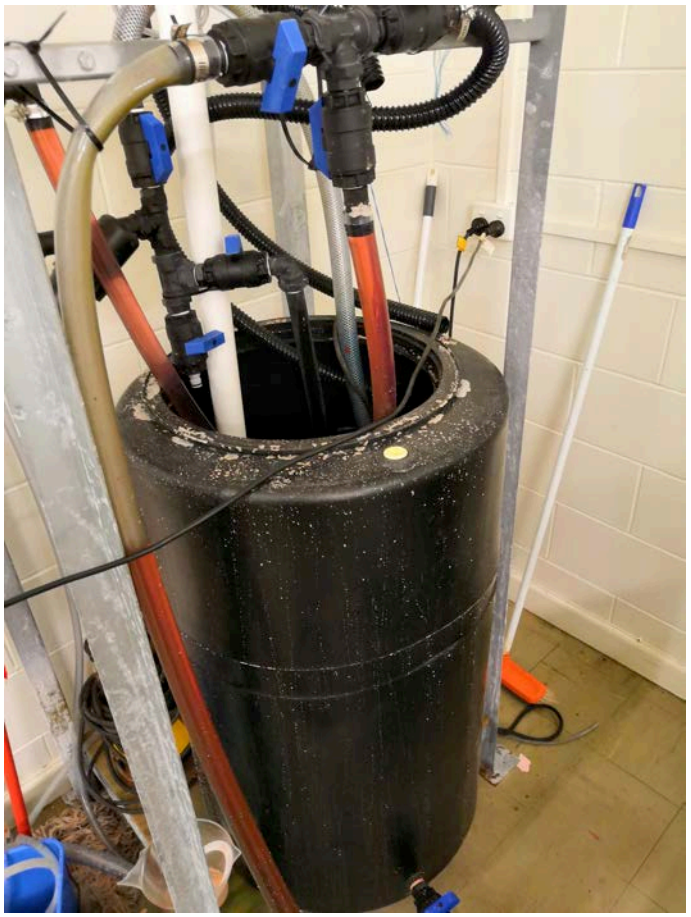

FIGURE 3.20: Picture of saline reservoir.

Density meter

The fresh water used in the experiment is from the Townsville drinking water supply, while the saline water is made by dissolving salt in the fresh water. The density difference between the fresh and saline water plays an important role in determining the Froude number. Therefore, the density of the two fluid needs to be measured during the experiment by density meter. The density meter used here is a Mettler Toledo Densito 30PX density meter (accuracy: 0.001 g/cm^3), as shown in Figure 3.24. When measuring the density, the sampling tube is placed into the fluid, then the trigger is pulled and the value is subsequently displayed on the screen.

High-speed cameras

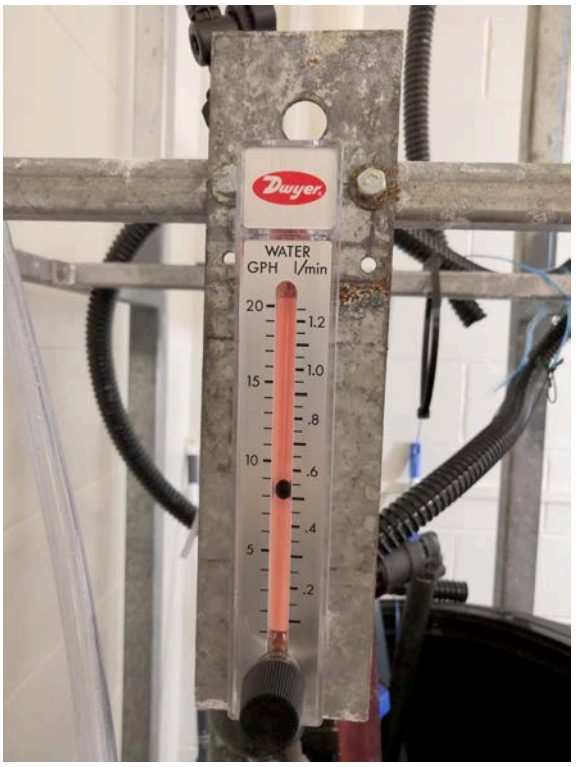

FIGURE 3.21: Picture of needle valve and flow meter.

FIGURE 3.22: Picture of 3D printed round nozzles.

As shown in Figure 3.25, two Photron FASTCAM Mini UX100 High-Speed Cameras (HSC) are selected to capture the details of the fountain behavior. These HSCs are a compact option, allows 1280×1024 pixels from 24 fps to $800,000$ fps with reduced resolution. These two HSCs are used to record the images of the same fountain but focus on different locations separately.

FIGURE 3.23: Picture of perspex testing tank.

FIGURE 3.24: Picture of Mettler Toledo Densito 30PX density meter.

The 'End Trigger' model is set for the HSCs during the experiment, which means the HSCs will continuously record the images but only the data in a specific period

FIGURE 3.25: Picture of Photron FASTCAM Mini UX100 High-Speed Camera.

before clicking the trigger will be saved in the memory. 1280×1024 pixels and 500 fps are selected to enable 17.468 seconds of recording, which allows to cover the development of the intrusion.

Video camera

Since the recording duration of HSCs are limited, a video camera is used to record the entire development of the filling process. The record provides the information on stratification surface level and fountain penetration height. The SONY HDR-PJ810 video camera shown in Figure 3.26 can record images at 1280×1024 pixels and 250 fps.

3.3.3 Analysis techniques and errors

In this thesis 40 individual fountain filling box flows have been recorded. The fountain penetration height and intrusion front are measured by the Photron FASTCAM Viewer (PFV) software after the experiment.

FIGURE 3.26: Picture of SONY HDR-PJ810 Video camera.

3.3.3.1 Photron FASTCAM Viewer (PFV) software

Using the measurement of the intrusion front as an example, here a brief description about the procedure to used the PFV software is presented.

- Open the PFV file of a case using the PFV software, as shown in Figure 3.27.

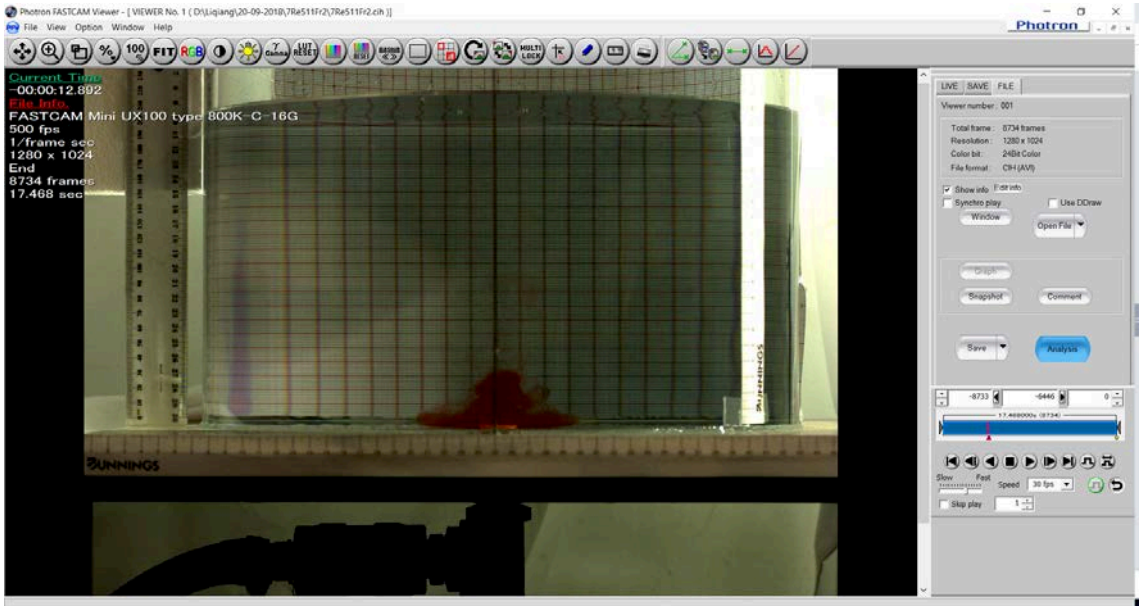

FIGURE 3.27: Window of Photron FASTCAM Viewer.

- Use the scale tool to relate the image to the corresponding actual distance. As shown in Figure 3.28, the side ruler is focused on by using the zoom tool. Then a scale calibration window is opened by clicking the scale tool button. Using **Calibrate distance of between 2 points**, two points on the ruler is selected, corresponding to 10 mm distance. This step may be repeated several times to obtain a trustful scale.

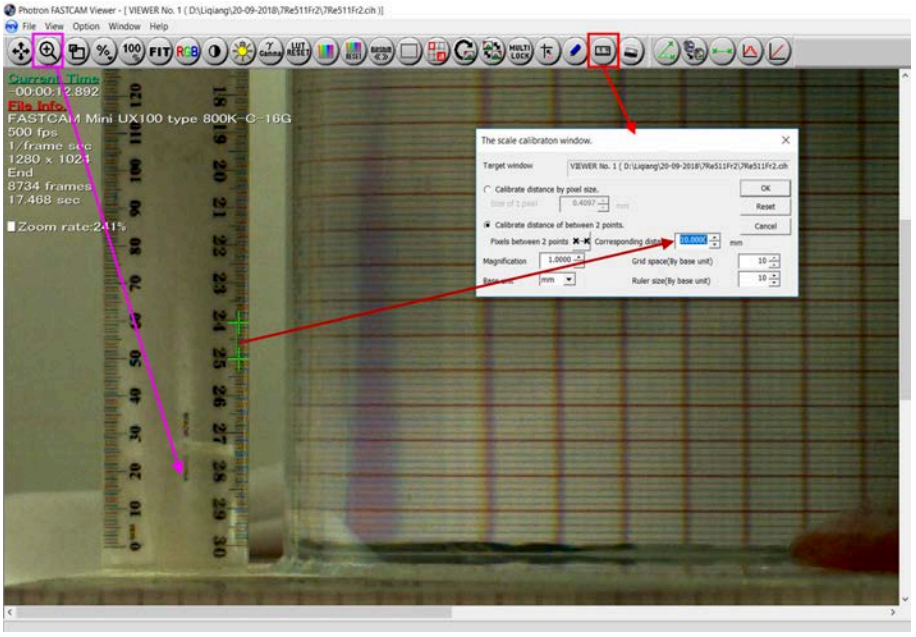

FIGURE 3.28: PFV - scale calibration.

- Play the video on until the intrusion begins.
- Use the ruler tool to measure the distance between the intrusion front and the nozzle edge at every 250 fps, as shown in Figure 3.29.
- Then the data is processed by the Origin software to get the time series of the intrusion front and the intrusion rate, with a raw result as illustrated in Figure 3.30.

The similar process is used for the data of fountain penetratin height and the intrusion front head thickness.

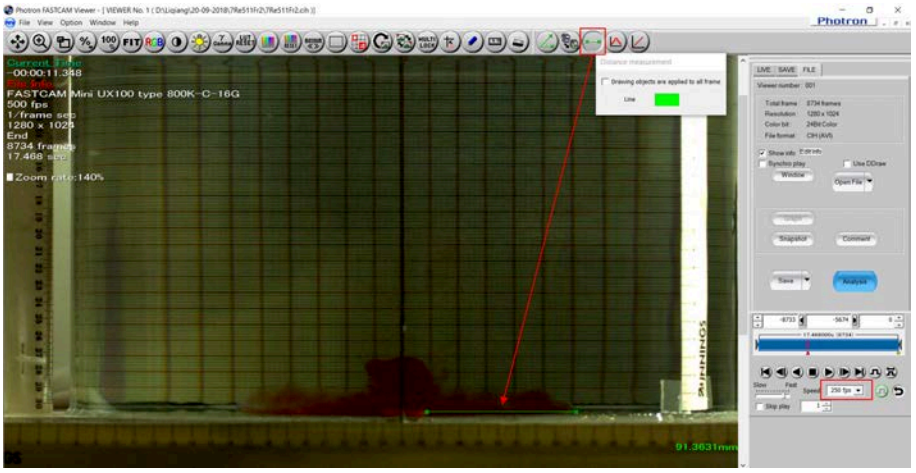

FIGURE 3.29: PFV - measurement of the intrusion front.

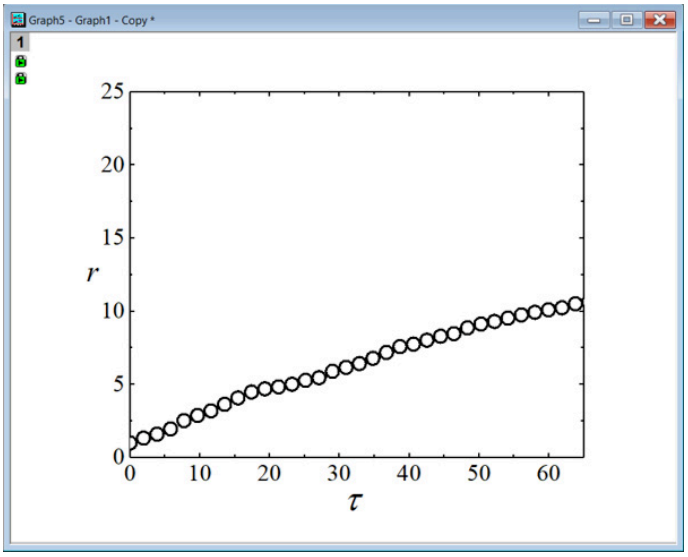

FIGURE 3.30: The time series of intrusion front processed by Origin.

3.3.3.2 Errors

Random and bias errors occurred during the experiment have a significant influence on the accuracy of the results. Before the experiments, a quantitative reliability assessment is carried out on the flow meter to ensure the reliability of the result. The following procedure is used to assess the flow meter,

- The pump is turned on to allow to circulate the saline in the tank and clean the bubbles in the pipe;

TABLE 3.2: Results from flow meter assessment [11].

Flow rate record	Time	Measured volume	Calculated Flow rate	Error
[L/min]	[s]	[mL]	[L/min]	(%)
0.4	60	405	0.405	1.25%
0.6	60	610	0.61	1.67%
0.8	60	810	0.81	1.25%
1.0	60	990	0.99	1.0%
1.2	30	610	1.22	1.67%

- The needle valve and flow meter is set to 0.4 L/min;
- Fill the saline into a scaled container and start the timer at the same time;
- The filling lasts for a minute and the volume of the saline is measured, thus the flow rate is calculated;
- This is repeated for other flow rates, as listed in the Table 3.2.

Table 3.2 shows a fair agreement between the flow meter reading and the experimentally calculated flow rate.

Additionally, to reduce the error source, some qualitative reliablity processes are applied during the experiment, including levelling both of the testing tank and HSCs using surface level, eliminating or minimizing air bubbles from the systems etc.

3.4 Summary

In the first part of this chapter, the governing equations and initial and boundary conditions are presented for the confined plane and round fountains in homogeneous environment. The finite volume method using by ANSYS Fluent 17 to solve these equations is then briefly described. The governing equations are discretized on a non-uniform mesh, with the standard 2nd-order central difference schemes used for the viscous and divergence terms and the 3rd-order QUICK scheme used for the advective terms. The 2nd-order Adams-Bashforth and Crank-Nicolson schemes are used for the time integration of the advective terms and the diffusive terms, respectively. The PRESTO scheme is used for the pressure gradient. The procedure to setup ANSYS Fluent 17 is also introduced.

In the second part of this chapter, the experimental procedure using high-speed camera techniques to investigate the long-term behavior of confined round fountains is presented. Two high-speed cameras and a video camera are used to record the details of confined fountains, including penetration, intrusion and stratification. The design of the experiment and details of the experimental apparatus have been described. Additionally, the analyzing software and the error source considered are also outlined.

Chapter 4

Confined weak planar fountains

4.1 Introduction

In this chapter, a series of 2D DNS runs were carried out for weak planar fountains in confined open channels with homogeneous ambient fluids over the ranges of $0.1 \leq Fr \leq 3.0$, $5 \leq Re \leq 800$, $0.7 \leq Pr \leq 100$ and $10 \leq \lambda \leq 35$. The evolution of the transient flow behavior of weak planar fountains in the confined open channels, including intrusion, secondary wall fountain and stratification, is described using numerical results. From these numerical results, the regimes of the intrusion speed, the characteristic time-scales for intrusion to impinge the sidewall and the wall fountain to reach its maximum penetration height, the development rate of the stratification, and the bulk entrainment rate, *etc.*, are also determined and quantified in terms of the governing parameters Fr, Re, Pr and λ.

The rest of this chapter is organized as follows. In § 4.2, the details of the 2D DNS runs carried out in this chapter are presented. Also presented in this section are the mesh and time-step independence testing results. The snapshots of the contours of temperature and stream functions obtained from the numerical results are shown in § 4.3 to provide a qualitative description of the evolution of the transient flow behavior of weak planar fountains in the confined open channels under

the influence of Fr, Re, Pr and λ. The influence of these governing parameter on the characteristics of the transient flow behavior of the confined weak planar fountains are then analyzed and discussed quantitatively in § 4.4, including the movement of the intrusion front and the wall fountain front, the development of stratification, and the associated bulk entrainment, in terms of Fr, Re, Pr and λ. Finally the conclusions are summarized in § 4.5.

4.2 DNS runs and mesh and time-step independence testing

There are 49 DNS runs carried out in this chapter, with the key information of these runs presented in Table 4.1. Water is selected as the fluid in the numerical simulation, with the density $\rho_a = 996.6$ kg/m^3, the kinematic viscosity $\upsilon = 8.58 \times 10^{-7}$ m^2/s and the volume expansion coefficient $\beta = 2.76 \times 10^{-4}$ 1/K at the reference temperature $T_a = 300$ K. The maximum temperature difference between the source and the ambient fluid $(T_a - T_0)$ of all the simulation runs is $(300 - 296.602 = 3.398$ K), which results in a small enough density ratio to ensure the Oberbeck-Boussinesq approximation to be valid.

TABLE 4.1: Key data of the DNS runs of confined weak planar fountains

Runs	Fr	Re	Pr	$\lambda \times h$	**Mesh**
1	0.1	200	7	20 × 10	702 × 334
2	0.15	200	7	20 × 10	702 × 334
3	0.25	100	7	20 × 20	1336 × 531
4	0.25	200	7	20 × 20	1336 × 531
5	0.5	10	7	20 × 20	1336 × 531
6	0.5	50	7	20 × 20	1336 × 531

Continued on next page

Table 4.1 – continued from previous page

Runs	Fr	Re	Pr	$\lambda \times h$	**Mesh**
7	0.5	100	7	20 × 20	1336 × 531
8	0.5	200	7	20 × 20	1336 × 531
9	0.5	500	7	20 × 20	4000 × 1359
10	0.5	800	7	20 × 20	4000 × 1359
11	1	5	7	20 × 20	1336 × 531
12	1	10	7	20 × 20	1336 × 531
13	1	20	7	20 × 20	1336 × 531
14	1	50	7	20 × 20	1336 × 531
15	1	100	7	20 × 20	1336 × 531
16	1	200	7	20 × 20	1336 × 531
17	1	500	7	20 × 20	4000 × 1359
18	1	800	7	20 × 20	4000 × 1359
19	1.25	100	7	20 × 20	1336 × 531
20	1.25	200	7	20 × 20	1336 × 531
21	1.5	10	7	20 × 20	1336 × 531
22	1.5	50	7	20 × 20	1336 × 531
23	1.5	100	7	20 × 20	1336 × 531
24	1.5	200	7	20 × 20	1336 × 531
25	1.5	500	7	20 × 30	4000 × 2359
26	1.5	800	7	20 × 30	4000 × 2359
27	1.75	100	7	20 × 30	1336 × 864
28	1.75	200	7	20 × 30	1336 × 864
29	2	10	7	20 × 20	1336 × 531
30	2	50	7	20 × 20	1336 × 531
31	2	100	7	20 × 30	1336 × 864
32	2	200	7	20 × 30	1336 × 864

Continued on next page

Table 4.1 – continued from previous page

Runs	Fr	Re	Pr	$\lambda \times h$	**Mesh**
33	2	500	7	20×30	4000×2359
34	2	800	7	20×30	4000×2359
35	2.5	100	7	20×30	1336×864
36	2.5	200	7	20×30	1336×864
37	3	100	7	20×30	1336×864
38	3	200	7	20×30	1336×864
39	1	200	0.7	20×20	1336×531
40	1	200	1	20×20	1336×531
41	1	200	10	20×20	1336×531
42	1	200	20	20×20	1336×531
43	1	200	50	20×20	1336×531
44	1	200	100	20×20	1336×531
45	1	200	7	10×30	668×864
46	1	200	7	15×30	1002×864
47	1	200	7	25×20	1668×531
48	1	200	7	30×20	2002×531
49	1	200	7	35×20	2336×531

As mentioned in Chapter 3, the quality and size of grids play an important role in the accuracy, stability and computation time of the numerical simulation. To ensure accuracy of the simulation with relatively economy computational source cost, non-uniform meshes were used for this study, with fine uniform grids in the bottom region and a relatively coarse stretched mesh in the top region. Extensive grid and time-step independence tests were conducted to ensure accurate results to be produced. For example, for the case of $Fr = 1$ and $Re = 200$, $\Delta x = \Delta y = 0.03$ is used in the uniform regions $0 \leq y \leq 10$. While in the remaining region, the meshes expand at a rate 0.5% in the vertical direction until it reaches the open

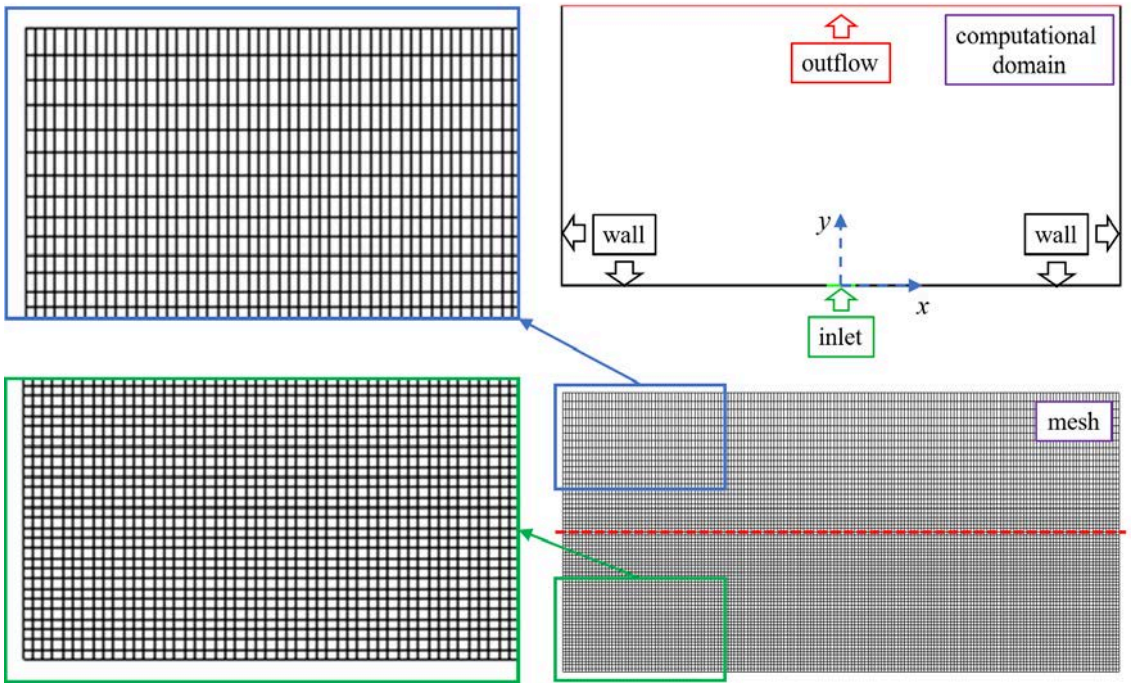

FIGURE 4.1: The computational domain and the typical mesh of a confined weak planar fountain.

top boundary, resulting in '1336×531' grids in the computational domain shown in Figure 4.1 as a basic mesh. Grid independence test was carried out by comparing the solution obtained on this basic mesh with its counterparts obtained on a relatively coarse and a fine mesh. $\Delta x = \Delta y = 0.05$ and $\Delta x = \Delta y = 0.02$ are used in the uniform region for the coarse mesh and the fine mesh, with the grid expansion rate unchanged, giving the meshes of '800×383' and '2000×751', respectively. The non-dimensional time-step for the mesh dependency testing is fixed at $\Delta\tau = 0.004$. The results are presented in the left column of Figure 4.2 including the horizontal temperature and velocities at $y = 0.2$. The variation between the solutions of the basic mesh and the fine mesh is very small, indicating that the basic mesh provides sufficient resolution for $Re \leq 200$. Subsequently, using the basic mesh, the time-step independence testing was carried out by comparing the results of simulations with $\Delta\tau = 0.004$, $\Delta\tau = 0.002$ and $\Delta\tau = 0.001$. As shown in the right column of Figure 4.2, $\Delta\tau = 0.004$ can meet the requirement of accuracy. For the run with basic mesh at mesh step-size $\Delta\tau = 0.004$, the run time for the flow reaching the

stage shown in Figure 4.2 is of the order of 30 hours on a Dell Optiplex 9020 MT desktop computer with Intel Core i7-4790 Processor, 8 M cache, 3.60 GHz and 32 GB DDR3 SDRAM Memory.

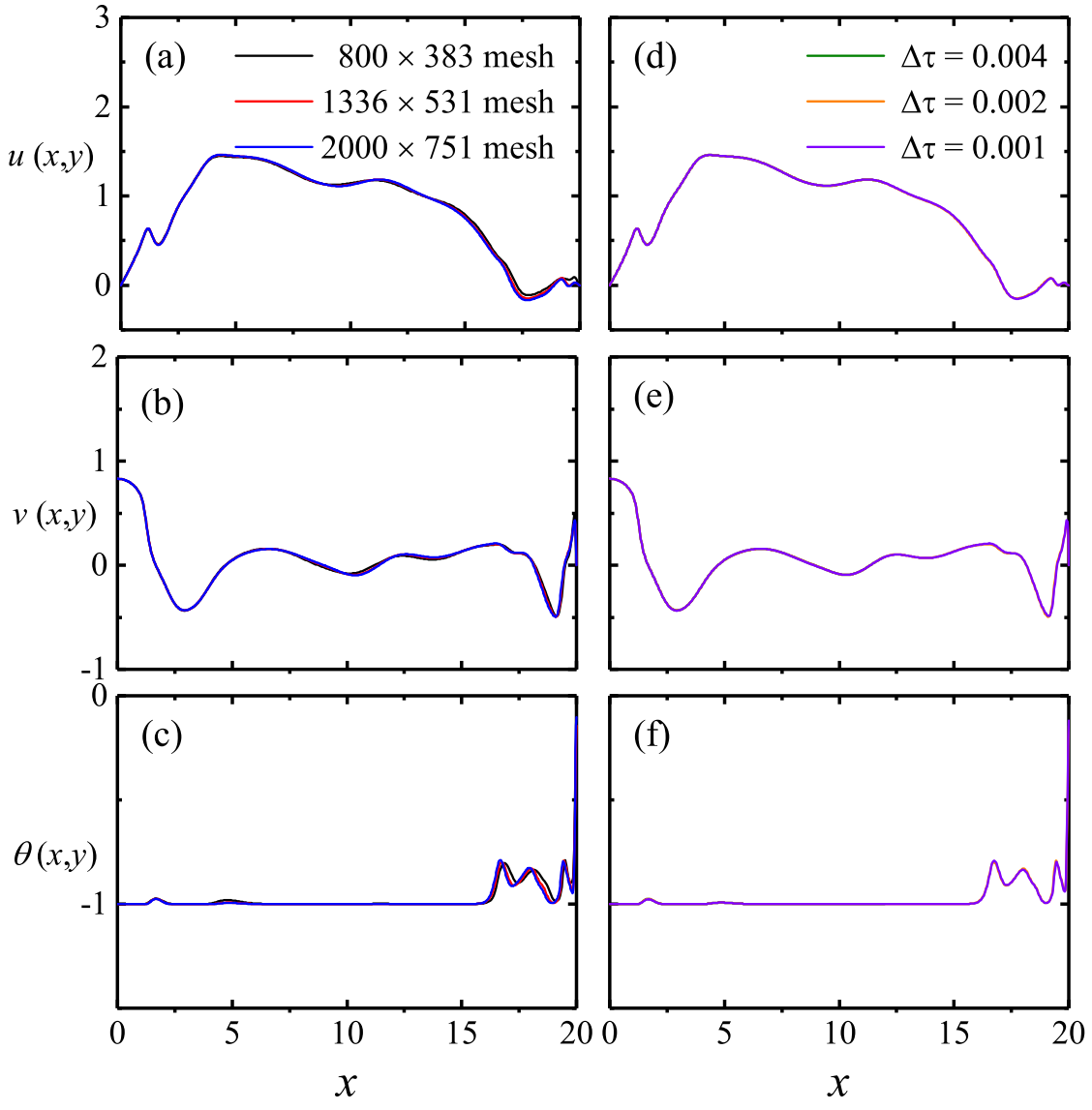

FIGURE 4.2: Comparison of the results from different meshes and time-steps for the runs of $Fr = 1.0$, $Re = 200$, $Pr = 7.0$ and $\lambda = 20$. The left column is for the mesh independence test, with three meshes of '800 × 383', '1336 × 531' and '2000 × 751' meshes: horizontal profiles of the horizontal velocity (a), vertical velocity (b), and temperature (c) at $y = 0.2$ when $\tau = 28.6$; the right column is for the time-step independence test, with three time-steps of $\Delta\tau = 0.004$, $\Delta\tau = 0.002$, and $\Delta\tau = 0.001$: horizontal profiles of the horizontal velocity (d), vertical velocity (e), and temperature (f) at $y = 0.2$ when $\tau = 28.6$.

Similar mesh and time-step size independence testing have also been carried out for $Re = 800$ cases to ensure the accuracy of the numerical solutions with

$500 \leq Re \leq 800$, as shown in Figure 4.3 . Three meshes of '2000×751', '4000×1359' and '5000×1647' are tested with $\Delta\tau = 0.0005$. Then the time-step independence testing was carried out with the basic mesh '4000×1359' by comparing the results of simulations with $\Delta\tau = 0.001$, $\Delta\tau = 0.0005$ and $\Delta\tau = 0.0004$. Base on the results, the mesh '4000×1359' and $\Delta\tau = 0.0005$ are chosen for the runs of $500 \leq Re \leq 800$.

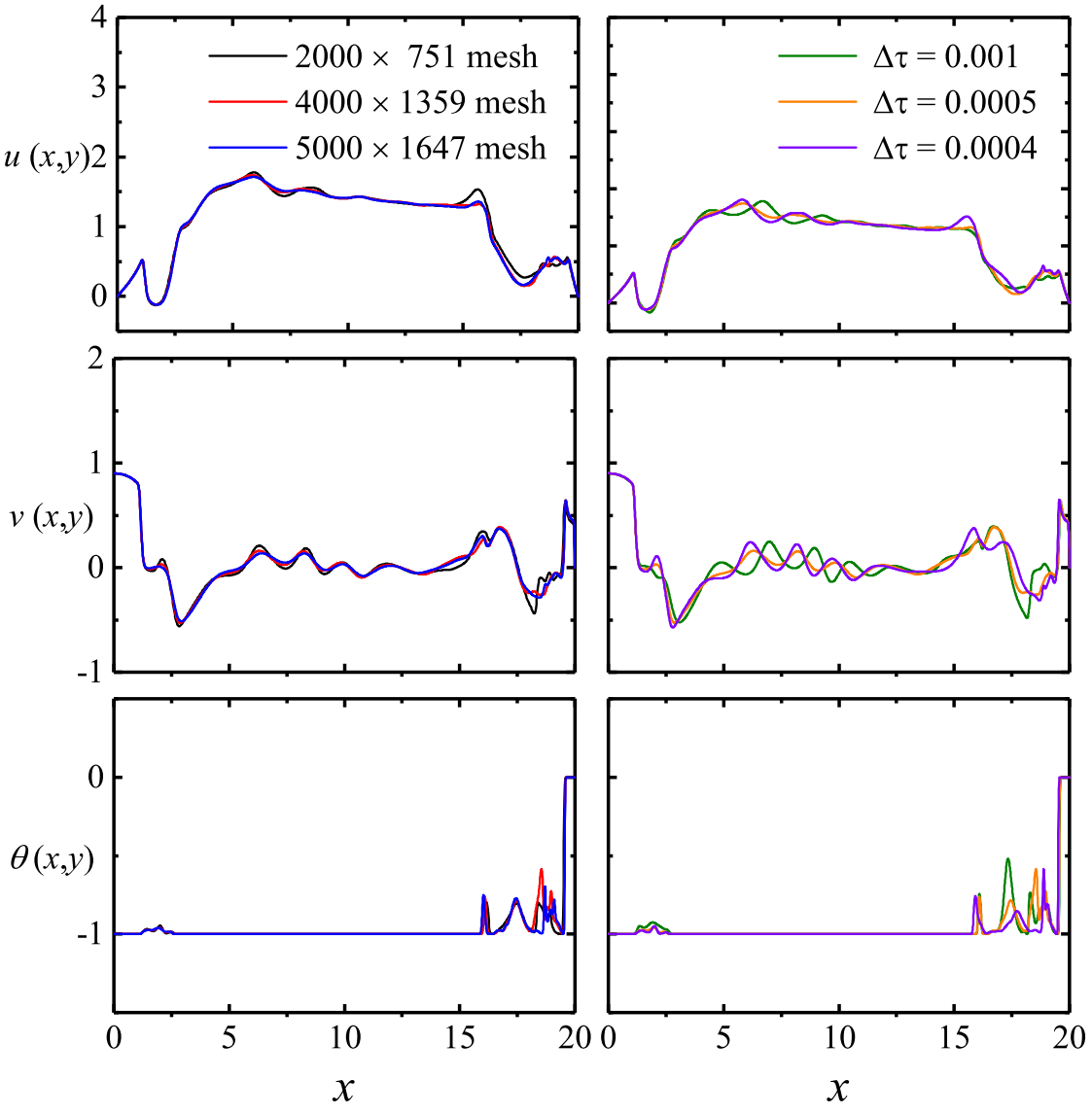

FIGURE 4.3: Comparison of the results from different meshes and time-steps for the runs of $Fr = 1.0$, $Re = 800$, $Pr = 7.0$ and $\lambda = 20$. The left column is for the mesh independence test, with three meshes of '2000×751', '4000×1359' and '5000×1647' meshes: horizontal profiles of the horizontal velocity (a), vertical velocity (b), and temperature (c) at $y = 0.5$ when $\tau = 21.9$; the right column is for the time-step independence test, with three time-steps of $\Delta\tau = 0.001$, $\Delta\tau = 0.0005$, and $\Delta\tau = 0.0004$: horizontal profiles of the horizontal velocity (d), vertical velocity (e), and temperature (f) at $y = 0.5$ when $\tau = 21.9$.

4.3 Qualitative observations

4.3.1 Evolution of typical confined weak plane fountain flow

In Figures 4.4 to Figure 4.7, the snapshots of the numerically simulated transient temperature contours and stream functions at different time instants are presented for the case of $Fr = 0.5$, $Re = 100$, $Pr = 7$ and $\lambda = 20$, providing an overview of the evolution of a typical confined weak planar fountain. The development of a confined weak planar fountain consists of five stages, *i.e.*, the formation of the fountain flow, the intrusion, the wall fountain, the reversed flow, and the stratification. For all the cases tested in this chapter, the flow behavior in the early stages (*i.e.*, the fountain formation, the intrusion and the wall fountain) is symmetric. However, a weak asymmetric flow behavior was observed for some cases in the later stages (*i.e.*, the reversed flow and the stratification), with enough long running. The asymmetry is strengthened with the increase of Fr, Re and Pr or the decrease of λ. Here, only the result on the right part of the simulation domain is presented in the figures, with the description of asymmetric behavior when it occurs.

Since the fountain flow remains heavier than the ambient fluid, it will descend to and spread along the floor after it reaches the maximum height, resulting in the formation of an eddy in the region bounded by the upflow, downflow and the floor as shown in Figure 4.4(b). A thin layer of denser fluid moving outwards along the floor is subsequently formed as illustrated in Figure 4.4(c)-(f). The intrusion can be treated as gravity current, whose behavior may be characterized at different regimes in terms of the governing forces, which will be further discussed in § 4.4.1. Since the evolution of the initial fountain formation and the intrusion was described in detail by Lin & Armfield [90], the description of these phases is omitted here.

The influence of the bounded sidewall on the gravity intrusion becomes significant as the intrusion flow approaches the sidewall. Figure 4.5(a)-(c) show that the circulation above the intrusion head is stretched and spread upward along the

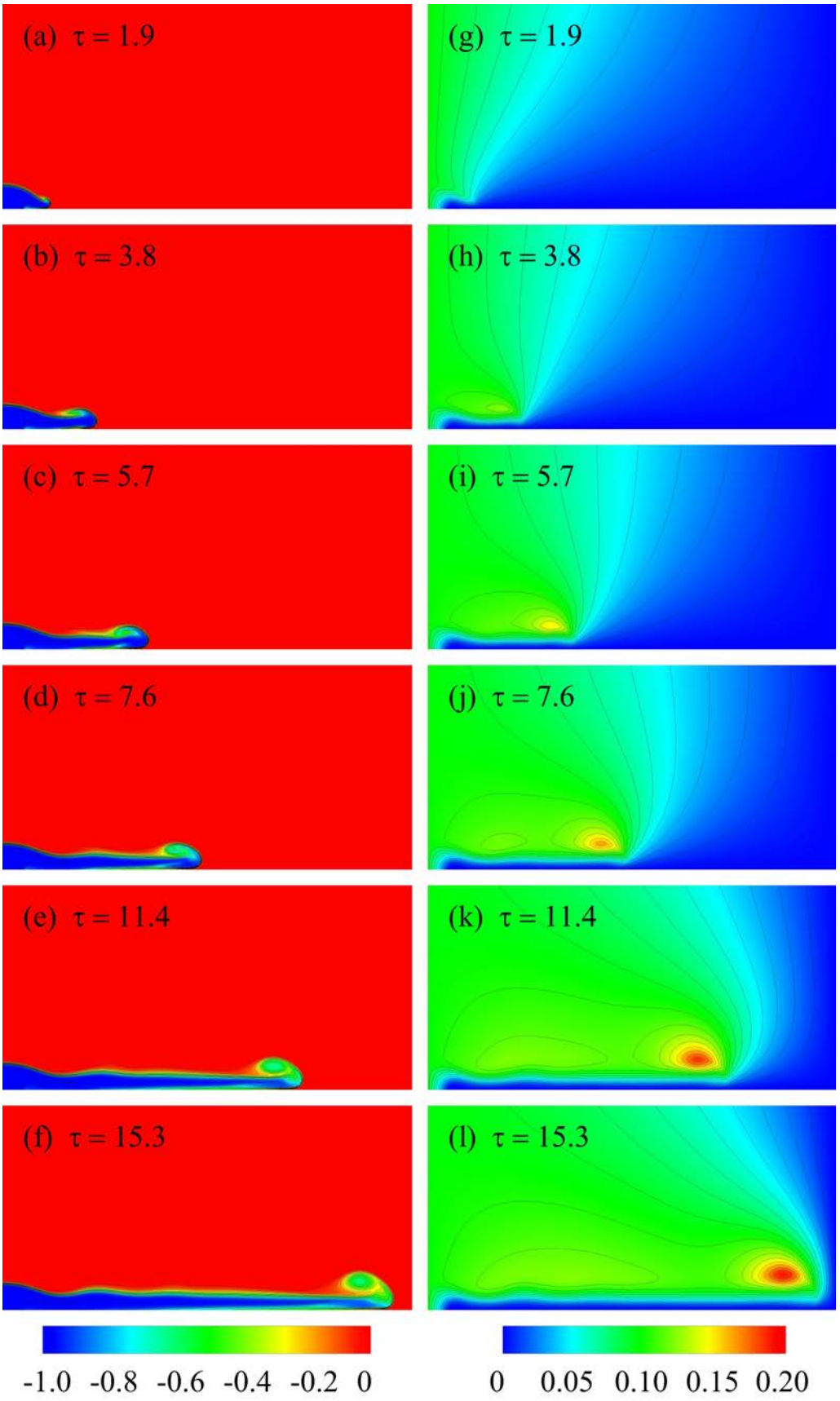

FIGURE 4.4: Temperature contours (the left column) and stream functions (the right column) of the intrusion for the planar fountain of $Fr = 0.5$, $Re = 100$, $Pr = 7$ and $\lambda = 20$ over the duration of $1.9 \leq \tau \leq 15.3$.

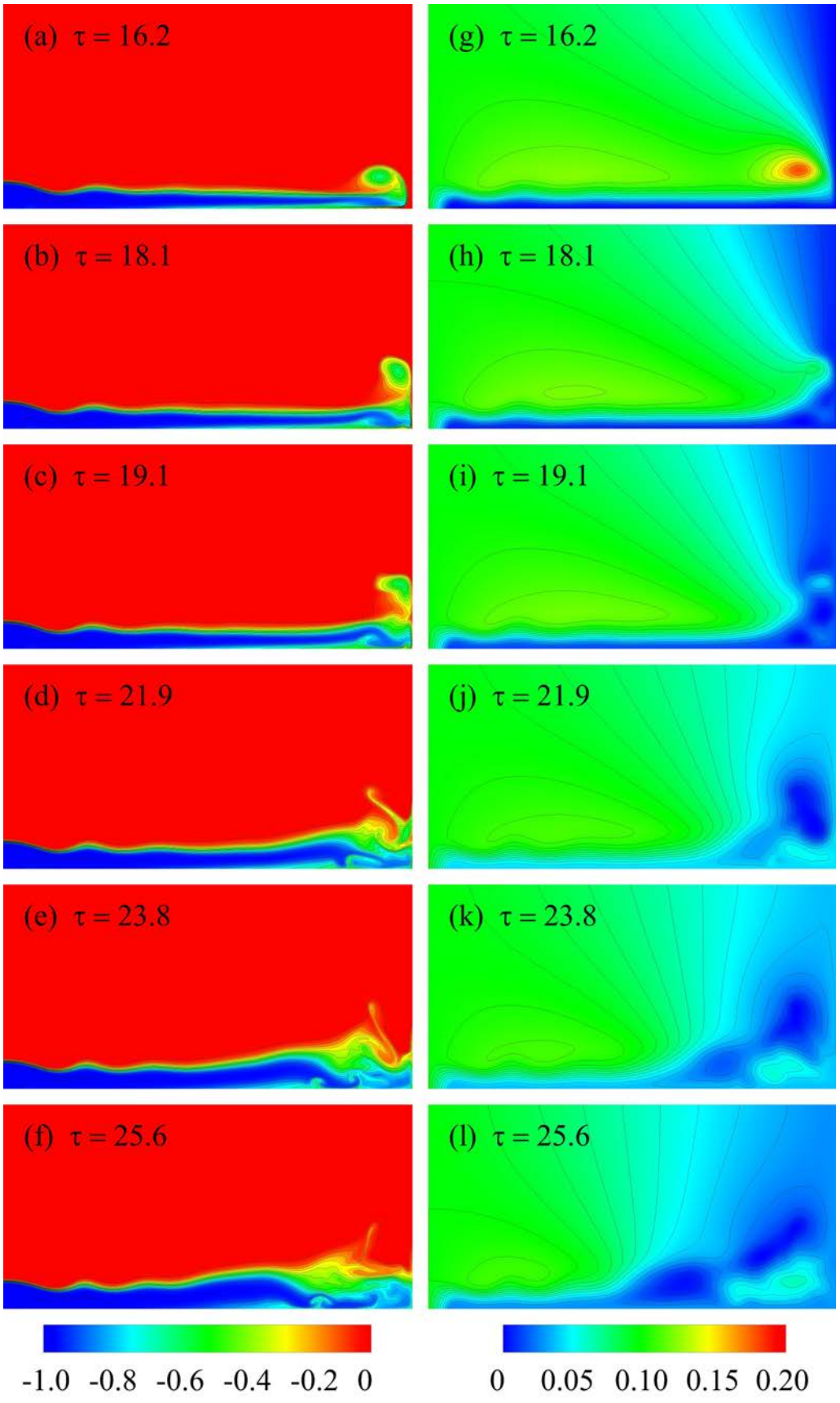

FIGURE 4.5: Temperature contours (the left column) and stream functions (the right column) of the wall fountain of the planar fountain of $Fr = 0.5$, $Re = 100$, $Pr = 7$ and $\lambda = 20$ over the duration of $16.2 \leq \tau \leq 25.6$.

sidewall with the current impinging on the sidewall. Since the flow is still heavier than the ambient flow, the upward flow along the sidewall can be treated as a wall fountain. The wall fountain keeps increasing to a certain height and then slumps back due to the negative buoyancy as shown in Figure 4.5(d)-(f). The wall fountain flow here is similar to its counterpart of jet filling box [97], which will be further discussed in § 4.4.2. The impingement results in the formation of several tiny circulations bounded by the floor, sidewall and the current, as shown in Figure 4.5(i). While the anti-clockwise circulation in the corner grows independently, other clockwise circulations combine with each other and develop into a medium wedge-shaped circulation. As shown in Figure 4.5(j)-(k), both circulations grow bigger due to the slumping of the wall fountain, and the anti-clockwise one pushes the wedge-shaped one towards the fountain core. Subsequently, the thickness of the current close to the sidewall region increases. Additionally, finger-like structures are observed to appear and disappear in Figure 4.5(b)-(f), which result from the interactions between the circulations.

After the wall-fountain slumps back, a two-layer structure is formed, as shown in Figure 4.6. The stream functions show that the wedge-shaped circulation is extruded and divided into two clockwise circulations by the growth of the anti-clockwise circulation in the corner. The lower clockwise circulation then moves back and eventually reaches the fountain core, resulting in an increase in the thickness of the bottom layer, as shown in Figure 4.6(a)-(d). Meanwhile, the upper clockwise circulation is stretched horizontally to the fountain core, resulting in a reversed flow from the sidewall to the center of the container. The reversed flow interacts with the sidewall, the denser bottom layer and the fountain core. As a result, the fountain height experiences a significant increase, until it reaches a certain height, then falls down again due to the gravity and creates a stronger intrusion.

Figures 4.7(a)-(b) present the reversed flow fronts from the sidewall colliding at the centre and are extruded to a higher position by the continuous reversed flow. Due to the negative buoyancy, the extrusion drops down and separates into the

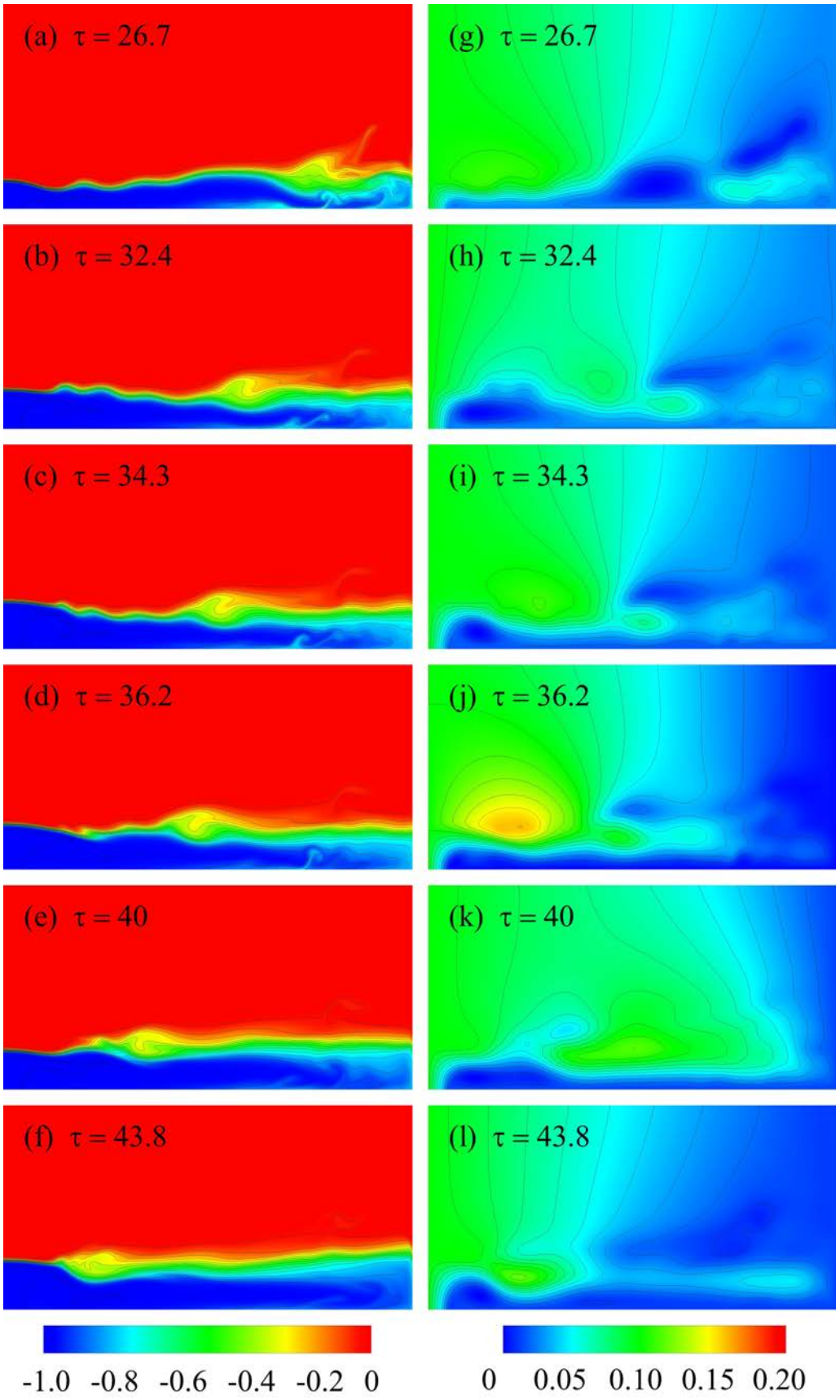

FIGURE 4.6: Temperature contours (the left column) and stream functions (the right column) of the reversed flow of the planar fountain of $Fr = 0.5$, $Re = 100$, $Pr = 7$ and $\lambda = 20$ over the duration of $26.7 \leq \tau \leq 43.8$.

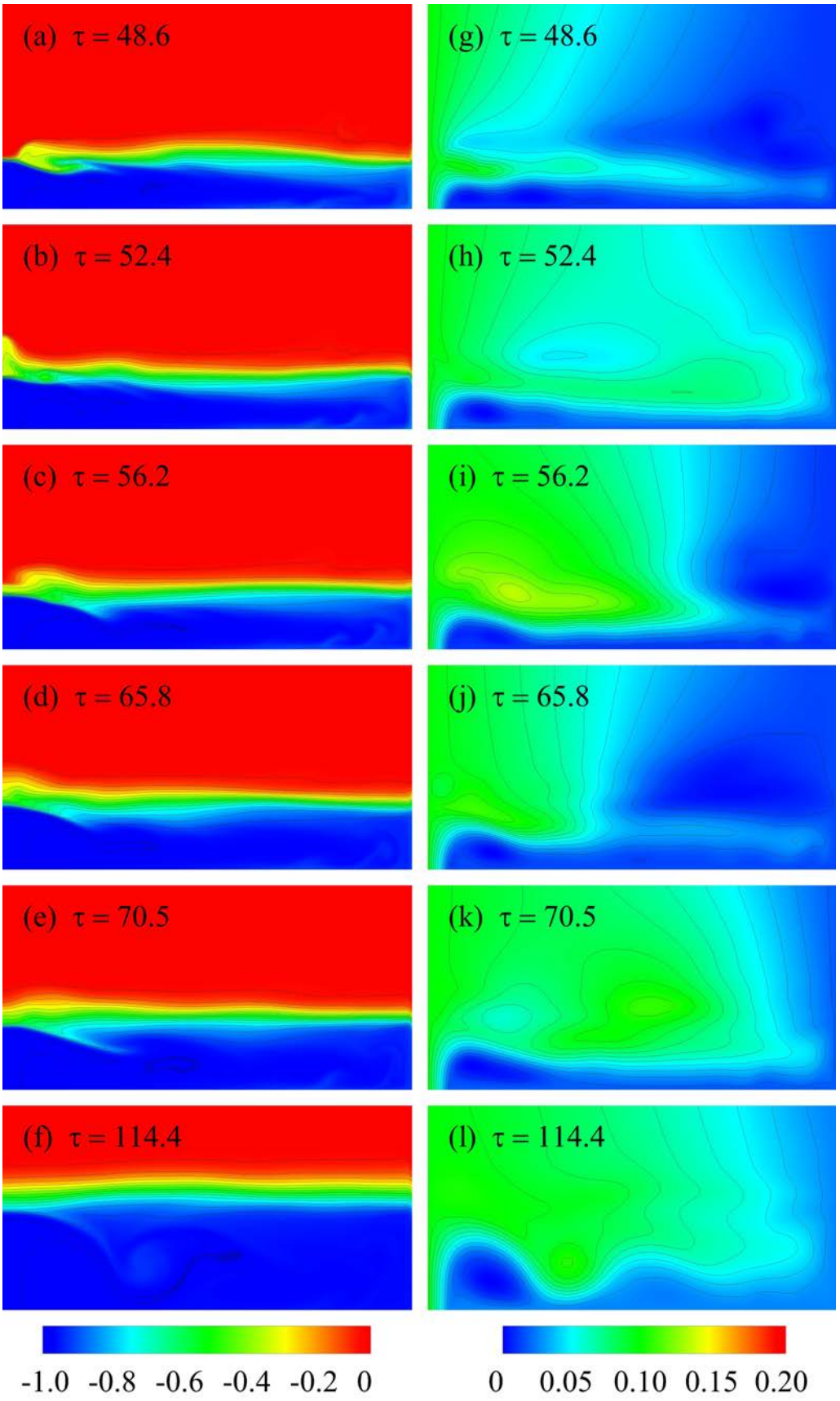

FIGURE 4.7: Temperature contours (the left column) and stream functions (the right column) of the thermal stratification of the planar fountain of $Fr = 0.5$, $Re = 100$, $Pr = 7$ and $\lambda = 20$ over the duration of $48.6 \leq \tau \leq 114.4$.

two reversed flow fronts as shown in Figure 4.7(c). This process repeats several times with a decreasing magnitude of the extrusion, as shown in Figure 4.7(d)-(e). After a certain time, a thermal stratification is formed with the fountain flow submerged which can be seen in Figure 4.7(f). In the long run, the formation of the stratified structure in the ambient fluid results from convection and thermal conduction. However, thermal conduction plays a minor role before the fountain is immersed in the stratified fluid. After that, the increase of the stratified fluid height is mainly due to the filling of the denser fluid.

4.3.2 The influence of the governing parameters

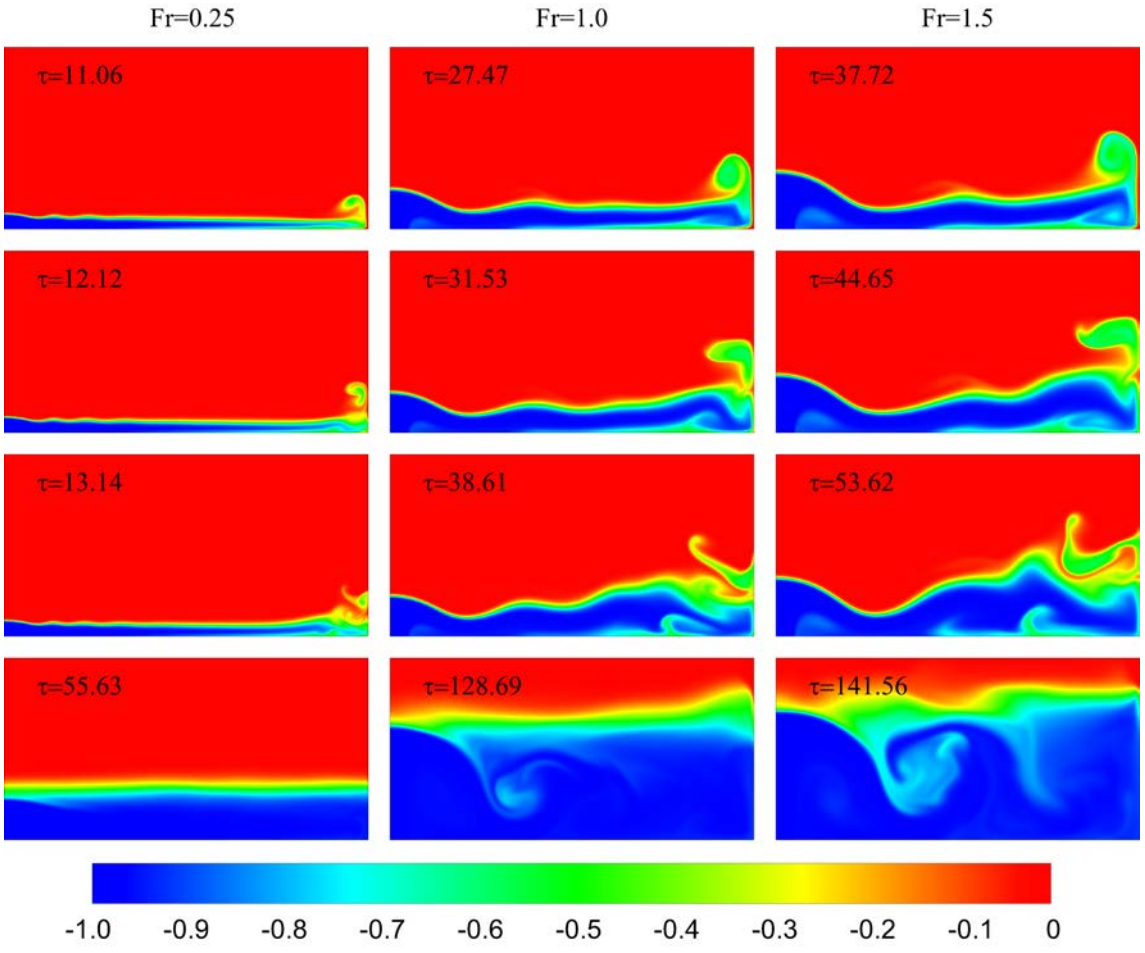

FIGURE 4.8: Temperature contours of the fountains of $Re = 100$, $Pr = 7$ and $\lambda = 20$. The left, middle and right columns are for $Fr = 0.25$, $Fr = 1.0$ and $Fr = 1.5$ respectively over the duration of $16 \leq \tau \leq 114$.

The evolution of temperature contours of the fountains of $Fr = 0.25$, $Fr = 1.0$ and $Fr = 1.5$ with $Re = 100$, $Pr = 7$ and $\lambda = 20$ is presented in Figure 4.8 and demonstrates the influence of Fr on the transient behavior of confined weak planar fountains. The first two rows show the time instants when the intrusion flow impinging the side-wall and the wall fountain reach its maximum height, where a thicker intrusion flow, wider jump region and wall fountain of higher penetration height are observed for the fountains with larger Fr. But the intrusion speed decreases with the increase of Fr. The third row and last row show the wall fountain slumping down and the quasi-steady stratification, respectively. It has been found that it takes longer for the larger Fr fountains to form the quasi-steady stratification. The interactions between the intrusion flow, the reversed flow and the ambient fluid become more significant when Fr increases, which results in a more turbulent structure. For brevity, the results of simulations with other Fr are omitted here, due to the similar development processes.

Figure 4.9 shows the temperature contours of the $Fr = 1$, $Pr = 7$ and $\lambda = 20$ fountains with $Re = 20$, $Re = 50$ and $Re = 200$ at different time instants, which provides an overview of the influence of Re on the long-term behavior of confined weak planar fountains. The impingement of the intrusion on the sidewall and the maximum penetration of the wall fountain in the first two rows present a thinner and faster intrusion flow for larger Re fountains. From the second and third row of Figure 4.9, three regimes are identified for the behavior of the secondary wall fountains. For the $Re = 50$ case, the wall fountain front reaches the maximum height at $\tau = 33.52$ and then slumps down at $\tau = 37.53$. For $Re = 200$ case, the wall fountain front rolls down after reaching the maximum penetration height ($\tau = 31.09$). There is no falling process observed for the wall fountain with $Re = 20$. As shown at $\tau = 58.98$ in the left column, the wall fountain front is pushed away from the sidewall by the stagnation pressure.

For all cases a reversed flow is then created and moves from the sidewall towards the fountain source, interacting with the intrusion flow, the ambient fluid and the

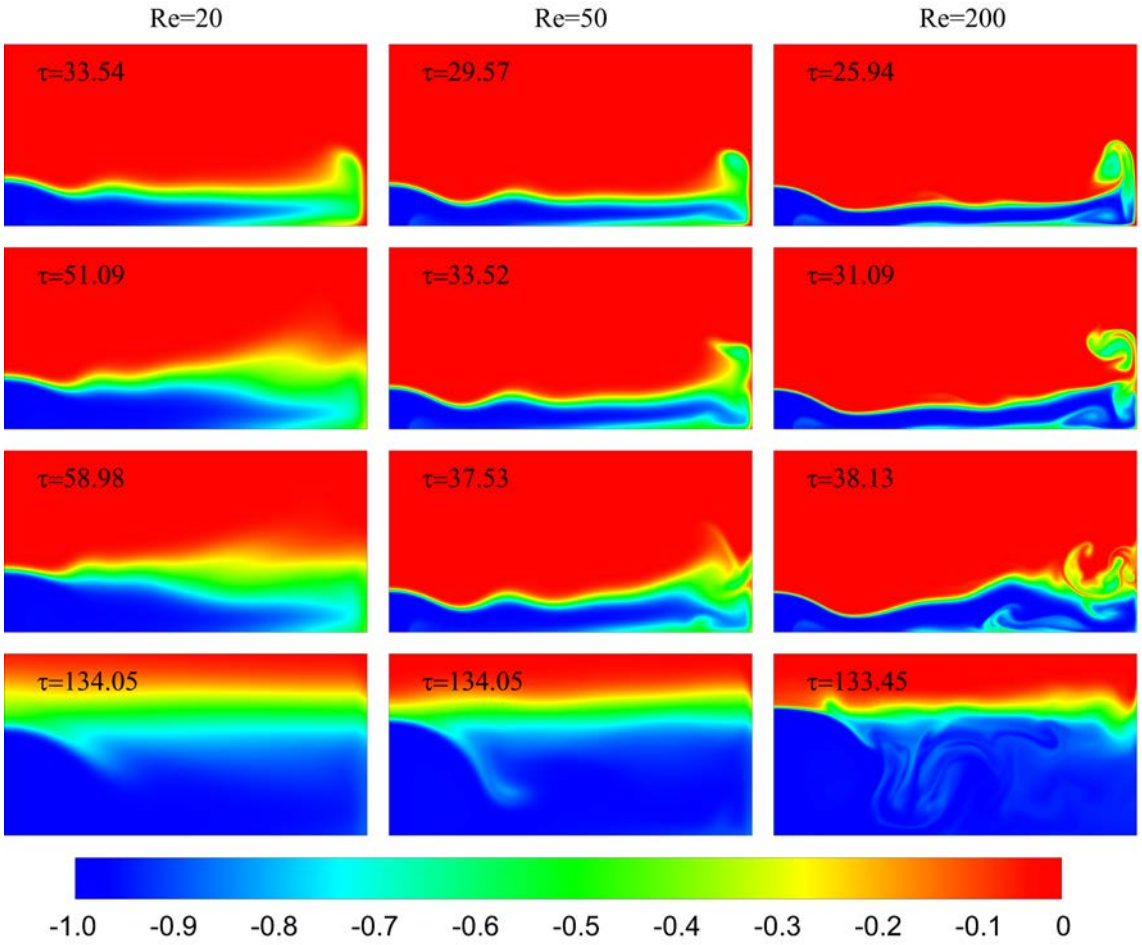

FIGURE 4.9: Temperature contours for the fountains of $Fr = 1.0$, $Pr = 7$ and $\lambda = 20$. The left, middle and right columns are for $Re = 20$, $Re = 50$ and $Re = 200$ over the duration of $16 \leq \tau \leq 114$.

fountain. The interactions become stronger with increasing Re. In the long run, a stratification is created and the fountain is submerged. The thickness of the stratification (distance between the blue part and the red part) increases with the decrease of Re, which indicates thermal conduction playing a more significant role.

To illustrate the effects of Pr, the temperature contours of fountains with $Fr = 1$, $Re = 200$, $\lambda = 20$ and $Pr = 0.7, 10, 20$ and 100 at three stages are presented in Figure 4.10. The left column of Figure 4.10 presents the snapshot of temperature contours for the intrusion flows at $\tau = 19.05$, where a thinner intrusion is present for the larger Pr, but the location of the intrusion front is at the same position. This is consistent with the numerical study carried out by Lin & Armfield [30],

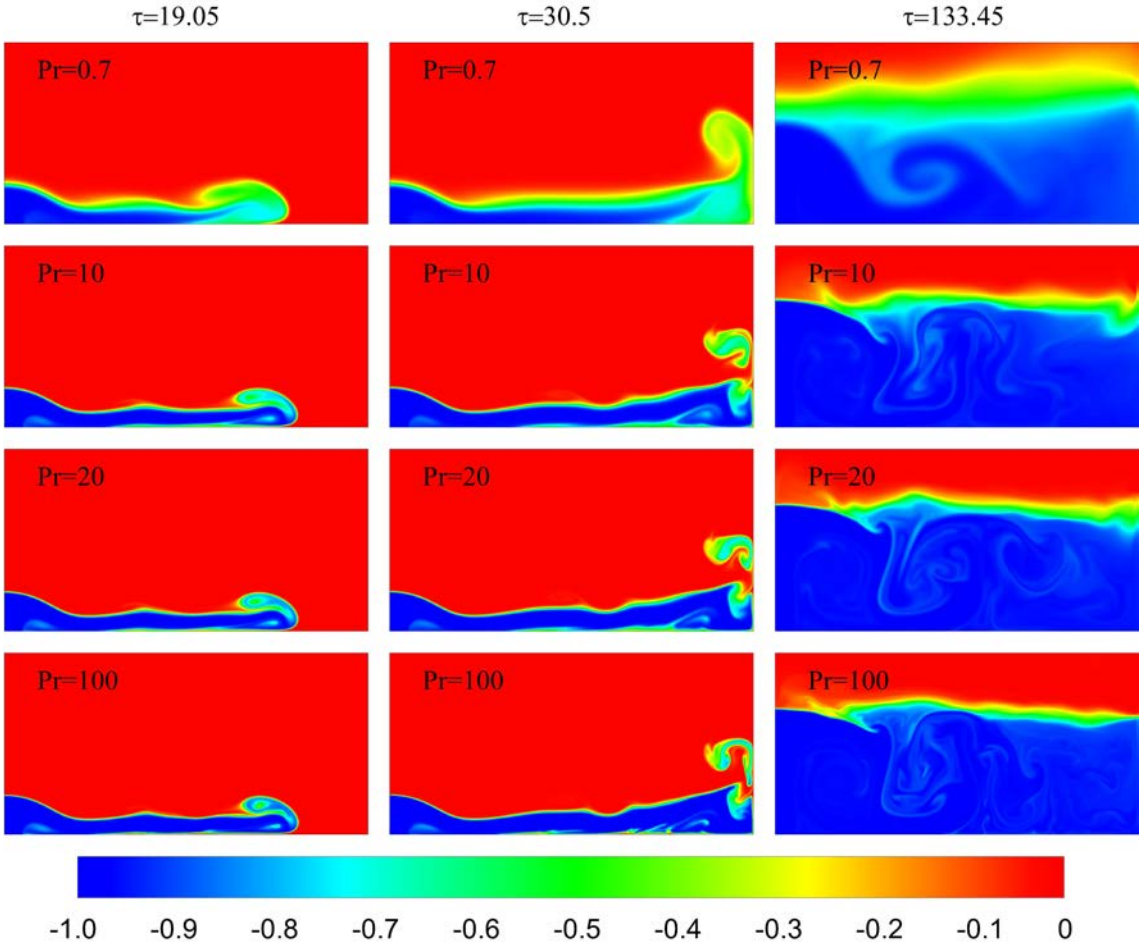

FIGURE 4.10: Temperature contours of the fountains of $Fr = 1.0$, $Re = 200$ and $\lambda = 20$. The left, middle and right columns are for $\tau = 19.05$, $\tau = 30.5$ and $\tau = 133.45$ respectively, with $0.7 \leq Pr \leq 100$.

which illustrated that Pr only influences the thermal layer thickness but has minor effects on the thermal structure. This is also valid for the wall fountain and thermal stratification of $10 \leq Pr$ at $\tau = 30.5$ and 133.45 as shown in the middle and left columns of Figure 4.10. However, when Pr is very small, *e.g.*, $Pr = 0.7$, the thermal conduction effect is significant, resulting in differences in not only the thermal layer thickness but also the thermal structure. The weak planar fountains with $Fr = 1$, $Re = 200$, $\lambda = 20$ and $Pr = 1$, 7 and 50 are also tested in this study, which confirm the results above, hence are not presented here.

Figure 4.11 presents the evolution of temperature contours of the $Fr = 1$, $Pr = 7$ and $Re = 200$ fountains with $\lambda = 10$, $\lambda = 20$ and $\lambda = 30$ at different times, to

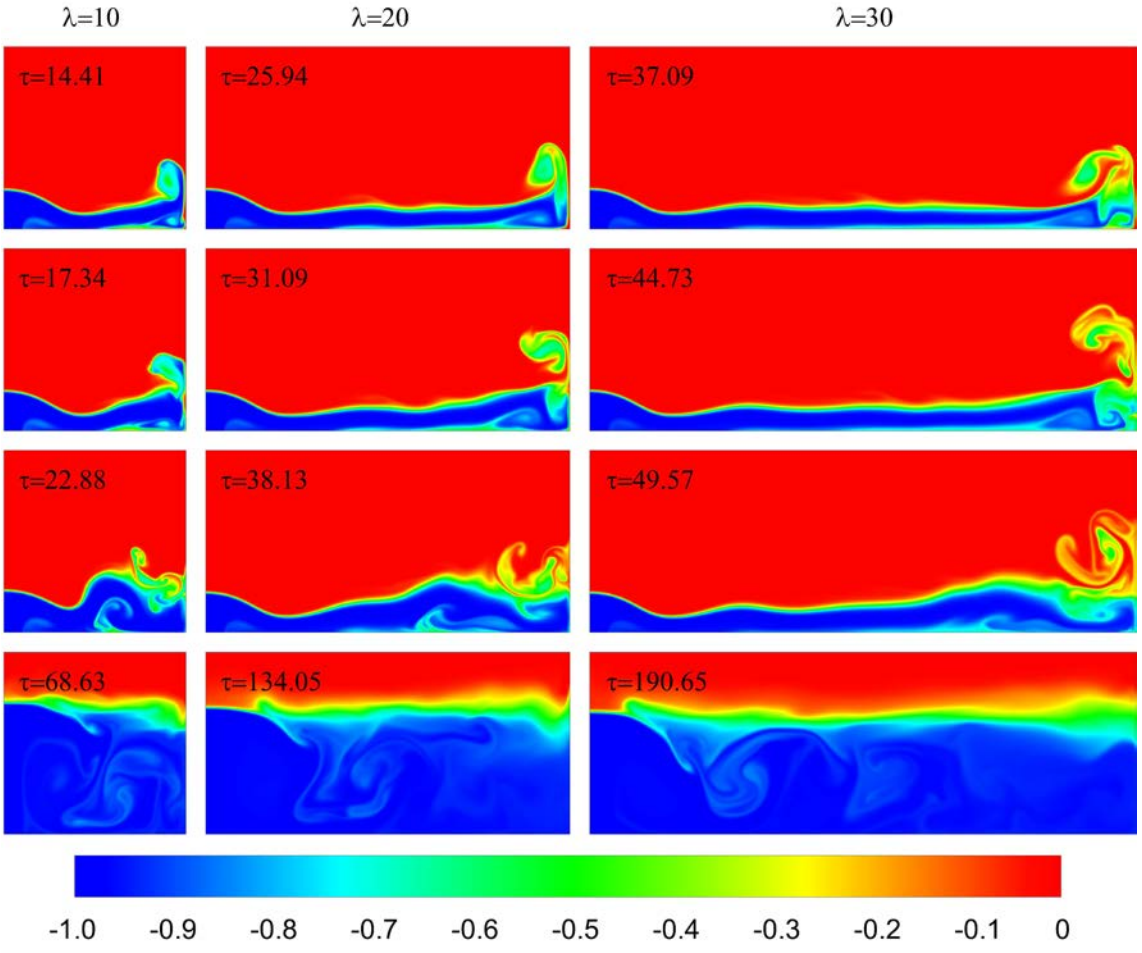

FIGURE 4.11: Temperature contours of the fountains of $Fr = 1.0$, $Re = 200$ and $Pr = 7$. The left, middle and right columns are for $\lambda = 10$, $\lambda = 20$ and $\lambda = 30$ at different times.

illustrate the influence of λ on the secondary wall fountain and stratification of the weak planar fountain filling box flow. A higher maximum penetration height of the wall fountain is observed for the channel with a larger size λ. For the channel with $\lambda = 10$, the wall fountain slumps down after it reaches the maximum height at $\tau = 17.34$. While for the channel with $\lambda = 20$ and 30, the wall fountain rolls down after the maximum height position as shown in the middle and right columns. For the channel with a larger λ, it takes a longer time to form the stratified structure. The simulations also cover the channels with $\lambda = 15$, 25 and 35, and thier results show the same trend which includes a rolling down wall fountain structure, hence are not presented here.

4.4 Quantitative observation

4.4.1 Intrusion

4.4.1.1 Passage of the intrusion front

In Figure 4.12, the time series of the passage of the intrusion front are presented for the planar fountains with the Fr, Re, Pr and λ over the ranges of $0.1 \leq Fr \leq 3.0$, $5 \leq Re \leq 800$, and $0.7 \leq Pr \leq 100$ and $10 \leq \lambda \leq 35$, respectively. The intrusion front is determined as the x-location at which the temperature $T(x) = T_a - 1\%(T_a - T_0)$ within the whole calculation domain.

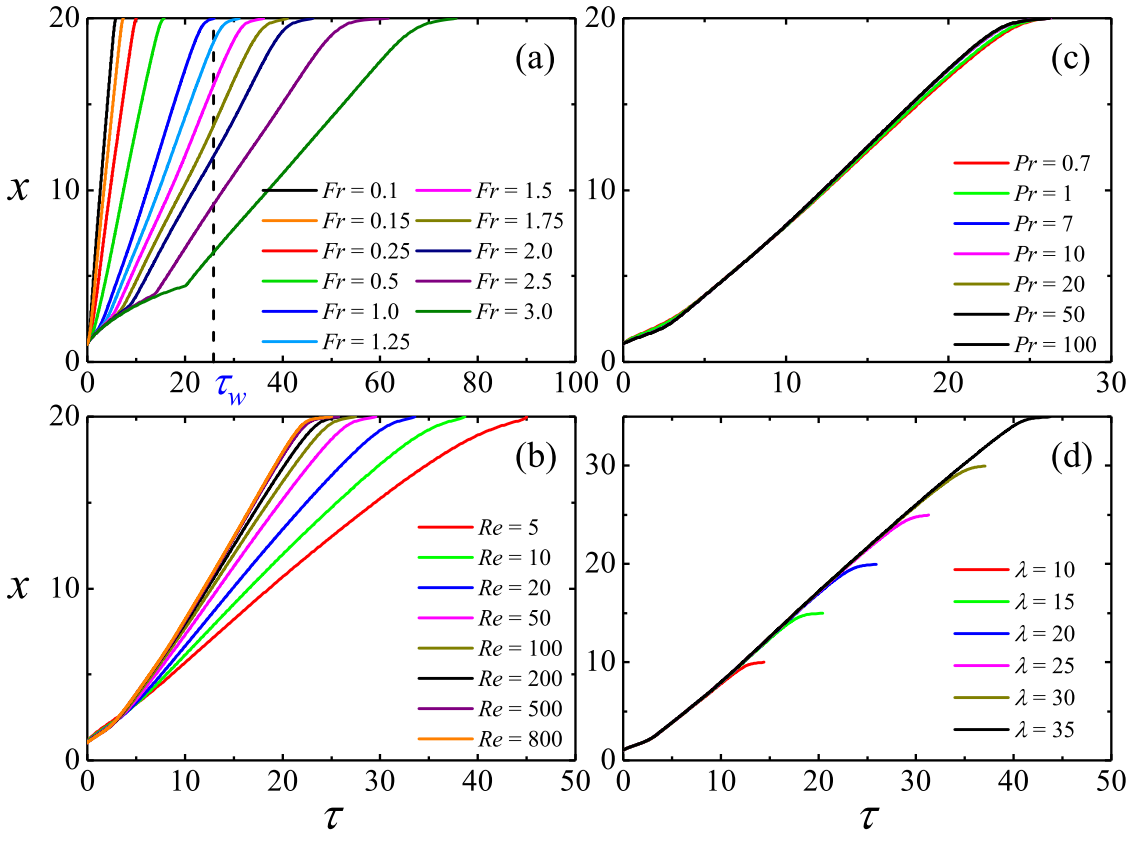

FIGURE 4.12: Time series of the passage of the intrusion front for fountains with (a) $Re = 200$, $Pr = 7$, $\lambda = 20$ and $0.1 \leq Fr \leq 3.0$; (b) $Fr = 1.0$, $Pr = 7$, $\lambda = 20$ and $5 \leq Re \leq 800$; (c) $Fr = 1.0$, $Re = 200$, $\lambda = 20$ and $0.7 \leq Pr \leq 100$; (d) $Fr = 1.0$, $Re = 200$, $Pr = 7$ and $10 \leq \lambda \leq 35$.

The end point of the time series profile is the time instant when the intrusion front impinges on the sidewall, which is defined as τ_w as shown in Figure 4.12(a). The results in Figure 4.12(a)-(b) show that it takes a longer time for the intrusion front of the fountain with larger Fr or smaller Re. However, the intrusion profiles overlap for the cases of $Re = 500$ and $Re = 800$, indicating that Re plays a less important role in the intrusion for $500 \leq Re$. Similarly, the changing of Pr has negligible influence on the passage of the intrusion front as illustrated in Figure 4.12(c), which is consistent with the qualitative observation. Figure 4.12(d) presents the intrusion profiles for the cases with various confinement sizes λ. It has been found that the effect of the confinement size becomes noticeable only when the intrusion approaches the sidewall.

4.4.1.2 Time-scale for the intrusion front impinging the side-wall

The effects of Fr, Re, Pr and λ on τ_w are shown in Figure 4.13. From Figure 4.13(a), three ranges can be distinguished, with two critical numbers at $Fr = 1.0$ and $Fr = 2.0$, and three corresponding correlations are determined from numerical results as follows:

$$\tau_w = \begin{cases} 25.71Fr^{0.65} - 0.31, & 0.1 \leq Fr \leq 1.0, \\ 20.1Fr + 5.65, & 1.0 \leq Fr \leq 2.0, \\ 29.15Fr - 12.49, & 2.0 \leq Fr \leq 3.0. \end{cases} \tag{4.1}$$

The regression constants for the three correlations are $R^2 = 0.998$, 1 and 1, respectively. Similarly, the influence of Re on τ_w is presented in Figure 4.13(b). $Re = 50$ and $Re = 200$ are found to distinguish the range into three parts, that is, for $5 \leq Re \leq 20$ and $50 \leq Re \leq 200$, τ_w follows power laws with the Re, while for $Re > 200$, the influence of Re on τ_w is negligible. The corresponding correlations

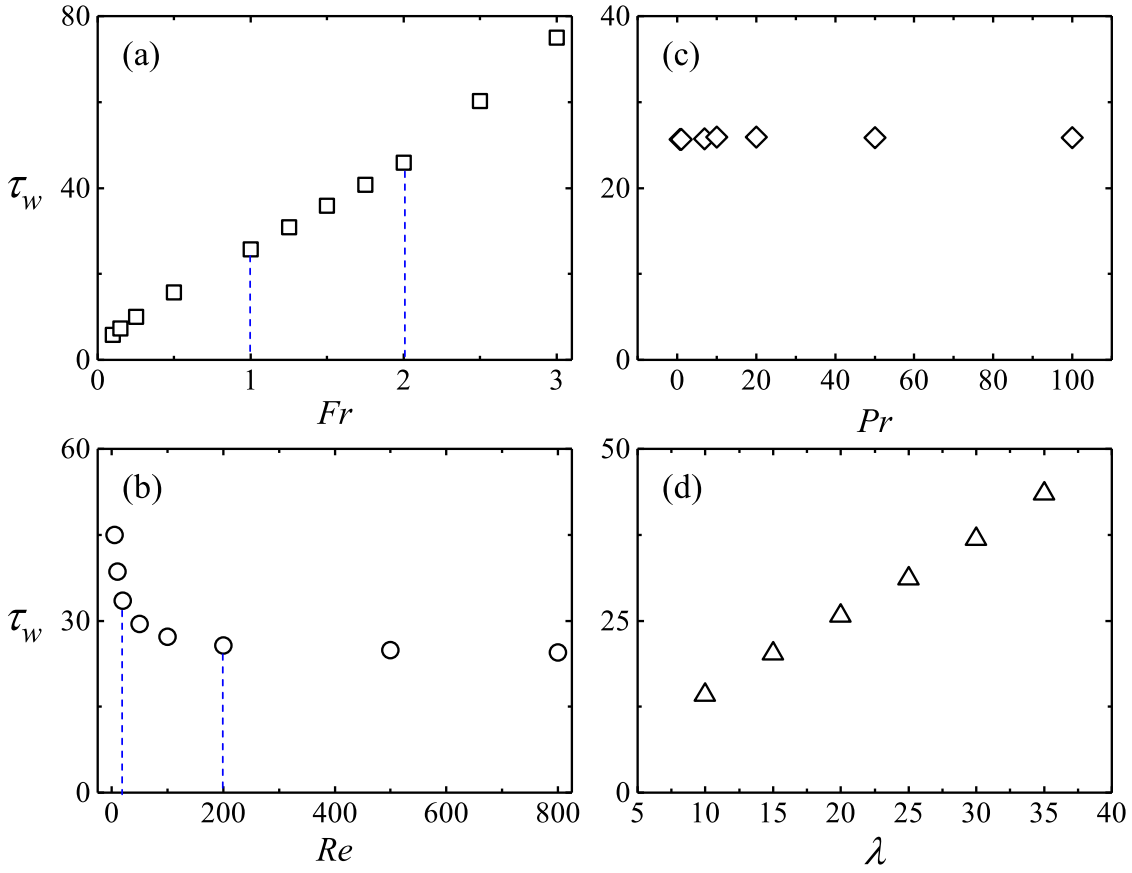

FIGURE 4.13: (a) τ_w plotted against Fr with $Re = 200$, $Pr = 7$ and $\lambda = 20$; (b) τ_w plotted against Re with $Fr = 1.0$, $Pr = 7$ and $\lambda = 20$; (c) τ_w plotted against Pr with $Fr = 1.0$, $Re = 200$ and $\lambda = 20$; (d) τ_w plotted against λ with $Fr = 1.0$, $Re = 200$ and $Pr = 7$.

are determined by power law regression with the numerical results as follows:

$$\tau_w = \begin{cases} 63.46Re^{-0.21} - 0.05, & 5 \leq Re \leq 20, \\ 43.15Re^{-0.12} - 0.12, & 50 \leq Re \leq 200, \end{cases} \tag{4.2}$$

with the regression constants of $R^2 = 0.989$ and 0.985, respectively. The influence of Pr on the τ_w is negligible, as shown in Figure 4.13(c). Figure 4.13(d) shows that τ_w has a linear relation with the confinement size of the channel as shown below,

$$\tau_w = 1.15\lambda + 2.65, \tag{4.3}$$

where the regression constant is $R^2 = 0.999$.

4.4.1.3 Intrusion speed

During the development of a pure gravity current, the flow may experience three regimes, *i.e.*, the wall jet regime (W-J), the buoyancy-inertial regime (B-I) and the buoyancy-viscosity regime (B-V), which are determined by the dominating forces [1]. For the initial stage, the flow is dominated by momentum as a plane wall jet, so a scaling relation $X(t) \sim M^{1/3}t^{2/3}$ was obtained, where M is the momentum flux. After that, the driving force of the current becomes buoyancy (gravity) which is balanced by the inertial force, thus the current is in a buoyancy-inertial regime. The balance between the gravity and the inertial force is maintained until the inertial force is small compared to the total viscous drag force resulting from the interfacial shear stress between the current and the ambient fluid or from the bottom shear stress, which changes the flow into another regime where the buoyancy force is balanced by the viscous drag force.

Two corresponding scaling relations, that is, $X(t) \sim B^{1/3}t$ and $X(t) \sim (BQ^2/\nu)^{1/5}t^{4/5}$, were obtained for the gravity current in the buoyancy-inertial and buoyancy-viscosity regimes, respectively [1], where $Q = X_0W_0$, $B = g(\rho_0 - \rho_a)/\rho_a Q$ are volume and buoyancy fluxes. Based on these scaling relations, the correlations between the intrusion speed and time may be written in dimensionless formation in terms of Fr and Re as follows:

$$v_i \sim \tau^{-1/3}, \tag{4.4}$$

for the wall jet regime,

$$v_i \sim Fr^{-2/3}, \tag{4.5}$$

for the buoyancy-inertial regime, and

$$v_i \sim Fr^{-2/5}Re^{1/5}\tau^{-1/5}, \tag{4.6}$$

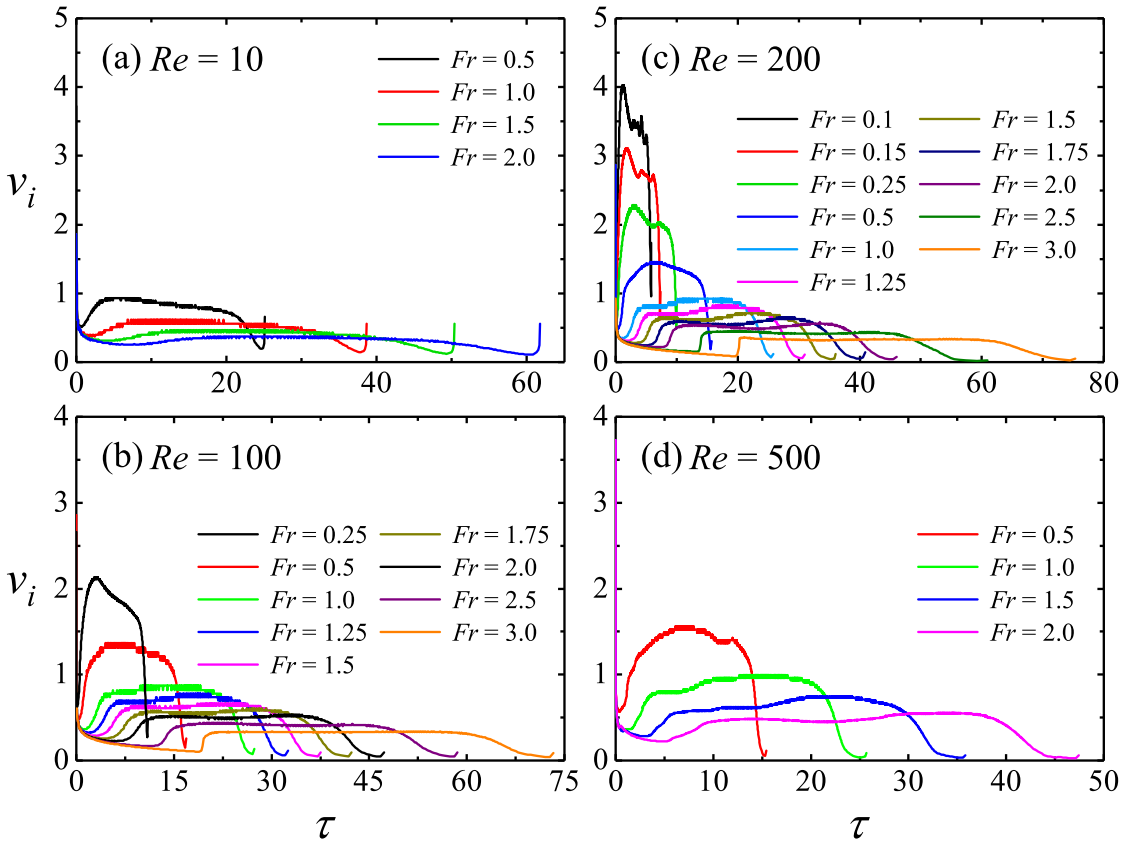

FIGURE 4.14: Time series of the intrusion speed for the fountains with $Pr = 7$, $\lambda = 20$: (a) $Re = 10$ and $0.5 \leq Fr \leq 2.0$; (b) $Re = 100$ and $0.25 \leq Fr \leq 3.0$; (c) $Re = 200$ and $0.1 \leq Fr \leq 3.0$; (d) $Re = 500$ and $0.5 \leq Fr \leq 2.0$.

for the buoyancy-viscosity regime, where v_i is the dimensionless intrusion velocity non-dimensionalized by W_0.

For free gravity current, Eq.(4.4) indicates that the intrusion speed for the wall jet regime is dependent on time, but independent of both Fr and Re. While for the buoyancy-inertial regime described by Eq.(4.5), the intrusion velocity does not change with time, which only depends on Fr. When the gravity current is developing into the buoyancy-viscosity regime, the intrusion speed begins time-dependent again and is dependent on both Fr and Re, as shown in Eq.(4.6).

Figures 4.14 and 4.15 present the time series of the intrusion front speed for a series of Fr and Re. It is found that only the cases with $Re = 200$ and $Fr \leq 0.25$

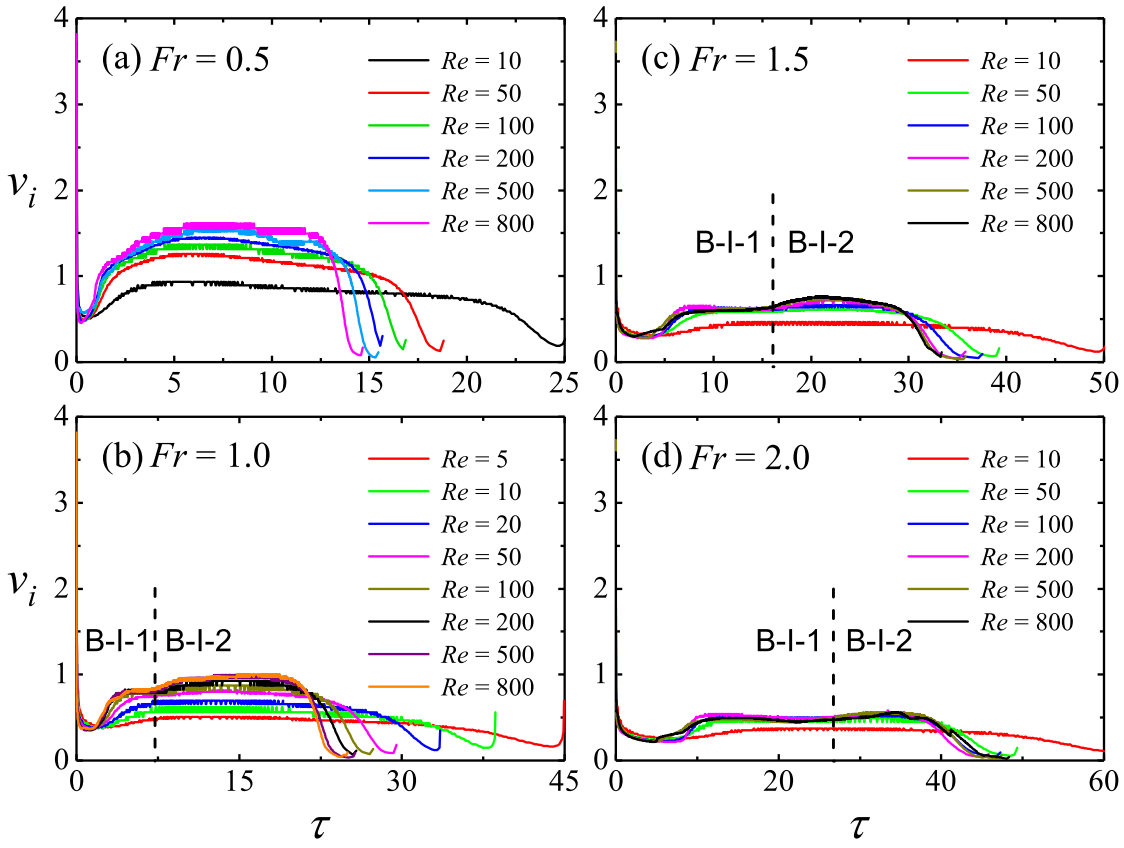

FIGURE 4.15: Time series of the intrusion speed for the fountains with $Pr = 7$, $\lambda = 20$: (a) $Fr = 0.5$ and $10 \leq Re \leq 800$; (b) $Fr = 1.0$ and $5 \leq Re \leq 800$; (c) $Re = 1.5$ and $10 \leq Re \leq 800$; (d) $Fr = 2.0$ and $10 \leq Re \leq 800$.

experienced a wall jet regime, as shown in Figure 4.14(c). The buoyancy-inertial regime (with constant velocity) is observed for the cases of $0.5 \leq Fr$. However, for the cases over the range of $1.0 \leq Fr \leq 2.0$ and $100 \leq Re \leq 800$, two stages at different constant speeds are observed, which are defined as the 'B-I-1' stage and the 'B-I-2' stage respectively. However, only one constant speed stage is present for the cases over the range of $Re \leq 50$ and $Fr \leq 0.5$, or $Fr \geq 2.5$. The results also show that the velocity profiles of the cases of $Fr \leq 1.0$ and $Re \leq 200$ all experienced the buoyancy-viscosity regime. But when $Fr > 1.0$, only the cases of $Fr = 1.5$, $Re = 10$ and 50, and $Fr = 2.0$ and $Re = 10$ developed into the buoyancy-viscosity stage.

Moreover, Eq.(4.5) indicates that only Fr can influence the intrusion speed in the buoyancy-inertial regime. Figure 4.16 presents the velocities against $Fr^{-2/3}$ for

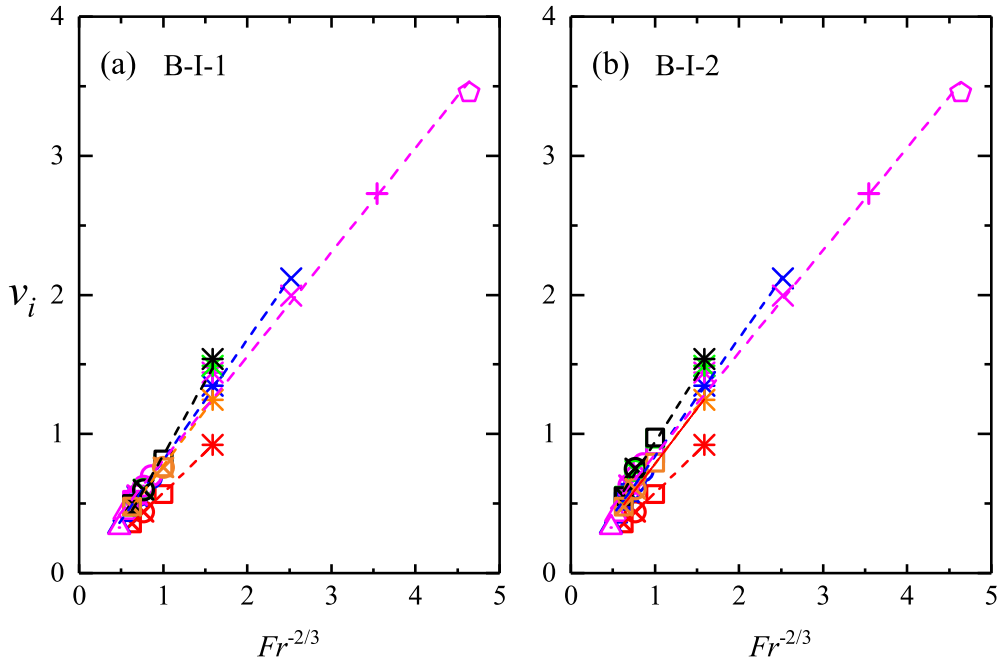

FIGURE 4.16: The B-I regimes for the intrusion current: (a) The B-I-1 regime, the first constant speed stage; (b) The B-I-2 regime, the second constant speed stage.

the 'B-I-1' and 'B-I-2' stages, which indicates that the $-2/3$ power law can describe the influence of Fr on v_i for the fixed Re cases very well. Eq.(4.5) is confirmed by the overlap parts in Figure 4.16(a) (*i.e.*, $Fr \geq 1.0$ and $Re \geq 100$) or Figure 4.16(b) (*i.e.*, $Re \geq 500$). However, the difference between the slopes of the trend lines for other cases is considerable, which should be caused by the influence of Re.

In regards to the influence of Re, Figure 4.17 presents the intrusion velocity plotted against $v_i \sim Fr^{-2/3}Re^m$, where m is the index determined by multivariate regression technique with the numerical results. Two corresponding modified correlations, *i.e.*, B-I-Modified-1 and B-I-Modified-2, are obtained as follows:

$$v_i = \begin{cases} 0.37Fr^{-2/3}Re^{1/5}, & 0.5 \leq Fr \leq 2.0, 5 \leq Re \leq 50, \\ 0.56Fr^{-2/3}Re^{1/10}, & 0.5 \leq Fr \leq 3.0, 50 \leq Re \leq 200, \end{cases} \tag{4.7}$$

with the regression constants of $R^2 = 0.998$ and 0.992, respectively.

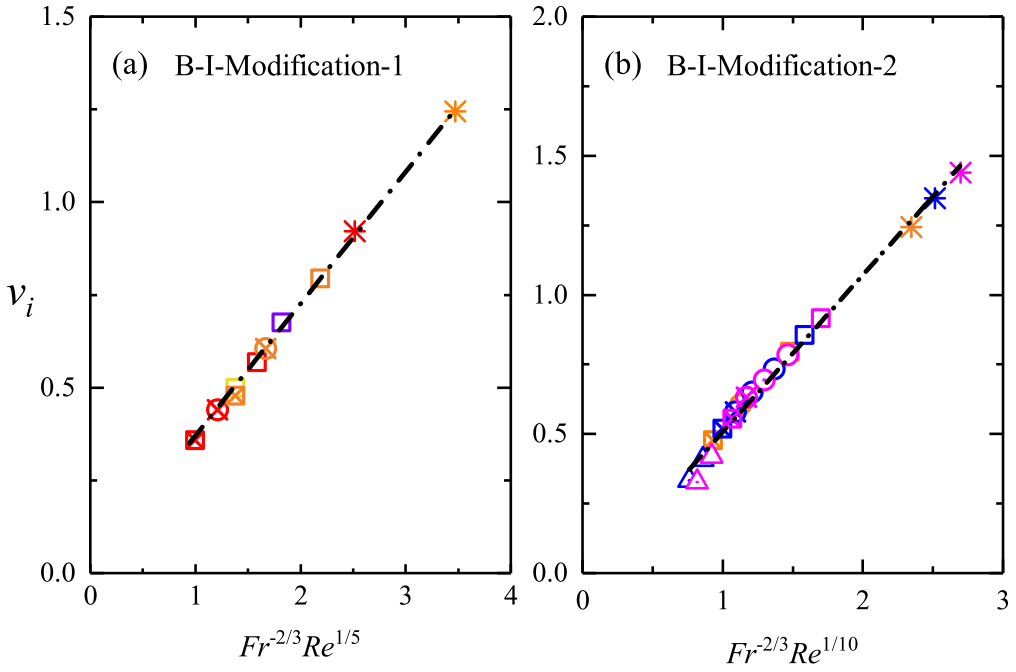

FIGURE 4.17: The intrusion velocity v_i plotted against (a) $Fr^{-2/3}Re^{1/5}$ for the B-I-Modification-1 regime, and (b) $Fr^{-2/3}Re^{1/10}$ for the B-I-Modification-2 regime, respectively.

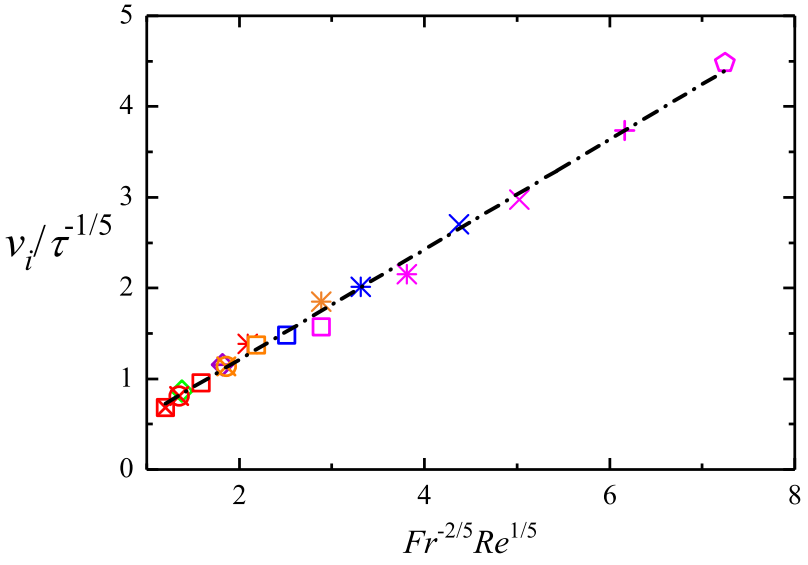

FIGURE 4.18: $v_i/\tau^{-1/5}$ plotted against $Fr^{-2/5}Re^{1/5}$ in the buoyancy-viscosity regime for the intrusion current.

The result of the buoyancy-viscosity regime is presented in Figure 4.18, which fits Eq.(4.6) very well. The quantified correlation is as following

$$v_i = 0.61 Fr^{-2/5} Re^{1/5} \tau^{-1/5}, \tag{4.8}$$

with the regression constant of $R^2 = 0.994$.

4.4.2 Wall fountain

4.4.2.1 Development of wall fountain along the sidewall

After the intrusion impinging with the sidewall, the flow is turned upward and develops along the sidewall. Due to the negative buoyancy, the flow penetrates to a certain height and then falls down, forming a wall fountain flow, which is also called as overturning in the filling box model [97]. Notably, the secondary wall fountain flow is not continuous. Here, the fountain behavior is characterized as no overturning, slumping down and rolling down according to the bulking behavior as listed in Table 4.2. From this table, it is found that the overturning behavior of the secondary wall fountain is mainly governed by Re; for small Re values ($5 \leq Re \leq 20$), no overturning is observed; for $50 \leq Re \leq 100$, the fountain slumps down after reaches the maximum height; and the fountain rolls down for higher Re values ($Re \geq 200$). Additionally, when the confinement size reduces to $\lambda = 10$, the fountain slumps down, which is different from the rolling down behavior for $\lambda \geq 15$. It is seen that the influence of Fr and Pr on the overturning behavior of the secondary wall fountain is minimal.

TABLE 4.2: Behavior of the secondary wall fountain

Runs	Fr	Re	Pr	λ	**Overturning**
1	0.1	200	7	20	R

Continued on next page

Table 4.2 – continued from previous page

Runs	Fr	Re	Pr	λ	**Overturning**
2	0.15	200	7	20	R
3	0.25	100	7	20	S
4	0.25	200	7	20	R
5	0.5	10	7	20	N
6	0.5	50	7	20	S
7	0.5	100	7	20	S
8	0.5	200	7	20	R
9	0.5	500	7	20	R
10	0.5	800	7	20	R
11	1	5	7	20	N
12	1	10	7	20	N
13	1	20	7	20	N
14	1	50	7	20	S
15	1	100	7	20	S
16	1	200	7	20	R
17	1	500	7	20	R
18	1	800	7	20	R
19	1.25	100	7	20	S
20	1.25	200	7	20	R
21	1.5	10	7	20	N
22	1.5	50	7	20	S
23	1.5	100	7	20	S
24	1.5	200	7	20	R
25	1.5	500	7	20	R
26	1.5	800	7	20	R
27	1.75	100	7	20	S

Continued on next page

Table 4.2 – continued from previous page

Runs	Fr	Re	Pr	λ	**Overturning**
28	1.75	200	7	20	R
29	2	10	7	20	N
30	2	50	7	20	S
31	2	100	7	20	S
32	2	200	7	20	R
33	2	500	7	20	R
34	2	800	7	20	R
35	2.5	100	7	20	S
36	2.5	200	7	20	R
37	3	100	7	20	S
38	3	200	7	20	R
39	1	200	0.7	20	R
40	1	200	1	20	R
41	1	200	10	20	R
42	1	200	20	20	R
43	1	200	50	20	R
44	1	200	100	20	R
45	1	200	7	10	S
46	1	200	7	15	R
47	1	200	7	25	R
48	1	200	7	30	R
49	1	200	7	35	R
N - No falling, S - Slumping, R - Rolling					

To further investigate the influence of these parameters on the wall fountain, the time series of the secondary wall fountain front along the sidewall are presented in Figure 4.19 over the ranges of $0.1 \leq Fr \leq 3.0$, $5 \leq Re \leq 800$, $0.7 \leq Pr \leq 100$ and

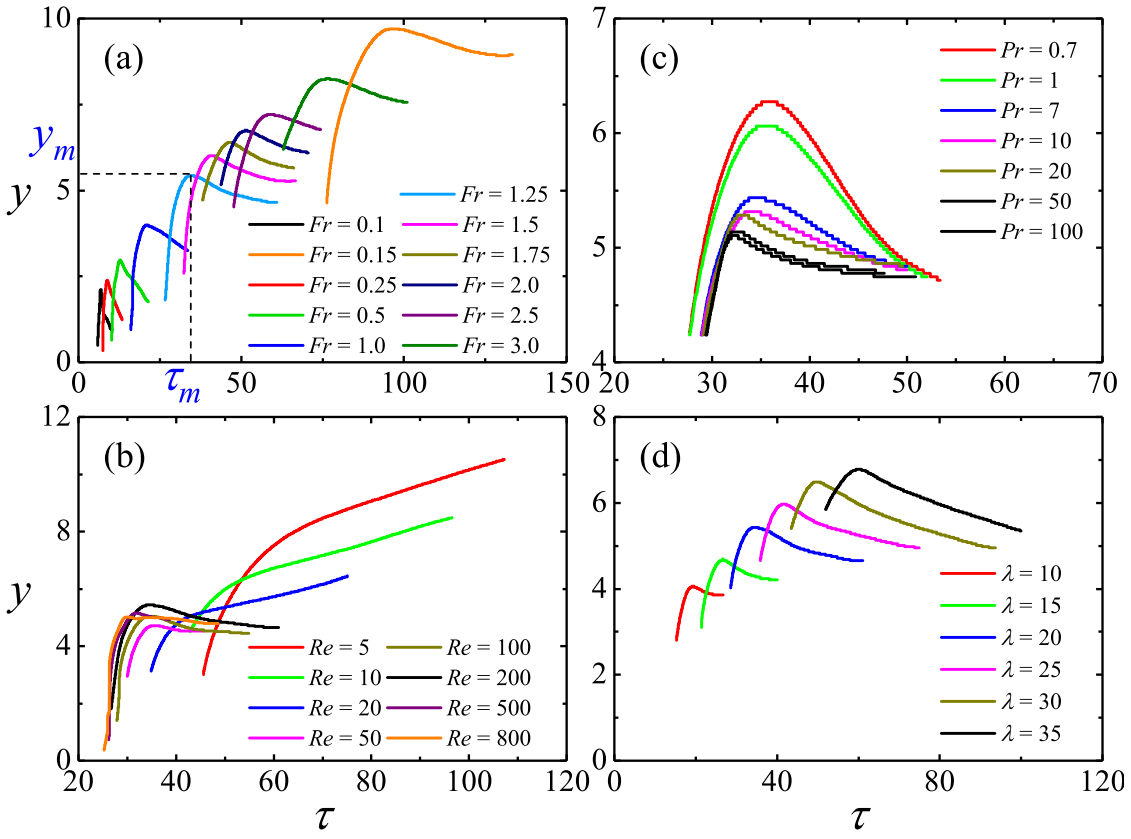

FIGURE 4.19: Time series of the wall fountain front for fountains with (a) $Re = 200$, $Pr = 7$, $\lambda = 20$ and $0.1 \leq Fr \leq 3.0$; (b) $Fr = 1.0$, $Pr = 7$, $\lambda = 20$ and $5 \leq Re \leq 800$; (c) $Fr = 1.0$, $Re = 200$, $\lambda = 20$ and $0.7 \leq Pr \leq 100$; (d) $Fr = 1.0$, $Re = 200$, $Pr = 7$ and $10 \leq \lambda \leq 35$.

$10 \leq \lambda \leq 35$. The wall fountain front on the sidewall is defined by the y-location at which the temperature $T(y) = T_a - 1\%(T_a - T_0)$ at $x = \pm\lambda$. From the time series, the maximum distance of the wall fountain developed on the side-wall is determined as y_m as shown in Figure 4.19(a) and the corresponding time τ_m, which is the time-scale for the secondary wall fountain reaches its maximum penetration height. It is found that the y_m increases with Fr and λ, but decreases with Re and Pr. Similarly, τ_m is larger with a larger Fr or λ, but becomes smaller with a larger Re or Pr.

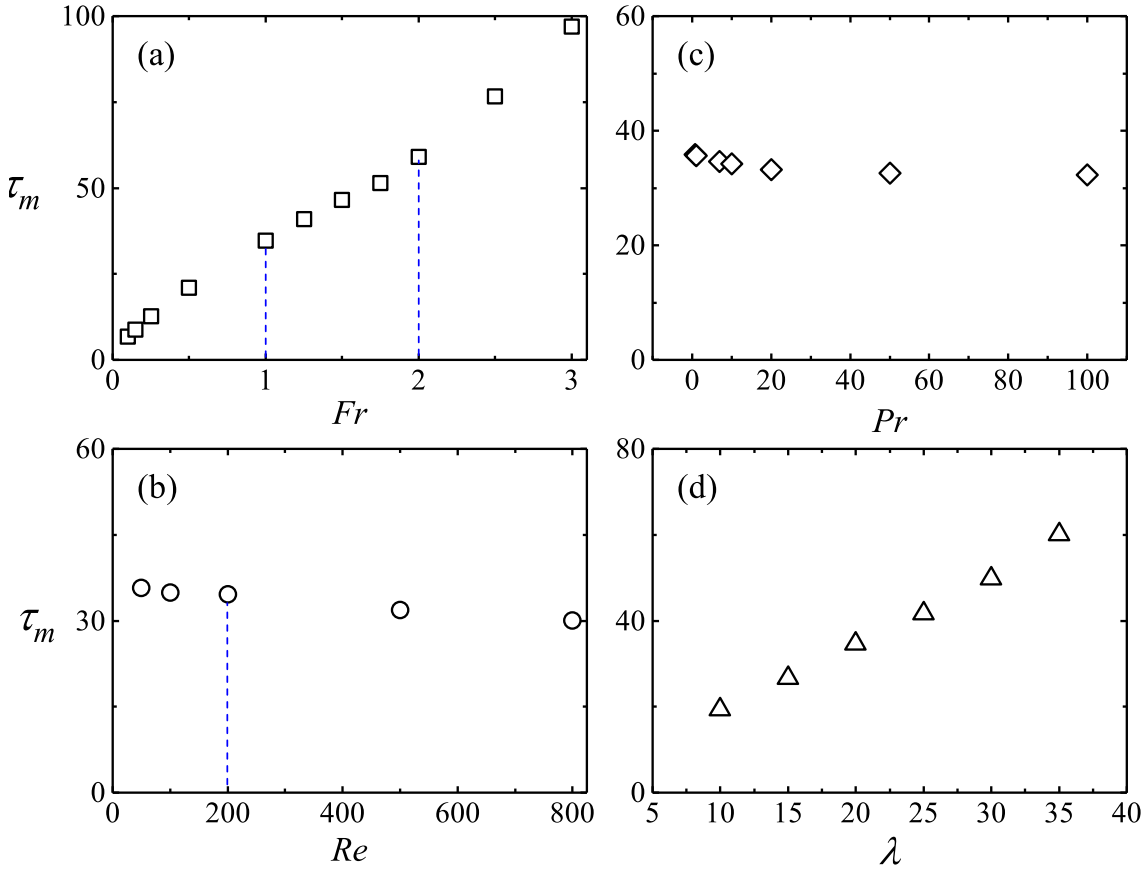

FIGURE 4.20: (a) τ_m plotted against Fr with $Re = 200$, $Pr = 7$ and $\lambda = 20$; (b) τ_m plotted against Re with $Fr = 1.0$, $Pr = 7$ and $\lambda = 20$; (c) τ_m plotted against Pr with $Fr = 1.0$, $Re = 200$ and $\lambda = 20$; (d) τ_m plotted against λ with $Fr = 1.0$, $Re = 200$ and $Pr = 7$.

4.4.2.2 Time-scale for the wall fountain reaching the maximum penetration height

The influence of Fr, Re, Pr and λ on the time-scale for the secondary wall fountain to reach its maximum height is shown in Figure 4.20. It is seen that the influence of Fr on τ_m can be distinguished into three ranges as identified in Figure 4.20(a), with $Fr = 1.0$ and $Fr = 2.0$ as the critical values, and the individual correlations

obtained with the numerical results are as follows,

$$\tau_m = \begin{cases} 34.7Fr^{0.71} - 0.12, & 0.1 \leq Fr \leq 1.0, \\ 23.76Fr + 10.93, & 1.0 \leq Fr \leq 2.0, \\ 37.83Fr - 17, & 2.0 \leq Fr \leq 3.0, \end{cases} \tag{4.9}$$

with the regression constants of $R^2 = 1.0$, 1.0 and 0.998, respectively.

From Figure 4.20(c), it is seen that the influence of Pr on τ_m can be approximated by the following power law correlations,

$$\tau_m = 35.65Pr^{-0.02} + 0.07 \tag{4.10}$$

with the regression constant of $R^2 = 0.97$.

Since there is no falling down process for the fountain with $Re \leq 20$, no τ_m exists for these cases. As shown in Figure 4.20(c), it is seen that the influence of Re on τ_m can be distinguished into two different ranges, with $Re = 200$ as the critical value.

A linear relation is found for the influence of λ on τ_m, as shown in Figure 4.20(d), which can be approximated by the following correlation,

$$\tau_m = 1.6\lambda + 2.69, \tag{4.11}$$

with the regression constant of $R^2 = 0.996$.

4.4.2.3 Maximum height of the wall fountain on the sidewall

Similarly, the relations between the maximum height of the secondary wall fountain on the sidewalls, y_m, and Fr, Re, Pr and λ are presented in Figure 4.21. From Figure 4.21(a), it is seen that, similar to the influence of Fr on τ_m, $Fr = 1.0$ and $Fr = 2.0$ distinguish the influence of Fr into three different ranges. The

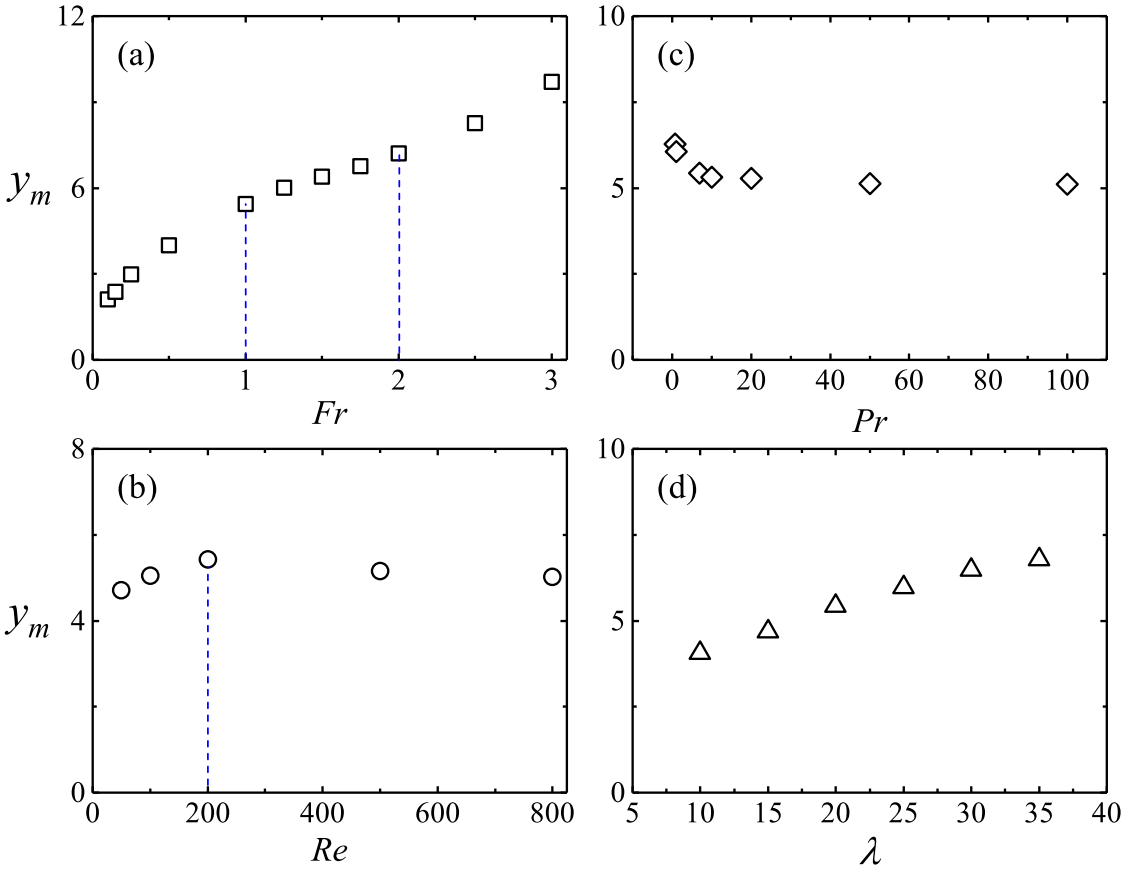

FIGURE 4.21: (a) y_m plotted against Fr with $Re = 200$, $Pr = 7$ and $\lambda = 20$; (b) y_m plotted against Re with $Fr = 1.0$, $Pr = 7$ and $\lambda = 20$; (c) y_m plotted against Pr with $Fr = 1.0$, $Re = 200$ and $\lambda = 20$; (d) y_m plotted against λ with $Fr = 1.0$, $Re = 200$ and $Pr = 7$.

corresponding correlations for the three individual ranges are obtained as follows,

$$y_m = \begin{cases} 5.45Fr^{0.42} - 0.05, & 0.1 \leq Fr \leq 1.0, \\ 1.72Fr + 3.78, & 1.0 \leq Fr \leq 2.0, \\ 2.49Fr + 2.17, & 2.0 \leq Fr \leq 3.0, \end{cases} \tag{4.12}$$

with the regress constants of $R^2 = 0.999$, 0.993 and 0.998, respectively.

From Figure 4.21(b), it is shown that before and after $Re = 200$, Re has significantly different influence on y_m, which should be caused by the different overturning behaviors, *i.e.*, slumping down for $50 \leq Re \leq 100$ and rolling down for $200 \leq Re \leq 800$.

The influence of Pr on y_m is shown in Figure 4.21(c), which can be approximated by the following power law correlation,

$$y_m = 6.21 Pr^{-0.042} - 0.17, \quad R^2 = 0.935 \tag{4.13}$$

with the regression constant of $R^2 = 0.935$.

The influence of λ on y_m can be approximated by the following linear correlation,

$$y_m = 0.11\lambda + 3.06, \tag{4.14}$$

with the regression constant of $R^2 = 0.984$, which is similar to the influence of λ on τ_m.

4.4.3 Stratification

The height of the thermally stratified fluid within the domain is defined as the vertical location where the temperature is $T(y) = T_a - 1\%(T_a - T_0)$, which is the height of the interface between the stratified fluid created by the filling of cold fluid through the fountain flow and the ambient fluid. The time series of the maximum, minimum and averaged heights of the thermally stratified fluid after the intrusion impinging with the sidewall are presented in Figure 4.22 for various Fr, Re, Pr and λ. The magnitudes of the differences among these heights are initially significant, due to the key roles played by convection and mixing. After that, over a relatively long time, the differences decrease and the time series of these heights follow essentially the same trend when filling becomes dominant in the subsequent

stratification formation. From this figure, it is seen that the development rate of the quasi-steady stratification can be approximately described by the rate of the averaged stratification height profile.

As shown in Figure 4.22(a), with the increase of Fr, the magnitudes of the differences among the maximum, average and minimum height profiles increase and a longer time needs for the confined fountain to reach a steady stratification. Similarly, the differences among these heights increase when Re increases, however, the time for the fountain to reach a steady stratification is decreased. Additionally, the development rate of the stratification decreases with the increase of Re. The increase of Pr can also reduce the rate of the stratification, due to the influence of thermal conduction as presented in Figure 4.22(c).

For a purely filling box, the development rate of the stratification height, v_s, is the reciprocal of λ ($v_s = 1/\lambda$), based on the conservation of mass. The rate of the averaged stratification height profile and the corresponding purely filling rate are plotted in Figure 4.23 to illustrate the influence of Fr, Re, Pr and λ on v_s with the filling by fountains. Figure 4.23(a) indicates that the effect of Fr on v_s, again, can be distinguished into three ranges by $Fr = 1.0$ and $Fr = 2.0$, although no suitable correlations are obtained due to the limited data obtained.

The influence of Re on v_s, as shown in Figure 4.23(b), can be divided into three different regimes, with $Re = 20$ and $Re = 200$ as the critical values. For $Re < 200$, the influence of Re can be quantified by the following correlations,

$$v_s = \begin{cases} 0.09Re^{-0.14}, & R^2 = 0.983, \quad 5 \leq Re \leq 20, \\ 0.07Re^{-0.06}, & R^2 = 0.974, \quad 20 \leq Re \leq 200, \end{cases} \tag{4.15}$$

with the regression constants of $R^2 = 0.983$ and 0.974, respectively. However, v_s becomes independent of Re when Re is beyond 200.

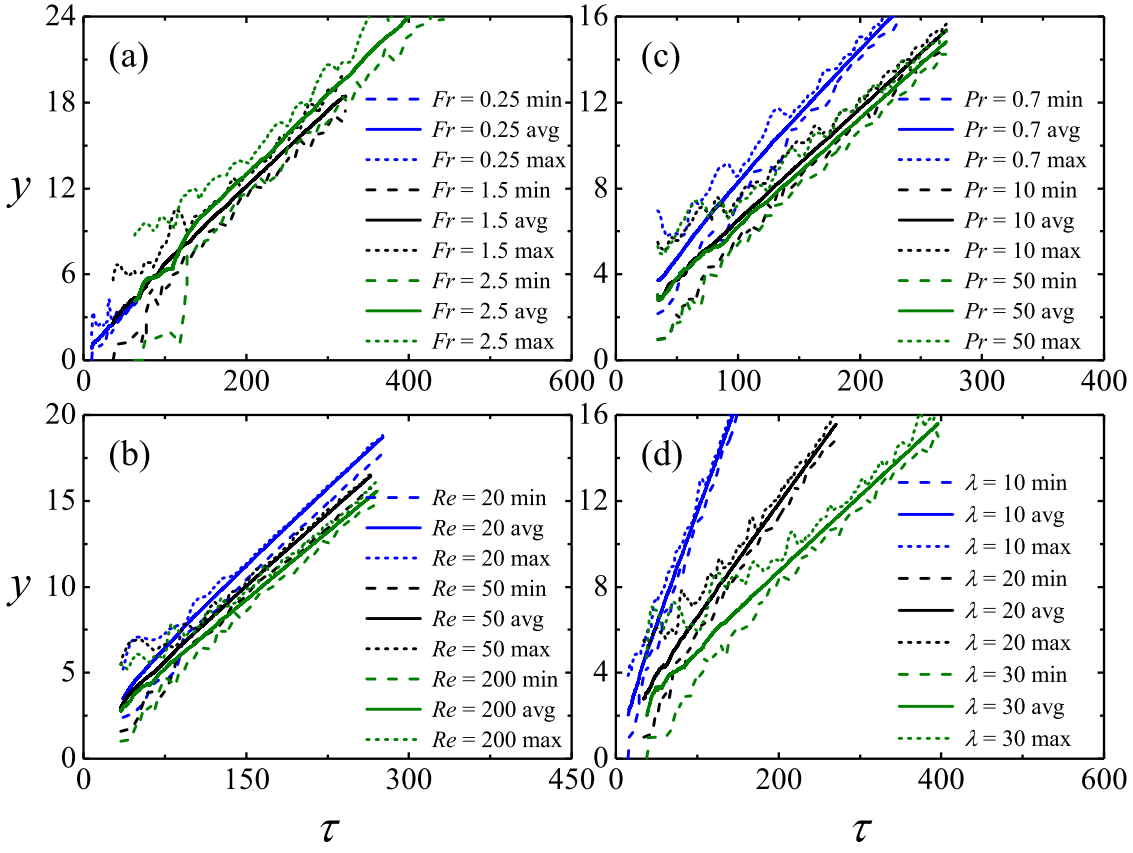

FIGURE 4.22: Time series of the maximum, minimum and average stratification heights for fountains with (a) $Re = 200$, $Pr = 7$, $\lambda = 20$ and $Fr = 0.25, 1.5, 2.5$; (b) $Fr = 1.0$, $Pr = 7$, $\lambda = 20$ and $Re = 20, 50, 200$; (c) $Fr = 1.0$, $Re = 200$, $\lambda = 20$ and $Pr = 0.7, 10, 50$; (d) $Fr = 1.0$, $Re = 200$, $Pr = 7$ and $\lambda = 10, 20, 30$.

The influence of Pr on v_s is presented in Figure 4.23(c), which shows that it can be approximated by the following power law correlation,

$$v_s = 0.0586 Pr^{-0.035}, \tag{4.16}$$

with the regression constant of $R^2 = 0.916$. The results also show that the stratification rate approximately coincides with the purely filling rate for very high Pr, indicating that the influence of thermal conduction is negligible.

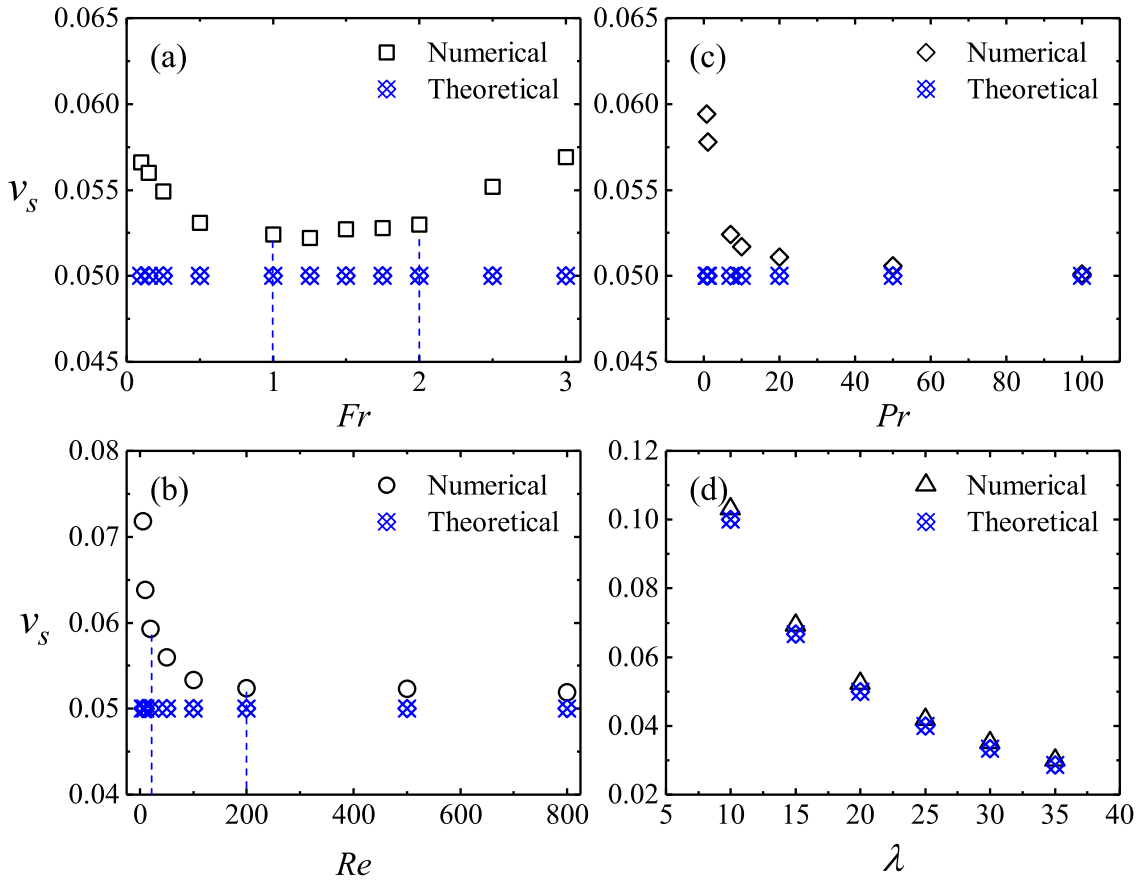

FIGURE 4.23: (a) v_s plotted against Fr with $Re = 200$, $Pr = 7$ and $\lambda = 20$; (b) v_s plotted against Re with $Fr = 1.0$, $Pr = 7$ and $\lambda = 20$; (c) v_s plotted against Pr with $Fr = 1.0$, $Re = 200$ and $\lambda = 20$; (d) v_s plotted against λ with $Fr = 1.0$, $Re = 200$ and $Pr = 7$.

The relation between v_s and λ is shown in Figure 4.23(d), and can be approximated by the following correlation,

$$v_s = 0.99\lambda^{-0.98}, \tag{4.17}$$

with the regression constant of $R^2 = 1.0$.

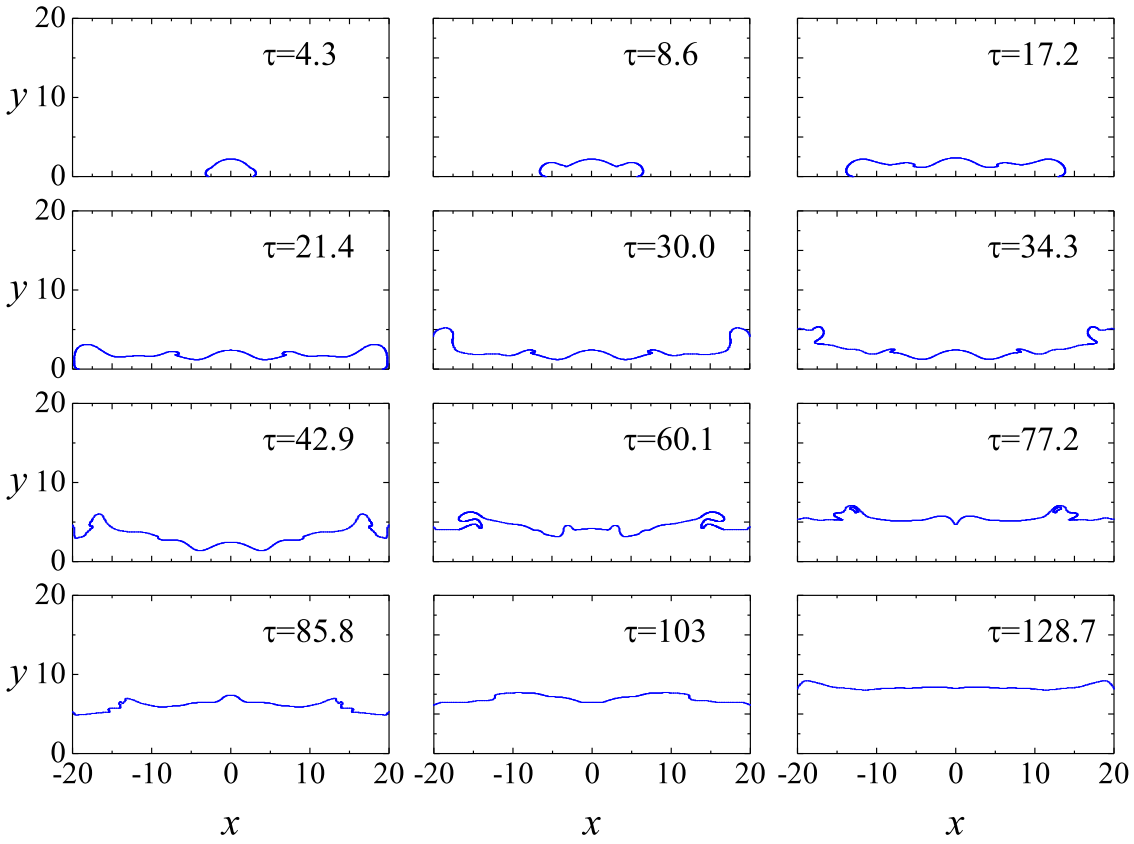

FIGURE 4.24: The evolution of the volume flux of the stratified fluid at different times for the case of $Fr = 1.0$, $Re = 100$, $Pr = 7$ and $\lambda = 20$.

4.4.4 Bulk entrainment or dilution

Since no assumptions are required for interactions between the upflow and downflow, or the entrainment process between fountains and surroundings, the bulk entrainment is selected to estimate the mean dilution of the buoyancy scalar over the fountain as a whole instead of to resolve the local entrainment rate. As mentioned in Chapter 2, the bulk entrainment rate is defined as Q_E/Q_0, where Q_E is the bulk entrainment by the fountain and Q_0 is the source volume flux. In this study, Q_E is calculated by $Q_E = Q_s - Q_0$, where Q_s represents the volume flux of the stratified fluid, which is calculated by integrating the area under the thermal stratified surface, as an example shown, with the results presented in Figure 4.24.

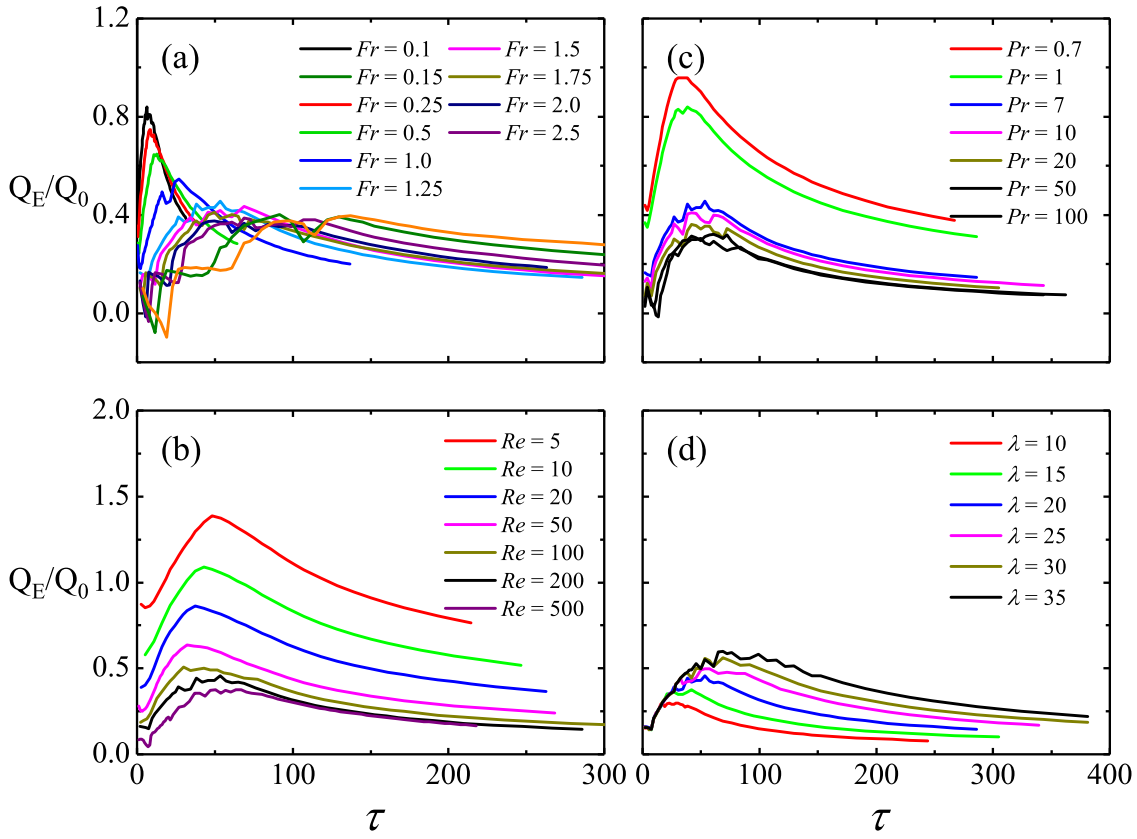

FIGURE 4.25: Time series of the entrainment rate Q_E/Q_0 for fountains with (a) $Re = 200$, $Pr = 7$, $\lambda = 20$ and $0.1 \leq Fr \leq 3.0$; (b) $Fr = 1.0$, $Pr = 7$, $\lambda = 20$ and $5 \leq Re \leq 500$; (c) $Fr = 1.0$, $Re = 200$, $\lambda = 20$ and $0.7 \leq Pr \leq 100$; (d) $Fr = 1.0$, $Re = 200$, $Pr = 7$ and $10 \leq \lambda \leq 35$.

The values of Q_E/Q_0 are calculated for the confined weak planar fountains over the range of $0.1 \leq Fr \leq 3.0$, $5 \leq Re \leq 800$, $0.7 \leq Pr \leq 100$ and $10 \leq \lambda \leq 35$, from the initial formation stage to the filling stage, with the time series of Q_E/Q_0 presented in Figure 4.25. It is found that the bulk entrainment rate increases monotonically with time until it attains a maximum value, and then decreases gradually. This is because after a certain time, thermal conduction dominates the dilution process, and the filling by fountains model turns to the purely filling box model. The influence of Fr, Re, Pr and λ on Q_E/Q_0 is in agreement with the results presented in § 4.4.3 for the stratification rate. However, before the entrainment rate reaches the maximum value, its changing rate decreases with Fr, but increases with Re as

shown in Figure 4.25(a)-(b), indicating that the convection has significant influence.

4.5 Summary

A 'weak plane fountain filling box' model is developed by the discharge of a weak plane fountain into an open channel with a homogeneous ambient fluid. A series of 2D direct numerical simulations are carried out to investigate the transient behavior of fountains over the ranges $0.1 \leq Fr \leq 3.0$, $5 \leq Re \leq 800$, $0.7 \leq Pr \leq 100$ and $10 \leq \lambda \leq 35$. A detailed description is given for the typical evolution of the confined weak plane fountains. With detailed qualitative and quantitative analysis, the following conclusions can be summarized,

- An intrusion current results from the downflow of the fountain impinging on the floor. The decrease of Fr or the increase of Re can enhance the intrusion speed v_i. The behavior of the intrusion flow can be approximately quantified by the scaling relations obtained by Chen [1] for gravity currents. However for the buoyancy-inertial regime, a two-constant speed stage is observed and the influence of Re on v_i cannot be ignored which is different from previous studies.

- Three mechanisms are observed for the behavior of the secondary wall fountain, *i.e.*, no falling, slumping down and rolling down. The maximum penetration height y_m of the wall fountain increases with the increase of Fr and λ, due to the reduction of buoyancy flux. However, the increase of Pr reduces y_m, due to the decrease of thermal conduction.

- For the fountains with $0.1 \leq Fr \leq 1.0$, $\tau_w \sim Fr^{0.65}$ and $\tau_m \sim Fr^{0.71}$ are obtained, where τ_w and τ_m are the time scales for the intrusion front and the wall fountain front. For the space with the same dimension, only the buoyancy flux keeps constant, the time-scale will follow a 2/3 power law with Fr. For

$Fr \leq 1.0$, the intrusion current spreads fast and remains laminar, hence the buoyancy flux has a minor changing.

- Convection, filling and conduction all contribute to the formation of thermal stratification. In the initial stage, convection and mixing play a key role. After a quasi steady stratification is formed, filling and thermal conduction become dominant. The behavior of intrusion and wall fountain for the fountain at $Re \leq 20$, due to its conduction-dominant nature, is significantly different from that at larger Re values considered ($50 \leq Re \leq 800$), where convection plays a more significant role. Additionally, $Fr = 1.0$ and $Fr = 2.0$ are found to distinguish the influence of Fr into three ranges. The influence of Pr applies through thermal conduction. With a smaller Re or Pr, the influence of the thermal conduction becomes more significant.

Chapter 5

Confined weak round fountains

5.1 Introduction

In the previous chapter, the transient behavior of weak planar fountains in an open channel with a homogeneous ambient fluid was studied using a series of 2D DNS runs. The influence of the major governing parameters (Fr, Re, Pr and λ) on the different evolution stages of the flow was explored using the numerical results. Moreover, the intrusion and stratification were compared with the existing theories for the pure gravity current and the filling box model. As reviewed in Chapter 2, the round fountain is another basic type of fountains, which widely exists in both nature and engineering. Hence, it is necessary to investigate the transient behavior of confined round fountains as well.

In this chapter, a series of 3D DNS runs are carried out to study the transient behavior of round fountains in cylindrical containers. In § 5.2, the details of the three-dimensional DNS runs carried out in this chapter, along with the mesh and time-step size independence testing results, are described. In § 5.3, the evolution of the typical confined weak round fountains is described qualitatively with the snapshots of the contours of temperature obtained from the DNS runs, along with the qualitative discussions on the influence of Fr, Re, Pr and λ on the flow behavior.

A quantitative analysis is then presented in § 5.4, to quantify the influence of Fr, Re, Pr and λ on the characteristics of the transient behavior of confined weak round fountains, including the intrusion, the wall fountain, the stratification and the bulk entrainment/dilution rate, over the ranges of $0.25 \leq Fr \leq 3.0$, $5 \leq Re \leq 800$, $0.7 \leq Pr \leq 100$ and $10 \leq \lambda \leq 35$. Finally the major conclusions of this chapter are drawn in § 5.5.

5.2 DNS runs and the mesh and time-step size independence testing

There are totally 46 DNS runs carried out in this chapter using ANSYS Fluent 17.0, with the key information about these runs presented in Table 5.1. Water is again selected as the fluid in the numerical simulations, similar to the cases for confined weak planar fountains studied in the previous chapter. The density, the kinematic viscosity and the volume expansion coefficient of water used in the DNS runs are $\rho_a = 996.6$ kg/m^3, $\upsilon = 8.58 \times 10^{-7}$ m^2/s and $\beta = 2.76 \times 10^{-4}$ 1/K with the reference temperature of $T_a = 300$ K. The maximum temperature difference between the source and the ambient fluid $(T_a - T_0)$ of all DNS runs is $(300 - 296.602) = 3.398$ K, which results in a small enough density ratio to ensure the Oberbeck-Boussinesq approximation is valid. The specific values of Fr, Re and Pr are determined by changing X_0, W_0 and T_0, with T_a fixed at 300 K.

For all DNS runs, cylindrical computational domains with radius R and height H are used. The radius of the nozzle for the inlet of fountain fluid is R_0, as sketched in Figure 1.8. To eliminate the influence of the open top boundary on the flow behaviors of interest, the value of H is chosen large enough. Similar to the planar fountain cases in the previous chapter, a fine uniform grid is used in the bottom region (below $H/2$), while for the top region (over $H/2$) a coarser and stretched

mesh is used as shown in Figure 5.1, to provide accurate results with a relatively economic computational source cost.

TABLE 5.1: Key data of the DNS runs of confined weak round fountains (Note: $\lambda = R/R_0$ and $h = H/R_0$).

Runs	Fr	Re	Pr	$\lambda \times h$	**Grids** (million)
1	0.25	100	7	20 × 20	4.06
2	0.25	200	7	20 × 20	4.06
3	0.5	10	7	20 × 20	4.06
4	0.5	50	7	20 × 20	4.06
5	0.5	100	7	20 × 20	4.06
6	0.5	200	7	20 × 20	4.06
7	0.5	500	7	20 × 12	5.88
8	0.5	800	7	20 × 12	5.88
9	1	5	7	20 × 20	4.06
10	1	10	7	20 × 20	4.06
11	1	20	7	20 × 20	4.06
12	1	50	7	20 × 20	4.06
13	1	100	7	20 × 20	4.06
14	1	200	7	20 × 20	4.06
15	1	500	7	20 × 12	5.88
16	1	800	7	20 × 12	5.88
17	1.25	100	7	20 × 20	4.06
18	1.25	200	7	20 × 20	4.06
19	1.5	10	7	20 × 20	4.06
20	1.5	50	7	20 × 20	4.06
21	1.5	100	7	20 × 20	4.06
22	1.5	200	7	20 × 20	4.06
23	1.5	500	7	20 × 12	5.88

Continued on next page

Table 5.1 – continued from previous page

Runs	Fr	Re	Pr	$\lambda \times h$	**Grids**(million)
24	1.5	800	7	20 × 12	5.88
25	1.75	100	7	20 × 20	4.06
26	1.75	200	7	20 × 20	4.06
27	2	10	7	20 × 20	4.06
28	2	50	7	20 × 20	4.06
29	2	100	7	20 × 20	4.06
30	2	200	7	20 × 20	4.06
31	2	800	7	20 × 12	5.88
32	2.5	100	7	20 × 20	4.06
33	2.5	200	7	20 × 20	4.06
34	3	100	7	20 × 20	4.06
35	3	200	7	20 × 20	4.06
36	1	200	0.7	20 × 20	4.06
37	1	200	1	20 × 20	4.06
38	1	200	10	20 × 20	4.06
39	1	200	20	20 × 20	4.06
40	1	200	50	20 × 20	4.06
41	1	200	100	20 × 20	4.06
42	1	200	7	10 × 30	3.84
43	1	200	7	15 × 30	5.78
44	1	200	7	25 × 20	4.07
45	1	200	7	30 × 20	4.89
46	1	200	7	35 × 20	5.7

Again extensive mesh and time-step size independence testing were carried out to ensure accurate results to be obtained for the DNS runs. The results for one typical example of the testing are presented in Figure 5.2 for the case of $Fr = 1.5$, $Re = 200$,

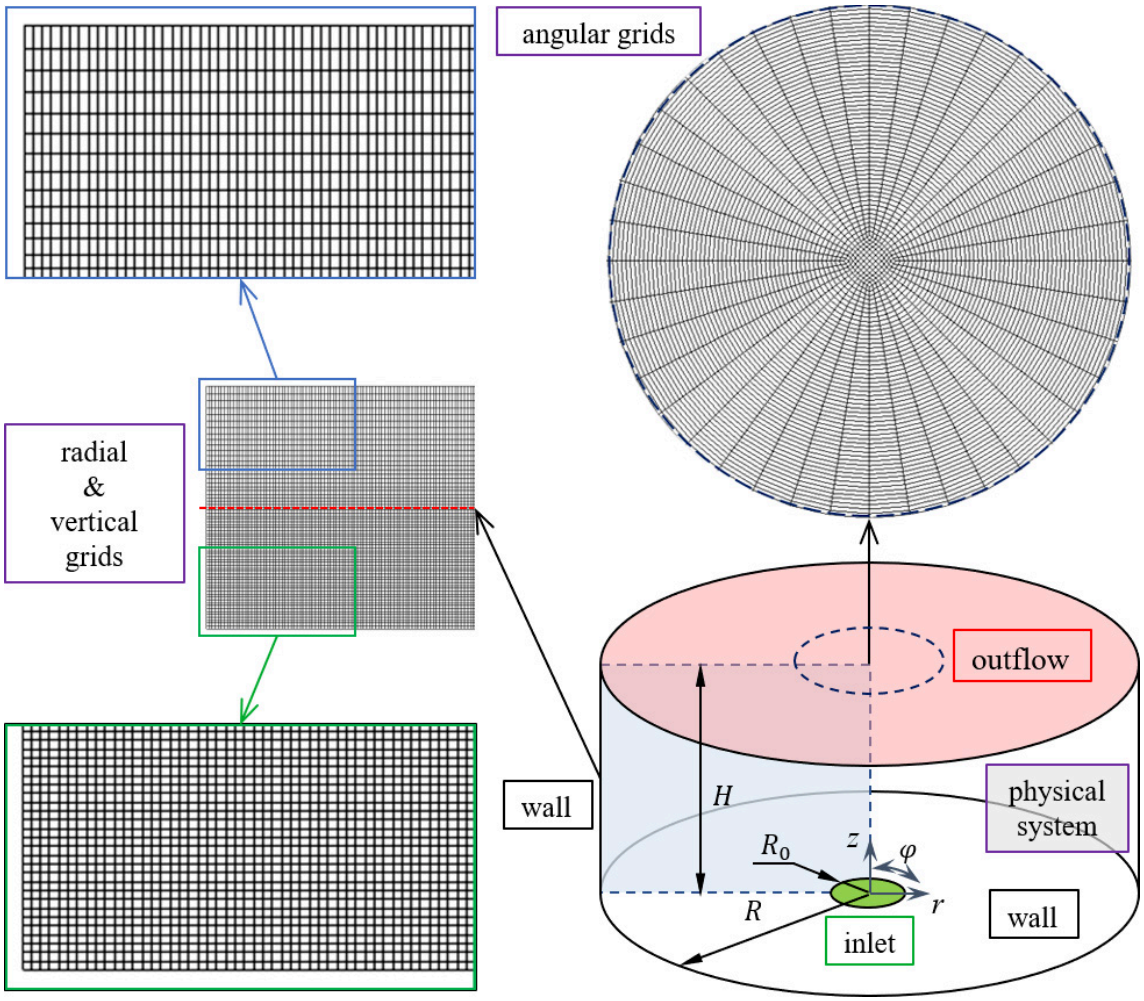

FIGURE 5.1: The computational domain and the typical mesh of a confined weak round fountain.

$Pr = 7$ and $\lambda = 20$. Three meshes (coarse, basic and fine) were created by ICEM software for the mesh independence testing. For the basic mesh of 3.7 million grids as shown in Figure 5.1, the uniform grids of the sizes of $\Delta r = 0.067$ and $\Delta z = 0.067$, which are made dimensionless by R_0, are used in the region of $0 \leq z \leq 10$, while in the remaining region, the grid sizes expand at a rate of 0.5% in vertical direction until they reach the open top boundary, along with 40 uniform grids created in the angular direction. When larger grid sizes of $\Delta r = 0.1$ and $\Delta z = 0.1$ were used in the uniform region and the grid size expansion rate is unchanged for the non-uniform region, the coarse mesh is created with 1.5 million grids. In the uniform region of the fine mesh, the grid sizes are reduced to $\Delta r = 0.05$ and $\Delta z = 0.05$, resulting in

5.2 million grids. Using the same non-dimensional time-step size $\Delta\tau = 0.0076$, the results of the mesh independence test are presented in the left column of Figure 5.2, including the temperature and velocities distributions at $z = 0.67$ in the central surface ($y = 0$). The variation between the solutions of the basic mesh and the fine mesh is very small, indicating that the basic mesh can produce a sufficient resolution for $Re \leq 200$.

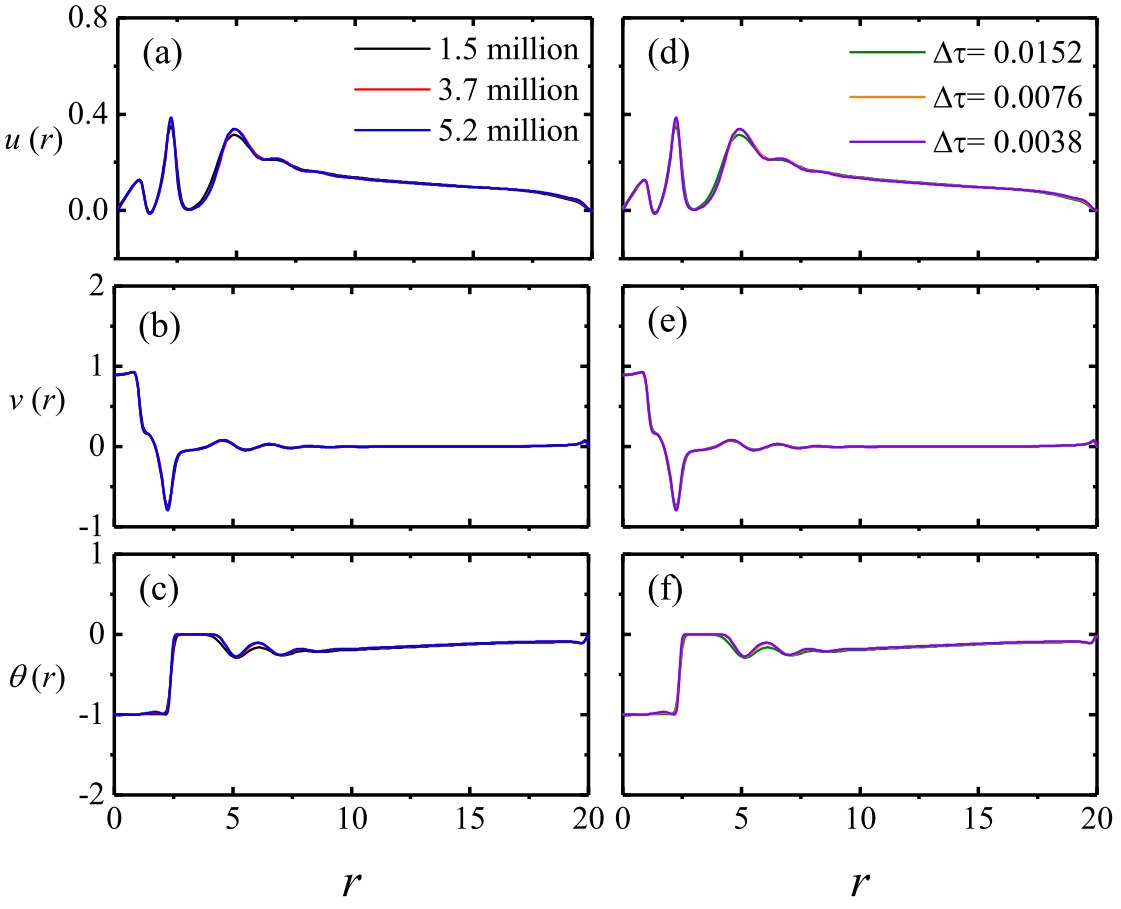

FIGURE 5.2: Comparison of the results from different meshes and time-step sizes. The left column is for the results obtained using the meshes of '1.5million' (coarse mesh), '3.7million' (basic mesh) and '5.2million' (fine mesh), at the time-step of $\Delta\tau = 0.0076$: (a) horizontal profiles of the horizontal velocity, (b) vertical velocity, and (c) temperature at $y = 0$, $z = 0.67$ when $\tau = 125.8$. The right column is for the results obtained using the time-steps of $\Delta\tau = 0.0152$, 0.0076, and 0.0038 with the basic mesh: (d) horizontal profiles of the horizontal velocity, (e) vertical velocity, and (f) temperature, at $y = 0$, $z = 0.67$ when $\tau = 125.8$.

The time-step independence test is conducted with three different time-step sizes, *i.e.*, $\Delta\tau = 0.0152$, 0.0076 and 0.0038, respectively, using the basic mesh. The testing results are presented in the right column of Figure 5.2, which show that the non-dimensional time-step size $\Delta\tau = 0.0076$ can meet the requirement of accuracy. Similar mesh and time-step independence testing have also been carried out for $Re \geq 800$ cases to ensure the chosen meshes and time-steps produce accurate numerical solutions.

To ensure the accuracy of the DNS results, the numerical simulation results of 7 DNS runs are compared to the experimental results for approximately the same corresponding individual cases. The details about the benchmark will be presented in Chapter 6. The results of the benchmark show that the meshes and time-steps used for these DNS runs produce sufficiently accurate solutions.

5.3 Qualitative observations

5.3.1 Evolution of typical confined weak round fountain flows

A series of snapshots of the transient temperature contours for the fountain of $Fr = 0.5$, $Re = 200$, $Pr = 7$ and $\lambda = 20$ are presented in Figures 5.3 to Figure 5.6, which provide an overview of the evolution of a typical confined weak round fountain. Similar to the planar case, the development of a confined weak round fountain, after the formation of the fountain flow, can be divided into four stages, *i.e.*, the intrusion, the wall fountain, the reversed flow and the stratification. Due to the axisymmetric behavior of the weak fountain flow considered here, only the two-dimensional contours of temperature on the section of $y = 0$, $0 \leq x \leq 20$ in the right half of the computational domain are presented in the left columns of these figures for 4 different time instants at each time duration considered, while the right columns of these figures contain the corresponding individual three-dimensional contours of temperature of the whole computational domain. Notably, the legend

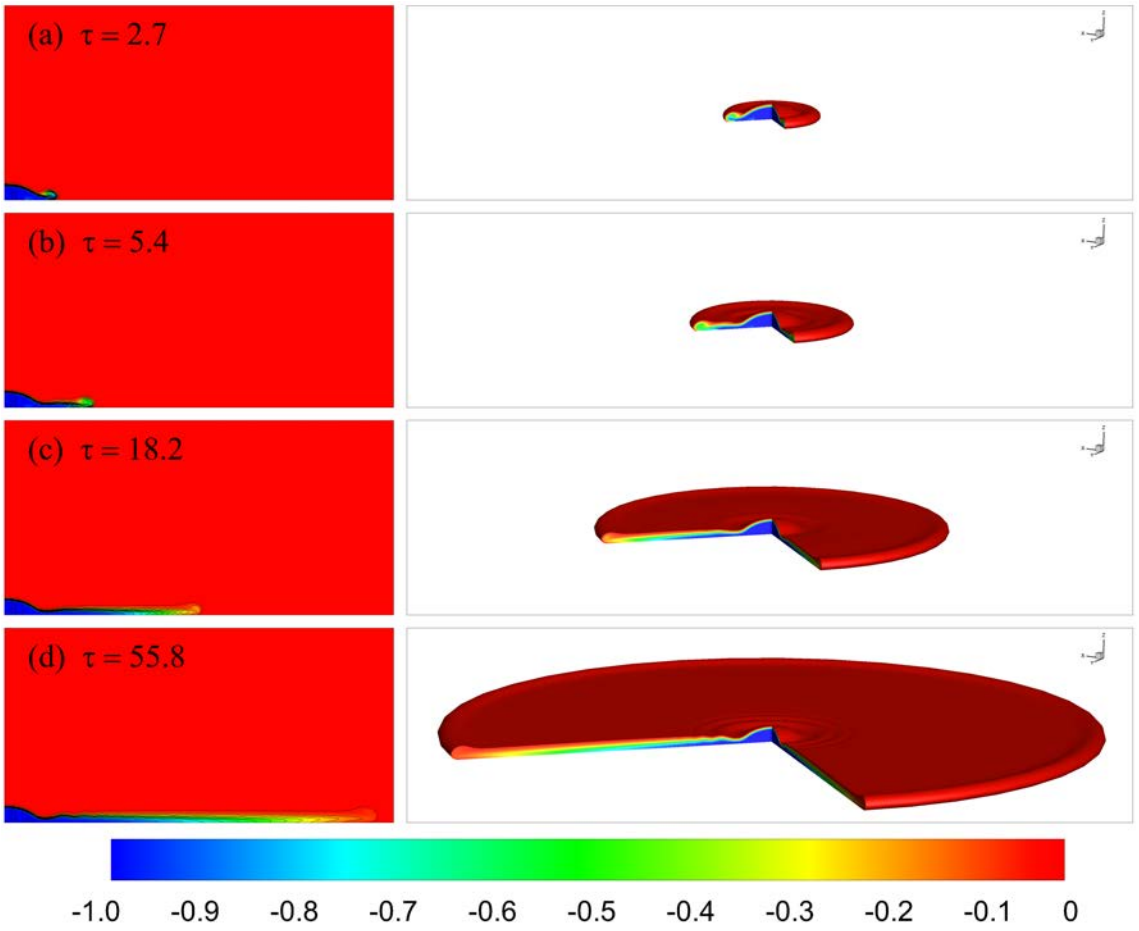

FIGURE 5.3: The two-dimensional temperature contours on the section $y = 0$, $0 \leq x \leq 20$ (the left column) and the three-dimensional temperature contour (the right column) of the round fountain of $Fr = 0.5$, $Re = 200$, $Pr = 7$ and $\lambda = 20$ over the period $2.7 \leq \tau \leq 55.8$.

of temperature for the Figures 5.3 to Figure 5.6 is also applied for the temperature contours of the following qualitative results.

The flow gets minor influence from the confinement when the fountain and intrusion flow are initially formed, resulting in the similar behavior to its counterpart of the free round fountain, which has been illustrated in detail by Lin & Armfield [4]. Thus the description of this phase is omitted here. With a weak momentum flux at the source, the fountain streamline curves and spreads outward along the bottom as shown in Figure 5.3, behaving as a radial gravity current. Similar to the planar fountain case, the evolution of the radial intrusion flow also experiences several regimes, *i.e.*, the wall jet, the gravity-inertial and gravity-viscosity regimes in terms

of the governing forces. A detailed discussion of the intrusion flow will be presented in § 5.4.1.

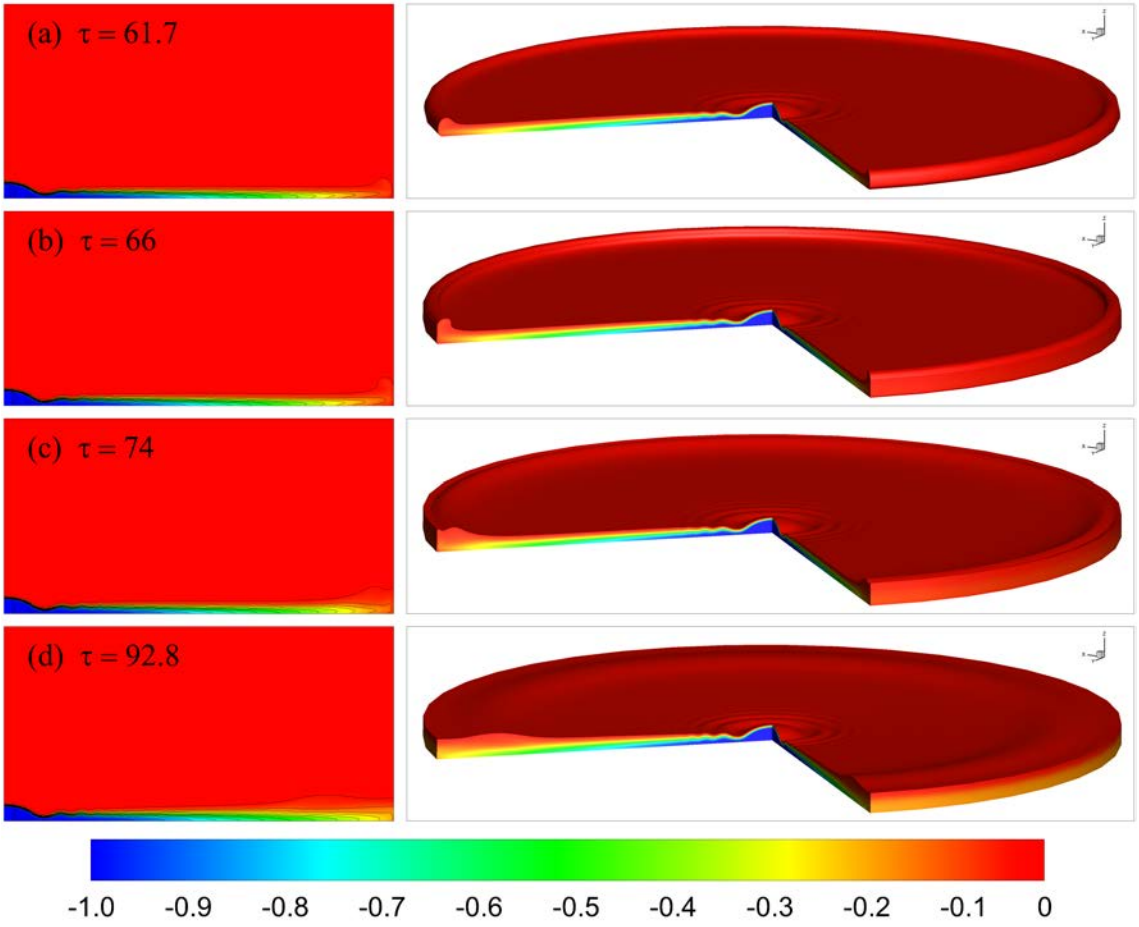

FIGURE 5.4: The two-dimensional temperature contours on the section $y = 0$, $0 \leq x \leq 20$ (the left column) and the three-dimensional temperature contour (the right column) of the round fountain of $Fr = 0.5$, $Re = 200$, $Pr = 7$ and $\lambda = 20$ over the period $61.7 \leq \tau \leq 92.8$.

A secondary wall fountain flow is created after the intrusion impinging with the sidewall as shown in Figure 5.4, where the dense flow spreads upward along the sidewall to reach a finite distance and then falls down under the effect of negative buoyancy. The fountain behavior will be further studied in § 5.4.2. A flow reversal moving from the sidewall to the fountain is subsequently created due to the stagnation pressure from the sidewall, resulting in a two-layer structure as presented in Figure 5.5. The thickness of the bottom dense layer increases due to the interaction between the reversed flow and the intrusion, the fountain flow and the ambient fluid. The interaction is strengthened with the reversed flow approaching

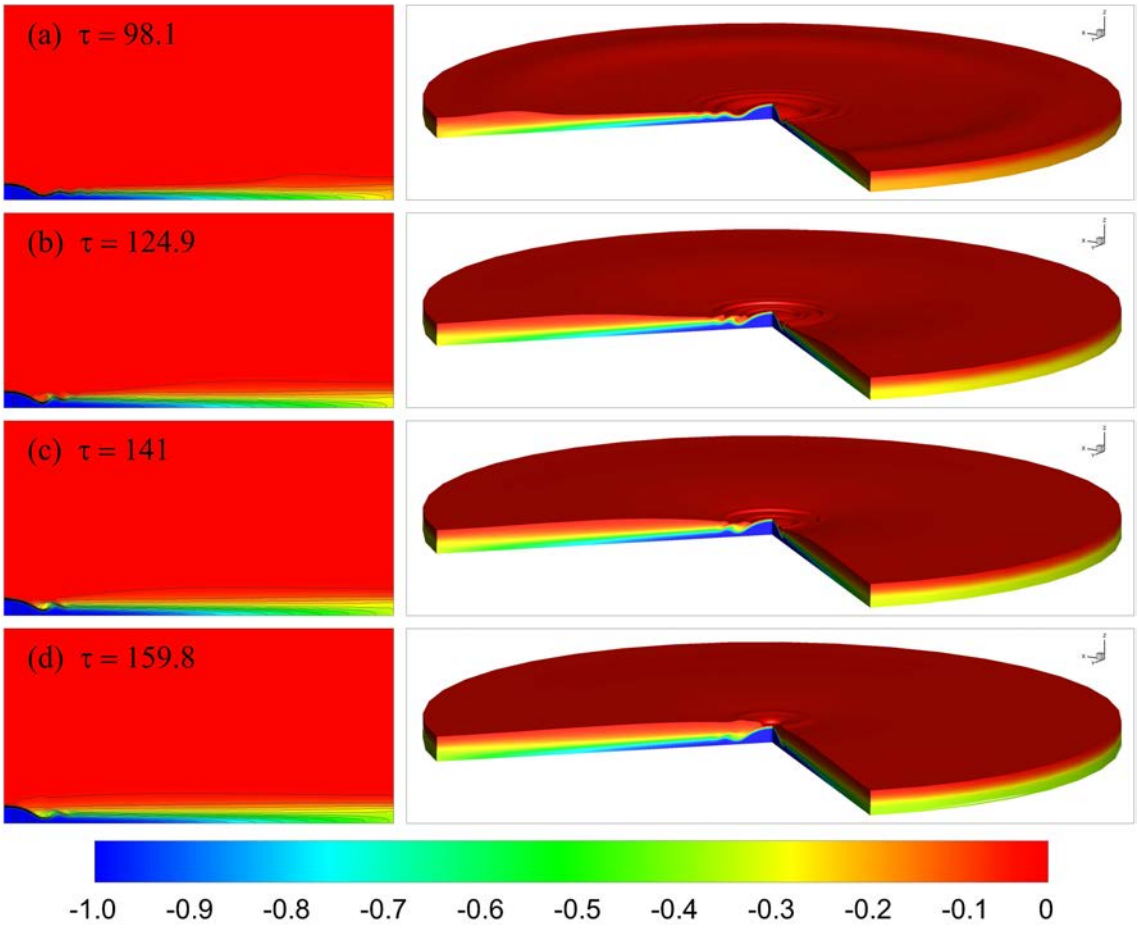

FIGURE 5.5: The two-dimensional temperature contours on the section $y = 0$, $0 \leq x \leq 20$ (the left column) and the three-dimensional temperature contour (the right column) of the round fountain of $Fr = 0.5$, $Re = 200$, $Pr = 7$ and $\lambda = 20$ over the period $98.1 \leq \tau \leq 159.8$.

the fountain core. Subsequently, a collision of the intrusion flow occurs at the center of the container, extruding the dense fluid to a finite height. Because of the negative buoyancy, the extrusion falls down as shown in Figure 5.6(b). With the continuous supply of the fountain flow, a thermal stratification is eventually created, with the fountain flow submerged in the stratified fluid as shown in Figure 5.6(d). After that filling and thermal conduction dominate the development of the thermal stratification stratification.

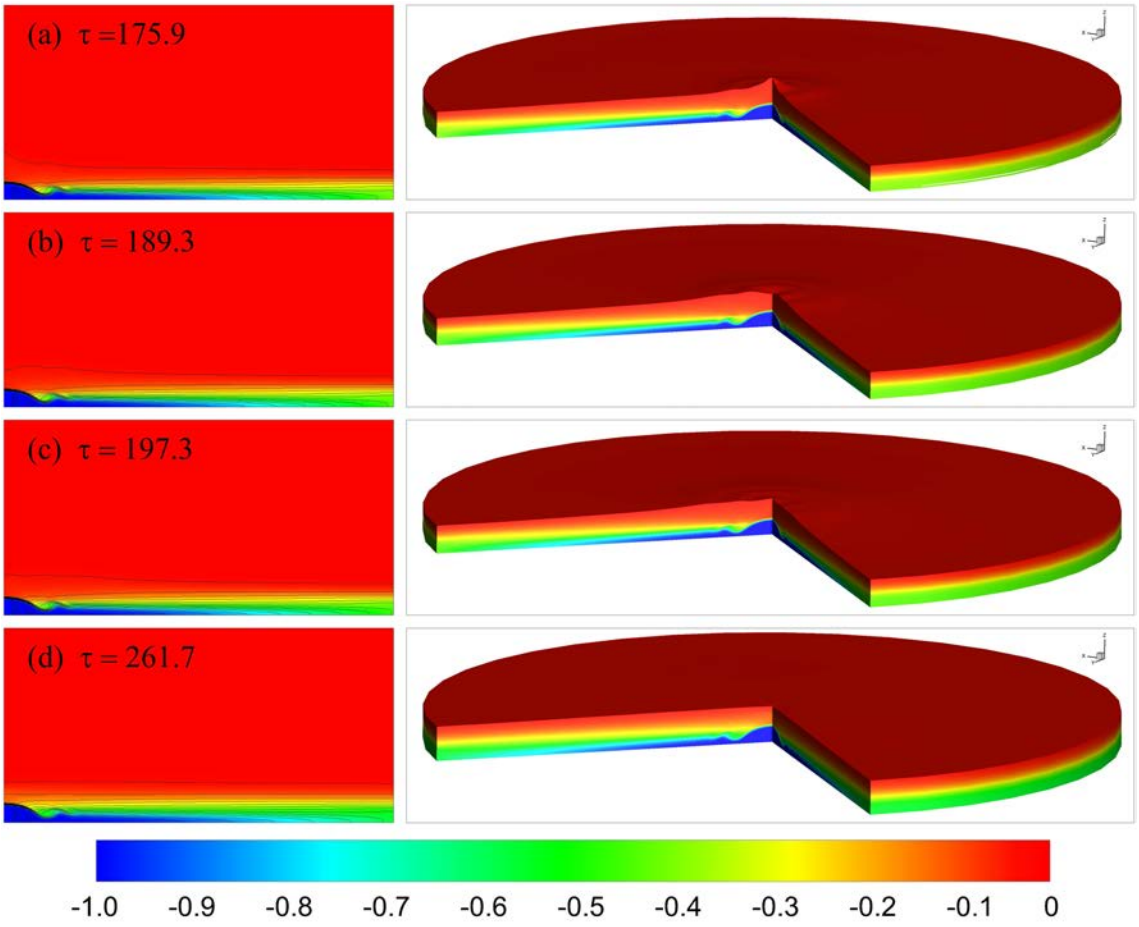

FIGURE 5.6: The two-dimensional temperature contours on the section $y = 0$, $0 \leq x \leq 20$ (the left column) and the three-dimensional temperature contour (the right column) of the round fountain of $Fr = 0.5$, $Re = 200$, $Pr = 7$ and $\lambda = 20$ over the period $175.9 \leq \tau \leq 261.7$.

5.3.2 The influence of the governing parameters

Figure. 5.7 presents the two-dimensional temperature contours of the fountains of $Fr = 1.0$, $Fr = 1.5$ and $Fr = 2.0$ with $Re = 200$, $Pr = 7$ and $\lambda = 20$ on the section $y = 0$ at different time instants to illustrate the influence of Fr on the behavior of confined weak round fountains. Similar to the planar fountain cases, when Fr increases, it will take a longer time for the intrusion front to impinge with the sidewall and for the wall fountain flow to reach its maximum height, as shown in the first and second rows, respectively. Meanwhile, the intrusion thickness and the wall fountain's maximum penetration height increase when Fr becomes larger. The reversed flow

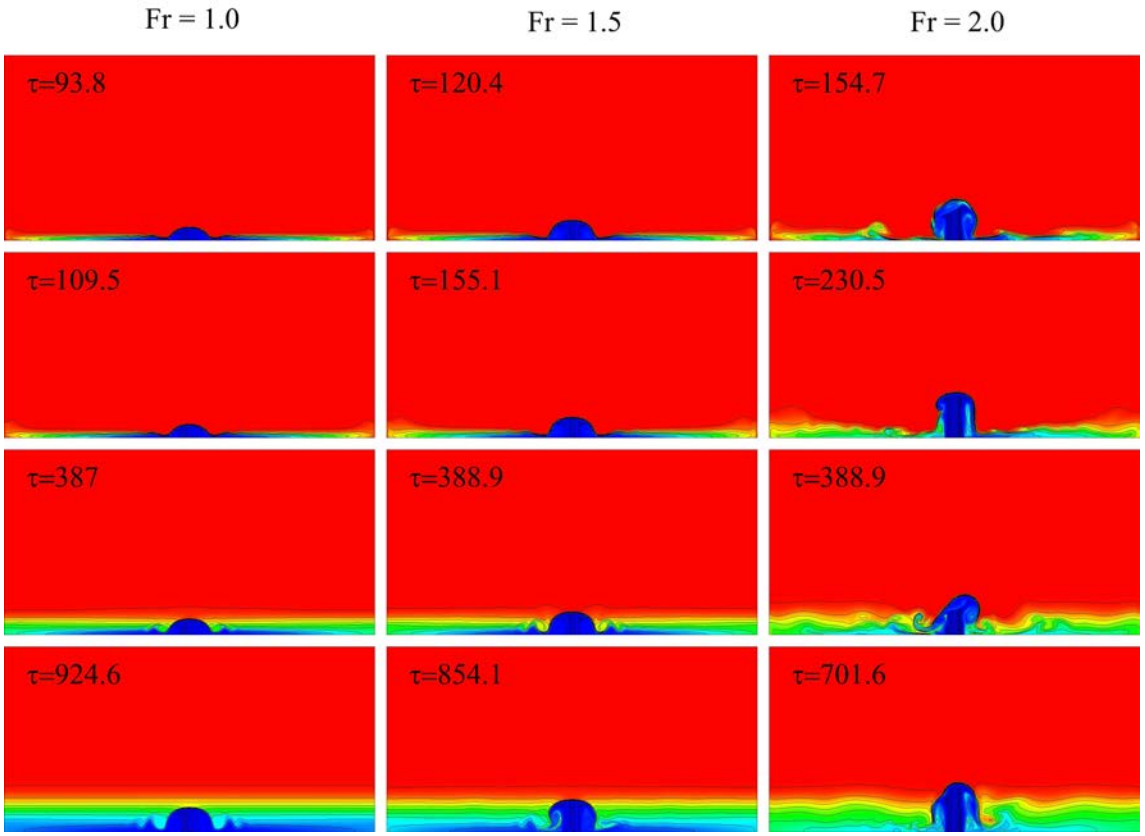

FIGURE 5.7: The two-dimensional temperature contours on the section $y = 0$ for the fountains of $Re = 200$, $Pr = 7$ and $\lambda = 20$. The left, middle and right columns are for $Fr = 1.0$, $Fr = 1.5$ and $Fr = 2.5$, respectively.

and thermal stratification shown in the last two rows indicate a stronger interaction among the reversed flow, the intrusion and the ambient fluid with increasing Fr, which results in a longer time for the reversed flow to collide at the center, but a shorter time for the thermal stratified surface to reach the same height. In the long run, the increase of Fr changes the behavior of the fountain and its secondary flows from symmetric to asymmetric and from laminar to turbulent, as demonstrated by the corresponding three-dimensional temperature contours presented in Figure 5.8.

The evolution of two-dimensional and three-dimensional temperature contours of the fountains of $Fr = 1.0$, $Pr = 7$ and $\lambda = 20$ with $Re = 50$, $Re = 200$ and $Re = 800$ are presented in Figure 5.9 and Figure 5.10 to illustrate the influence of Re. The two-dimensional temperature contours on the section $y = 0$ include the fountain behavior from the intrusion impinging the sidewall to the formation of the

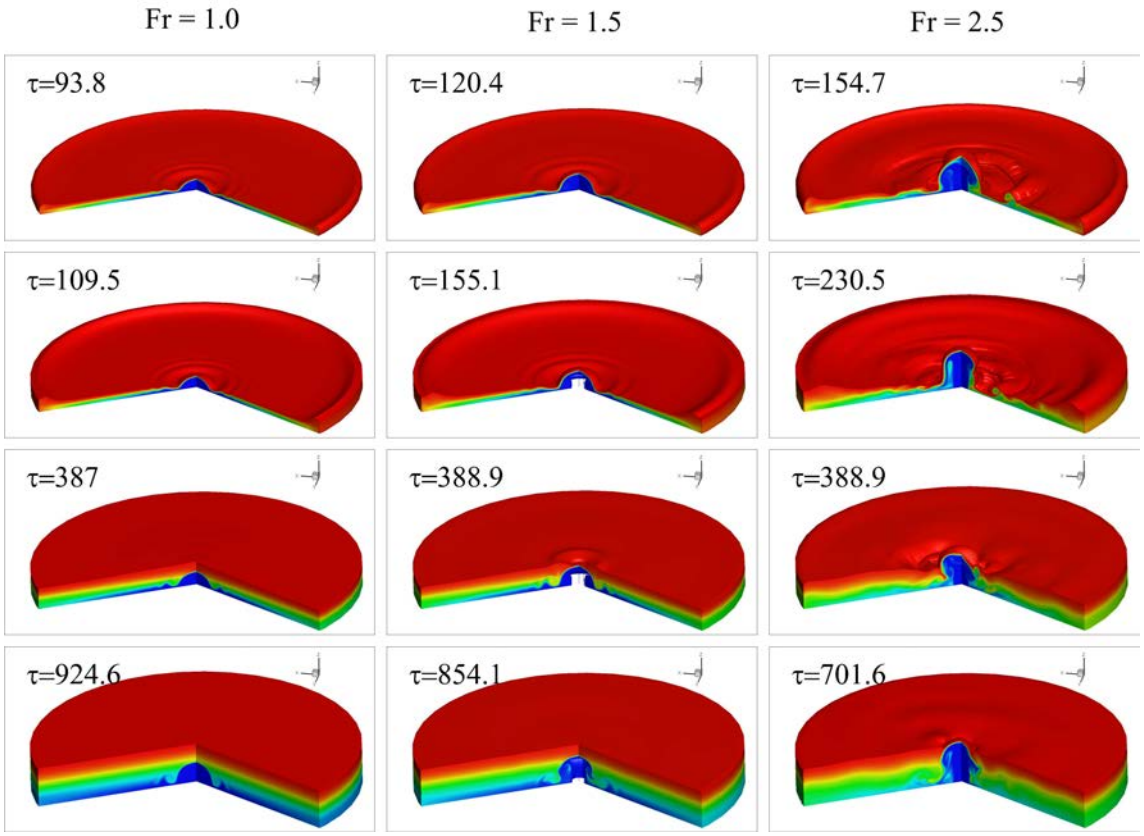

FIGURE 5.8: The three-dimensional temperature contours for the fountains of $Re = 200$, $Pr = 7$ and $\lambda = 20$. The left, middle and right columns are for $Fr = 1.0$, $Fr = 1.5$ and $Fr = 2.5$, respectively.

quasi-steady stratification, showing a thinner intrusion, a wall fountain with smaller maximum penetration height and a smaller stratification height for the fountain with a larger Re. The first row indicates the intrusion speed becomes larger with increasing Re and the time to reach the maximum height of the wall fountain is reduced as shown in the second row. However, it takes a longer time to form the stratification for the fountain with a larger Re as shown in the last row. The interaction between the fountain and its secondary flows becomes more significant with increasing Re, resulting in the extension for the region of the fountain core (the blue part at the center). This is because a stratified structure with a denser fluid (blue) surrounding the fountain is formed, which will reduce the stability of the fountain flow. Hence, a weak asymmetric behavior appears for the intrusion near the fountain core for the fountain of $Re = 800$, as shown in Figure 5.10. What should

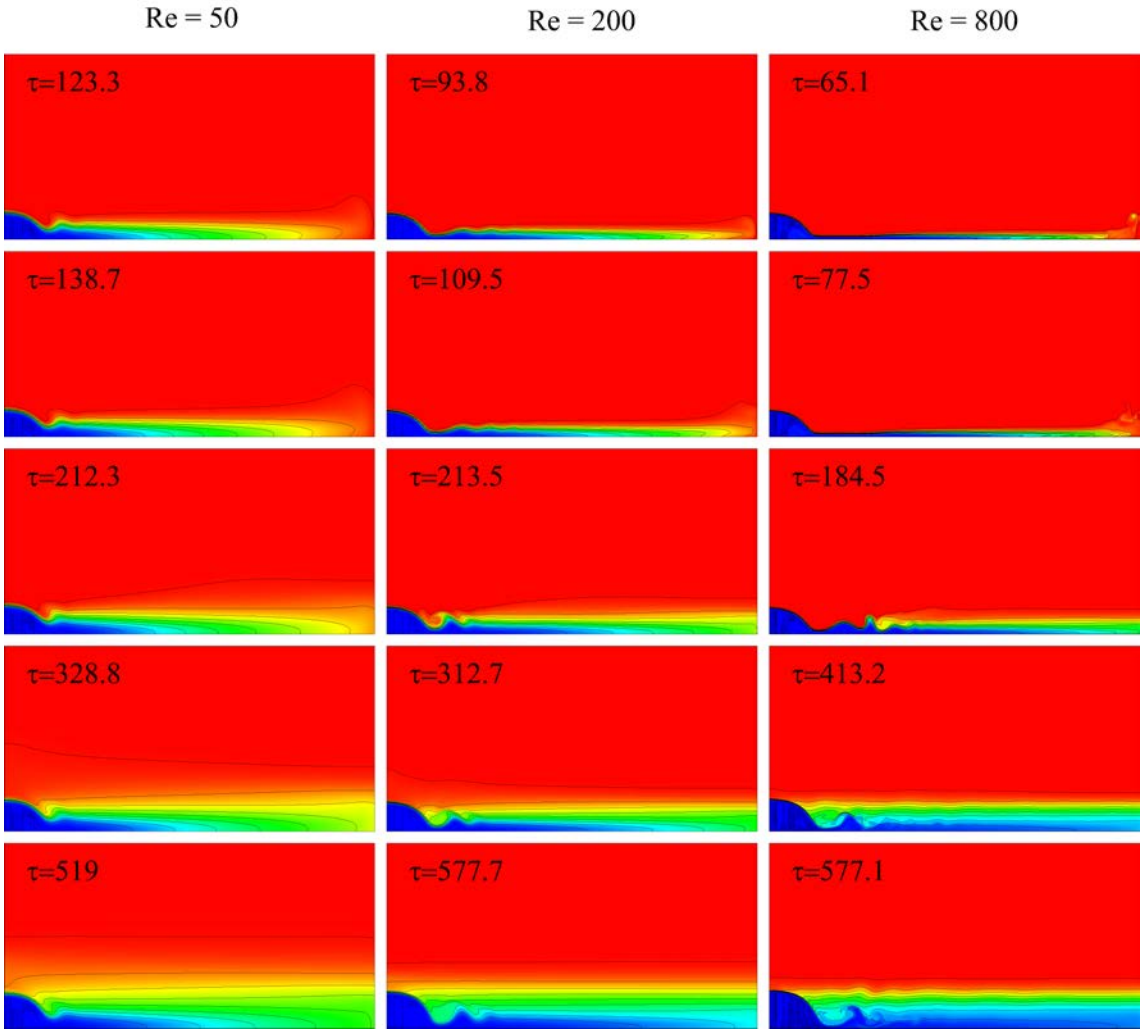

FIGURE 5.9: The two-dimensional temperature contours on the section $y = 0$, $0 \leq x \leq 20$ for the fountains of $Fr = 1.0$, $Pr = 7$ and $\lambda = 20$. The left, middle and right columns are for $Re = 50$, $Re = 200$ and $Re = 800$, respectively.

be noted here is that no falling of the wall fountain is observed for the fountain of $Re \leq 20$.

The influence of Pr is illustrated by Figure 5.11 and Figure 5.12, where the two-dimensional and three-dimensional temperature contours are presented for the fountains of $Fr = 1.0$, $Re = 200$ and $\lambda = 20$ with $Pr = 0.7$, $Pr = 10$ and $Pr = 50$, respectively. In the first row of Figure 5.11, the intrusion front of these fountains reach the same location at the same time instant, with a thicker intrusion for the fountain with smaller a Pr, indicating little influence of Pr on the thermal structure, which is consistent with the previous studies (see, *e.g.*, [30]). However, in the later

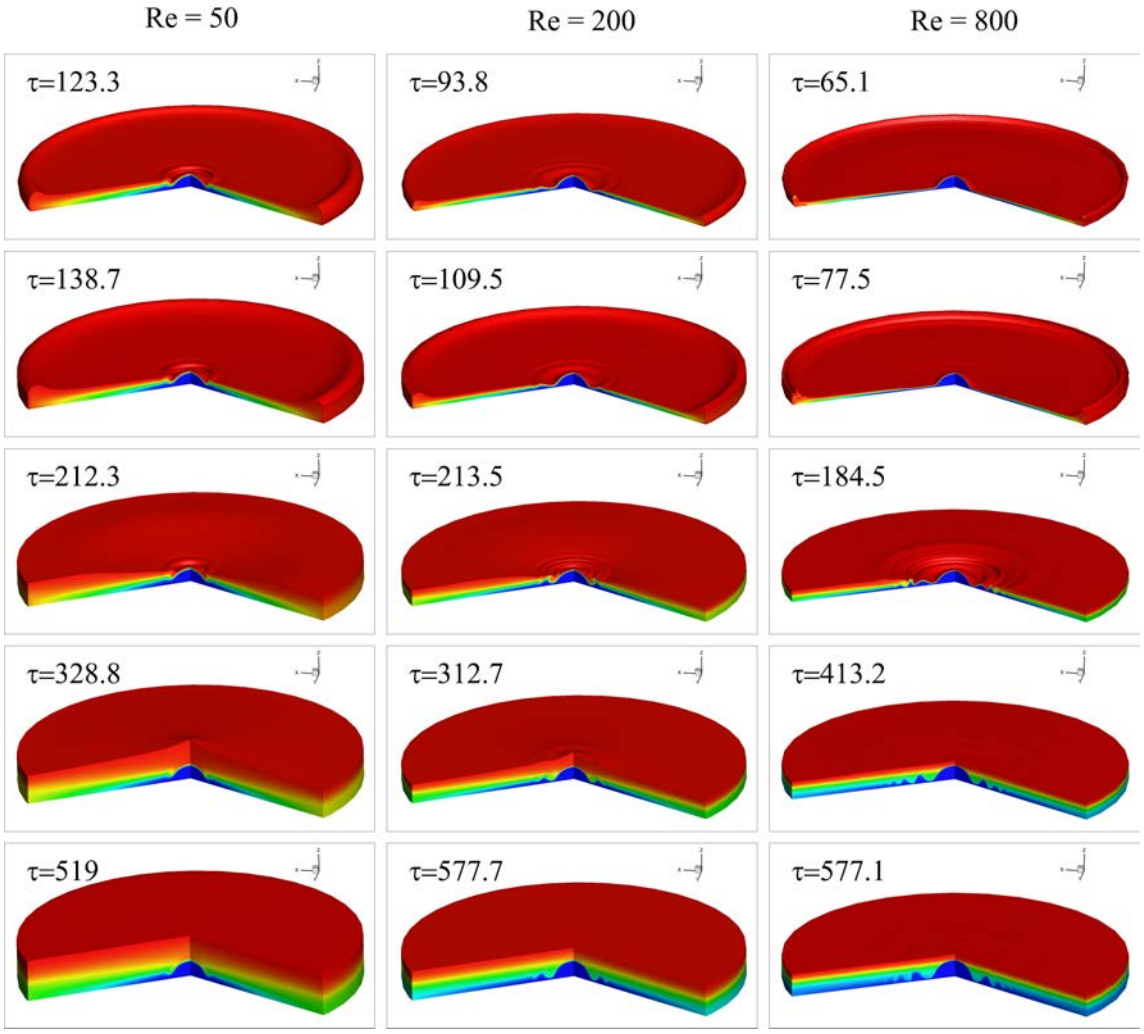

FIGURE 5.10: The three-dimensional temperature contours for the fountains of $Fr = 1.0$, $Pr = 7$ and $\lambda = 20$. The left, middle and right columns are for $Re = 50$, $Re = 200$ and $Re = 800$, respectively.

evolution stages, it takes a longer time for the intrusion to impinge with the sidewall (the second row), for the wall fountain to reach its maximum height (the third row) and for the quasi-steady stratification to form (the last row) with the increase of Pr, indicating that the influence of thermal conduction becomes more significant when Pr is very small, which influences not only the thermal layer thickness, but also the thermal structure. Additionally, an asymmetric behavior is observed for the fountain of $Pr \geq 20$, *e.g.*, the case of $Pr = 50$ as shown in the last row of Figure 5.12, which is due to the denser bottom structure resulted from the influence of a larger Pr.

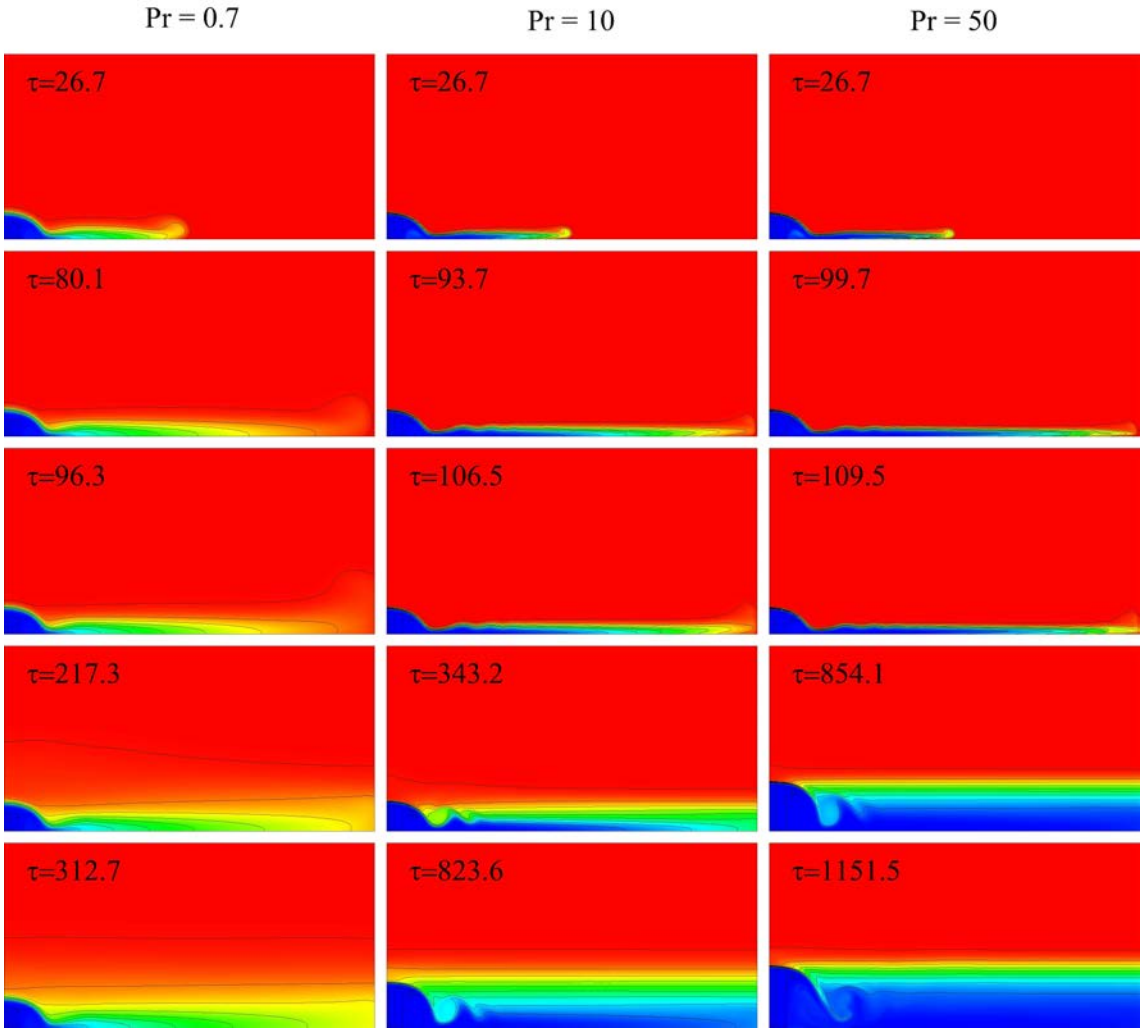

FIGURE 5.11: The two-dimensional temperature contours on the section $y = 0, 0 \leq x \leq 20$ for the fountains of $Fr = 1.0$, $Re = 200$ and $\lambda = 20$. The left, middle and right columns are for $Pr = 0.7$, $Pr = 10$ and $Pr = 50$, respectively.

Figure 5.13 and Figure 5.14 present the evolution of the two-dimensional and three-dimensional temperature contours for the fountains of $Fr = 1$, $Pr = 7$ and $Re = 200$ with $\lambda = 10$, $\lambda = 20$ and $\lambda = 30$ to demonstrate the influence of λ. The second row of Figure 5.13 presents the time instant when the wall fountain reaches its maximum height, indicating a higher maximum penetration height for the fountain with a larger λ. With the development of the flow, a stratified structure with a denser fluid close to the bottom is formed with decreasing λ, which will enhance the instability of the fountain performance. In such a stratified structure, the fountain extends its width and eventually changes from symmetric to asymmetric as shown

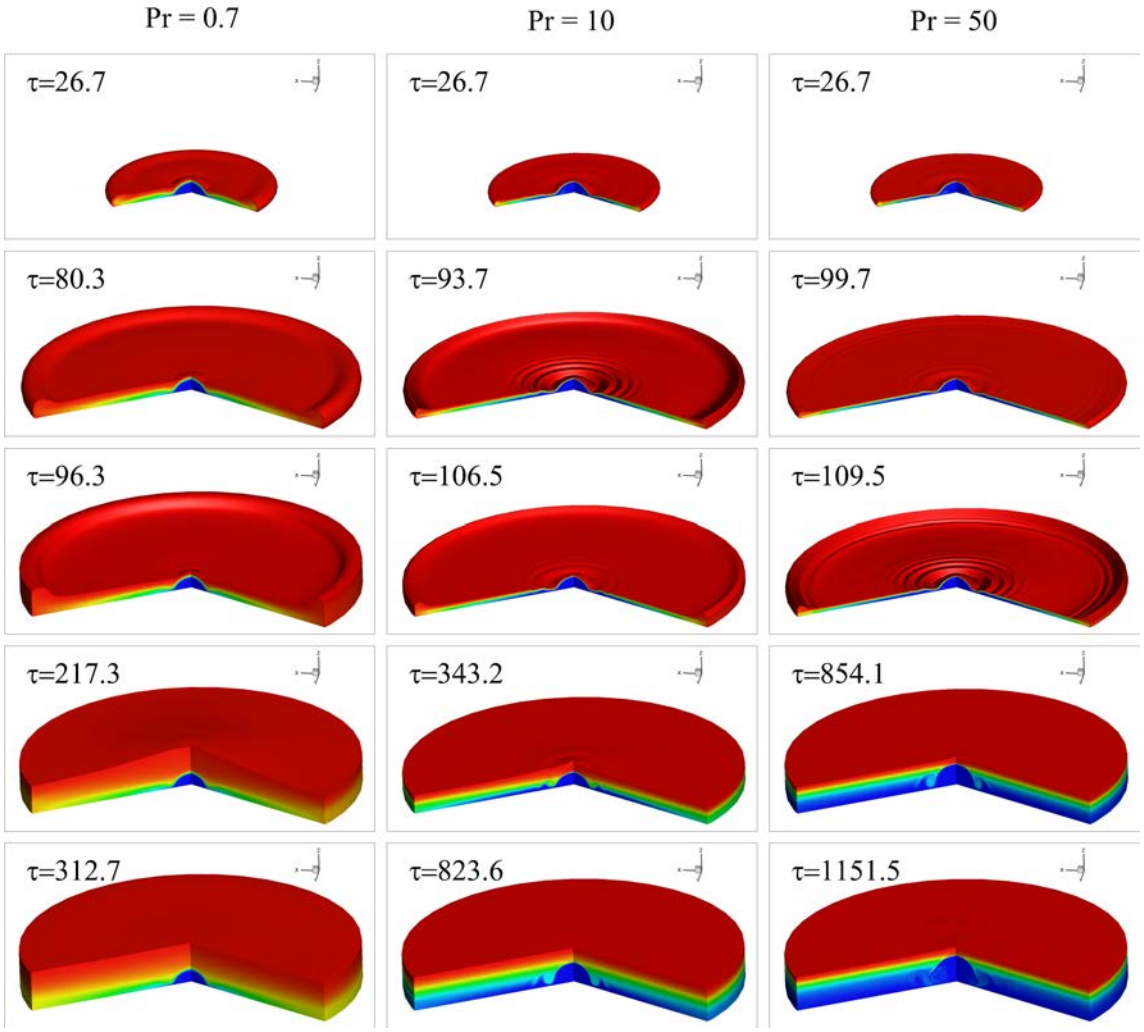

FIGURE 5.12: The three-dimensional temperature contours of the fountains of $Fr = 1.0$, $Re = 200$ and $\lambda = 20$. The left, middle and right columns are for $Pr = 0.7$, $Pr = 10$ and $Pr = 50$, respectively.

in the last row of Figure. 5.14. Meanwhile, a more turbulent structure appears for a very small λ, *e.g.*, $\lambda = 10$.

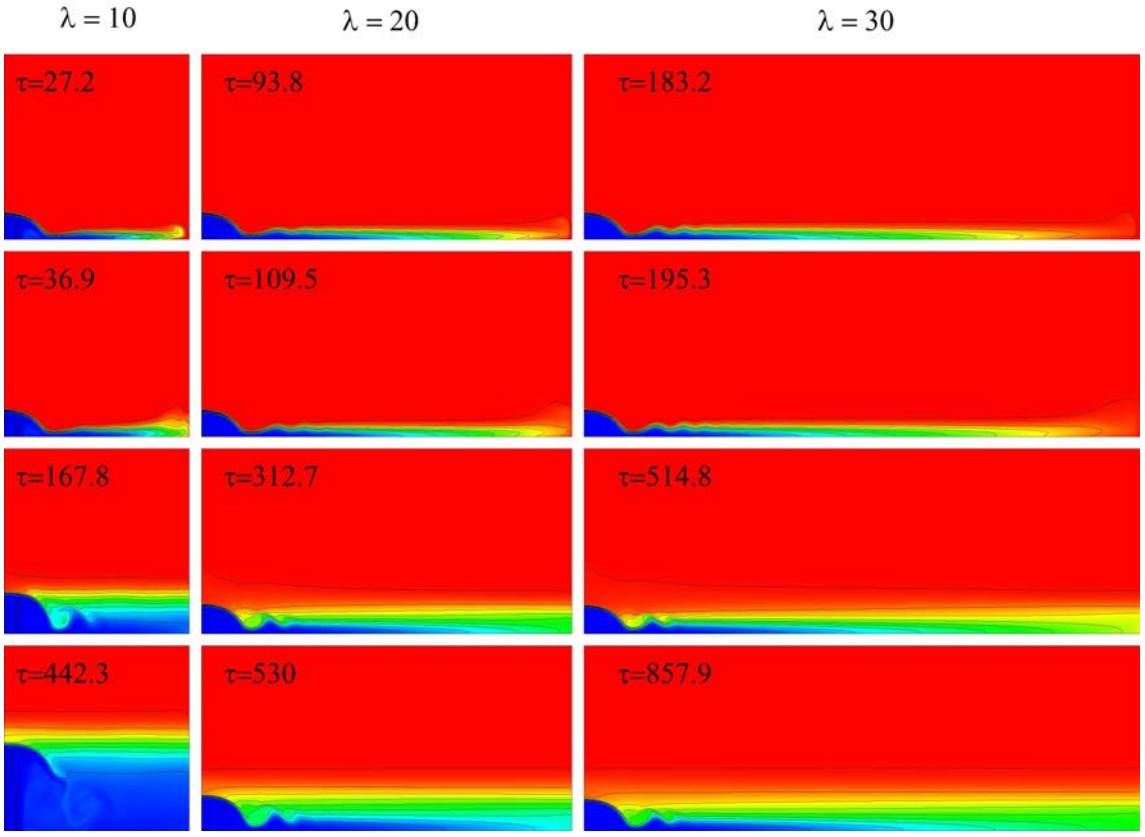

FIGURE 5.13: The two-dimensional temperature contours on the section $y = 0$, $0 \leq x \leq 20$ for the fountains of $Fr = 1.0$, $Re = 200$ and $Pr = 7$. The left, middle and right columns are for $\lambda = 10$, $\lambda = 20$ and $\lambda = 30$, respectively.

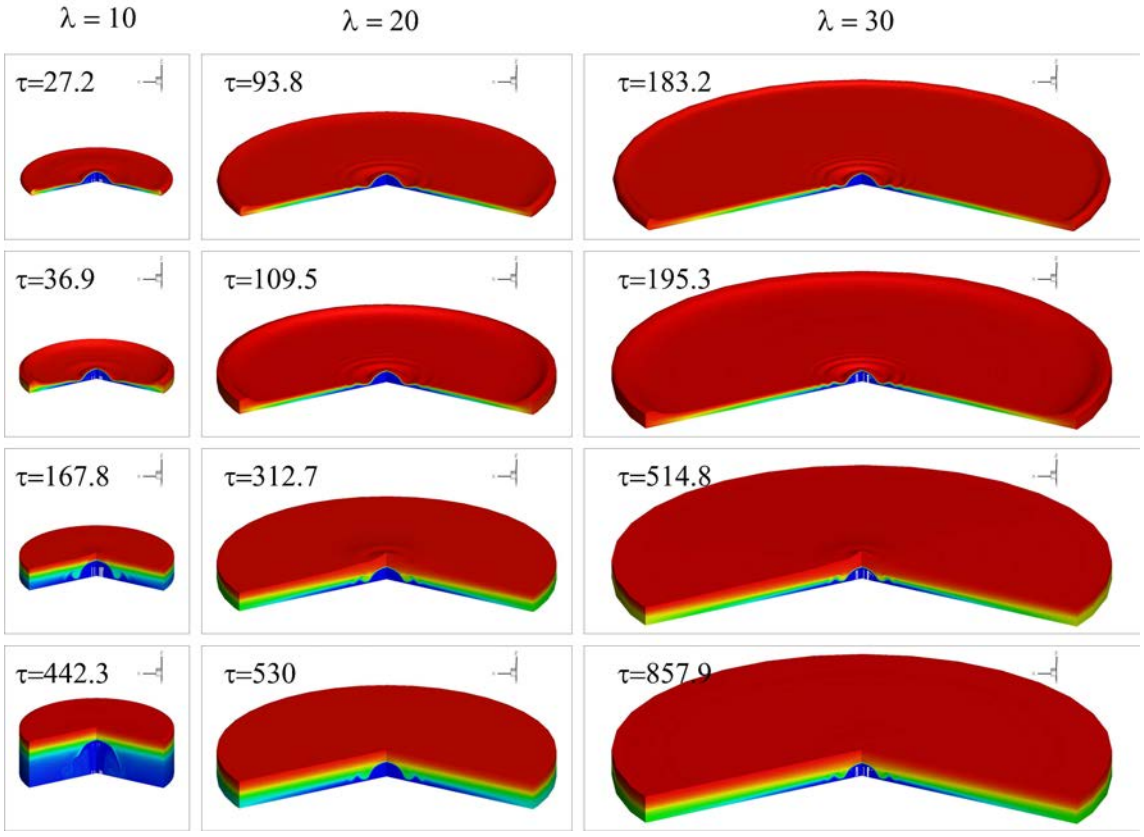

FIGURE 5.14: The three-dimensional temperature contours of the fountains of $Fr = 1.0$, $Re = 200$ and $Pr = 7$. The left, middle and right columns are for $\lambda = 10$, $\lambda = 20$ and $\lambda = 30$, respectively.

5.4 Quantitative observations

5.4.1 Intrusion

5.4.1.1 Passage of the intrusion front

Similar to the study on confined weak planar fountains, the time series of the intrusion front for the confined round fountains of $0.25 \leq Fr \leq 3.0$, $5 \leq Re \leq 800$, $0.7 \leq Pr \leq 100$ and $10 \leq \lambda \leq 35$ are presented in Figure 5.15. Similarly, the intrusion front is determined as the r-location where the temperature $T(r) = T_a - 1\%(T_a - T_0)$ within the whole cylindrical domain.

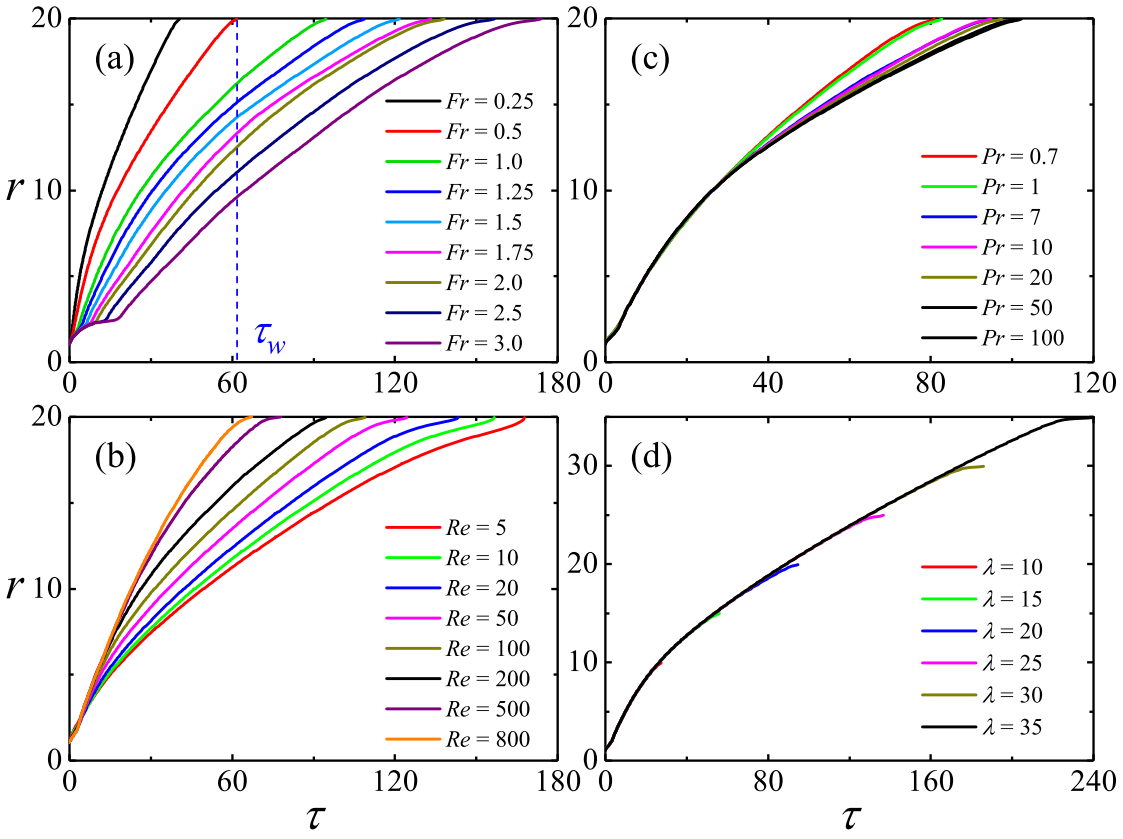

FIGURE 5.15: The time series of the passage of the intrusion front for round fountains with (a) $Re = 200$, $Pr = 7$, $\lambda = 20$ and $0.1 \leq Fr \leq 3.0$; (b) $Fr = 1.0$, $Pr = 7$, $\lambda = 20$ and $5 \leq Re \leq 800$; (c) $Fr = 1.0$, $Re = 200$, $\lambda = 20$ and $0.7 \leq Pr \leq 100$; (d) $Fr = 1.0$, $Re = 200$, $Pr = 7$ and $10 \leq \lambda \leq 35$.

The end point of the times series is again defined as the characteristic time scale for the intrusion front impinging with the sidewall, τ_w. Similar to the planar fountain cases, the intrusion speed is found to increases with decreasing Fr or increasing Re as shown in Figure 5.15(a)-(b). Notably, for planar fountains, the intrusion passage overlaps for the cases of $Re = 500$ and $Re = 800$, indicating a minor effect from Re for $Re \geq 500$. However, for round fountains, only the early stage of the intrusion passage overlaps for fountains of $Re \geq 500$. Similarly, in the early evolution stage of the fountains with varying Pr, the intrusion front passage profiles overlap as shown in Figure 5.15(c). But after a certain distance, the intrusion speed declines with increasing Pr. The influence of λ is presented in Figure 5.15(d), which shows that the λ effects becomes significant only in the region close to the sidewall. All these are consistent with the above qualitative observations, indicating the effect of thermal conduction becomes more significant with larger Fr or smaller Re and Pr.

5.4.1.2 Time-scale for the intrusion front impinging the side-wall

To illustrate the influence of the governing parameters on τ_w, τ_w is plotted against Fr, Re, Pr and λ in Figure 5.16. From Figure 5.16(a), $Fr = 1.0$ and $Fr = 1.75$ are identified as the critical numbers to distinguish the influence of Fr into three ranges, with three different correlations are determined as follows:

$$\tau_w = \begin{cases} 941Fr^{0.61} - 0.26, & 0.25 \leq Fr \leq 1.0, \\ 50.8Fr + 43.7, & 1.0 \leq Fr \leq 1.75, \\ 35.2Fr + 66.1, & 2.0 \leq Fr \leq 3.0. \end{cases} \tag{5.1}$$

with $R^2 = 1$, 0.998 and 0.999, respectively. Figure 5.16(b) demonstrates the influence of Re on τ_w. Similarly, two ranges of Re, *i.e.*, $5 \leq Re \leq 200$ and $200 \leq Re \leq 800$ are determined, with the correlations between τ_w and Re can

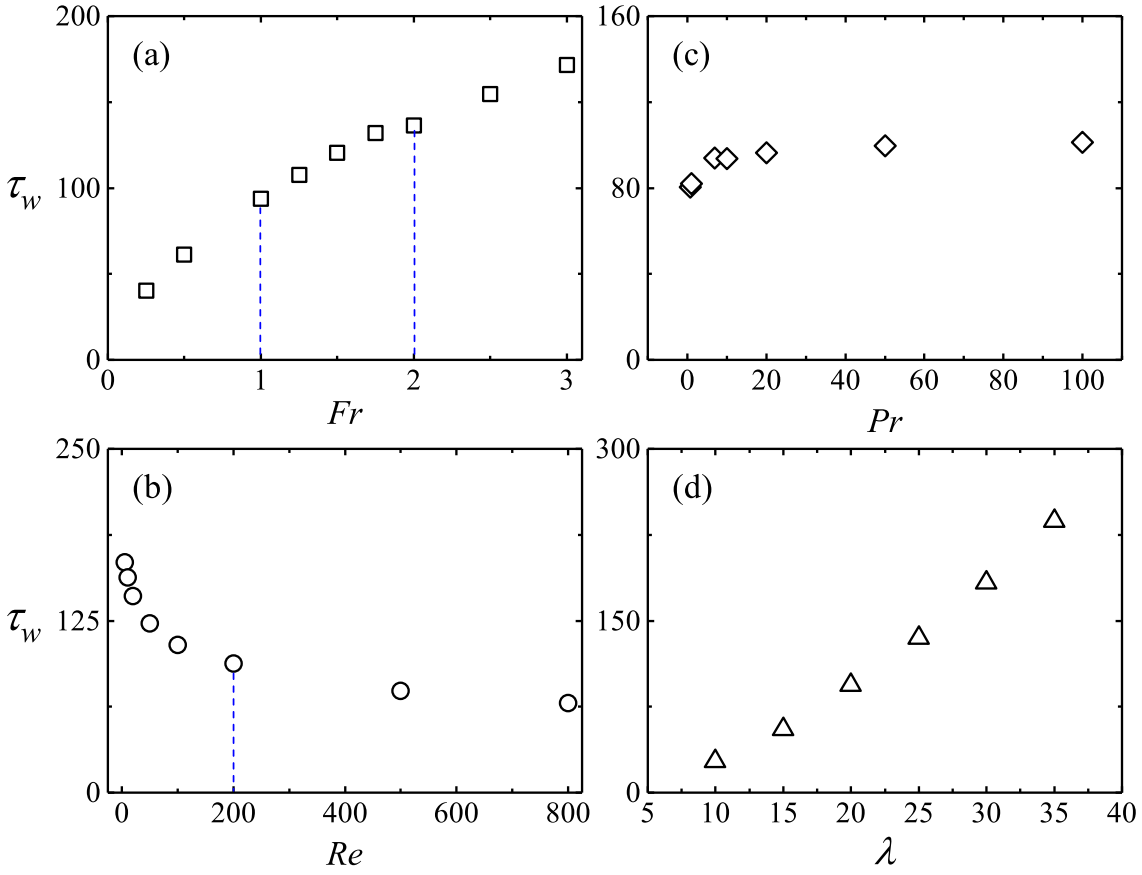

FIGURE 5.16: τ_w, the time-scale for intrusion front impinging with the sidewall, plotted against: (a) Fr with $Re = 200$, $Pr = 7$ and $\lambda = 20$; (b) Re with $Fr = 1.0$, $Pr = 7$ and $\lambda = 20$; (c) Pr with $Fr = 1.0$, $Re = 200$ and $\lambda = 20$; (d) λ with $Fr = 1.0$, $Re = 200$ and $Pr = 7$.

be quantified by the following:

$$\tau_w = \begin{cases} 217.4Re^{-0.159} + 3.8, & 5 \leq Re \leq 200, \\ 377.8Re^{-0.263} + 0.1, & 200 \leq Re \leq 800, \end{cases} \tag{5.2}$$

with $R^2 = 0.985$ and 1 respectively. With the numerical results shown in Figure 5.16(c), a power law correlation between τ_w and Pr over the range of $0.7 \leq Pr \leq 100$ are determined as follows:

$$\tau_w = 78.9Re^{0.05} + 3.7 \tag{5.3}$$

with $R^2 = 0.982$. The effect of λ on τ_w is presented in Figure 5.16(d), represented by the following power law correlation:

$$\tau_w = 0.5\lambda^{1.73} + 1.7 \tag{5.4}$$

with $R^2 = 1$.

5.4.1.3 Intrusion speed

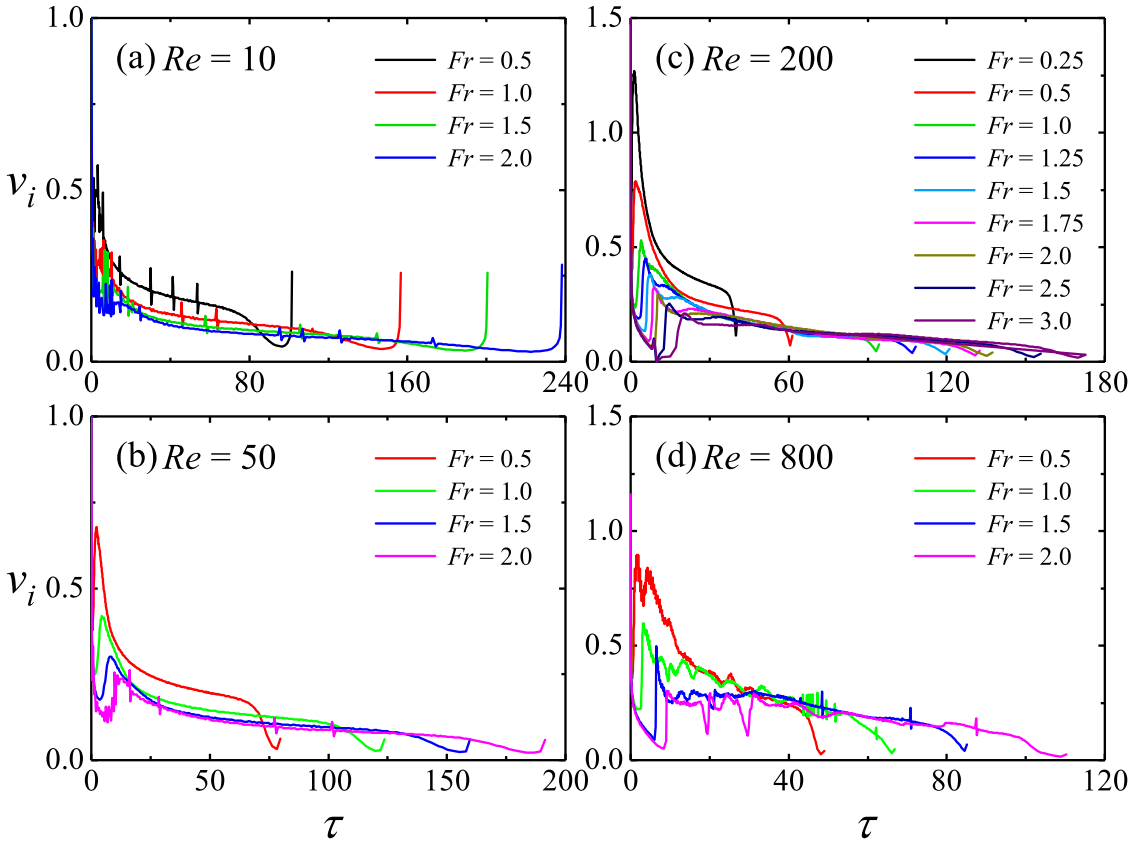

FIGURE 5.17: The time series of the intrusion speed for the fountains with $Pr = 7$, $\lambda = 20$: (a) $Re = 10$ and $0.5 \leq Fr \leq 2.0$; (b) $Re = 50$ and $0.25 \leq Fr \leq 2.0$; (c) $Re = 200$ and $0.25 \leq Fr \leq 3.0$; (d) $Re = 800$ and $0.5 \leq Fr \leq 2.0$.

A detailed study on gravity current carried out by Chen [1] illustrates that a radial gravity current may experience three regimes, *i.e.*, the radial wall jet regime (W-J), the buoyancy-inertia regime (B-I) and the buoyancy-viscosity regime (B-V)

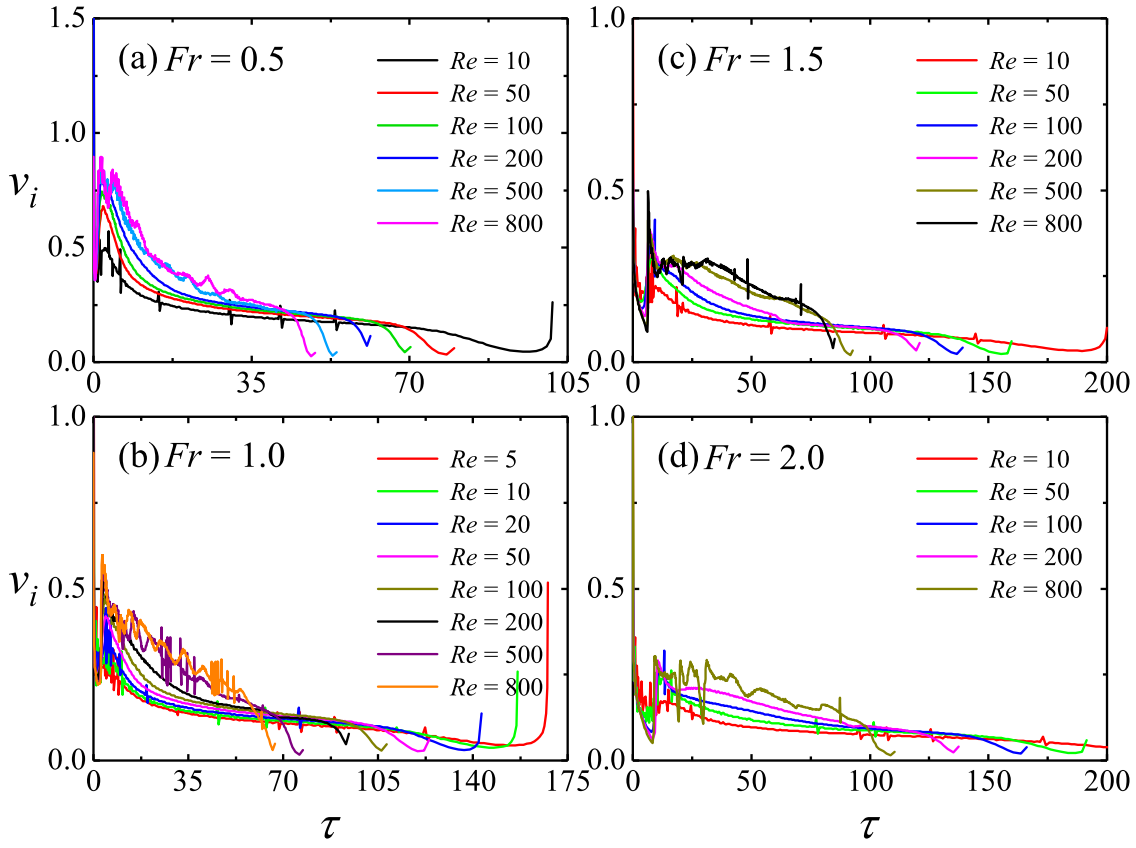

FIGURE 5.18: The time series of the intrusion speed for the fountains with $Pr = 7$, $\lambda = 20$: (a) $Fr = 0.5$ and $10 \leq Re \leq 800$; (b) $Fr = 1.0$ and $5 \leq Re \leq 800$; (c) $Re = 1.5$ and $10 \leq Re \leq 800$; (d) $Fr = 2.0$ and $10 \leq Re \leq 800$.

in terms of the governing forces. When the gravity current is initially dominated by momentum flux, M, the current behaves as a radial wall jet, where an increase is observed for the current thickness with its spreading. In the radial wall jet regime, the location of the intrusion front follows a scaling relation of $R(t) \sim M^{1/4}t^{1/2}$ with time. Then, buoyancy (or gravity) becomes the driving force of the current, which is balanced by the inertial force, resulting in a scaling relation $R(t) \sim B^{1/4}t^{3/4}$ for the buoyancy-inertia regime. The balance between buoyancy and inertia is later replaced by a new balance between buoyancy and viscous drag force, when the viscous drag force becomes larger than the inertial force, thus the current enter the buoyancy-viscosity regime and the scaling relation $R(t) \sim (BQ^2/\nu)^{1/8}t^{1/2}$ is obtained. The momentum flux M, buoyancy flux B and volume flux Q for the round fountain are

determined as $Q = \pi R_0^2 W_0^2$, $B = g(\rho_0 - \rho_a)/\rho_a Q$ and $Q = \pi R_0^2 W_0$. Similar to the planar fountain case, non-dimensional correlations are obtained from the above scaling relation for the intrusion speed in terms of Fr and Re as follows,

$$v_i \sim \tau^{-1/2}, \tag{5.5}$$

for the radial wall jet regime,

$$v_i \sim Fr^{-1/2}\tau^{-1/4}, \tag{5.6}$$

for the buoyancy-inertial regime, and

$$v_i \sim Fr^{-1/4}Re^{1/8}\tau^{-1/2}. \tag{5.7}$$

for the buoyancy-viscosity regime, where v_i is the dimensionless radial intrusion velocity which is non-dimensionalized by W_0.

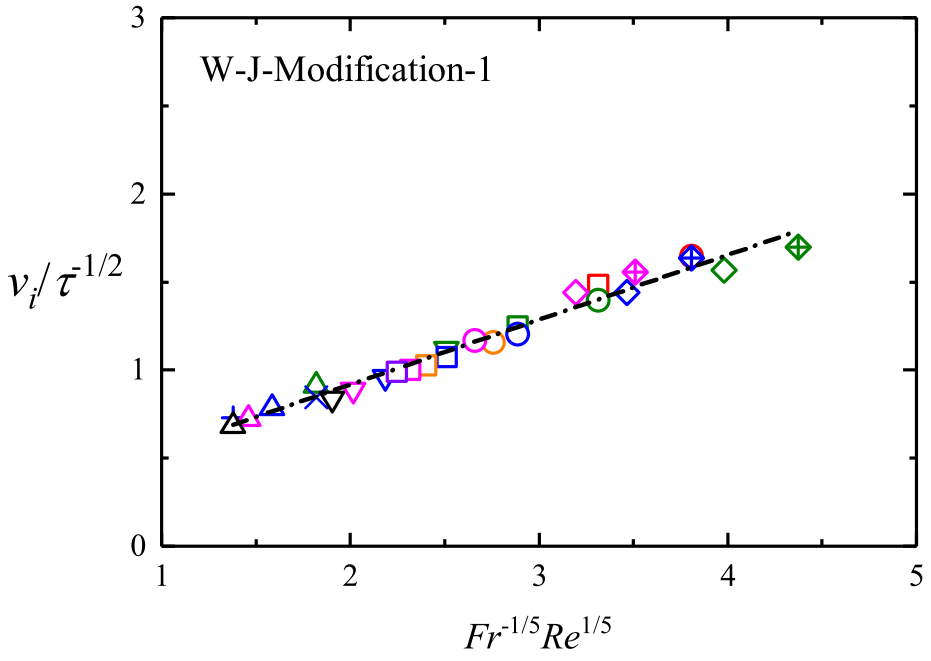

FIGURE 5.19: The modified correlations for the intrusion speed in wall-jet regime, considering the influence of Fr and Re.

Similar to the planar fountain, in the wall jet regime, v_i is only time-dependent, but independent of Fr and Re as indicated in Eq.(5.5). By contrast, Eq.(5.6) shows that v_i for the buoyancy-inertial regime is dependent of Fr and time, but is not affected by Re. It is found that Fr together with Re decides the time-dependent v_i, when the intrusion develops into the buoyancy-viscosity regime as presented in Eq.(5.7).

The time series of the intrusion front speed for a series of Fr and Re are shown in Figure 5.17 and Figure 5.18 confirm that v_i increases with decreasing Fr or increasing Re, and is slowed down with time after it created. Additionally, significant fluctuations are observed in the intrusion speed profiles for fountains with $Re \geq 500$. Similar to the intrusion of the planar fountain cases, v_i is found to be influenced by both Fr and Re for all three regimes, as further discussed below.

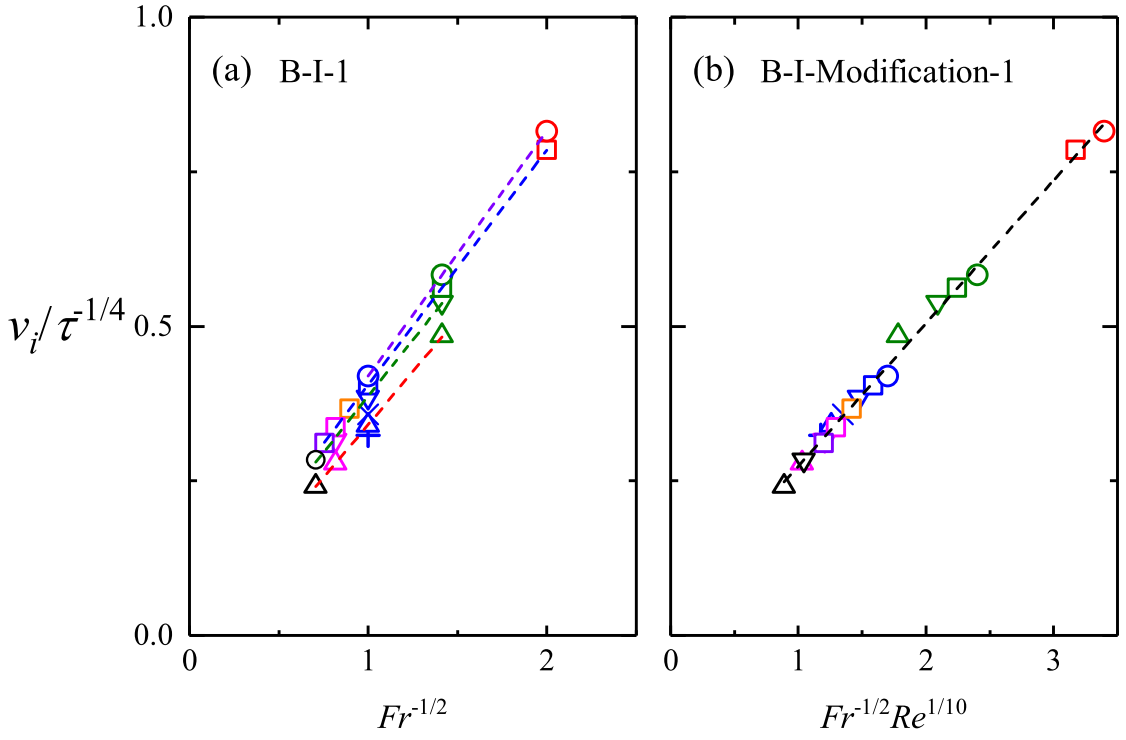

FIGURE 5.20: The intrusion speed for buoyancy-inertial regime: (a) processed based on gravity current theory; (b) modified correlations considering the influence of Re.

Eq.(5.5) shows that v_i only depends on time. However, it is found that the influence of Fr and Re cannot be ignored, as indicated in Figure 5.17 and Figure 5.18 respectively. Thus a modified correlation is obtained with the consideration of the influence of Fr and Re by using multivariate regression technique, as follows,

$$v_i = 0.37 Fr^{-1/5} Re^{1/5} \tau^{-1/2} + 0.18 \tag{5.8}$$

with $R^2 = 0.978$. The dependence of $v_i/\tau^{-1/2}$ on $Fr^{-1/5}Re^{1/5}$ shown in Figure 5.19 indicates a good fit for the modified correlation shown in Eq.(5.8).

Similarly, Figure 5.20(a) plots $v_i/\tau^{-1/4}$ against $Fr^{-1/2}$ according to Eq.(5.6) for the buoyancy-inertial regime, showing that the influence of Re needs to be considered. Hence a modified correlation is obtained based on the numerical results, as follows,

$$v_i = 0.23 Fr^{-1/2} Re^{1/10} \tau^{-1/4} + 0.04 \tag{5.9}$$

with $R^2 = 0.995$. The modified correlation in Eq.(5.9) is presented in Figure 5.20(b).

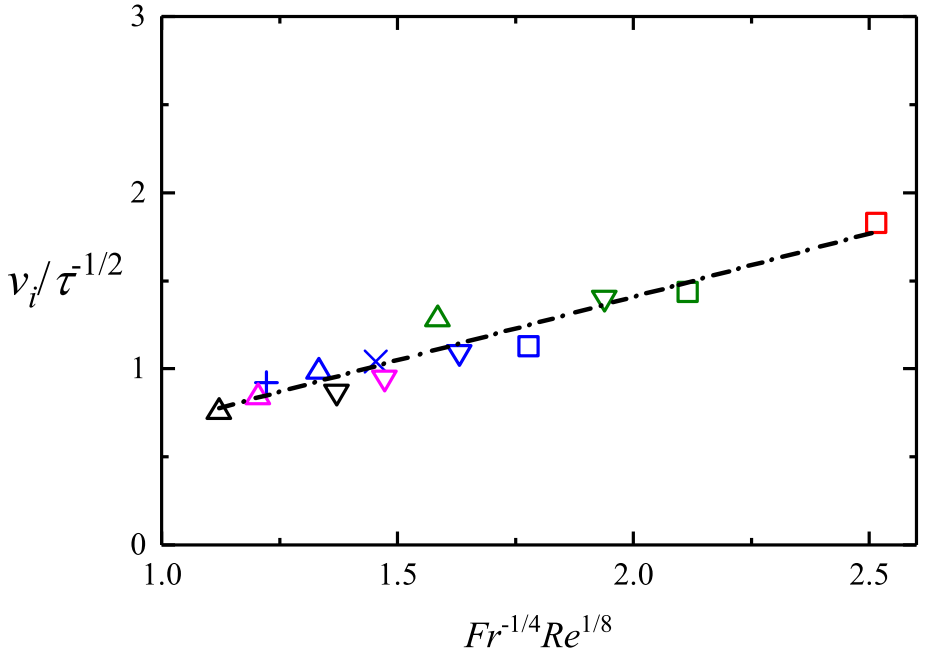

FIGURE 5.21: $v_i/\tau^{-1/2}$ plotted against $Fr^{-1/4}Re^{1/8}$ for the intrusion current in the buoyancy-viscosity regime.

Figure 5.21 shows the results for $v_i/\tau^{-1/2}$ plotted against $Fr^{1/4}Re^{1/8}$ for the intrusion current in the buoyancy-viscosity regime, which fits Eq.(5.7) well. The quantified correlation is as follows,

$$v_i = 0.72Fr^{-1/4}Re^{1/8}\tau^{-1/2} - 0.03, \tag{5.10}$$

with $R^2 = 0.931$.

5.4.2 Wall fountain

5.4.2.1 Development of wall fountain in sidewall region

Similar to the confined weak planar fountains, a discontinuous wall fountain is formed after the intrusion impinges with the sidewall. The behavior of the wall fountain is still mainly dependent on Re, that is, no falling is observed for the wall fountain with $Re \leq 20$, while the wall fountain slumps down after reaching its maximum penetration height for $50 \leq Re \leq 800$. However, no rolling down behavior is found for the wall fountain of the DNS runs here.

In § 4.4.2.1, the height of the wall fountain front is determined by the vertical location on the sidewall where the temperature $T(y) = T_a - 1\%(T_a - T_0)$. If the same definition is used to describe the wall fountain height of the round fountain, no falling down exists in the time series of the wall fountain front for the fountain with $\lambda \leq 20$, except for very small Fr, like $Fr = 0.25$ and 0.5. For example in Figure 5.22, only the wall fountain front passage for fountains of $Fr = 1.0$, $Re = 200$ and $Pr = 7$ with $\lambda \geq 25$ experiences a falling phase. Hence, to illustrate the influence of governing parameters on the wall fountain behavior for confined round fountains, the wall fountain front is re-defined as the z-location in the region close to the sidewall at which the temperature $T(z) = T_a - 1\%(T_a - T_0)$.

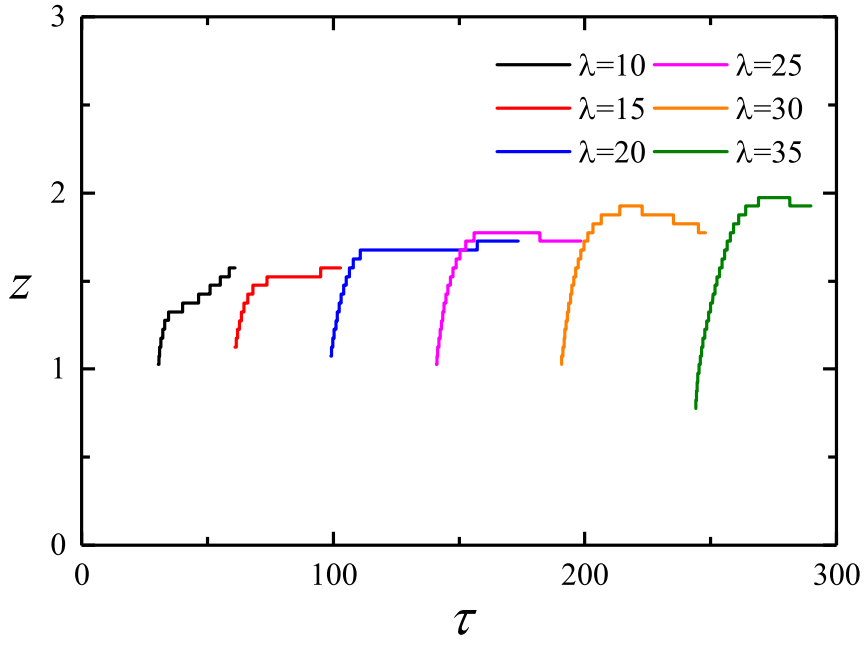

FIGURE 5.22: Time series of the passage of the wall fountain front on the sidewall for fountains with $Fr = 1.0$, $Re = 200$, $Pr = 7$ and $10 \leq \lambda \leq 35$.

Based on the new definition, the time series of the wall fountain front in sidewall region are shown in Figure 5.23 over the range of $0.25 \leq Fr \leq 3.0$, $5 \leq Re \leq 800$, $0.7 \leq Pr \leq 100$ and $10 \leq \lambda \leq 35$. The maximum height of the wall fountain z_m and the corresponding time-scale τ_m are determined from the figure. For $Fr \leq 1.75$, z_m is found to increase with Fr, along with a larger corresponding τ_m, while the conclusion is not valid for $2.0 \leq Fr$, due to the stronger convection as shown in Figure 5.7. Similarly, with the increase of λ, z_m and τ_m increase. The increase of Re and Pr both results in a smaller z_m. However the time for the wall fountain to reach its maximum height is longer with the decrease of Re and the increase of Pr. The influence of the governing parameters on τ_m and z_m will be quantitatively discussed below.

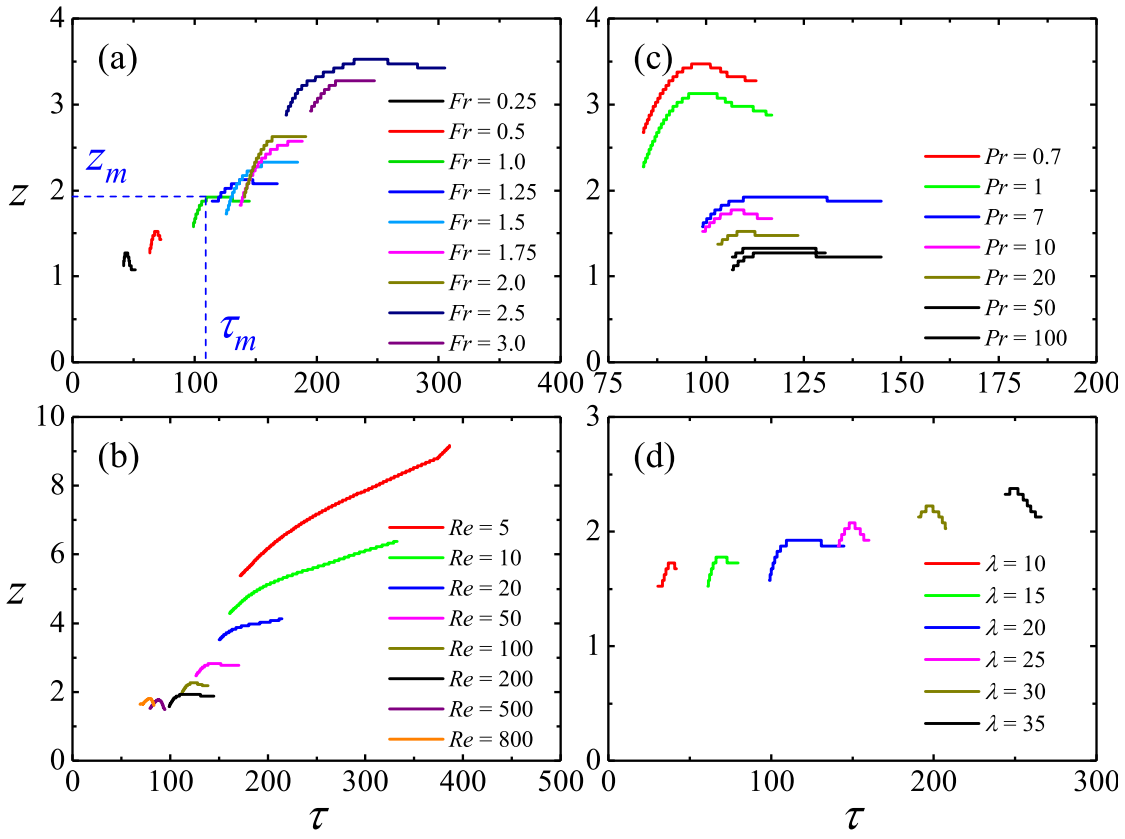

FIGURE 5.23: The time series of the wall fountain front for fountains with (a) $Re = 200$, $Pr = 7$, $\lambda = 20$ and $0.25 \leq Fr \leq 3.0$; (b) $Fr = 1.0$, $Pr = 7$, $\lambda = 20$ and $5 \leq Re \leq 800$; (c) $Fr = 1.0$, $Re = 200$, $\lambda = 20$ and $0.7 \leq Pr \leq 100$; (d) $Fr = 1.0$, $Re = 200$, $Pr = 7$ and $10 \leq \lambda \leq 35$.

5.4.2.2 Influence of Fr, Re, Pr and λ on τ_m

Figure 5.24 demonstrates the influence of Fr, Re, Pr and λ on τ_m. $Fr = 1.0$ and $Fr = 2.0$ are determined as the critical values to distinguish the influence of Fr into three ranges as shown in Figure 5.24(a). The corresponding correlations between τ_m and Fr are obtained as follows,

$$\tau_m = \begin{cases} 109.4Fr^{0.68} - 0.21, & 0.25 \leq Fr \leq 1.0, \\ 92.1Fr + 20.1, & 1.0 \leq Fr \leq 1.75, \end{cases} \tag{5.11}$$

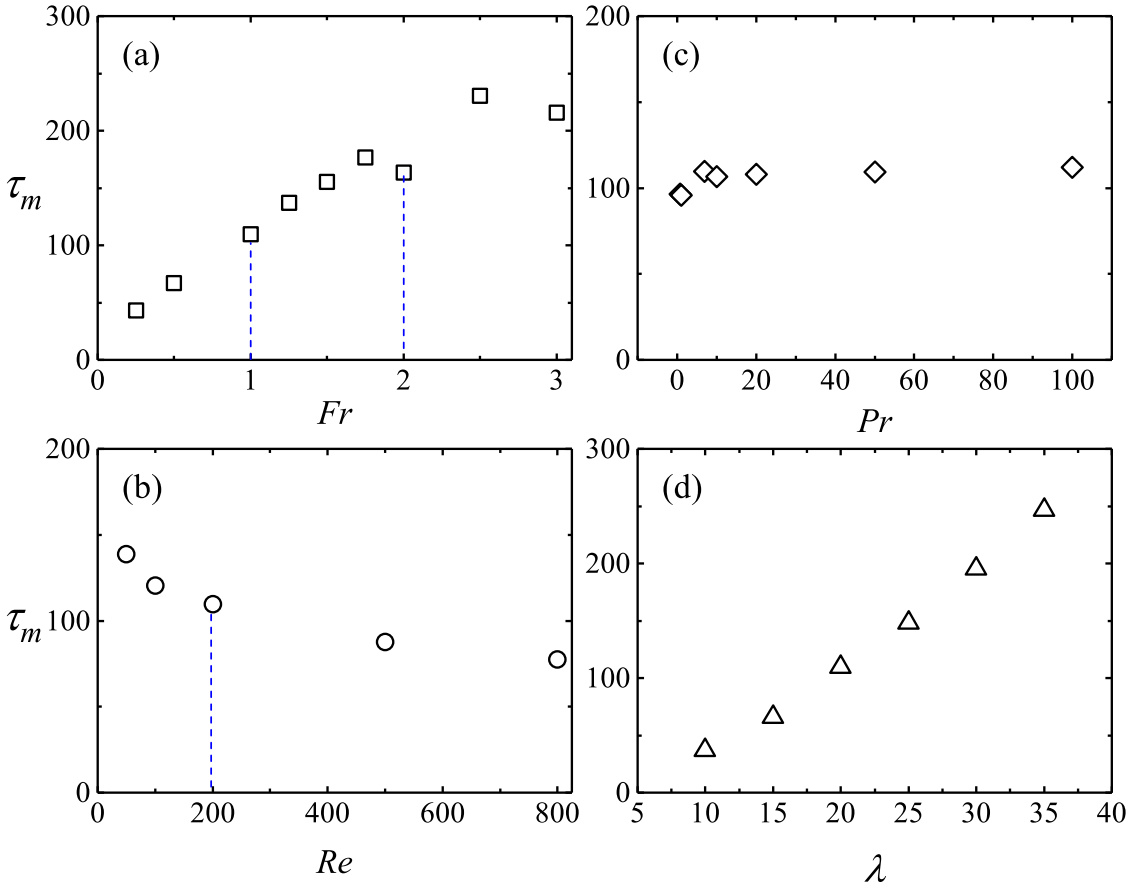

FIGURE 5.24: τ_m plotted against (a) Fr with $Re = 200$, $Pr = 7$ and $\lambda = 20$; (b) Re with $Fr = 1.0$, $Pr = 7$ and $\lambda = 20$; (c) Pr with $Fr = 1.0$, $Re = 200$ and $\lambda = 20$; (d) λ with $Fr = 1.0$, $Re = 200$ and $Pr = 7$.

with $R^2 = 1$ and 0.998, respectively. There is no clear correlation fits for the range of $2.0 \leq Fr \leq 3.0$, which is due to the more asymmetric and turbulent structure with increasing Fr, particularly for $2.0 \leq Fr \leq 3.0$.

No τ_m is obtained for the fountains with $Re \leq 20$ since there is no slumping down behavior for their secondary wall fountain flows. For the fountains with $50 \leq Re \leq 800$, the influence of Re is distinguished into two ranges by $Re = 200$ as shown in Figure 5.24(b), with two power law correlations are determined with the numerical

results as follows,

$$\tau_m = \begin{cases} 270.9Re^{-0.17} - 1.47, & 50 \leq Re \leq 200, \\ 410.5Re^{-0.25} + 0.45, & 200 \leq Re \leq 800, \end{cases} \tag{5.12}$$

with $R^2 = 0.99$ and 1, respectively.

The results shown in Figure 5.24(c) indicate a power law correlation for the influence of Pr on τ_m, quantified with the numerical results as follows,

$$\tau_m = 95.8Pr^{0.033} + 1.31, \tag{5.13}$$

with $R^2 = 0.97$.

Similarly, a power law correlation is identified between τ_w and λ with the numerical results, as shown in Figure 5.24(d), which is as follows,

$$\tau_m = 1.1\lambda^{1.53} + 1.16, \tag{5.14}$$

with $R^2 = 0.999$.

5.4.2.3 Maximum height of the wall fountain on the sidewall

Similarly, Figure 5.25 demonstrates the influence of these governing parameters on the maximum penetration height of the wall fountain on the sidewall region. In Figure 5.25(a), the influence of Fr on z_m is again divided into three ranges by $Fr = 1.0$ and $Fr = 2.0$. The following correlations are obtained from the numerical results for the ranges of $0.25 \leq Fr \leq 1.0$ and $1.0 \leq Fr \leq 1.75$,

$$\tau_m = \begin{cases} 1.92Fr^{0.3} - 0.01, & 0.25 \leq Fr \leq 1.0, \\ 0.86Fr + 1.06, & 1.0 \leq Fr \leq 1.75, \end{cases} \tag{5.15}$$

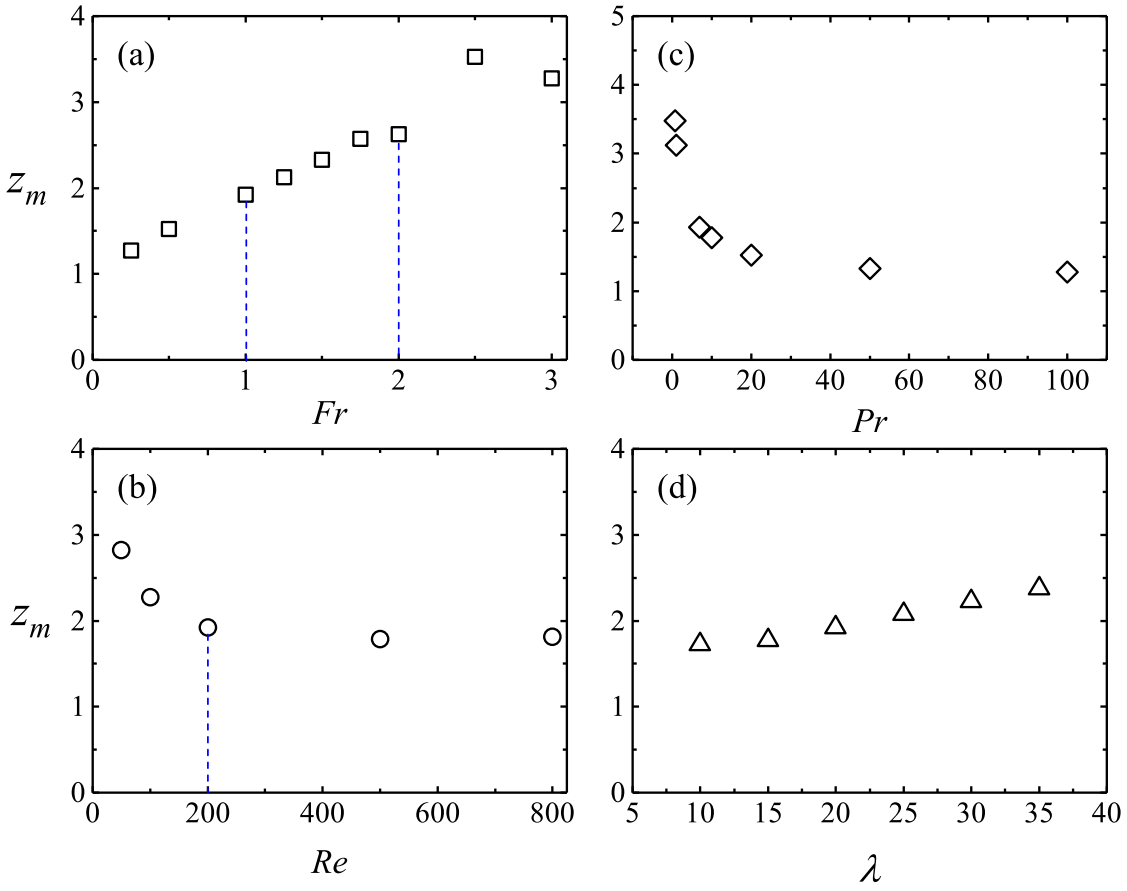

FIGURE 5.25: z_m plotted against (a) Fr with $Re = 200$, $Pr = 7$ and $\lambda = 20$; (b) Re with $Fr = 1.0$, $Pr = 7$ and $\lambda = 20$; (c) Pr with $Fr = 1.0$, $Re = 200$ and $\lambda = 20$; (d) λ with $Fr = 1.0$, $Re = 200$ and $Pr = 7$.

with $R^2 = 0.995$ and 0.998 respectively, while there is no clear correlation for the range of $2.0 \leq Fr \leq 3.0$.

Figure 5.25(b) shows the influence of Re on z_m. For $Re \geq 200$, the effect of Re on z_m is minumal, while for $50 \leq Re \leq 200$, the following correlation is obtained from the numerical results,

$$y_m = 8.38Re^{-0.28} - 0.03, \tag{5.16}$$

with $R^2 = 0.995$.

The following power law correlation is obtained between z_m and Pr from the numerical results, as shown in Figure 5.25(c),

$$y_m = 3.16Pr^{-0.022} - 0.04 \tag{5.17}$$

with $R^2 = 0.987$.

The influence of λ on z_m presented in Figure 5.25(d) can be quantified by the following linear correlation,

$$z_m = 0.027\lambda + 1.41 \tag{5.18}$$

with $R^2 = 0.985$.

5.4.3 Stratification

Similar to the confined planar fountain cases, the time series of the maximum, averaged and minimum heights of the thermally stratified surface are used to illustrate the influence of Fr, Re, Pr and λ on the evolution of the stratification, as shown in Figure 5.26. The stratified surface for a round fountain is determined by the z-location at which the temperature $T(z) = T_a - 1\%(T_a - T_0)$ within the whole cylindrical domain. The profiles of the stratified surface passage in the figures start from the time instant when the intrusion impinges with the sidewall until a quasi-steady stratification is formed when the differences among the maximum, averaged and minimum heights become small enough or overlap. In the initial stage, the differences among the height profiles are significant. This is because convection and mixing play dominant roles in the flow development, which is mainly resulted from the interactions among the fountain flow, its secondary flows, the ambient fluid and the sidewall. After a long run, the three profiles follow the same trend and the extents of the differences are reduced, indicating that thermal conduction and filling become the dominant factors in the later evolution of the stratification.

Moreover, the slope of the averaged height profile can be approximately treated as the development rate of the thermally stratified surface.

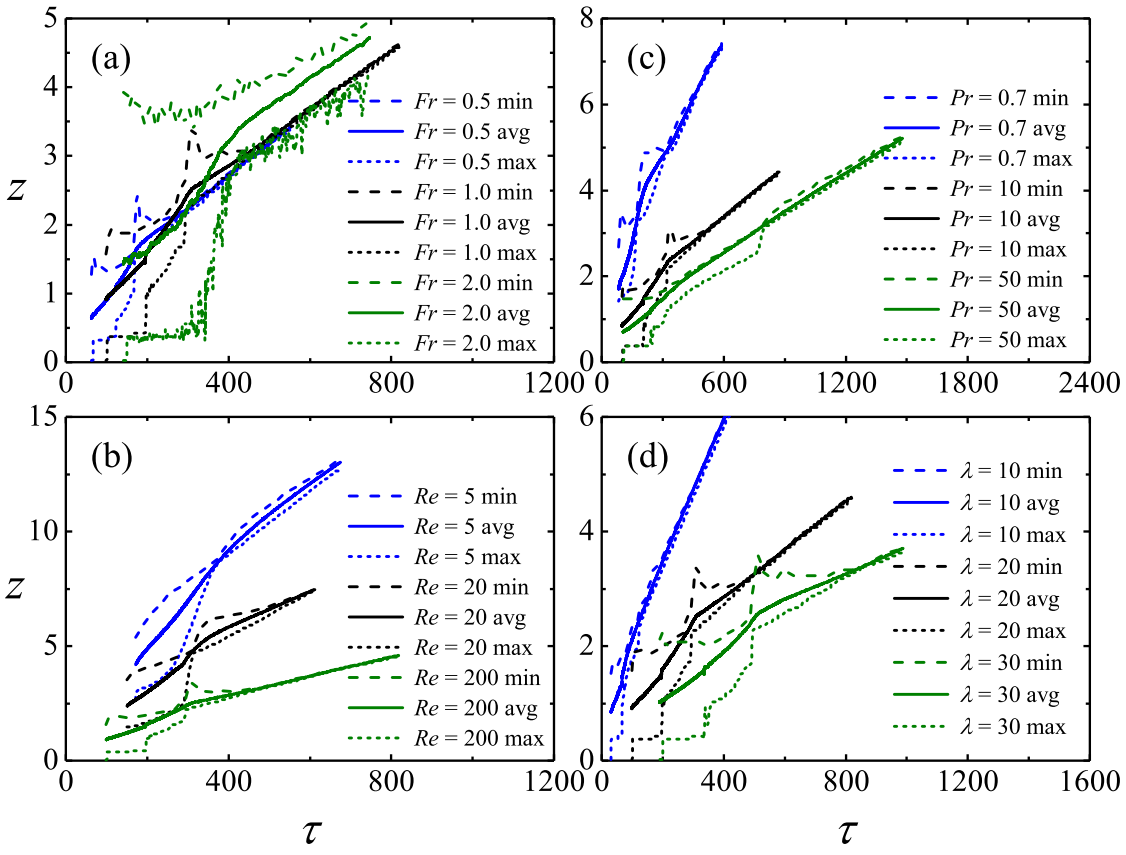

FIGURE 5.26: Time series of the maximum, minimum and average stratification heights for fountains with (a) $Re = 200$, $Pr = 7$, $\lambda = 20$ and $Fr = 0.5$, 1.0, 2.0; (b) $Fr = 1.0$, $Pr = 7$, $\lambda = 20$ and $Re = 5$, 20, 200; (c) $Fr = 1.0$, $Re = 200$, $\lambda = 20$ and $Pr = 0.7$, 10, 50; (d) $Fr = 1.0$, $Re = 200$, $Pr = 7$ and $\lambda = 10$, 20, 30.

Figure 5.26(a) shows that the magnitude of the differences among the height profiles becomes more significant when Fr increases, and the time for the formation of the quasi-steady stratification also increases. While the results in Figure 5.26(b) indicate that the increase of Re results in smaller difference magnitudes and a shorter time for the stratification to reach steady, a smaller development rate of the quasi-steady stratification is observed for the fountain with larger Re, due to the influence of thermal conduction. Similarly, with the increase of Pr, the development rate of the thermal stratification is reduced, as shown in Figure 5.26(c). The magnitude of

the differences among the height profiles is more significant for the fountain with increasing λ, as shown in Figure 5.26(d), which is because of the higher penetration height of the wall fountain.

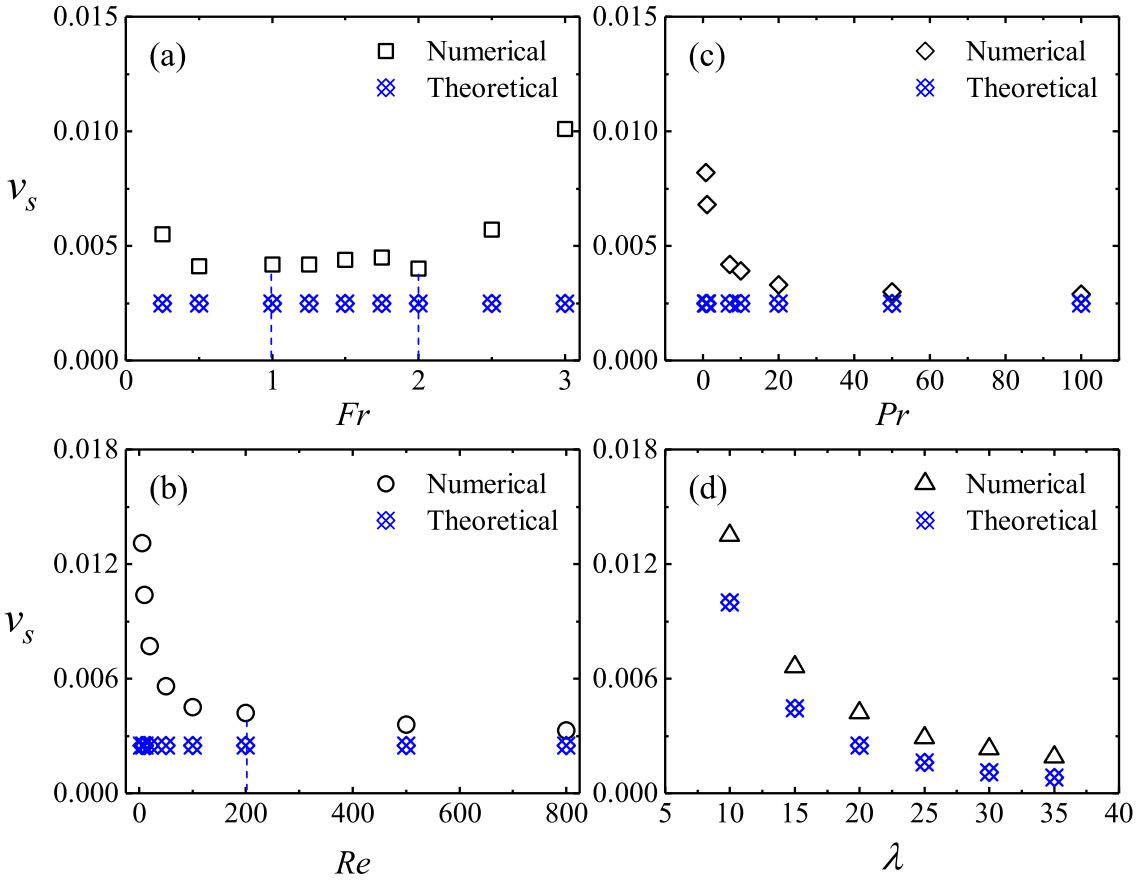

FIGURE 5.27: v_s plotted against (a) Fr with $Re = 200$, $Pr = 7$ and $\lambda = 20$; (b) Re with $Fr = 1.0$, $Pr = 7$ and $\lambda = 20$; (c) Pr with $Fr = 1.0$, $Re = 200$ and $\lambda = 20$; (d) λ with $Fr = 1.0$, $Re = 200$ and $Pr = 7$.

While the development rate of the stratification v_s, can be approximately obtained through the slope of the averaged stratification profiles after the quasi-steady stratification is formed, the counterpart development rate for a purely filling flow in a cylindrical container can be calculated by $v_s = 1/\lambda^2$ based on the conservation law of mass. Figure 5.27 presents the development rate of the averaged stratification and its corresponding purely filling rate for the fountains to illustrate the influence of the governing parameters on v_s. Again, $Fr = 1.0$ and $Fr = 2.0$ are determined

as the critical values to distinguish the influence of Fr into three ranges, as shown in Figure 5.27(a). For $0.25 \leq Fr < 1.0$, the increase of Fr results in a declining v_s. But v_s remains almost constant for $1.0 \leq Fr \leq 2.0$. However, with the further increase of Fr, v_s increases noticeably in the range of $2.0 < Fr \leq 3.0$. Figure 5.27(b) illustrates the influence of Re on v_s, where the influence of Re can be distinguished into two ranges by some specific value between $Re = 100$ and $Re = 200$, with two power law correlations obtained as follows,

$$v_s = \begin{cases} 0.09Re^{-0.362}, & 5 \leq Re \leq 100, \\ 0.07Re^{-0.173}, & 200 \leq Re \leq 800, \end{cases} \tag{5.19}$$

with $R^2 = 0.998$ and 1.0 respectively.

The following power-aw correlation is obtained for the influence of Pr on v_s over the range of $0.7 \leq Pr \leq 50$, as shown in Figure 5.27(c),

$$v_s = 0.0074Pr^{-0.238} - 0.0002, \tag{5.20}$$

with $R^2 = 0.98$. But the change of v_s for $50 \leq Pr$ is negligible, which is also close to the purely filling rate, showing a minor influence from thermal conduction when Pr is very high.

Based on the results in Figure 5.27(d), the following correlation is obtained between v_s and λ,

$$v_s = 0.5077Pr^{-1.574} - 0.0002, \tag{5.21}$$

with $R^2 = 0.998$.

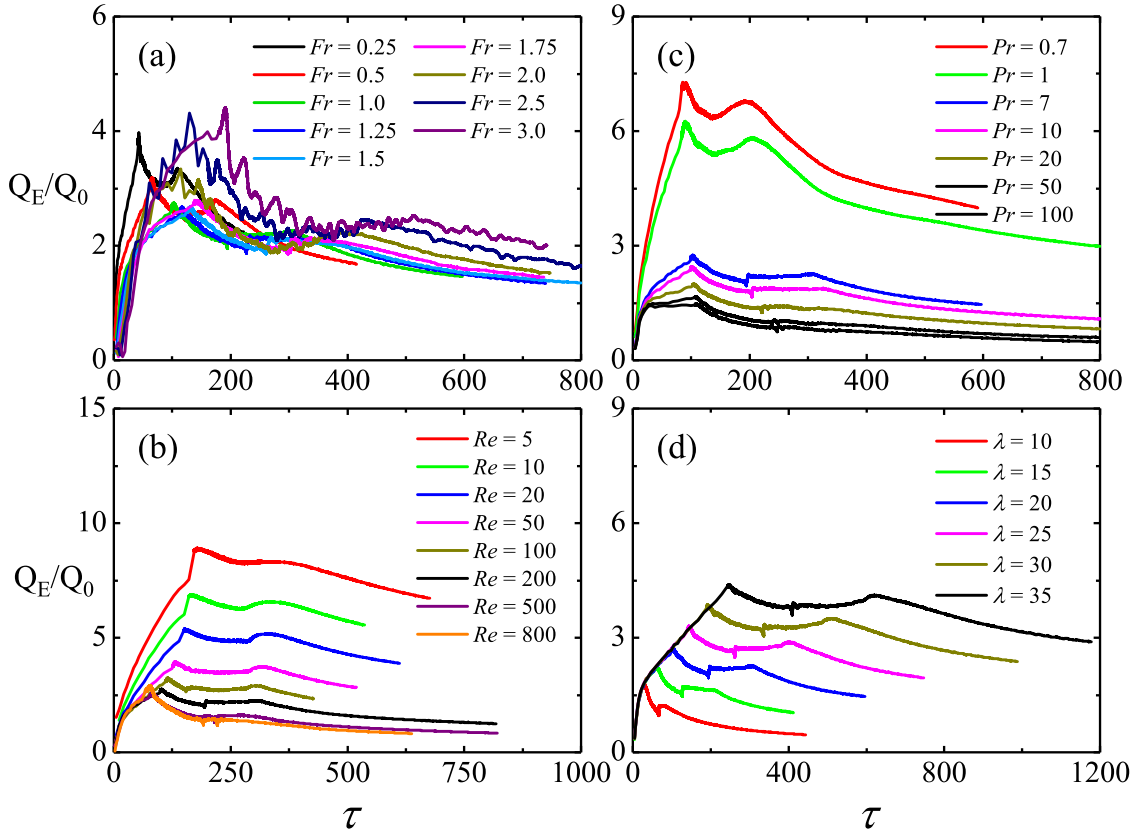

FIGURE 5.28: Time series of the entrainment rate Q_E/Q_0 for fountains with (a) $Re = 200$, $Pr = 7$, $\lambda = 20$ and $0.25 \leq Fr \leq 3.0$; (b) $Fr = 1.0$, $Pr = 7$, $\lambda = 20$ and $5 \leq Re \leq 500$; (c) $Fr = 1.0$, $Re = 200$, $\lambda = 20$ and $0.7 \leq Pr \leq 100$; (d) $Fr = 1.0$, $Re = 200$, $Pr = 7$ and $10 \leq \lambda \leq 35$.

5.4.4 Bulk entrainment or dilution

The bulk entrainment rate determined by Q_E/Q_0 is used to describe the mean dilution of the buoyancy scalar over the filling box as a whole, which is again employed here to investigate the entrainment/dilution behavior for the filling flow with weak round fountains. For a confined round fountain, the source volume flux is $Q_0 = \pi R_0^2 W_0$, whereas the bulk entrainment Q_E is calculated by $Q_E = Q_s - Q_0$, where Q_s is the volume flux of the stratified fluid, which is calculated by integrating the volume under the thermal stratified surface.

The entrainment rates (Q_E/Q_0) for the confined round fountains over the range

of $0.25 \leq Fr \leq 3.0$, $5 \leq Re \leq 800$, $0.7 \leq Pr \leq 100$ and $10 \leq \lambda \leq 35$ are calculate and plotted against τ as shown in Figure 5.28, to demonstrate the influence of these governing parameters. The time series of the entrainment rate profile starts from the formation stage of the fountain until the formation of the quasi-steady stratification. As presented in Figure 5.28, the entrainment rate profiles can be approximately distinguished into three stages. In the first stage, the entrainment rate increases monotonically with time until reaching the first peak points. The first stage corresponds to the period of the intrusion development, where the ambient fluid is mainly engulfed by the eddy over the intrusion head. With the intrusion front impinging with the sidewall, the entrainment rate profile reaches the peak, due to the stronger convection and mixing resulted from the impingement and the subsequent secondary wall fountain flow. Then the convection and the interactions among the intrusion, the reversed flow and the ambient fluid keep the entrainment rate at a relatively high value until the reversed flows collide at the center of the container. For some cases, see, *e.g.*, $Pr = 0.7$ and 1, the colliding at the center results in another peaking value for the the entrainment rate. After that the entrainment rate profiles decrease gradually. This is because thermal conduction plays the dominant roles in the dilution process, with the confined fountain flow turning into a filling box model. It should be noted that thermal conduction keeps influencing the dilution process at all stages. The influence of Fr, Re, Pr and λ on Q_E/Q_0 is consistent with the results presented in § 5.4.3 for the stratification rate.

5.5 Summary

The upward ejection of a round fountain into a cylindrical container with a homogeneous ambient fluid results in a 'weak round fountain filling box model'. A series of 3D DNS runs for the round fountains over the ranges of $0.25 \leq Fr \leq 3.0$, $5 \leq Re \leq 800$, $0.7 \leq Pr \leq 100$ and $10 \leq \lambda \leq 35$ are carried out to illustrate the behavior of the confined weak round fountains. The typical evolution of the confined

weak round fountains is described in detail, along with the qualitative and quantitative analysis of the influence of Fr, Re, Pr and λ with the numerical results. The major conclusions of this chapter are summarized as follows:

- A secondary radial intrusion flow is created with the impingement of the fountain downflow on the bottom of the container. The intrusion flow behavior can be approximately described by the scaling relations obtained by Chen [1] for radial gravity currents. However, for the 'wall-jet' regime and 'buoyancy-inertial' regime, both Re and Fr influence v_i, which is different from the results of the existing studies. Additionally, the influence of Pr on vi becomes significant after the intrusion spreads a certain distance, particularly for very small Pr, *e.g.*, $Pr = 0.7$ and 1, due to the influence of thermal conduction.

- The behavior of the secondary wall fountain for the fountains with specific values of Fr, Re and Pr is significantly influenced by the confinement λ. The wall fountain front on the sidewall changes from no falling to falling with the increase of λ. The maximum penetration height z_m is found to increase with λ and Fr for $Fr \leq 2.0$, whereas z_m decreases with increasing Re and Pr.

- Three stages are determined based on the time series of the bulk entrainment rate. At first, the entrainment rate monotonically increases due to the ambient fluid engulfed by the intrusion head. With the intrusion impinging with the sidewall, the entrainment rate reaches a peaking value. Then the subsequent interactions among the intrusion, the reversed flow and the ambient fluid create convection and mixing, leading to the second stage with relatively high entrainment rate. After the second peak, the entrainment rate gradually decreases, which is because the dominant factors governing the stratification development switch to filling and thermal conduction. The stratification rate v_s deceases with the increase of Re and Pr, which reduces the effect of thermal conduction.

- With the qualitative and quantitative analysis, $Fr = 1.0$ and 2.0 are identified as the critical values to distinguish the behavior of the intrusion, wall fountain and stratification. This is consistent with the existing classifications of the round fountains [2], while $Re = 200$ is determined as the critical value to divide the influence of Re, which also agrees well with the existing results [30].

Chapter 6

Confined intermediate and forced turbulent round fountains

6.1 Introduction

The previous two chapters have focused on the transient behavior of confined weak planar and round fountains through direct numerical simulation. In this chapter, the transient behavior of confined weak, intermediate and forced round fountains is studied through a series of experiments. In § 6.2, the details of the experiments are described. To benchmark the numerical results of confined weak round fountain produced by DNS runs in the previous chapter, several experiments with typical Fr and Re values were carried out and the comparison between the numerical and experimental results are presented in § 6.3. The qualitative and quantitative results obtained from experiments are detailed and discussed in § 6.4. The main conclusions of this chapter are summarized in § 6.5.

6.2 Experimental details

The details of the experimental system, setup, and methods were described in § 3.3. In the current experiments, saline water of various densities was ejected upward into a cylindrical container with quiescent free water at specific constant flow rates, to form the confined round fountains with Fr and Re over the range of $1.0 \leq Fr \leq 20.0$ and $102 \leq Re \leq 1502$. The inner diameter of the cylindrical Perspex-sided test tank is $R = 0.39$m. The changes of the nozzles with diameters of 0.007 m, 0.006 m, 0.005 m and 0.004 m, from which the fountain is ejected, result in the dimensionless confinement size $\lambda = 27.9$, 32.5, 39.0 and 48.75, respectively, with the majority of the experiments using the nozzle of the diameter of 0.007 m ($\lambda = 27.9$). Since the fluid for the experiments is water, Pr is fixed as $Pr = 7$. Hence only the influence of Fr, Re and λ on the transient behavior of confined round fountains are studied experimentally here. The transient behavior of confined fountain was recorded by a system of two Photron FASTCAM Mini UX100 High-Speed Cameras and a SONY HDR-PJ810 video camera.

There are totally 39 experiments were carried out, with the key information for these experiments presented in Table 6.1.

Table 6.1: Key data of the experiments of confined round fountains

Runs	Fr	Re	R_0 (m)	W_0 (m/s)	ρ_0 (kg/m^3)	ρ_a (kg/m^3)
1	1	102	0.007	0.013533584	996.9	999.5
2	1	204	0.007	0.027067167	996.5	1007.6
3	1	511	0.007	0.067667918	996.7	1063.4
4	1.5	102	0.007	0.013533584	996.5	997.7
5	1.5	204	0.007	0.027067167	996.5	1001.3
6	1.5	307	0.007	0.040600751	996.7	1007.5

Continued on next page

Table 6.1 – continued from previous page

Runs	Fr	Re	R_0 (m)	W_0 (m/s)	ρ_0 (kg/m^3)	ρ_a (kg/m^3)
7	1.5	409	0.007	0.054134334	996.8	1015.7
8	1.5	511	0.007	0.067667918	996.6	1026.1
9	2	102	0.007	0.013533584	996.5	997.2
10	2	204	0.007	0.027067167	996.5	999.3
11	2	511	0.007	0.067667918	996.6	1013.3
12	3	102	0.007	0.013533584	996.7	997
13	3	204	0.007	0.027067167	996.6	997.8
14	3	511	0.007	0.067667918	996.6	1004.2
15	3	695	0.007	0.092028368	996.6	1010.5
16	3	1002	0.007	0.132629119	996.6	1025
17	5	204	0.007	0.027067167	996.9	997.3
18	5	511	0.007	0.067667918	996.4	999.1
19	5	695	0.007	0.092028368	996.6	1001.6
20	3	1002	0.007	0.132629119	996.7	1007.1
21	1.5	501	0.006	0.077366986	996.7	1041.6
22	5	501	0.006	0.077366986	996.6	1000.7
23	8	1002	0.006	0.185680767	996.6	1003.1
24	5	501	0.005	0.095492966	996.6	1004
25	8	1002	0.005	0.185680767	996.6	1007.5
26	1.5	501	0.004	0.116050479	996.8	1148.2
27	5	501	0.004	0.116050479	996.7	1010.1
28	5	1502	0.004	0.348151438	996.7	1121
29	8	215	0.004	0.04973592	997	998

Continued on next page

Table 6.1 – continued from previous page

Runs	Fr	Re	R_0 (m)	W_0 (m/s)	ρ_0 (kg/m^3)	ρ_a (kg/m^3)
30	8	501	0.004	0.116050479	996.7	1002.1
31	8	716	0.004	0.165786399	996.5	1007.5
32	8	1002	0.004	0.232100959	996.6	1017.8
33	8	1502	0.004	0.348151438	996.5	1044.7
34	15	501	0.004	0.116050479	997	998.5
35	15	716	0.004	0.165786399	996.7	999.8
36	15	1002	0.004	0.232100959	996.6	1002.7
37	15	1502	0.004	0.348151438	996.5	1009.8
38	20	1002	0.004	0.232100959	996.5	1000
39	20	1502	0.004	0.348151438	996.7	1004.4

6.3 DNS results benchmarking

To ensure accurate numerical results to be obtained by the DNS runs, the DNS results of several typical confined weak round fountains obtained in Chapter 5 are compared against the experimental results of approximately the same corresponding fountains, both qualitatively and quantitatively. The DNS runs selected for the benchmark include those of Fr = 1.0, 1.5, 2.0, and 3.0 at Re = 200 and λ = 20, and Re = 100, 200, and 500 at Fr = 1.5 and λ = 20. The experiments chosen for the DNS benchmark are those of Fr = 1.0, 1.5, 2.0 and 3.0 at Re = 204 and λ = 27.9 (*i.e.*, runs 2, 5, 10 and 13), and Re = 102, 204 and 511 at Fr = 1.5 and λ = 27.9 (*i.e.*, runs 4, 5 and 8), with each experiment corresponding to the closest to its counterpart of the DNS run.

The evolution of the flow behavior of a typical confined weak round fountain was presented in § 5.3 with the DNS results, which includes five major development

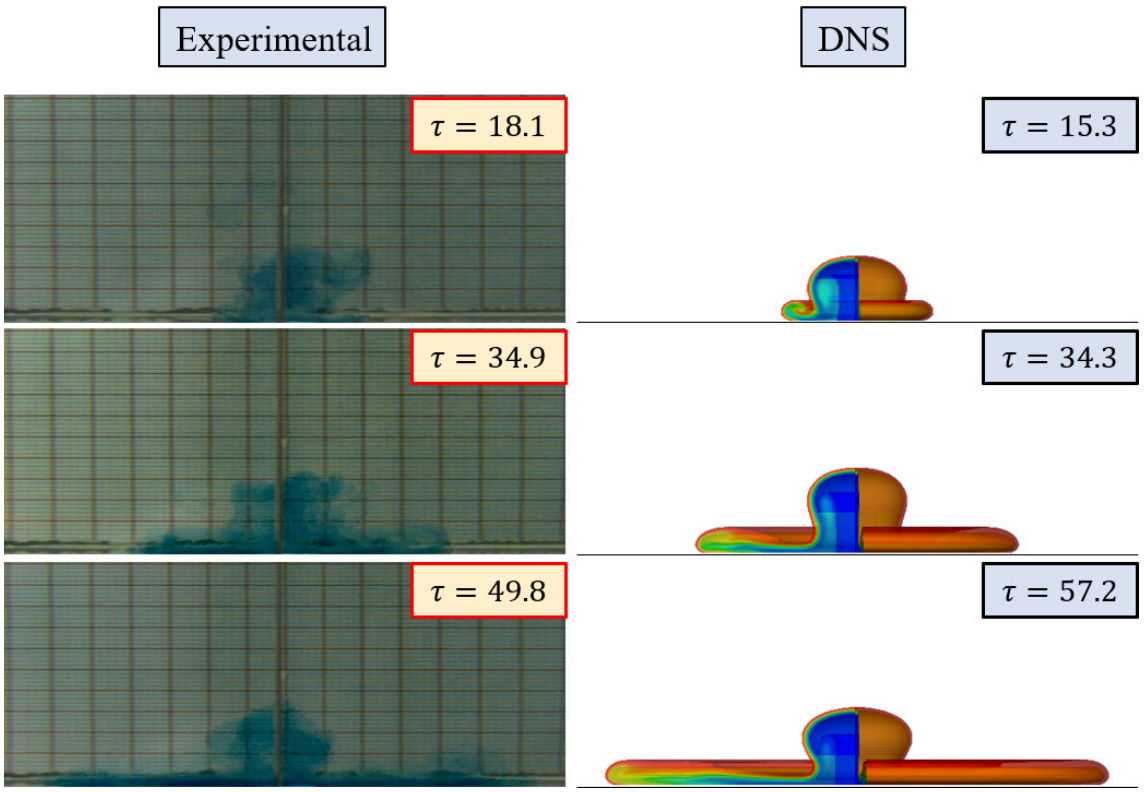

FIGURE 6.1: The comparison of the images of the density field from the experiment for the confined weak round fountain of $Fr = 2.0$, $Re = 204$, $Pr = 7$ and $\lambda = 27.9$ and the contours of the temperature field from the DNS for the corresponding confined weak round fountain of $Fr = 1.5$, $Re = 200$, $Pr = 7$ and $\lambda = 20$, during the intrusion flow stage.

stages, *i.e.*, the formation of the fountain flow, the intrusion flow, the wall fountain flow on the sidewall, the reversed flow and the stratification. In Figure 6.1 to Figure 6.3, the images of the density field from the experiment for the confined weak round fountain of $Fr = 2.0$, $Re = 204$, $Pr = 7$ and $\lambda = 27.9$ and the contours of the temperature field from the DNS for the corresponding confined weak round fountain of $Fr = 2.0$, $Re = 200$, $Pr = 7$ and $\lambda = 20$ are presented for the stages of the intrusion flow, the wall fountain flow and the stratification, respectively. As the description of the evolution of the flow behavior of such a confined weak round fountain was detailed in the previous chapter, it will not be repeated here.

The importance of these figures is that the experimental results and the DNS results are qualitatively in good agreement, as the DNS results captures the major

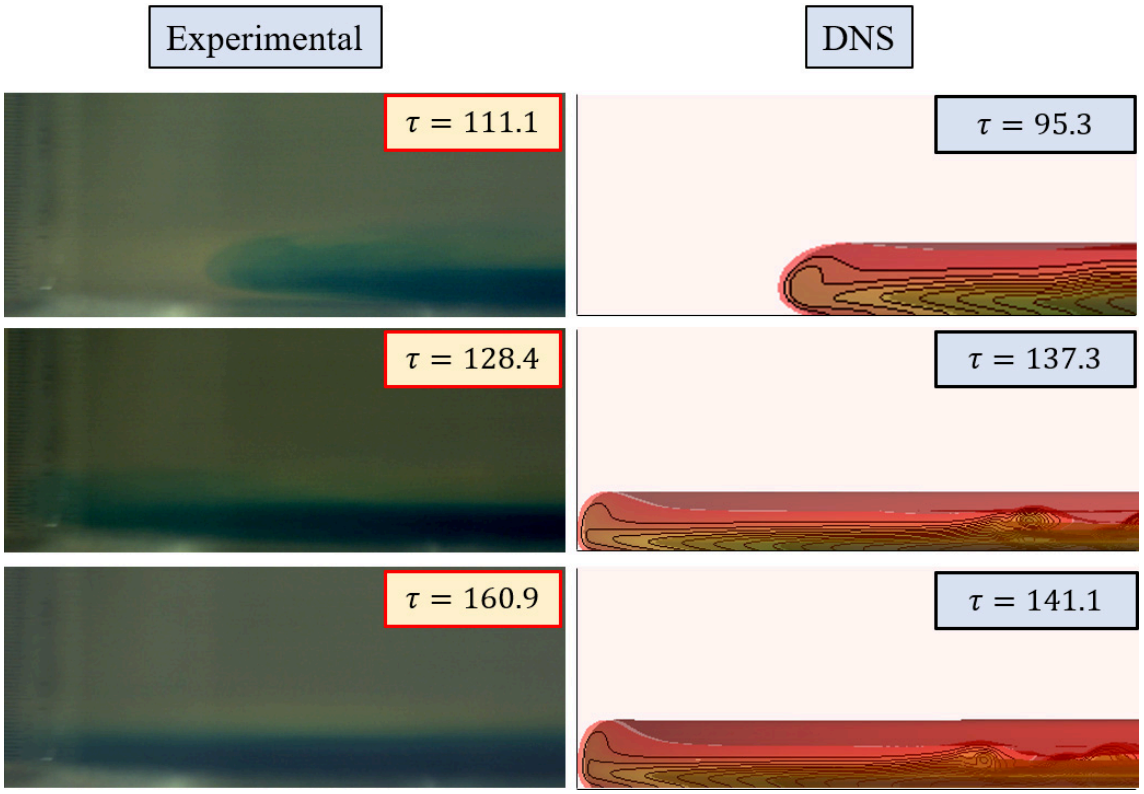

FIGURE 6.2: The comparison of the images of the density field from the experiment for the confined weak round fountain of $Fr = 2.0$, $Re = 204$, $Pr = 7$ and $\lambda = 27.9$ and the contours of the temperature field from the DNS for the corresponding confined weak round fountain of $Fr = 1.5$, $Re = 200$, $Pr = 7$ and $\lambda = 20$, during the wall fountain flow stage.

features of the flow behavior with sufficient accuracy, although noticeable quantitative differences are also clearly shown between the experimental and DNS results.

Similarly, the quantitative comparisons between the numerical and experimental results of the time series of the penetration height of the fountains and the intrusion front, as shown in Figure 6.4 to Figure 6.7 also clearly show that in general the DNS results are in good agreement with the experimental results in terms of the intrusion front, again indicating the DNS runs predict the flow behavior with sufficient accuracy.

The results show that the DNS data, in general, match the experimental results satisfactorily and capture all the major features of the flow behavior of confined round fountains, although some noticeable quantitative differences are also clearly

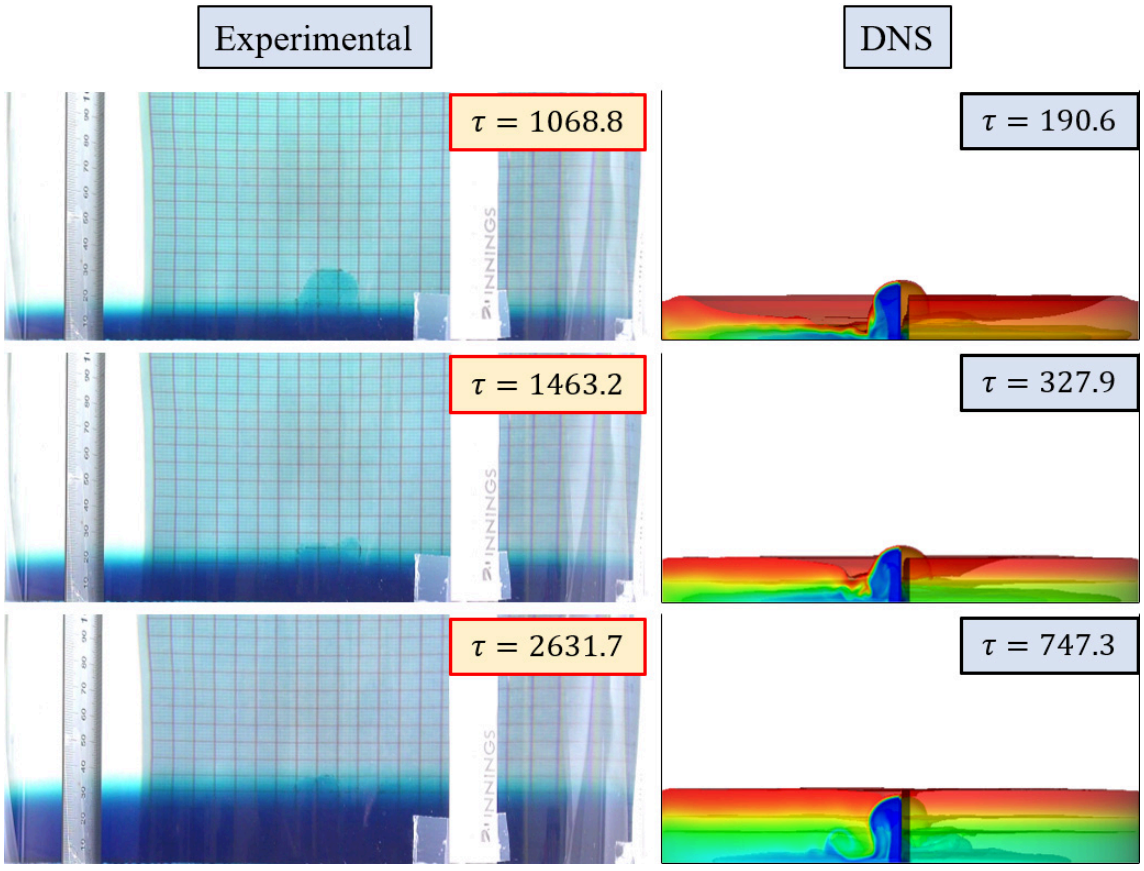

FIGURE 6.3: The comparison of the images of the density field from the experiment for the confined weak round fountain of $Fr = 2.0$, $Re = 204$, $Pr = 7$ and $\lambda = 27.9$ and the contours of the temperature field from the DNS for the corresponding confined weak round fountain of $Fr = 1.5$, $Re = 200$, $Pr = 7$ and $\lambda = 20$, during the stratification stage.

seen. Some of the possible factors contributed to these differences were discussed by Mahmud [54] who used the similar experimental facility to the current one for his PhD thesis. These factors can be briefly summarized as follows:

- Determination of the density difference: In the DNS runs, the density difference was determined by the temperature difference using the Oberbeck-Boussinesq approximation, whereas in the experiments, it was determined by the salinity of fluid. The substantial difference in the Schmidt number between the saline water used in the experiments and the pure water used in the DNS runs results in considerably different molecular diffusion rates of the fluids and thus a noticeable different thermal boundary layer calculated by the DNS runs compared to that obtained by the experiments. It is speculated

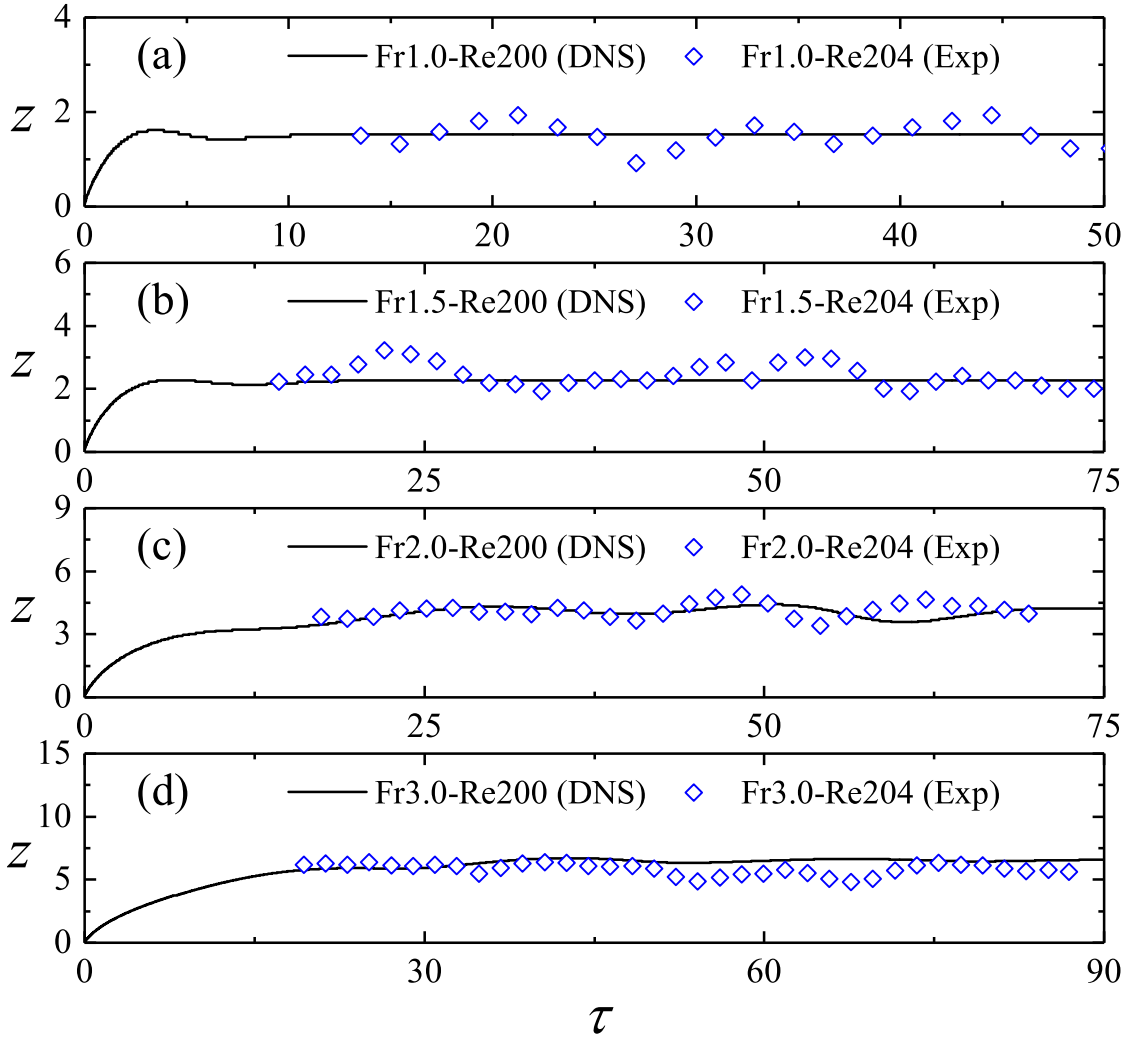

FIGURE 6.4: The time series of the penetration height of the fountains of (a) $Fr = 1.0$ with $Re = 200$ for the DNS run (solid line), and $Fr = 1.0$ with $Re = 204$ for the experimental run (scatters); (b) $Fr = 1.5$ with $Re = 200$ for the DNS run (solid line), and $Fr = 1.5$ with $Re = 204$ for the experimental run (scatters); (c) $Fr = 2.0$ with $Re = 200$ for the DNS run (solid line), and $Fr = 2.0$ with $Re = 204$ for the experimental run (scatters); (d) $Fr = 3.0$ with $Re = 200$ for the DNS run (solid line), and $Fr = 3.0$ with $Re = 204$ for experimental run (scatters).

that this should be the major factor contributed to the observed differences between the DNS results and the experimental results.

- Measurement errors in the experiments: The errors in the experimental measurements of the densities, velocities, fountain penetration height, intrusion speed and thickness, stratification level, nozzle size, flow rate, etc., are inevitable. Such errors are other major sources for the observed differences.

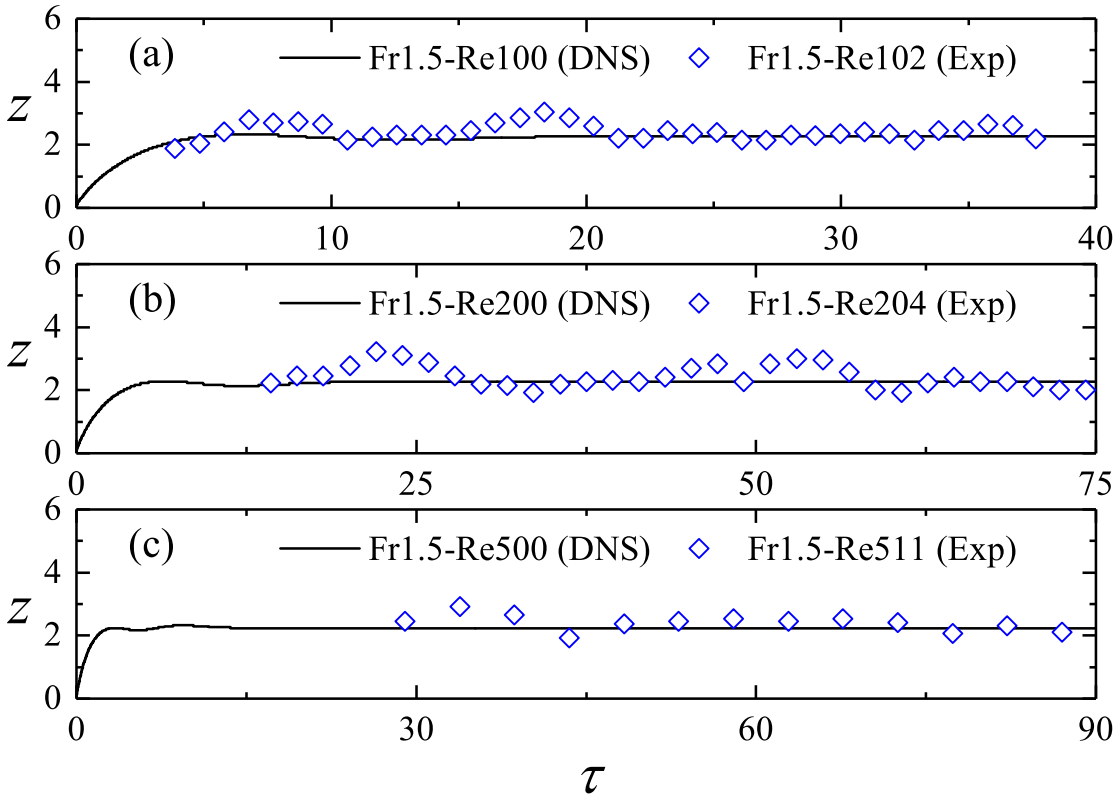

FIGURE 6.5: The time series of the penetration height of the fountains of (a) $Fr = 1.5$ with $Re = 100$ for the DNS run (solid line), and $Fr = 1.5$ with $Re = 102$ for the experimental run (scatters); (b) $Fr = 1.5$ with $Re = 200$ for the DNS run (solid line), and $Fr = 1.5$ with $Re = 204$ for the experimental run (scatters); (c) $Fr = 1.5$ with $Re = 500$ for the DNS run (solid line), and $Fr = 1.5$ with $Re = 511$ for experimental run (scatters).

- Difference in the inlet velocity profiles: In the DNS runs, a 'top-hat' uniform inlet velocity profile was assumed whereas in the experiments the specific inlet velocity profile was unknown but it is certain that it should not be a uniform one. Such a difference surely will make a noticeable contribution to the observed differences.

- Difference in the ambient fluids: In the DNS runs, a uniform ambient fluid was assumed at the commencement of the runs, while in the experiments such a uniform ambient fluid was hard to achieve. In addition, in the DNS runs, the ambient fluid was pure water, whereas in the experiments, dye particles were added in the water which is itself not pure, but with numerous small

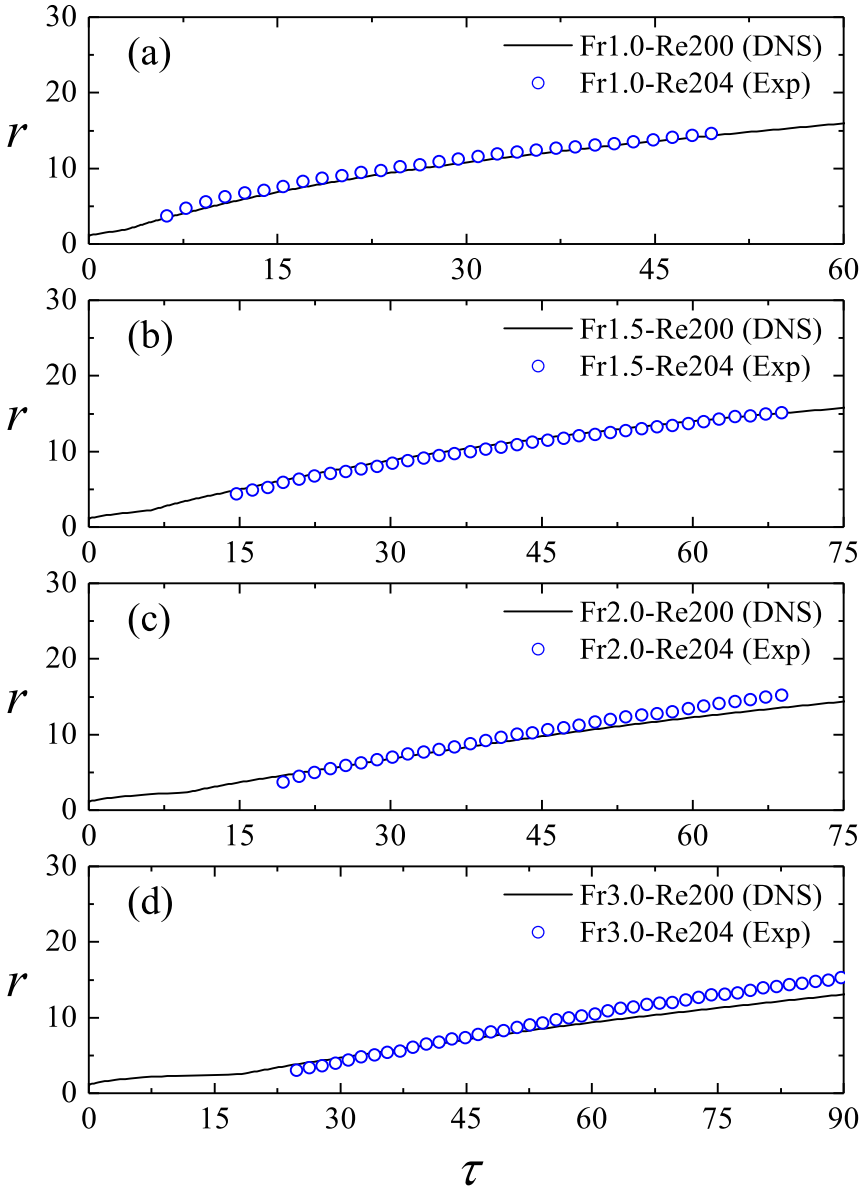

FIGURE 6.6: The time series of the intrusion front for fountains of (a) $Fr = 1.0$ with $Re = 200$ for the DNS run (solid line), $Re = 204$ for the experimental run (scatters); (b) $Fr = 1.5$ with $Re = 200$ for the DNS run (solid line), $Re = 204$ for the experimental run (scatters); (c) $Fr = 2.0$ with $Re = 200$ for the DNS run (solid line), $Re = 204$ for the experimental run (scatters); (d) $Fr = 3.0$ with $Re = 200$ for the DNS run (solid line), $Re = 204$ for experimental run (scatters).

solid particles, although very tiny and very dilute, will also makes a noticeable contribution to the observed differences.

- In the experiments, the fountain penetration height, the passage of the intrusion and the stratification height were determined from the images captured

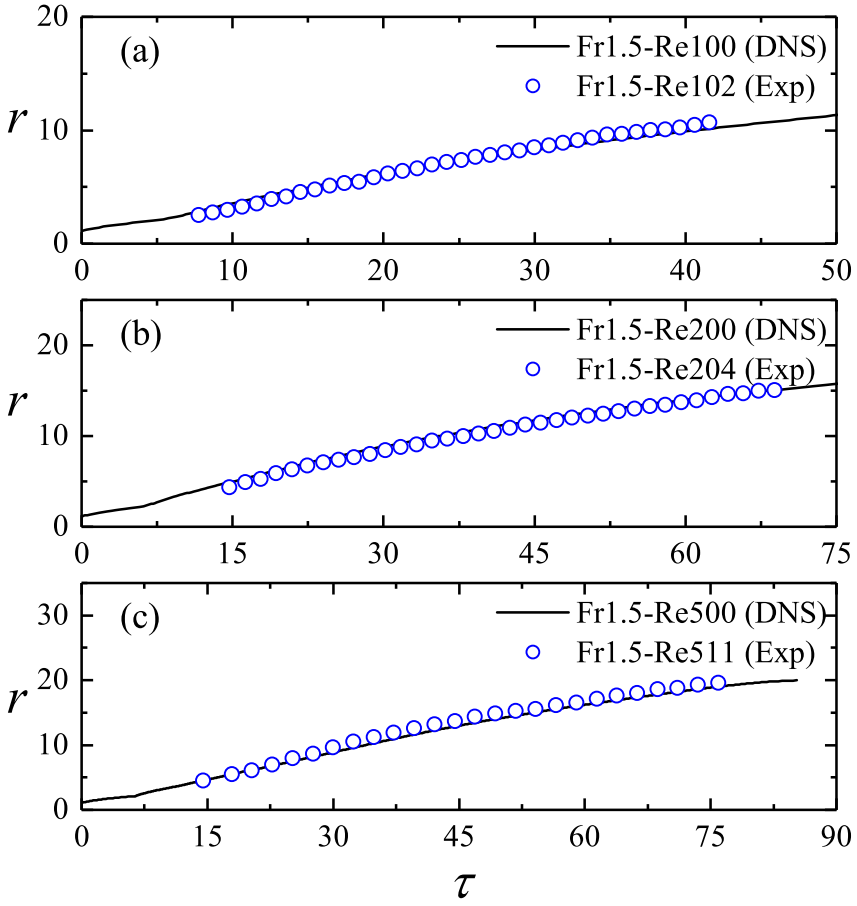

FIGURE 6.7: The time series of the intrusion front for fountains of (a) $Fr = 1.5$ with $Re = 100$ for the DNS run (solid line), $Re = 102$ for the experimental run (scatters); (b) $Fr = 1.5$ with $Re = 200$ for the DNS run (solid line), $Re = 204$ for the experimental run (scatters); (c) $Fr = 1.5$ with $Re = 500$ for the DNS run (solid line), $Re = 511$ for the experimental run (scatters).

by the CCD camera with the help of dye. Such PIV images can be severely affected by the light reflected from the air, the glass wall or the ambient and fountain fluids, which will also make a contribution to the observed differences between the DNS results and the experimental results.

Nevertheless, all the benchmarking results, as noted above, clearly show that the code used for the DNS runs is able to provide satisfactorily accurate and reliable numerical results which capture all the major features of the bulk behavior of confined round fountains in a homogeneous fluid.

6.4 Experimental results and discussion

Hunt and Burridge [2] classified round fountains into very weak fountains ($0.3 \lesssim Fr \lesssim 1.0$), weak fountains ($1.0 \lesssim Fr \lesssim 2.0$), intermediate fountains ($2.0 \lesssim Fr \lesssim 4.0$), and forced / highly forced fountains ($Fr \gtrsim 4.0$) with the consideration of the dominant physics of these flows with different Fr values. Similar to the characteristics of the flow behavior of confined weak round fountains, the evolution of the filling box flow induced by intermediate and forced turbulent fountains also experiences the formation of the fountain, the intrusion flow, the wall fountain flow, the reversed flow and the stratification, although both the fountain flow and the secondary flows present are turbulent instead of laminar as for confined weak round fountains. In the subsequent sections, the evolution of these flows and the influence of Fr, Re and λ on their bulk behavior, including penetration height, intrusion thickness, intrusion speed and stratification rate, are described and discussed both qualitatively and quantitatively.

6.4.1 Qualitative observations

Without the PIV system assistance, the cameras can only capture the bulk behavior of the fountain flow and its secondary flows projected onto the sidewall in front. As a result, the images captured from experiments, as those presented in Figure 6.1 to Figure 6.3, can only determine the maximum value of the dense flow in vertical and horizontal directions. For example, the intrusion flow shown in the camera images actually reflects the radial location and the vertical thickness of the intrusion front, whereas the density stratification (dark region) in the camera images is actually the maximum height of the stratified surface in the vertical direction. Hence, the internal structure and some of the flow behavior (*e.g.*, the wall fountain and reversed flow) cannot be captured by the camera systems in this study.

6.4.1.1 The evolution of the confined intermediate round fountain of $Fr = 3.0$

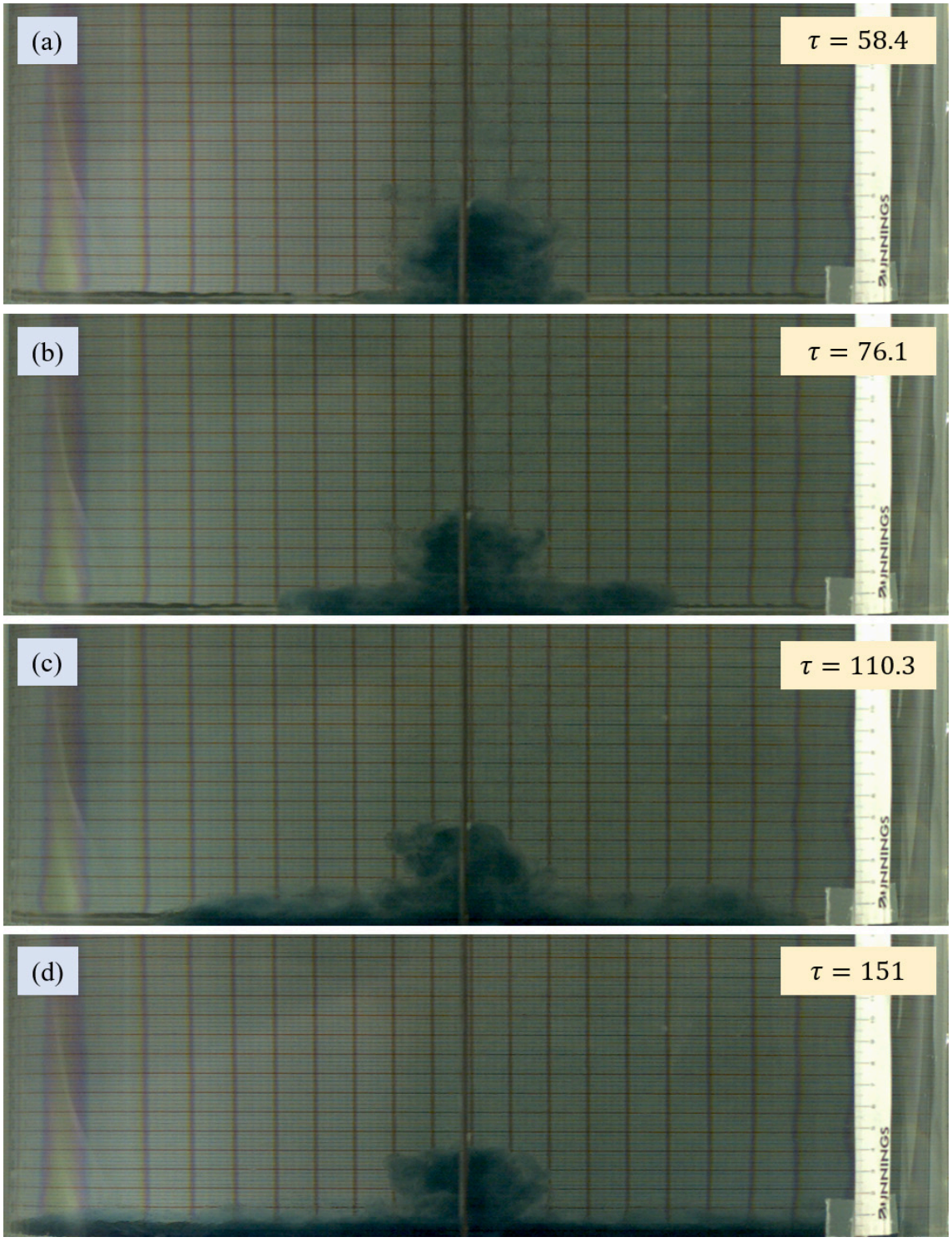

FIGURE 6.8: The images show the evolution of the confined round fountain of $Fr = 3.0$, $Re = 695$, $Pr = 7$ and $\lambda = 27.9$ over the duration of the intrusion flow: (a) at $\tau = 58.4$; (b) at $\tau = 76.1$; (c) at $\tau = 110.3$; (d) at $\tau = 151.0$.

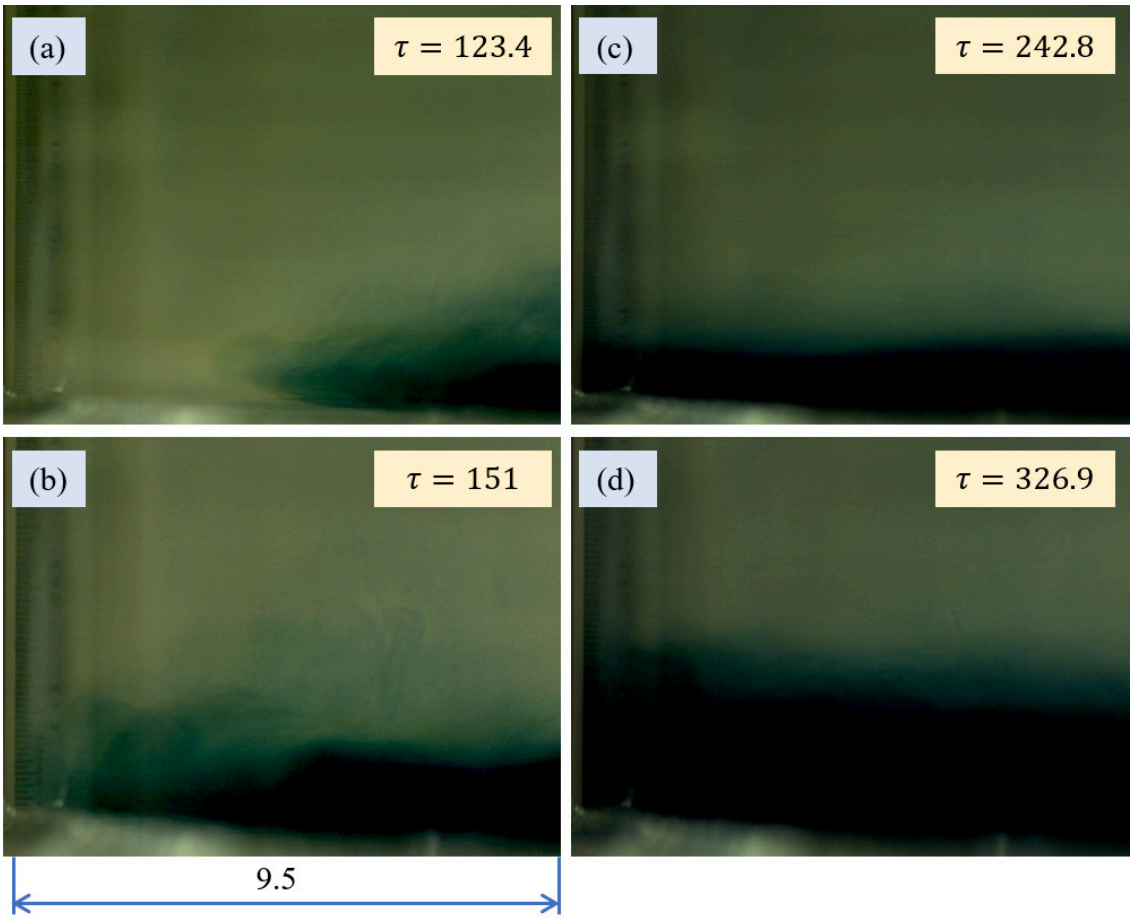

FIGURE 6.9: The images show the evolution of the confined round fountain of $Fr = 3.0$, $Re = 695$, $Pr = 7$ and $\lambda = 27.9$ over the duration of the wall fountain flow: (a) at $\tau = 119.5$; (b) at $\tau = 151.0$; (c) at $\tau = 242.8$; (d) at $\tau = 326.9$.

Figure 6.8 to Figure 6.10 present the snapshots of the flow of the intermediate round fountain of $Fr = 3.0$, $Re = 695$, $Pr = 7$ and $\lambda = 27.9$, to illustrate the evolution of the flow behavior of the fountain. Figure 6.8 shows the passage of the intrusion flow. As the intrusion flow spreads, the thickness of the intrusion decreases following a correlation $h_i \sim Fr\tau^{-1/2}$ as shown in [113]. This is apparently confirmed by the snapshots presented in Figure 6.8. After the intrusion flow reaches the sidewall, as shown in Figure 6.9, it impinges with the sidewall and forms a vertical wall fountain along the sidewall. After reaching a finite height, the wall fountain flow falls down and interacts with the intrusion flow and the ambient fluid to form the reversed flow which moves above the intrusion flow and towards the fountain source. The reversed flow results in the increase of the fountain penetration height.

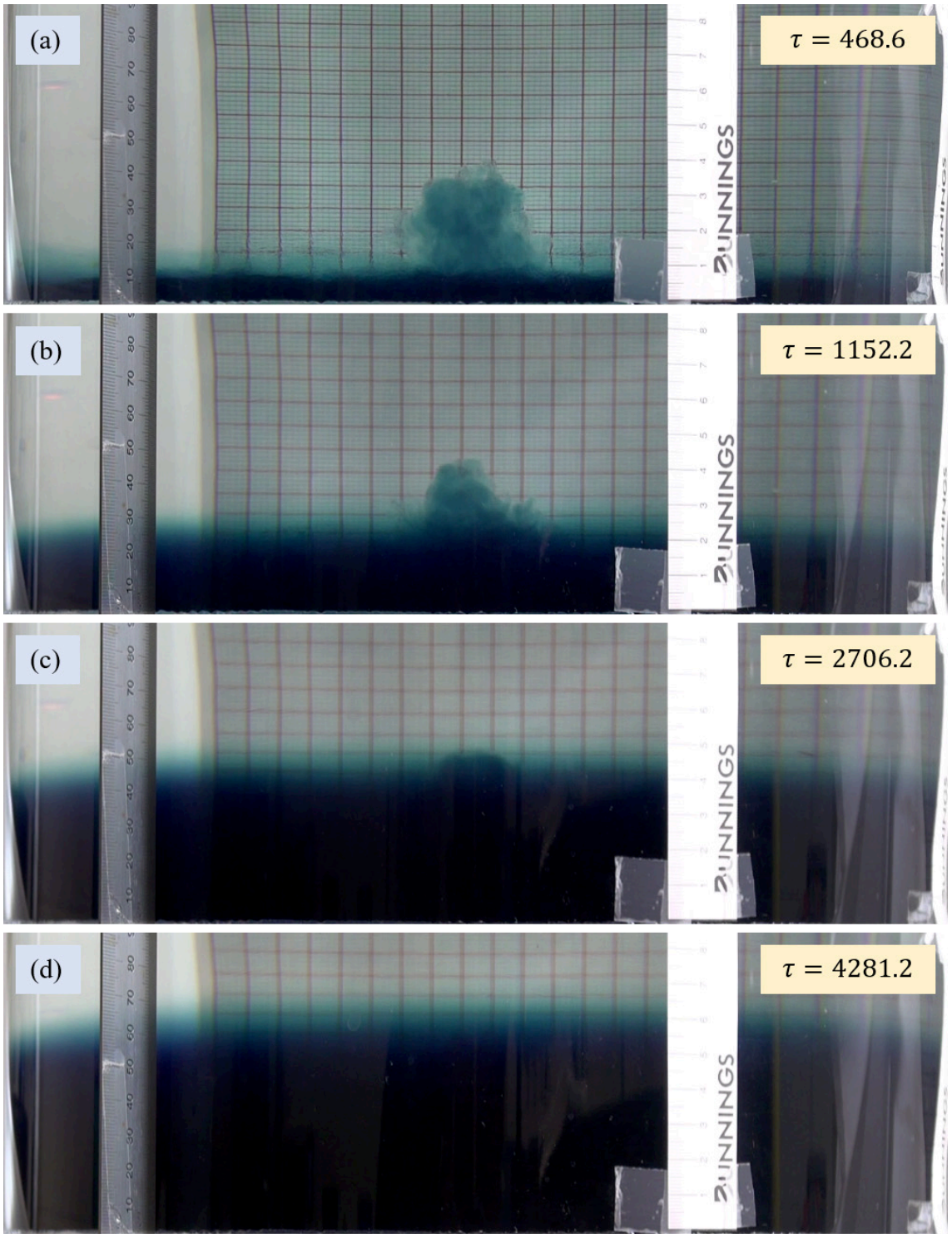

FIGURE 6.10: The images show the evolution of the confined round fountain of $Fr = 3.0$, $Re = 695$, $Pr = 7$ and $\lambda = 27.9$ over the duration of the reserved flow and stratification: (a) at $\tau = 468.6$; (b) at $\tau = 1152.2$; (c) at $\tau = 2706.2$; (d) at $\tau = 4281.2$.

Subsequently, the continuous fountain flow, intrusion flow, wall fountain flow and reversed flow collectively form the stratification. After a very long time of such flow,

a stratification will gradually establish in the domain and the fountain flow will be totally submerged within the stratified fluid. Such a development of stratification is clearly shown in the images presented in Figure 6.10.

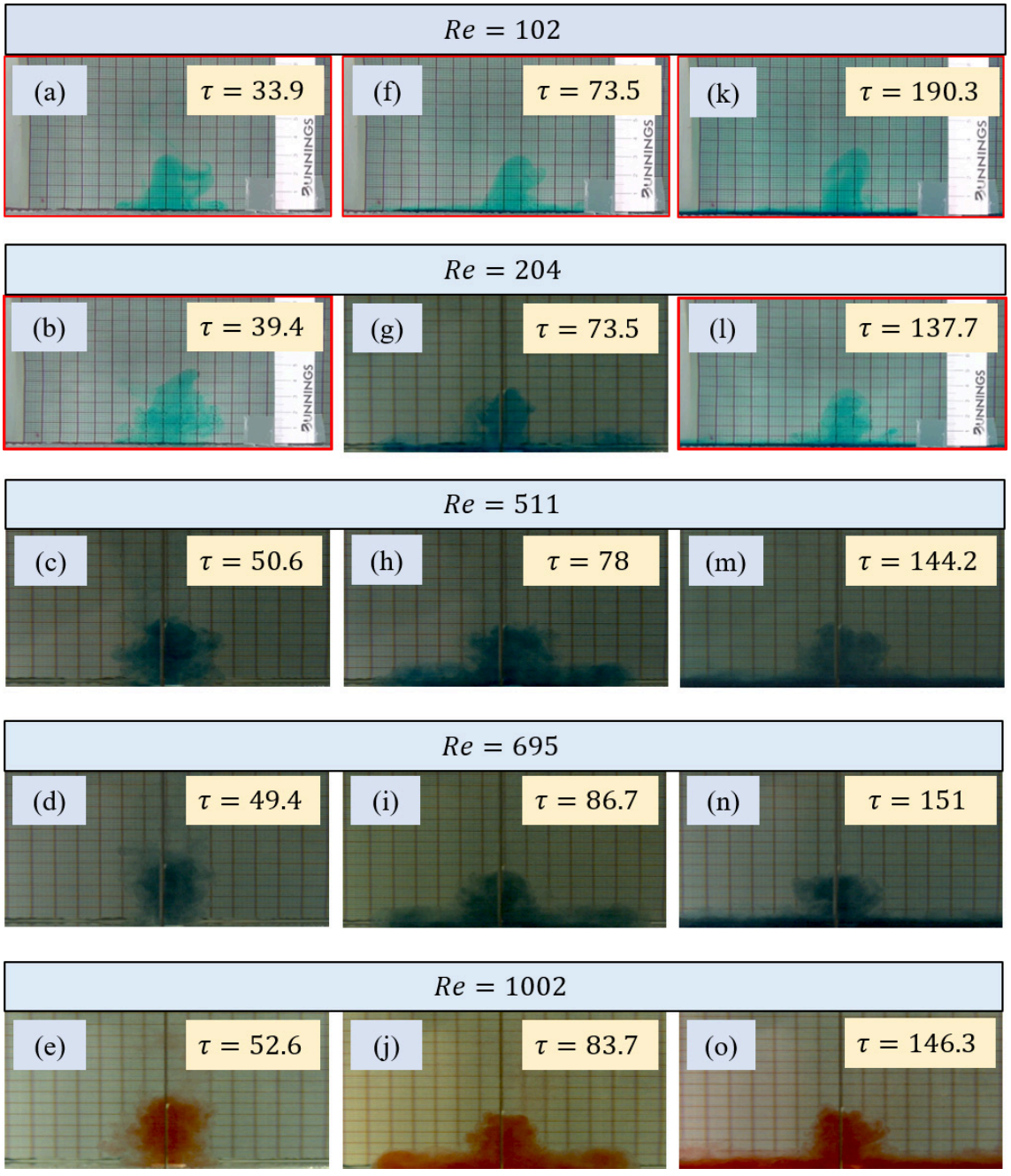

FIGURE 6.11: The images show the evolution of the intrusion flow for the fountain of $Fr = 3.0$, $Pr = 7$ and $\lambda = 27.9$ at: the first row, $Re = 102$; the second row, $Re = 204$; the third row, $Re = 511$; the fourth row, $Re = 695$; the fifth row, $Re = 1002$.

The influence of Re on the flow behavior of the confined intermediate round fountain of $Fr = 3.0$ is illustrated in Figure 6.11, where the snapshots of the central

region of the flow for the fountains of $Fr = 3.0$ and $\lambda = 27.9$ at five Re values (that is, Re = 102, 204, 511, 695 and 1002) over the duration of the intrusion flow are presented.

The snapshots in Figure 6.11(a)-(e) show the density field of the flow after the instant when the downflow of the fountain impinges with the bottom and the intrusion flow is creating, where the structure with an inner jet-like upflow and an annular downflow is identified. It is observed that both the upflow and downflow change from weak to forced turbulent with the increase of Re, and their interactions are also strengthened meanwhile. Although a flapping behavior is observed for the fountains of $Re = 102$ and 204, both the upflow and downflow behave in a laminar manner and the interaction is weak, allowing a quicker falling of the downflow to impinge with the bottom and creating the intrusion earlier, while the stronger interaction between the upflow and downflow for the fountains with $Re \gtrsim 500$ reduces the falling of the downflow. Hence, the time for the downflow to reach the bottom increases with increasing Re for $Re \lesssim 500$. But the counterpart time for fountains with $Re \gtrsim 500$ is similar as shown in Figure 6.11(c)-(e).

Figure 6.11(k)-(o) presents the flow when the intrusion front impinges with the sidewall. For the fountain of $Re \gtrsim 204$, the time for the intrusion front to reach the wall (τ_w) is essentially independent of Re, indicating that when the fountain is in turbulent regime, the influence of Re on τ_w is negligible. This is consistent with the numerical study. In such confined forced fountains, the intrusion flow is dominated by the wall-jet and/or buoyancy-inertial regime, where the intrusion front speed can be described by the correlation of $v_i \sim \tau^{-1/2}$ and $v_i \sim Fr^{-1/2}\tau^{-1/4}$, indicating little influence from Re. Then the earlier starting time of the intrusion for the fountain of $Re = 204$ than those of $Re \gtrsim 500$ results in a smaller τ_w. However, when Re is small ($Re = 102$), the flow is in the laminar regime, experiencing both the buoyancy-inertial and buoyancy-viscosity regimes. The intrusion speed for the buoyancy-viscosity regime follows the correlation of $v_i \sim Fr^{-1/4}Re^{1/8}\tau^{-1/2}$, resulting in a slower intrusion speed in the second-half spreading for the fountain of $Re = 102$.

Hence the fountain of $Re = 102$ takes a noticeably longer time for the intrusion front to reach the sidewall, although with the earliest formation of the intrusion.

Additionally, the results in the figure show that, in terms of the penetration height, the influence of Re is not significant, which is consistent with the prediction by the correlation of $z_m \sim Fr$ [2]. The thicknesses of the intrusion flow are similar for different Re values, *e.g.*, Figure 6.11(m)-(k), also indicating that the influence of Re on the intrusion flow thickness is minimal. However, it is observed that with the increase of Re, the fountain flow and its secondary flows become more turbulent. The results in Figure 6.11(a), (b), (f), (k) and (l) marked in red line are provided by the video camera, while the others are from the High-Speed Camera (The same as in the subsequent figures). This is because the recording capacity of the High-Speed Camera under the current setting is 17.466 seconds, thus only a short evolution of the flow can be captured. What should be noted here is that errors need to be considered in processing the contour and calculating the dimensionless time when the images are from different camera sources.

6.4.1.2 The evolution of the confined forced round fountain of $Fr = 5.0$ and 8.0

To illustrate the evolution of the flow behavior of confined forced turbulent fountains, two such fountains, *i.e.*, the fountain of $Fr = 5.0$, $Re = 695$, $Pr = 7$ and $\lambda = 27.9$, and the fountain of $Fr = 8.0$, $Re = 1502$, $Pr = 7$ and $\lambda = 48.75$, are selected as examples. The images obtained experimentally showing the evolution of the flow behavior of such confined forced turbulent fountains and the Re influence are presented in Figure 6.12 to Figure 6.19. For the $Fr = 5.0$ fountain, as shown in Figure 6.12(b)-(d), the intrusion thickness is significantly thicker than its counterpart of the intermediate fountains of $Fr = 3.0$, which is in agreement with the correlation of $h_i \sim Fr\tau^{-1/2}$ [113]. However, different from the fountain of $Fr = 3.0$, there is no decrease observed in the intrusion thickness with time. This is because

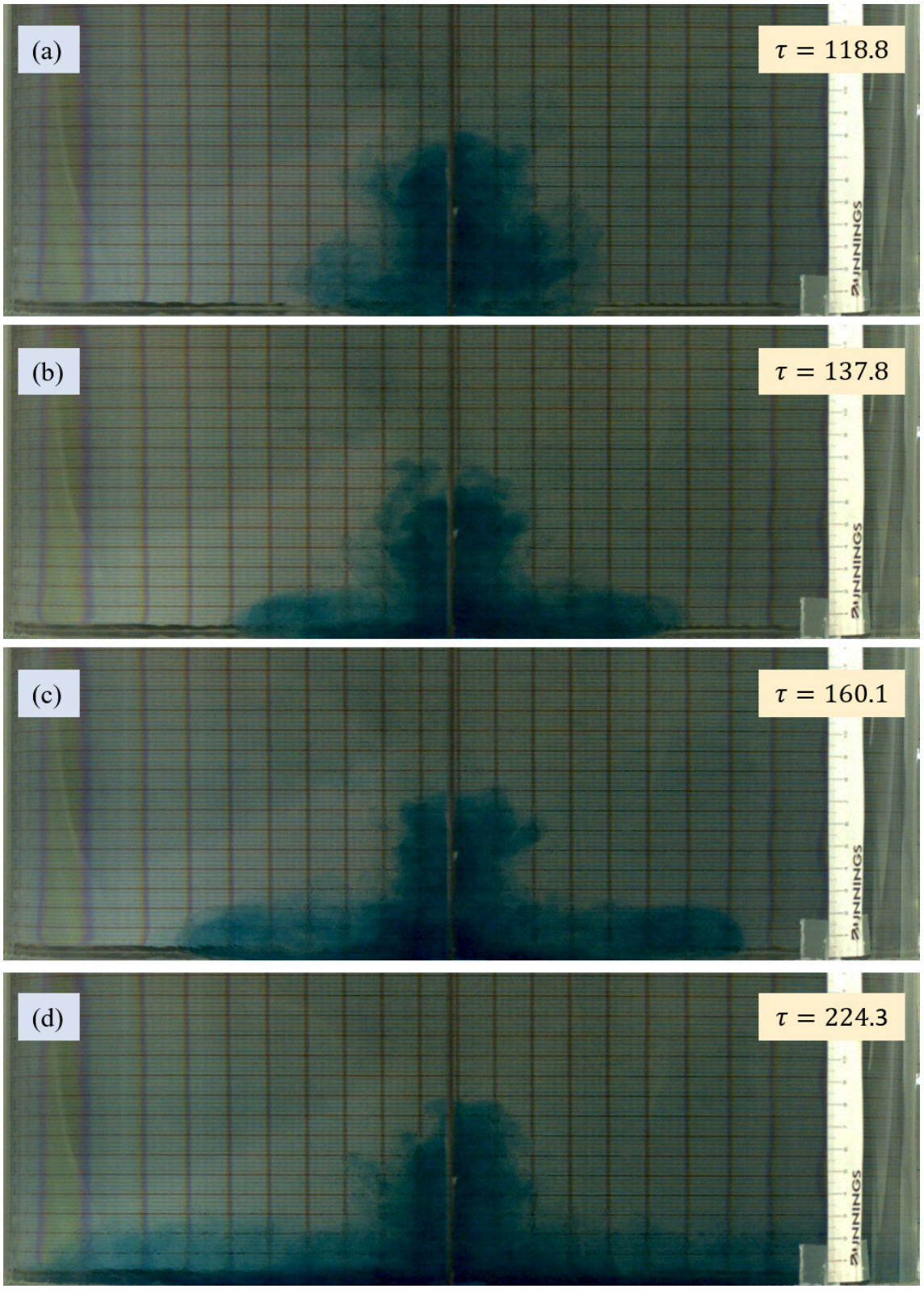

FIGURE 6.12: The images show the evolution of the confined round fountain of $Fr = 5.0$, $Re = 695$, $Pr = 7$ and $\lambda = 27.9$ over the duration of the intrusion flow: (a) at $\tau = 118.8$; (b) at $\tau = 137.8$; (c) at $\tau = 160.1$; (d) at $\tau = 224.3$.

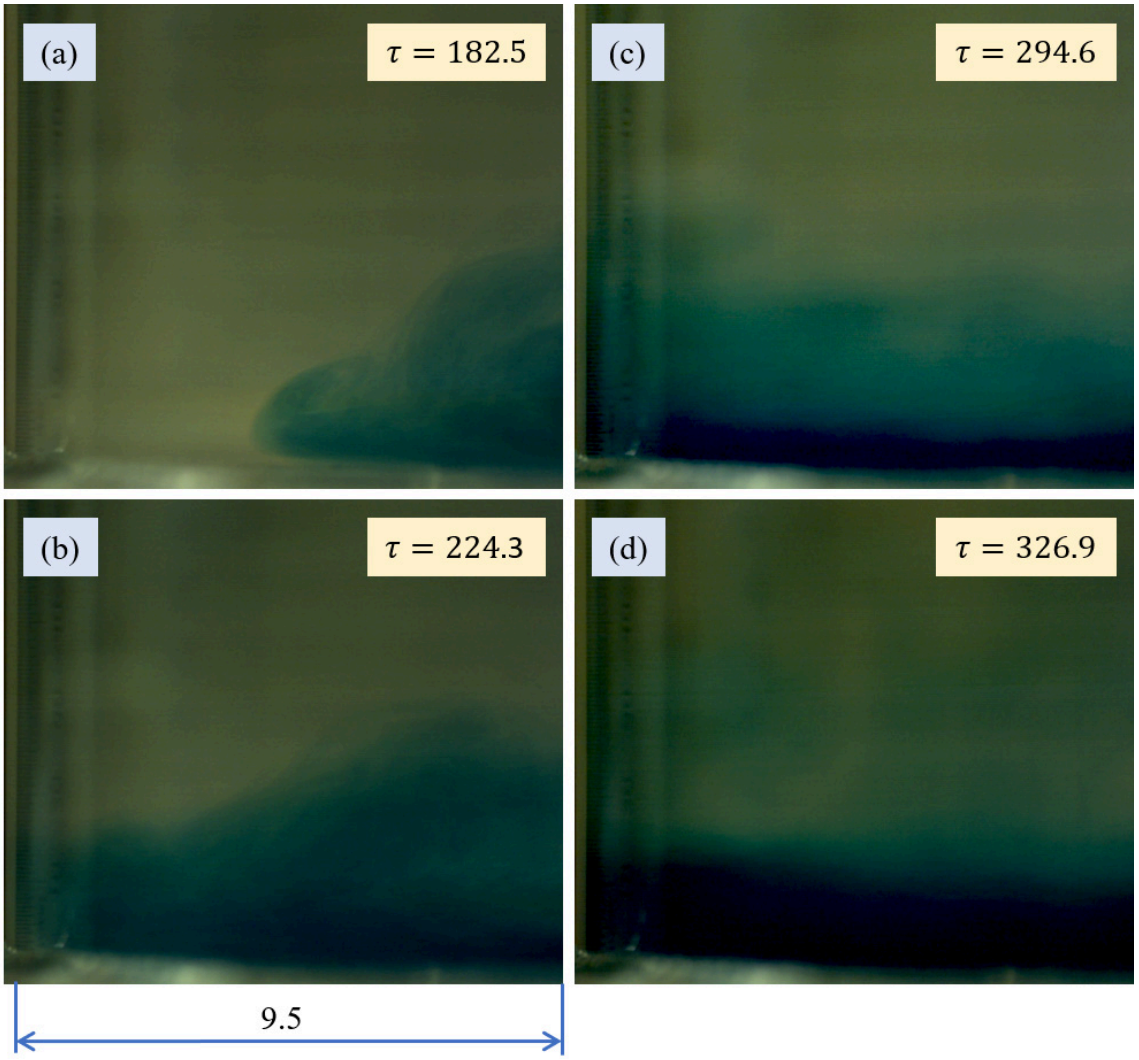

FIGURE 6.13: The images show the evolution of the confined round fountain of $Fr = 5.0$, $Re = 695$, $Pr = 7$ and $\lambda = 27.9$ over the duration of the wall fountain flow: (a) at $\tau = 182.5$; (b) at $\tau = 224.3$; (c) at $\tau = 294.6$; (d) at $\tau = 326.9$.

the strengthened effect of convection and diffusion with increasing Fr contributes to the entrainment of the ambient fluid into the intrusion flow during the spreading, particularly in the intrusion head region, resulting in a constant or even increasing thickness presented in the figure. Figure 6.12(a) shows that it takes significant longer time for the downflow of the fountain of $Fr = 5.0$ than that of the fountain of $Fr = 3.0$ to impinge with the bottom, due to a more turbulent and higher penetration height of the fountain flow. It is observed that the intrusion flow of the fountain of $Fr = 5.0$ is slower than that of the fountain of $Fr = 3.0$ to impinge with

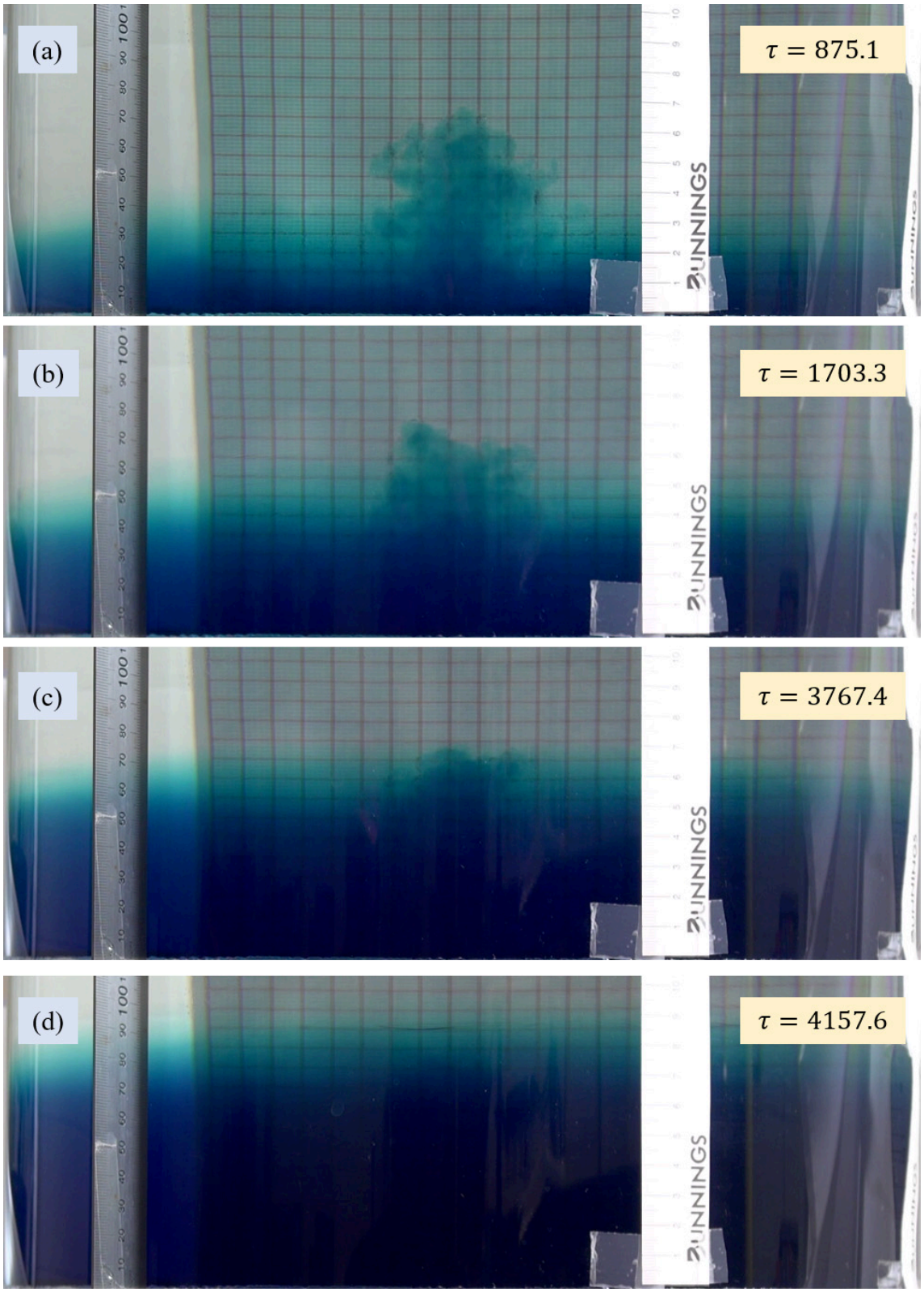

FIGURE 6.14: The images show the evolution of the confined round fountain of $Fr = 5.0$, $Re = 695$, $Pr = 7$ and $\lambda = 27.9$ over the duration of the reserved flow and stratification: (a) at $\tau = 875.1$; (b) at $\tau = 1703.3$; (c) at $\tau = 3767.4$; (d) at $\tau = 4157.6$.

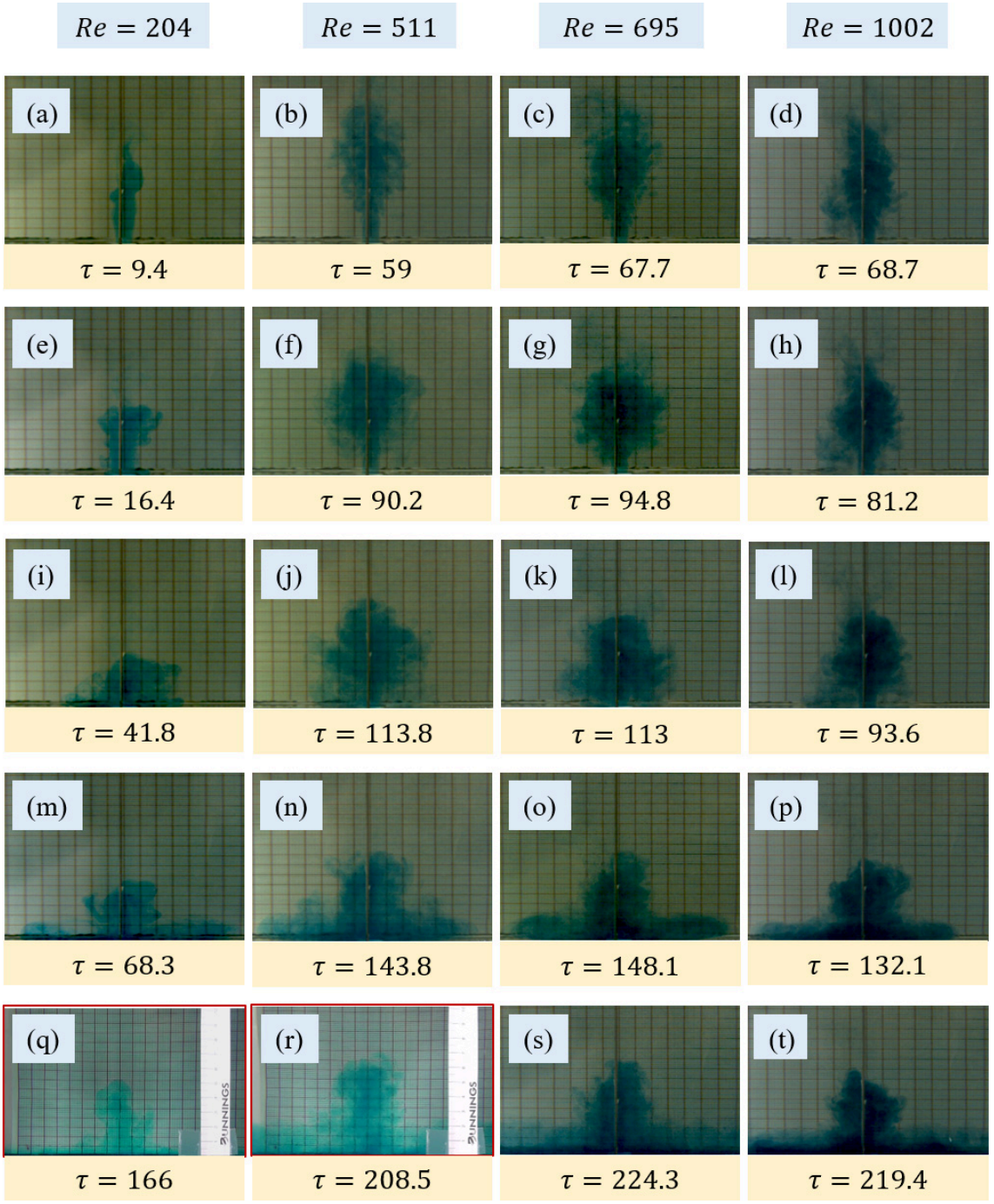

FIGURE 6.15: The images shown the evolution of the intrusion flow for the fountain of $Fr = 5.0$, $Pr = 7$ and $\lambda = 27.9$ at: the first column, $Re = 204$; the second column, $Re = 511$; the third column, $Re = 695$; the fourth column, $Re = 1002$.

sidewall, which again confirms the correlation of $v_i \sim Fr^{-1/2}\tau^{-1/4}$. After the intrusion impinges with the sidewall, a wall fountain structure (overturning) is observed, as shown in Figure 6.13. With the increasing time, a two-layer structure fountain is

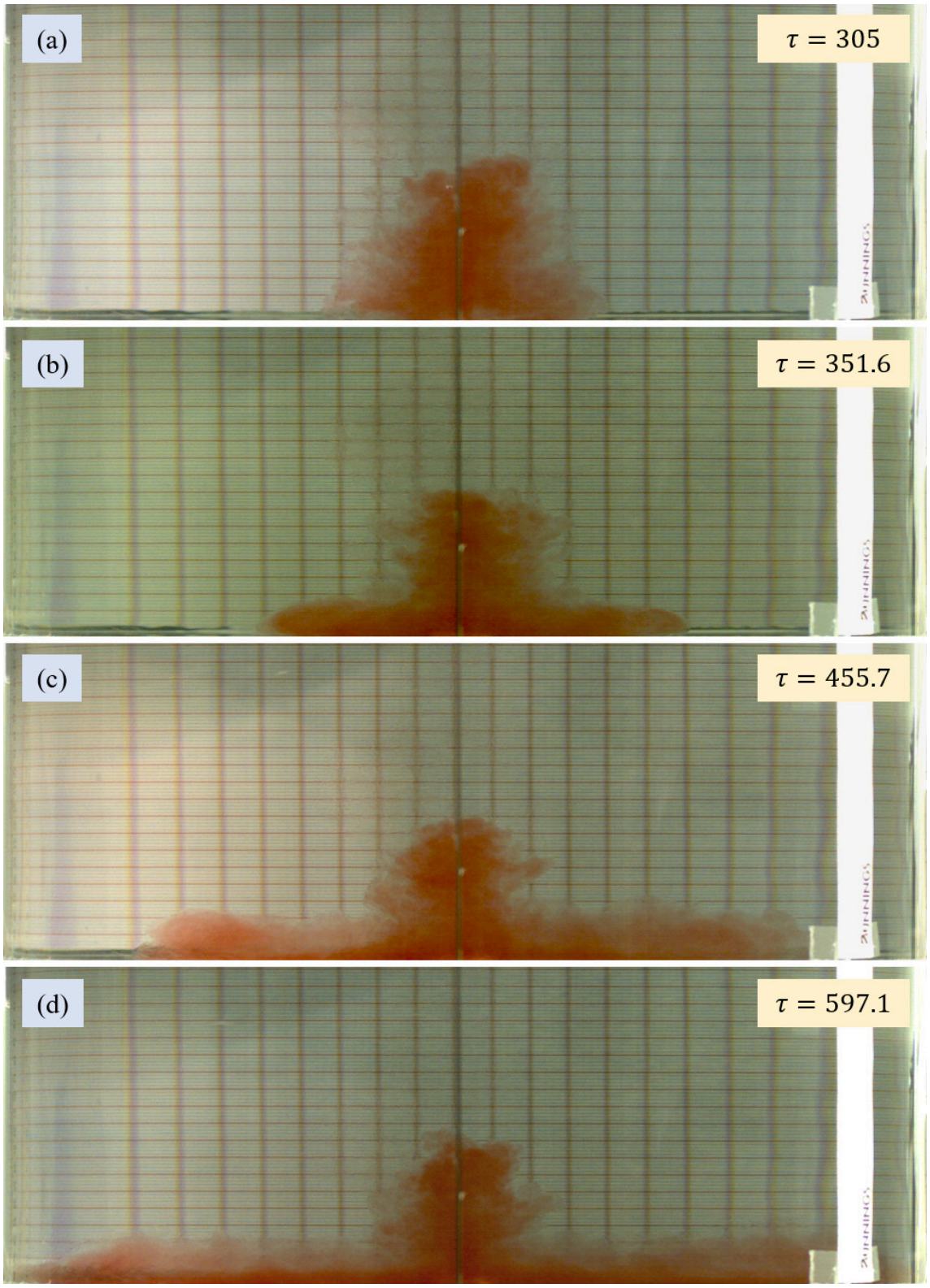

FIGURE 6.16: The images show the evolution of the confined round fountain of $Fr = 8.0$, $Re = 1502$, $Pr = 7$ and $\lambda = 48.75$ over the duration of the intrusion flow: (a) at $\tau = 305$; (b) at $\tau = 351.6$; (c) at $\tau = 455.7$; (d) at $\tau = 597.1$.

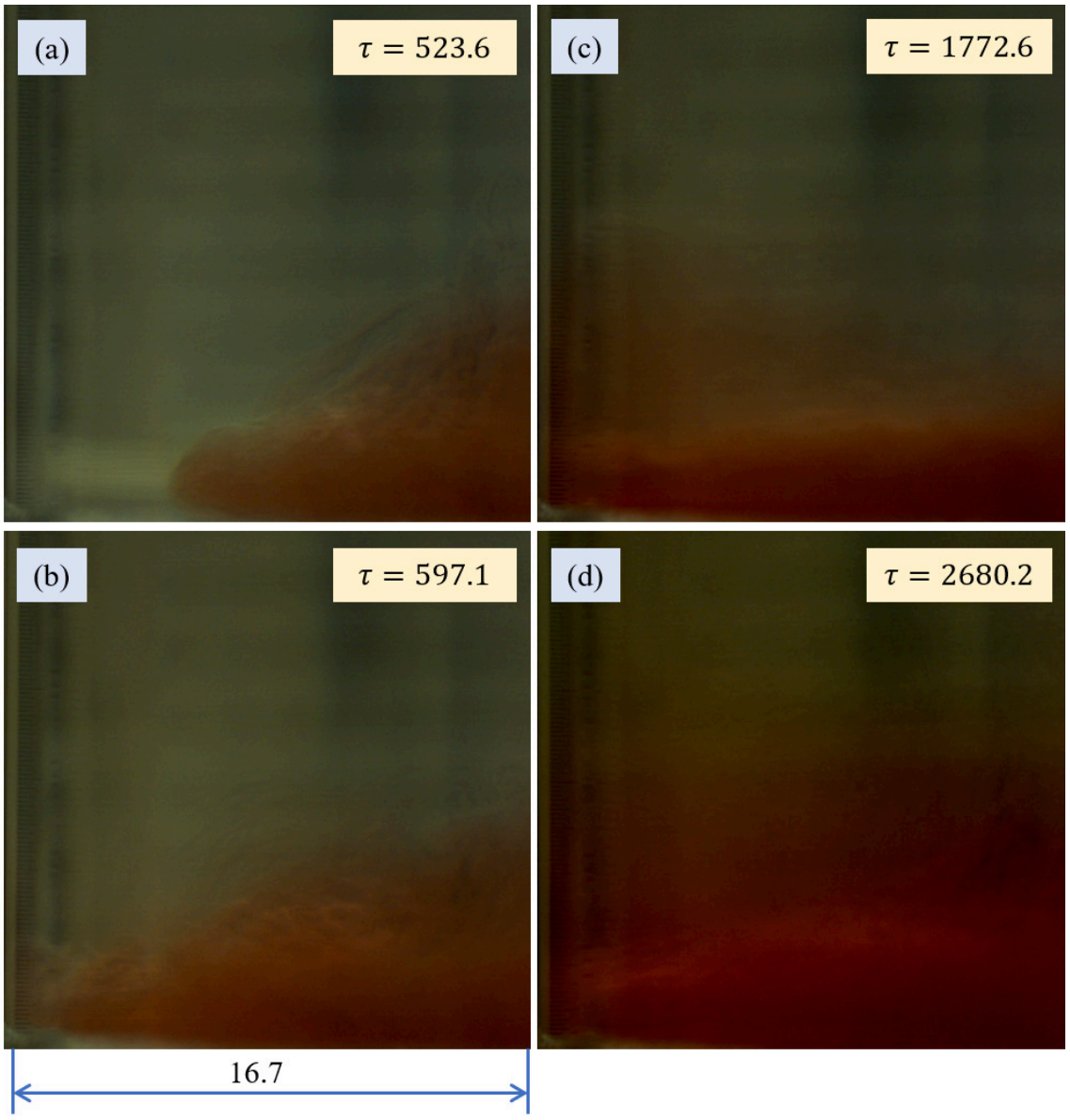

FIGURE 6.17: The images show the evolution of the confined round fountain of $Fr = 8.0$, $Re = 1502$, $Pr = 7$ and $\lambda = 48.75$ over the duration of the wall fountain flow: (a) at $\tau = 523.6$; (b) at $\tau = 597.1$; (c) at $\tau = 1772.6$; (d) at $\tau = 2680.2$.

clearly observed and the interaction between the fountain and secondary flows becomes stronger. With the density stratification gradually formed in the container, a higher penetration of the fountain is presented, as shown in Figure 6.14.

Similar to the $Fr = 3.0$ fountains, the fountain of $Fr = 5.0$ at $Re = 204$ shows laminar behavior, *e.g.*, flapping, with the much earlier impingement of the downflow with the bottom and the intrusion with the sidewall than that for the fountain of

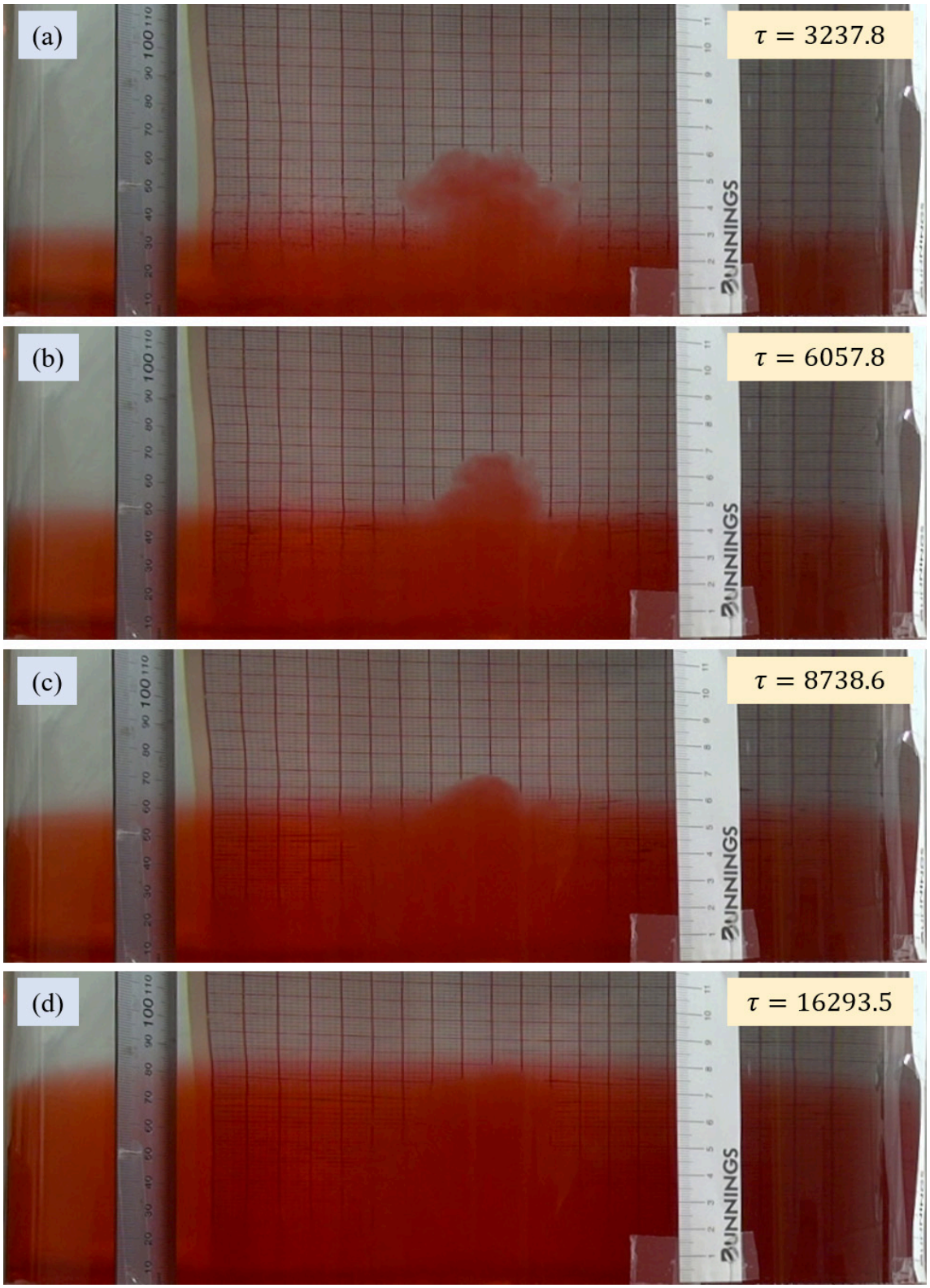

FIGURE 6.18: The images show the evolution of the confined round fountain of $Fr = 8.0$, $Re = 1502$, $Pr = 7$ and $\lambda = 48.75$ over the duration of the reserved flow and stratification: (a) at $\tau = 3237.8$; (b) at $\tau = 6057.8$; (c) at $\tau = 8738.6$; (d) at $\tau = 16293.5$.

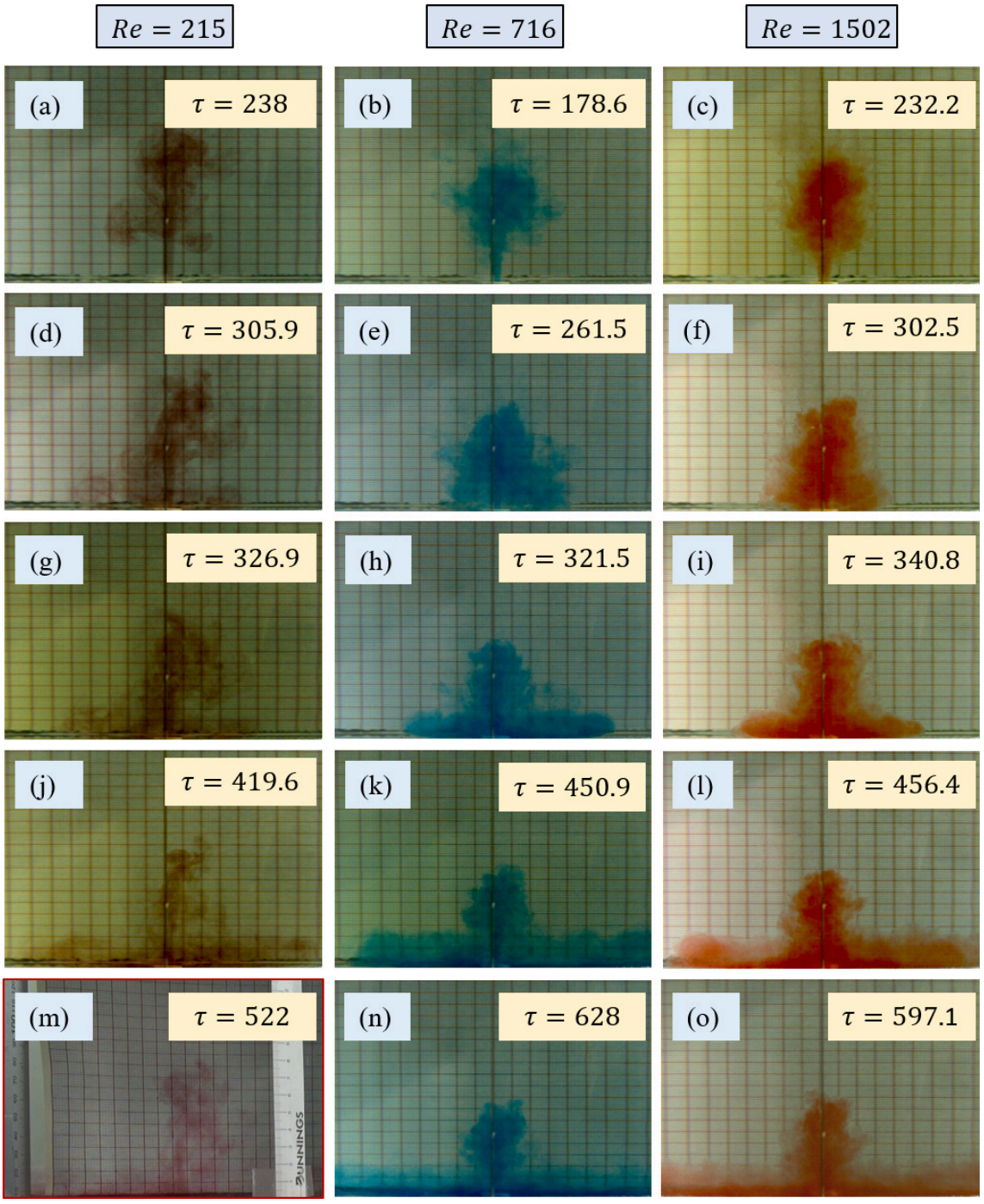

FIGURE 6.19: The images show the evolution of the intrusion flow for the fountain of $Fr = 8.0$, $Pr = 7$ and $\lambda = 48.75$ at: the left column, $Re = 204$; the middle column, $Re = 716$; the right column, $Re = 1502$.

$Re \gtrsim 511$, as shown in Figure 6.15(i)-(l). While, with the increase of $Re \gtrsim 511$, both the fountain and its secondary flows behave more turbulent. The influence of Re on the intrusion of such confined forced turbulent fountains is minimal, as illustrated in

Figure 6.15, where it is seen that the penetration height of the fountain, the intrusion thickness and τ_w are not influenced noticeably by Re, which further confirms the correlations of $z_m \sim Fr$ and $h_i \sim Fr\tau^{-1/2}$.

Another example presented here is the confined forced turbulent round fountain of $Fr = 8.0$. Figure 6.16 to Figure 6.18 present the images to show the evolution of the fountain of $Fr = 8.0$ with $Re = 1502$, $Pr = 7$ and $\lambda = 48.75$, and Figure 6.19 shows the flow behavior of the $Fr = 8.0$ fountains at $Re = 215$, 715 and 1502 over the duration of the intrusion flow. The results presented in these figures clearly show that the similar conclusions about the behavior of these confined forced turbulent fountains and influence of Re can be made, but the fountain flows and the secondary flows become more turbulent.

6.4.1.3 The influence of Fr

To illustrate the influence of Fr on the flow behavior of confined forced turbulent fountains, Figure 6.20 and Figure 6.21 present the images of the confined fountain flows of five Fr values (*i.e.*, Fr = 1.0, 1.5, 2.0, 3.0, and 5.0) at Re = 204 and Re = 511 with Pr = 7 and λ = 27.9. It is clearly seen that the fountain flow changes from the laminar behavior to the turbulent behavior with the increase of Fr.

The first row of these figures shows the flows when the intrusion front impinges with the sidewall, where it is observed that both the penetration height of the fountain flow and the thickness of the intrusion flow increase with Fr, which is consistent with the related previous studies [2, 113]. Additionally, the time for the intrusion to impinge with the sidewall increases with increasing Fr. After the impingement of the intrusion with the sidewall, a wall fountain structure is formed. Then a reversed flow moves backward to and interacts with the fountain flow, as presented in Figure 6.20(f)-(j) and Figure 6.21(f)-(j), where the interaction is strengthened with the increase of Fr. A sharper interface is observed for the fountain of decreasing Fr

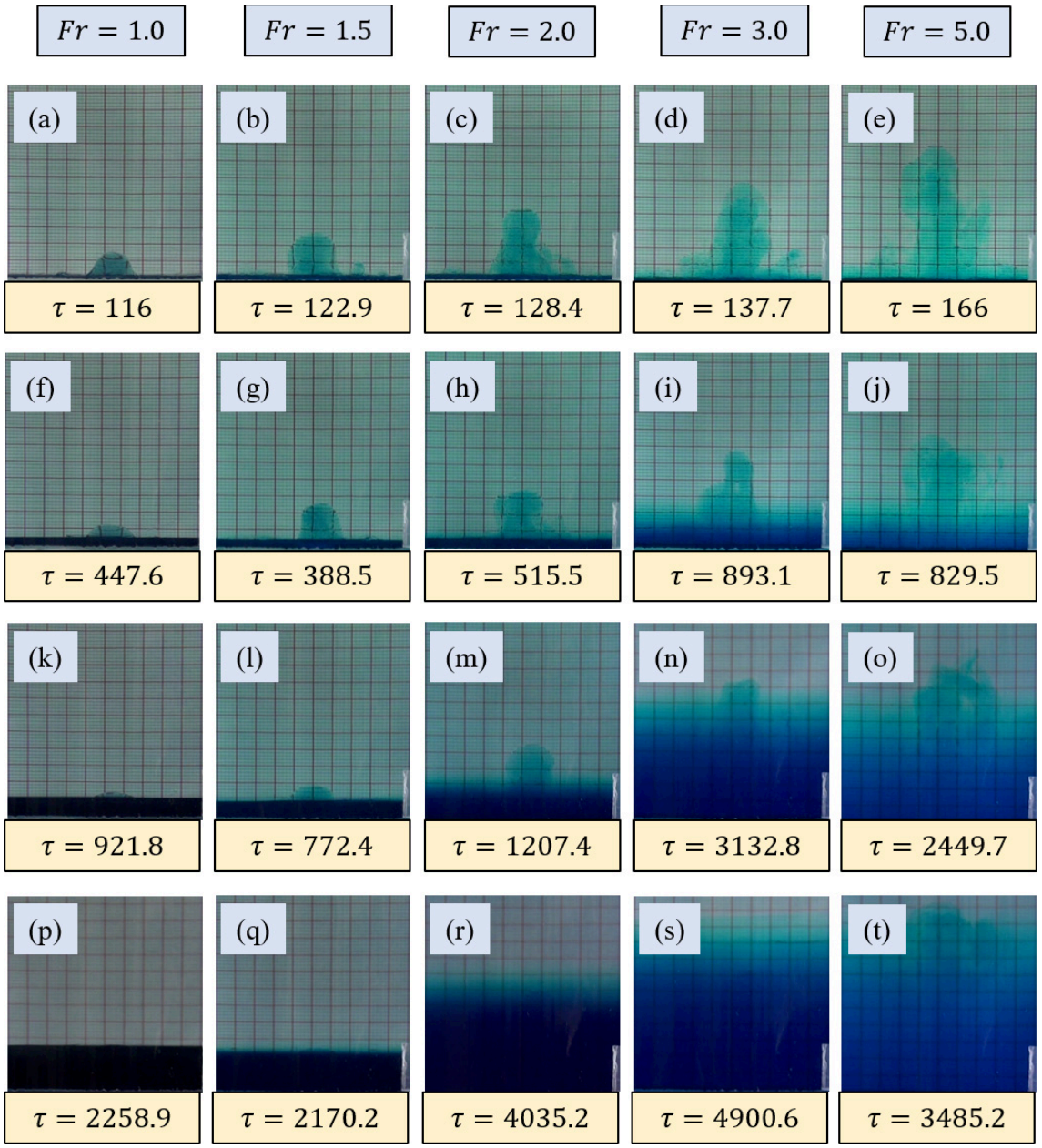

FIGURE 6.20: The images show the evolution of the filling flow for the confined fountain of $Re = 204$, $Pr = 7$ and $\lambda = 27.9$ with: the first column, $Fr = 1.0$; the second column, $Fr = 1.5$; the third column, $Fr = 2.0$; the fourth column, $Fr = 3.0$; the fifth column, $Fr = 5.0$.

between the fountain / its secondary flows and the ambient fluid, due to the reducing effect of diffusion. Moreover, the decreasing Fr also slows down the development rate of the stratification, which is consistent with the numerical results presented in the previous chapter.

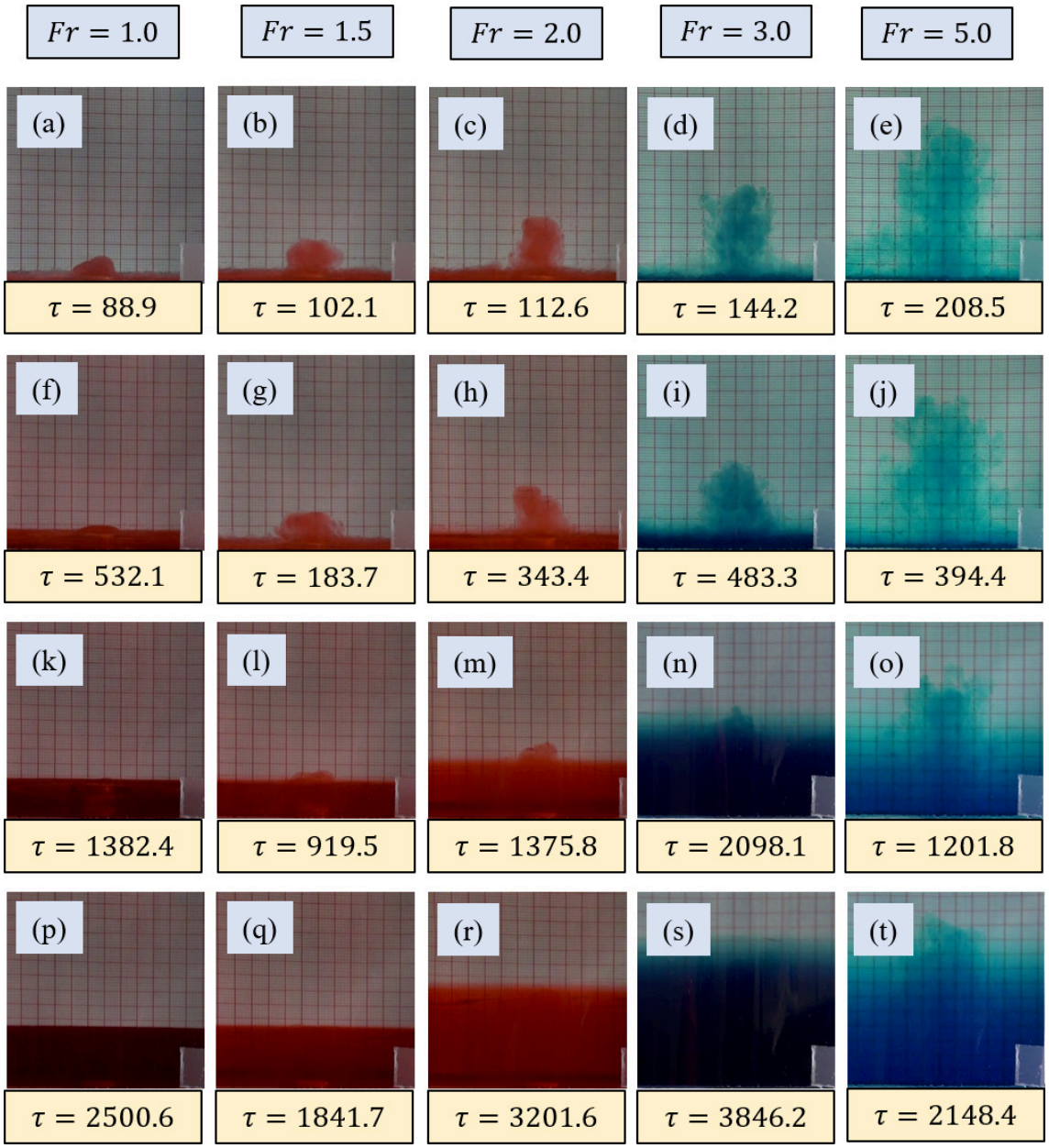

FIGURE 6.21: The images show the evolution of the filling flow for the confined fountain of $Re = 511$, $Pr = 7$ and $\lambda = 27.9$ with: the first column, $Fr = 1.0$; the second column, $Fr = 1.5$; the third column, $Fr = 2.0$; the fourth column, $Fr = 3.0$; the fifth column, $Fr = 5.0$.

6.4.2 Quantitative analysis

Similarly to the numerical studies carried out in the previous two chapters, the experimental results for the confined intermediate and forced turbulent fountains are analyzed quantitatively. The quantitative analysis focuses on the characteristic

time-scale for the intrusion front to impinge with the sidewall (*i.e.*, τ_w) and the development rate of the density stratification (*i.e.*, v_s) and in particular the quantified influence of Fr, Re and λ.

6.4.2.1 Time-scale for the intrusion front impinging the sidewall

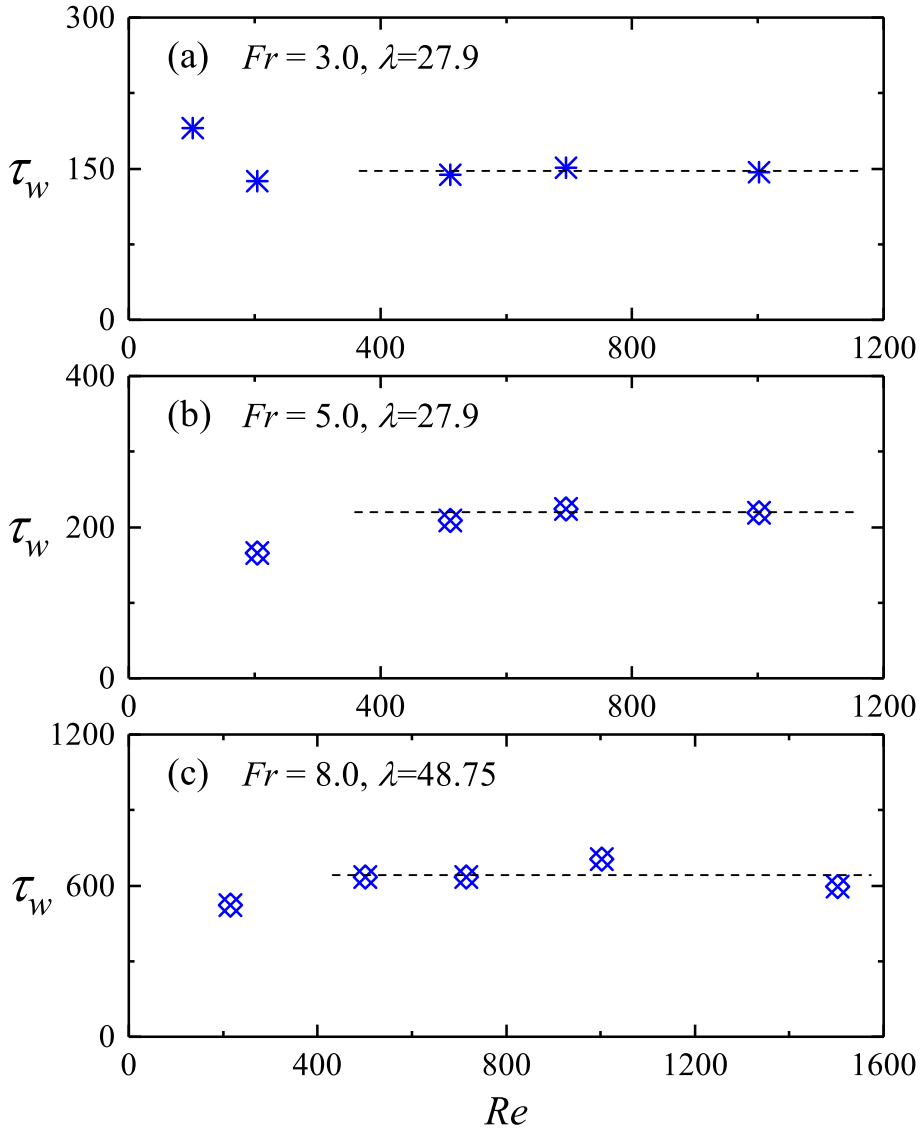

FIGURE 6.22: (a) τ_w for the fountains of $Fr = 3.0$, $Pr = 7$ and $\lambda = 27.9$ at $Re = 102$, 204, 511, 695 and 1002; (b) τ_w for the fountains of $Fr = 5.0$, $Pr = 7$ and $\lambda = 27.9$ at $Re = 204$, 511, 695 and 1002; (c) τ_w for the fountains of $Fr = 8.0$, $Pr = 7$ and $\lambda = 48.75$ at $Re = 215$, 501, 715, 1002 and 1502.

Figure 6.22 presents τ_w for the fountains of $Fr = 3.0$, 5.0 and 8.0 at several different Re values. As shown in Figure 6.22(a), τ_w is significantly longer for $Re = 102$, since the intrusion front speed slows down in the buoyancy-viscosity regime. While from $Re = 204$, the intrusion flow is dominated by the wall-jet and/or buoyancy-inertial regime, where the intrusion front speed can be described by the correlation of $v_i \sim \tau^{-1/2}$ and $v_i \sim Fr^{-1/2}\tau^{-1/4}$, indicating little influence from Re. Hence, τ_w is essentially independent of Re. Notably, smaller τ_w for the fountain of $Re = 204$ than those of $Re \gtrsim 500$ is resulted from its earlier formation, as discussed in § 6.4.1.1. Similarly, such results are also obtained for higher Fr values, at $Fr = 5.0$ and 8.0, as shown in Figure 6.22(b) and in Figure 6.22(c).

To illustrate the influence of Fr, τ_w for the fountains of various Fr values at four Re values (Re=204, 511, 1002 and 1502) is presented in Figure 6.23. For fountains of $Re = 204$, $Fr = 2.0$ is identified as the critical value to distinguish the influence of Fr into two regimes, as shown in Figure 6.23(a), where τ_w follows linear correlations with Fr within both regimes, as quantified as follows,

$$\tau_w = \begin{cases} 12.4Fr + 103.8, & 1.0 \leq Fr \leq 2.0, \\ 12.8Fr + 101.5, & 2.0 \leq Fr \leq 3.0, \end{cases} \tag{6.1}$$

with the regression constants of $R^2 = 0.996$ and 0.991, respectively, which are similar to the numerical results obtained in the previous chapter.

Similarly, as shown in Figure 6.23(b), τ_w for the fountains of $Re = 511$ and $\lambda = 27.9$ with various Fr also shows two different linear correlations in two individual regimes, quantified as follows,

$$\tau_w = \begin{cases} 32Fr + 48.5, & 1.0 \leq Fr \leq 2.0, \\ 23.7Fr + 65.7, & 2.0 \leq Fr \leq 5.0, \end{cases} \tag{6.2}$$

with the regression constants of $R^2 = 1.0$ and 0.996, respectively.

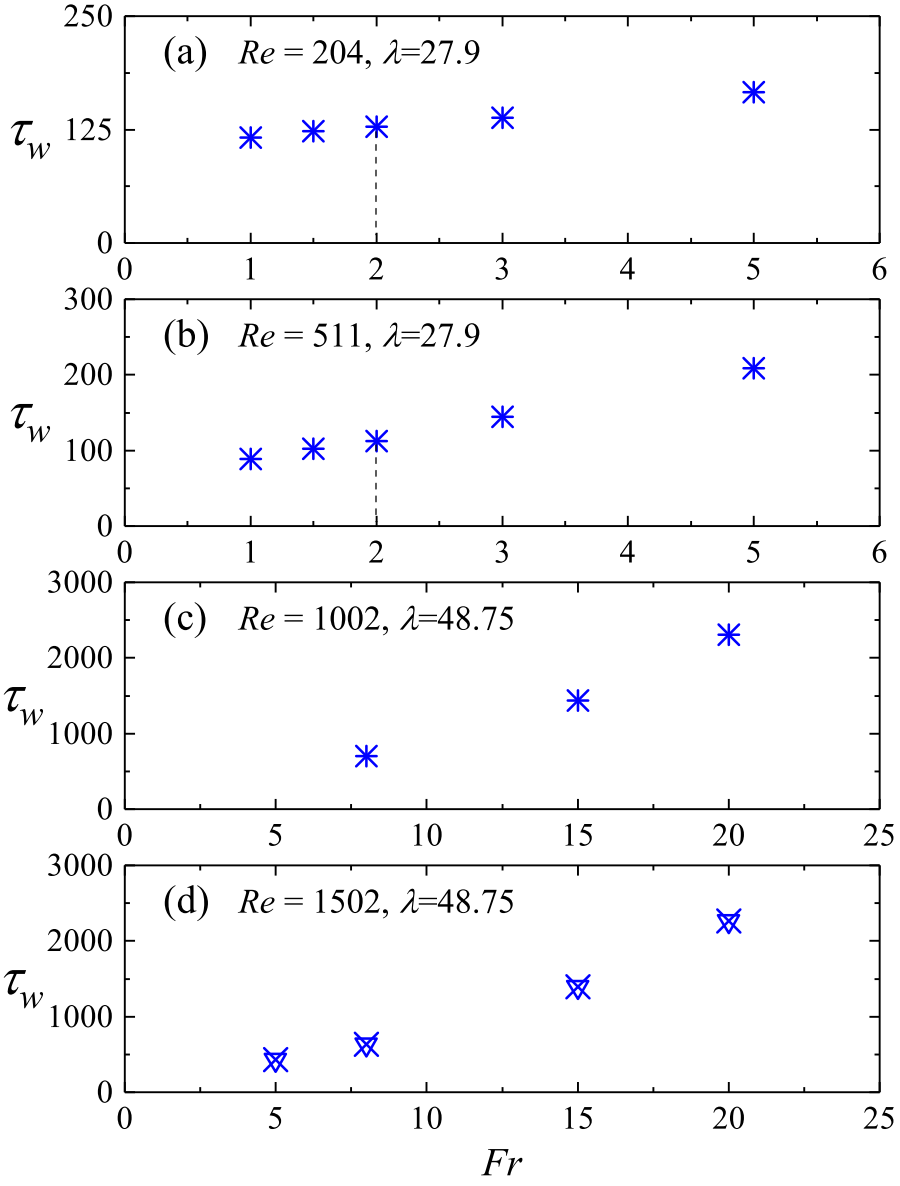

FIGURE 6.23: (a) τ_w for the fountain of $Re = 204$, $Pr = 7$ and $\lambda = 27.9$, with $Fr = 1.0$, 1.5, 2.0, 3.0 and 5.0; (b) τ_w for the fountain of $Re = 511$, $Pr = 7$ and $\lambda = 27.9$, with $Fr = 1.0$, 1.5, 2.0, 3.0 and 5.0; (c) τ_w for the fountain of $Re = 1002$, $Pr = 7$ and $\lambda = 48.74$, with $Fr = 8.0$, 15.0 and 20.0; (d) τ_w for the fountain of $Re = 1502$, $Pr = 7$ and $\lambda = 48.75$, with $Fr = 5.0$, 8.0, 15.0 and 20.0;

At larger Re values ($Re = 1002$ and 1502), a power law correlation is obtained to quantify the influence of Fr on τ_w at both Re values (*i.e.*, independent of Re), as shown in Figure 6.23(c)-(d), with the following quantified correlation,

$$\tau_w = 57.3Fr^{1.23} - 70.7, \tag{6.3}$$

where $R^2 = 0.986$.

A similar discussion is also done to study the influence of λ on τ_w. Figure 6.24 presents τ_w for the fountains of $Fr = 5.0$, $Re \approx 500$ with $\lambda = 27.9$, 32.5, 39 and 48.75 and the fountains of $Fr = 8.0$, $Re = 1002$ with $\lambda = 32.5$, 39 and 48.75. Two power law correlations are obtained to quantify the influence of λ on τ_w, as shown below,

$$\tau_w = \begin{cases} 2.28\lambda^{1.35} + 4.28, & Fr = 3.0, Re \approx 500, \\ 3.75\lambda^{1.35} - 17.71, & Fr = 8.0, Re = 1002, \end{cases} \tag{6.4}$$

with the regression constants of $R^2 = 0.987$ and 0.981, respectively.

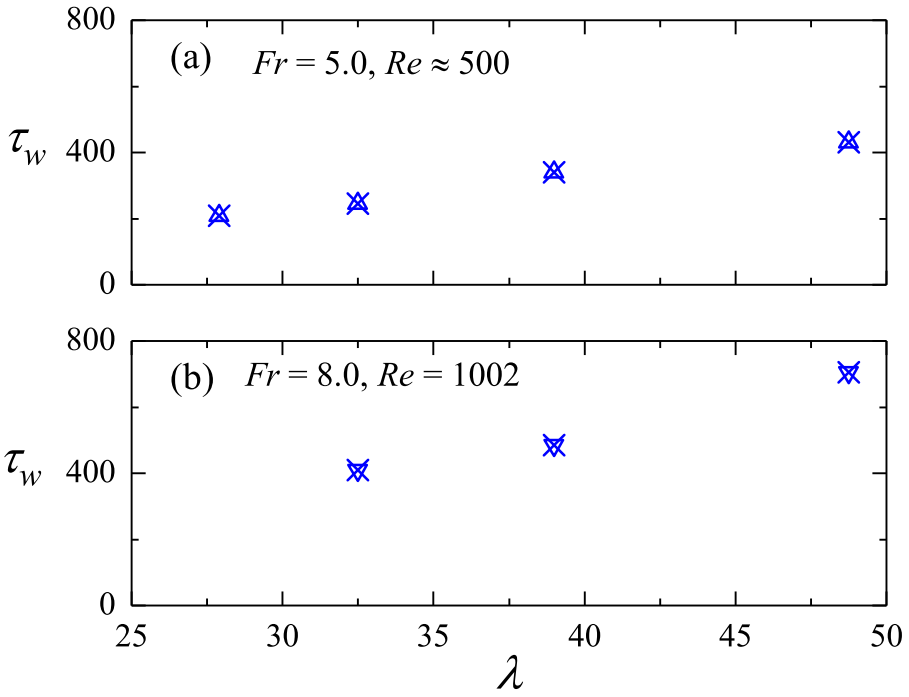

FIGURE 6.24: (a) τ_w for the fountain of $Fr = 5.0$, $Re \approx 500$ and $Pr = 7$, with $\lambda = 27.9$, 32.5, 39 and 48.75; (b) τ_w for the fountain of $Fr = 8.0$, $Re = 1002$ and $Pr = 7$, with $\lambda = 32.5$, 39 and 48.75;

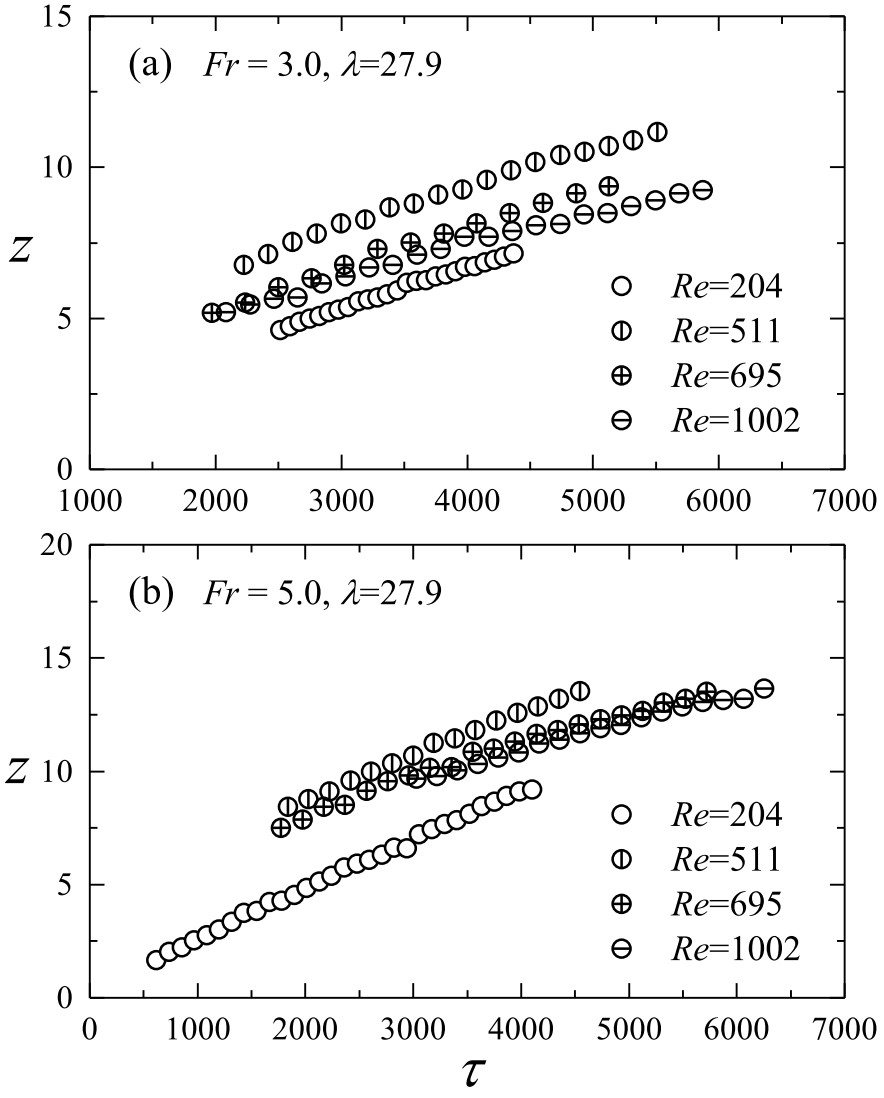

FIGURE 6.25: The time series of the stratification height projected on the sidewall for the fountains of (a) $Fr = 3.0$, $Pr = 7$ and $\lambda = 27.9$, with $Re = 204$, 511, 695 and 1002, and (b) $Fr = 5.0$, $Pr = 7$ and $\lambda = 27.9$ with $Re = 204$, 511, 695 and 1002.

6.4.2.2 The time series of stratified surface and the development rate of stratification

Since the cameras can only capture the bulk behavior of the fountain and its secondary flows projected onto the sidewall in front, the time-dependent profile of the stratification level in the video may be the maximum value of the wall fountain or the stratified surface for the corresponding time instant. Hence, to illustrate the development of the stratification, the experiment cases were run long enough to allow

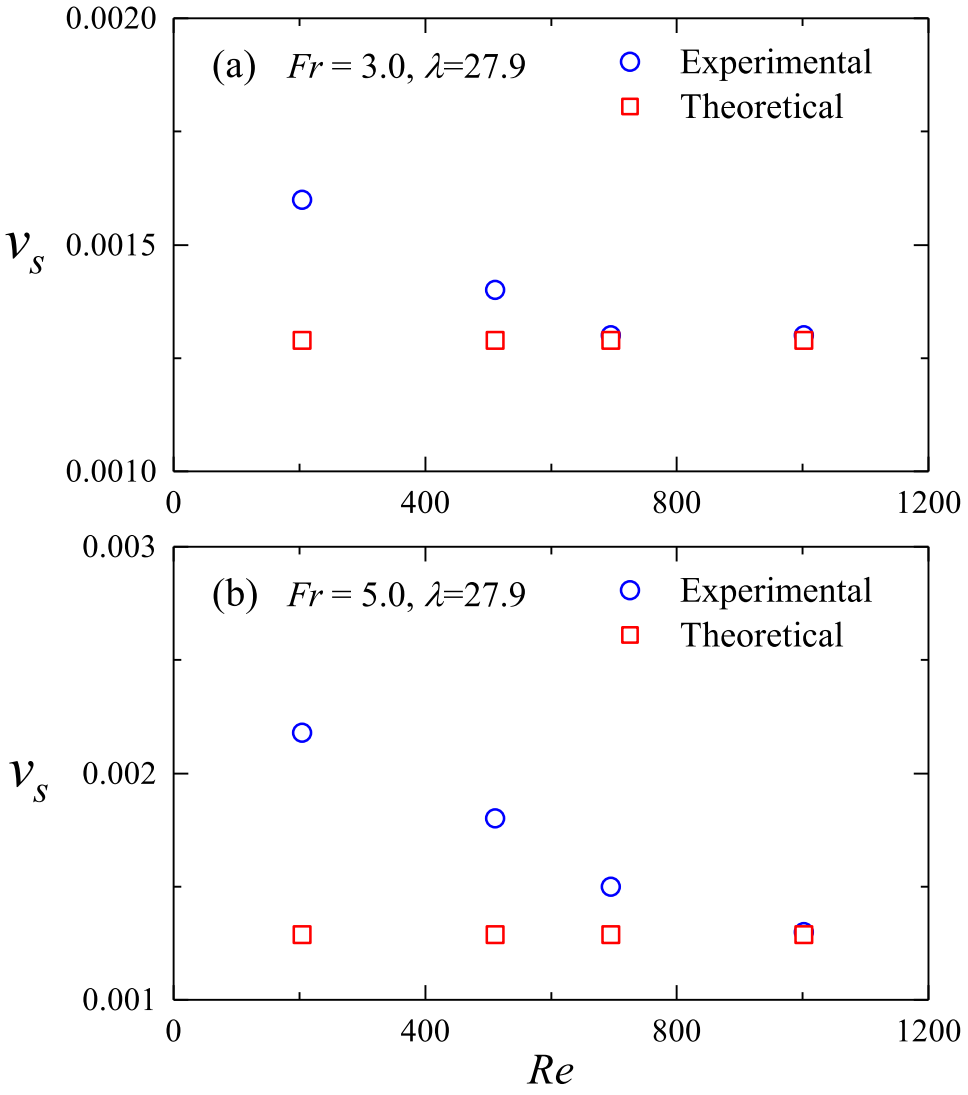

FIGURE 6.26: The experimental and theoretical development rates of the stratification height projected on the sidewall for the fountains of (a) $Fr = 3.0$, $Pr = 7$ and $\lambda = 27.9$, with $Re = 204$, 511, 695 and 1002, and (b) $Fr = 5.0$, $Pr = 7$ and $\lambda = 27.9$ with $Re = 204$, 511, 695 and 1002.

the stratification developing at a quasi-steady rate. Here, parts of the time series of the stratification level (the interface between the dark salty water and the fresh water) are presented and the corresponding development rates are determined. Based on these quantitative results, the influence of Fr, Re and λ on the stratification are analyzed in this section.

Figure 6.25 presents the time series of the stratification level for the fountains

of $Fr = 3.0$, $Pr = 7$ and $\lambda = 27.9$, with $Re = 204$, 511, 695 and 1002, and the fountains of $Fr = 5.0$, $Pr = 7$ and $\lambda = 27.9$ with $Re = 204$, 511, 695 and 1002. The corresponding development rates are denoted by v_s as shown in Figure 6.26. Similar to the numerical results, the development rate of the stratification, v_s, is found to decrease with Re. This is because the diffusion effect is reduced by increasing Re. For $Re \geq 695$, v_s remains at the same value $v_s = 0.0013$, which is very close to the pure filling rate $v_c = 1/\lambda^2 = 0.00129$. While for $204 \leq Re \leq 695$, the correlation between v_s and Re is determined as follows:

$$v_s = \begin{cases} -0.0006 Re^{-0.164} + 0.00001, & Fr = 3.0, \\ -0.0118 Re^{-0.321} + 0.00007, & Fr = 5.0, \end{cases} \tag{6.5}$$

with the regression constants of $R^2 = 0.988$ and 0.950, respectively.

For the time series of the stratification level profiles shown in Figure 6.25, it is expected for the fountain with a smaller Re to reach the same certain height earlier, which behaves like the profiles for $Re = 511$, 695 and 1002. However, the case of $Re = 204$ behaves differently with this trend, which takes longer time to reach the same level than other cases. This may be because the intrusion thickness for the fountain of $Re = 204$ is thinner than that of the fountains with a larger Re as shown in Figure 6.11.

With specific values of Re, Pr and λ, the experiments of various Fr are carried out to investigate the influence of Fr on the development of stratification for the confined turbulent fountains. The results are presented in Figure 6.27 and Figure 6.28, where the time series of the stratification surface level and the corresponding development rate for the fountains of $Re = 511$, $Pr = 7$ and $\lambda = 27.9$, with $Fr = 1.0$, 1.5, 2.0, 3.0 and 5.0, and the fountain of $Re = 1002$, $Pr = 7$ and $\lambda = 48.75$, with $Fr = 8.0$, 15.0 and 20.0, respectively, are shown. The time series of the stratification surface level indicate that it takes longer for the fountain with a smaller Fr to reach the same certain height. This is not only because the thickness of the intrusion flow

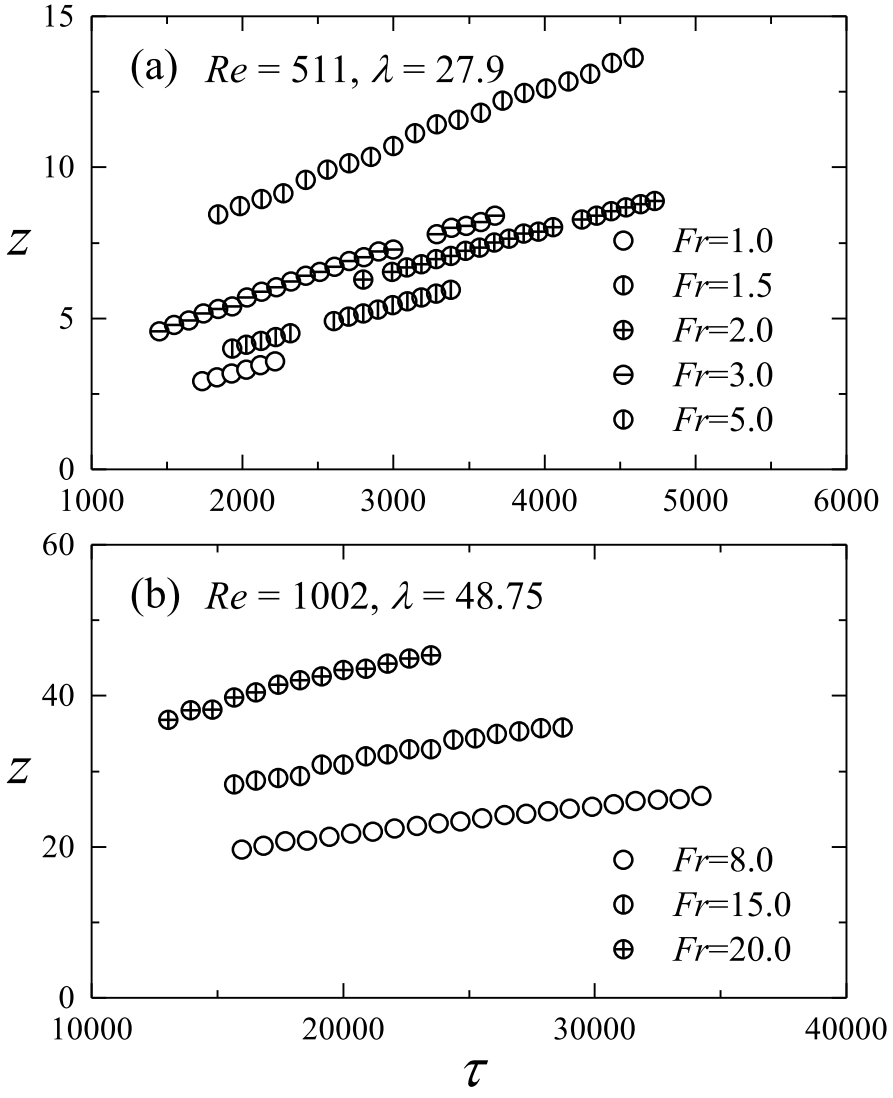

FIGURE 6.27: The time series of the stratification height projected on the sidewall for the fountain of (a) $Re = 511$, $Pr = 7$ and $\lambda = 27.9$, with $Fr = 1.0$, 1.5, 2.0, 3.0 and 5.0, and (b) $Re = 1002$, $Pr = 7$ and $\lambda = 48.75$, with $Fr = 8.0$, 15.0 and 20.0.

increases with Fr (*i.e.*, $h_i \sim Fr\tau^{-1/2}$), but also the increase of Fr enhances the effect of diffusion.

$Fr = 2.0$ was identified to distinguish the behavior of the fountain into weak and intermediate by Hunt and Burridge [2], which is also confirmed by the snapshots shown in Figure 6.21. From Figure 6.28, it is found that v_s increases with Fr. Similarly, $Fr = 2.0$ is identified as an critical value to distinguish the stratification behavior of the confined round fountains. For the fountain of $Re = 511$ with $Fr =$

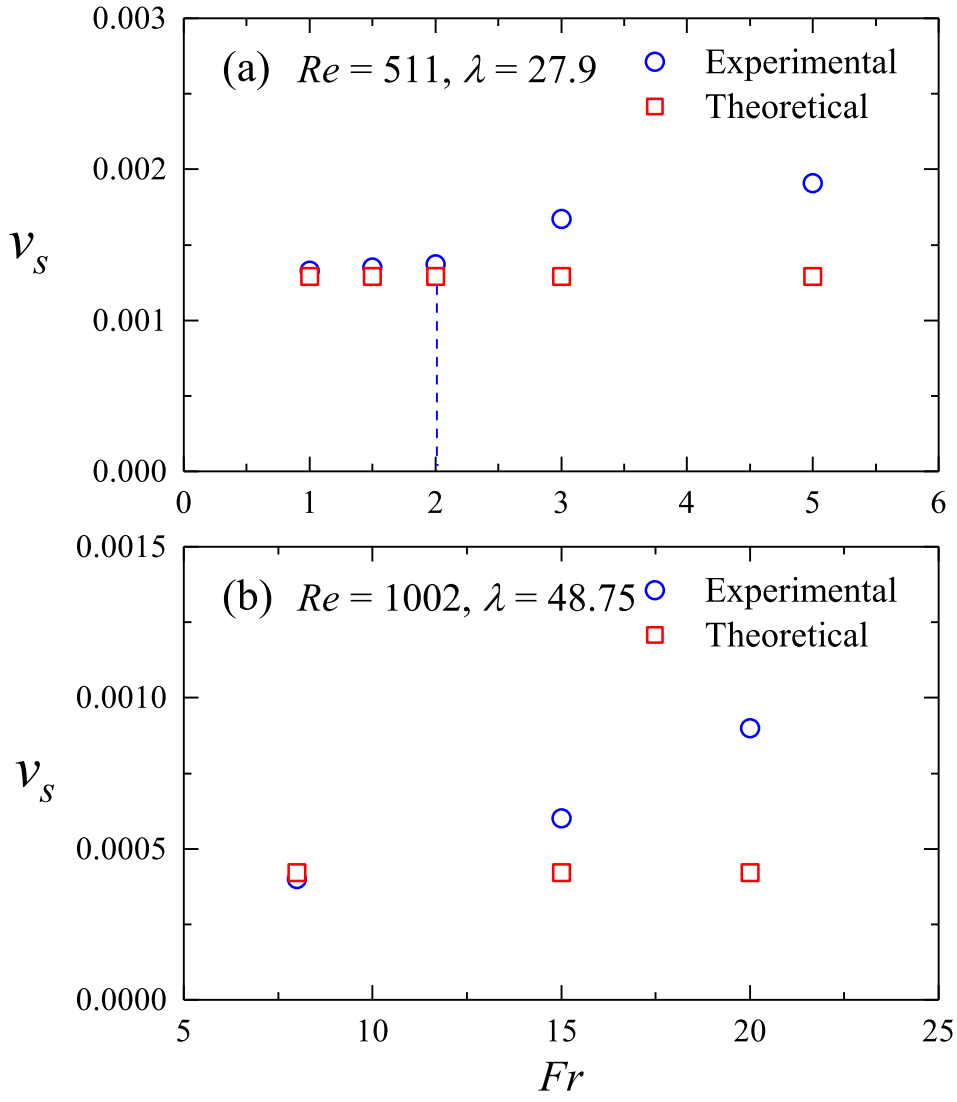

FIGURE 6.28: The experimental and theoretical development rates of the stratification height projected on the sidewall for the fountains of (a) $Re = 511$, $Pr = 7$ and $\lambda = 27.9$, with $Fr = 1.0$, 1.5, 2.0, 3.0 and 5.0, and (b) $Re = 1002$, $Pr = 7$ and $\lambda = 48.75$, with $Fr = 8.0$, 15.0 and 20.0.

1.0, 1.5 and 2.0, the relation between v_s and Fr is linear, as follows:

$$v_s = 0.0005Fr + 0.0013, \tag{6.6}$$

with $R^2 = 1.0$, whereas no suitable correlation is found for $Fr = 3.0$ and 5.0. Similarly, for the fountains of $Re = 1002$, v_s also increases with Fr, which can be

described by an exponential correlation as follows:

$$v_s = 0.0002e^{0.067Fr} - 0.00005, \tag{6.7}$$

with $R^2 = 0.991$.

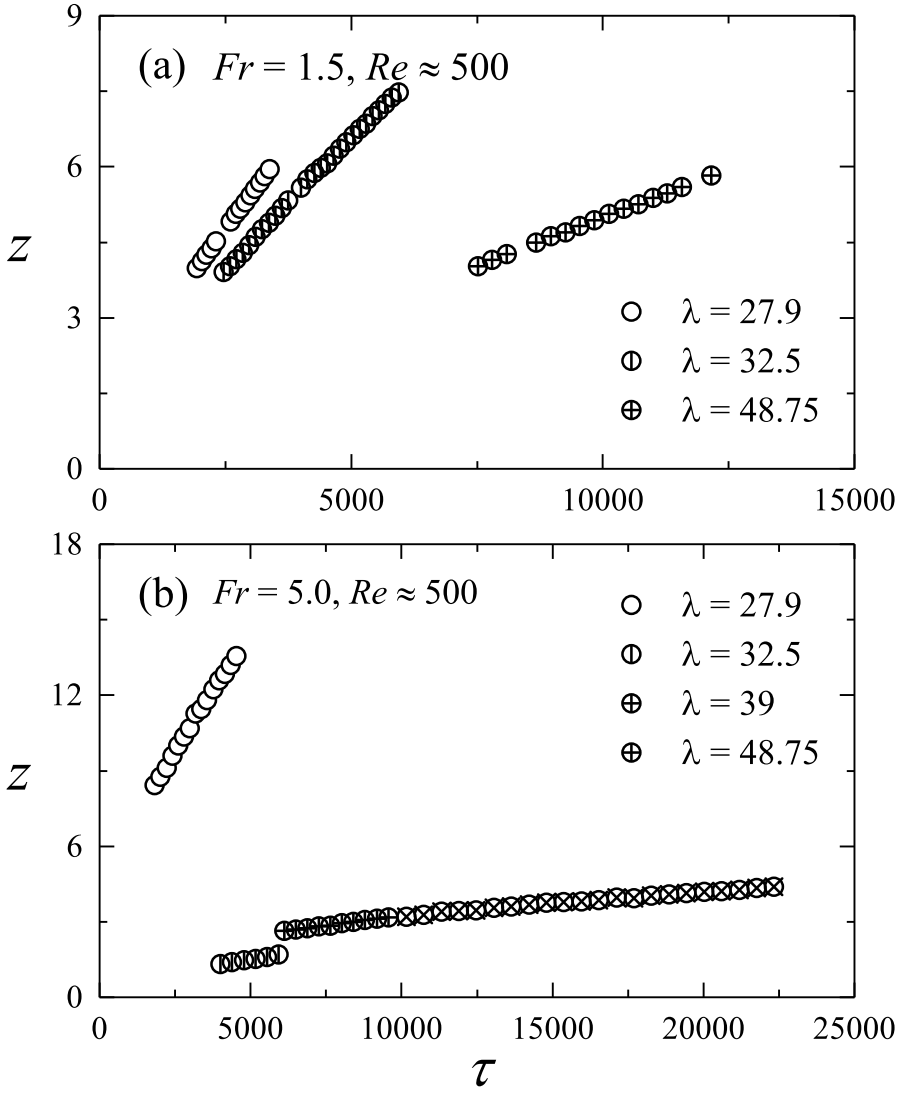

FIGURE 6.29: The time series of the stratification height projected on the sidewall for the fountains of (a) $Fr = 1.5$ and $Pr = 7$, with $Re = 511$ and $\lambda = 27.9$, $Re = 501$ and $\lambda = 32.5$, and $Re = 501$ and $\lambda = 48.75$, (b) $Fr = 5.0$ and $Pr = 7$, with $Re = 511$ and $\lambda = 27.9$, $Re = 501$ and $\lambda = 32.5$, $Re = 515$ and $\lambda = 39$, and $Re = 501$ and $\lambda = 48.75$.

The influence of the confinement size λ on the stratification is demonstrated with the results presented in Figure 6.29 and Figure 6.30 where the time series of

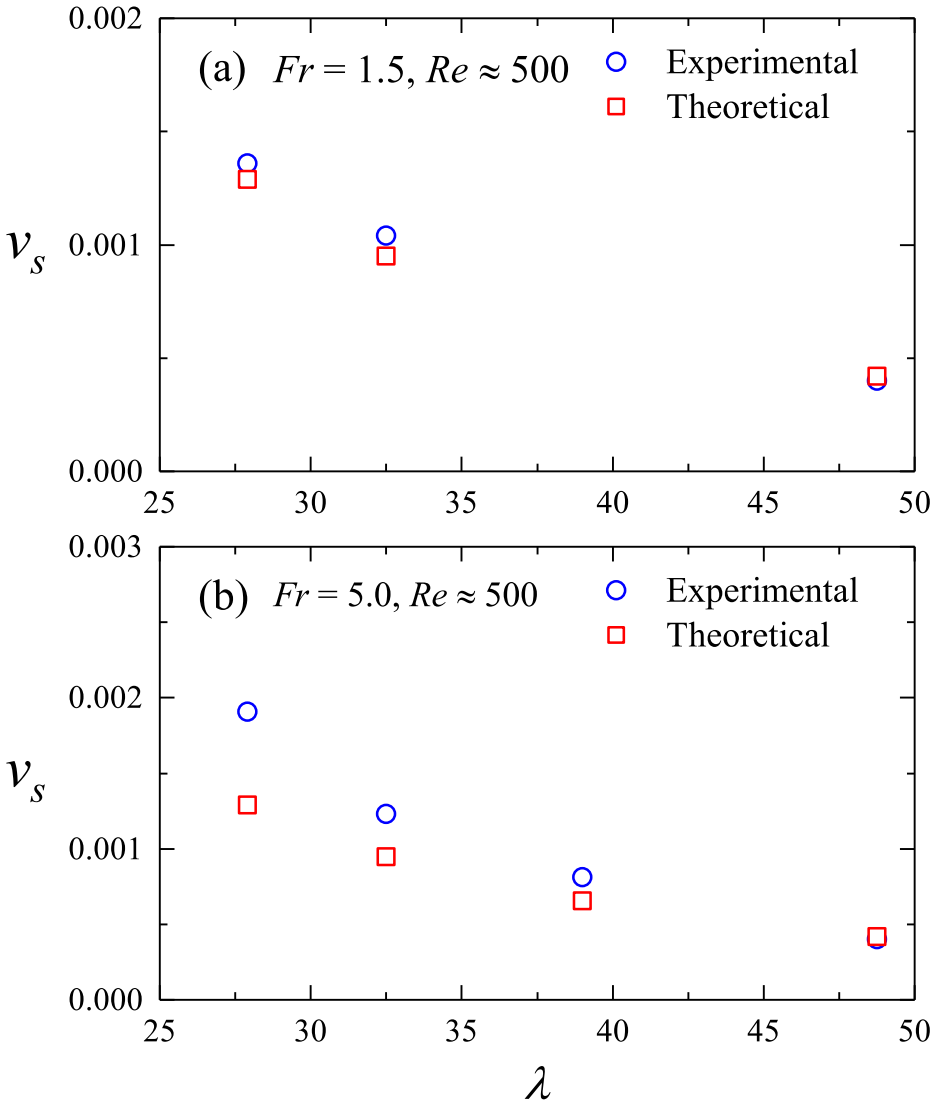

FIGURE 6.30: The experimental and theoretical development rates of the stratification height projected on the sidewall for the fountains of (a) $Fr = 1.5$ and $Pr = 7$, with $Re = 511$ and $\lambda = 27.9$, $Re = 501$ and $\lambda = 32.5$, and $Re = 501$ and $\lambda = 48.75$, (b) $Fr = 5.0$ and $Pr = 7$, with $Re = 511$ and $\lambda = 27.9$, $Re = 501$ and $\lambda = 32.5$, $Re = 515$ and $\lambda = 39$, and $Re = 501$ and $\lambda = 48.75$.

stratification surface levels and the corresponding v_s for the fountain of $Fr = 1.5$, $Re \approx 500$ and $Pr = 7$, with $\lambda = 27.9$, 32.5 and 48.75, and the fountains of $Fr = 5.0$, $Re \approx 500$ and $Pr = 7$ with $\lambda = 27.9$, 32.5, 39.0, and 48.75, respectively. The stratification surface increases at a higher v_s for the fountains with a smaller λ,

which can be described by the following power law correlations,

$$v_s = \begin{cases} 2.2562\lambda^{-2.227} + 0.00003, & Fr = 1.5, Re \approx 500, \\ 18.314\lambda^{-2.758} + 0.00005, & Fr = 5.0, Re \approx 500, \end{cases} \tag{6.8}$$

with the regression constants of $R^2 = 0.994$ and 0.997, respectively.

6.5 Summary

The behaviors of confined round fountains from weak to forced turbulent have been investigated by using high-speed camera technique. A series of experiments have been carried out over the ranges of $1.0 \leq Fr \leq 20.0$, $102 \leq Re \leq 1502$ and $27.9 \leq \lambda \leq 48.75$. Since the fountain flow is resulted from the upward ejection of dense salty water into the homogeneous fresh water, Pr for all the experiments here is treated as constant at $Pr = 7$. The qualitative and quantitative results have been analyzed and compared with the previous analytic and numerical studies, and the major conclusions can be summarized as follows:

- Some DNS results of the confined weak round fountain in the previous chapter have been verified by the experimental results, indicating the DNS code and its results are sufficiently accurate.

- Bobbing and flapping motions have been observed for the behavior of the fountains in the experiment. With the increase of Fr, the behavior of the fountain flow transfers from weak to turbulent. The secondary flows, *i.e.*, the intrusion flow and the stratification turn into turbulent for the intermediate and forced fountains and the turbulence of the fountain and its secondary flows is strengthened with increasing Re. The steady maximum penetration height of the fountain z_m and the thickness of the intrusion flow h_i are found to increase with Fr. The influence of Re on z_m and h_i is negligible for $200 < Re$.

These results are consistent with the existing theoretical results on fountain height [2] and gravity current [113], respectively.

- The time-scale for the intrusion front to impinge with the sidewall, τ_w, is identified and analyzed in terms of Fr, Re and λ. For intermediate (*e.g.*, $Fr = 3.0$) and forced turbulent fountains (*e.g.*, $Fr = 5.0, 8.0$) with a specific λ, τ_w is nearly constant for $Re \gtrsim 500$. This is because the secondary intrusion flow is dominated by the buoyancy-inertial regime where the location of the intrusion front is a time-dependent function of Fr, *i.e.*, $r \sim Fr^{1/2}\tau^{3/4}$ [1]. However, τ_w for the fountains of $Re \lesssim 204$ is significantly different, which may results from the change in the dominant regime for the intrusion or the interaction between the upflow, downflow of the fountain and the ambient fluids. For example, for the cases of $Fr = 3.0$ and $\lambda = 27.9$, τ_w for the fountain of $Re = 102$ is larger than that for the other fountains with a larger Re. Since the flow behavior is laminar, the secondary intrusion flow is not only governed by the buoyancy-inertial regime, but also the buoyancy-viscosity regime. While for the cases of $Fr = 3.0$, 5.0 and 8.0, τ_w for the fountain of $Re = 204$ is significantly smaller than that for the fountains with a larger Re. This is because the stronger interactions among the upflow, downflow of the fountain and the ambient fluid slow down the creation of the secondary intrusion for the cases with larger Re, thus the starting time of the intrusion for the fountain of $Re = 204$ is earlier, resulting in a smaller τ_w for $Re = 204$. Here $Re = 204$ is determined as a critical value for different behavior of the turbulent fountains. The correlations between Fr and τ_w is different at specific values of Re. For $Re = 204$ and $Re = 511$ with $\lambda = 27.9$, $Fr = 2.0$ is found to distinguish the influence of Fr ($1.0 \leq Fr \leq 5.0$) into two ranges, and linear correlations $\tau_w \sim Fr$ are determined. For $Re = 1002$ and $Re = 1502$ with $\lambda = 48.75$, a power law $\tau_w \sim Fr^{1.23}$ is determined for $8.0 \leq Fr \leq 20.0$. The influence of the confinement size λ on τ_w follows a power law, *i.e.*, $\tau_w \sim \lambda^{1.35}$.

- The secondary stratification resulted from the confined intermediate and forced turbulent fountain is also turbulent, which strengthens the influence of convection on the development of the stratification. From the time series of the stratification level, the quasi-steady development rate of the stratification v_s is determined and quantified in terms of Fr, Re and λ. v_s is found to increase with Fr, but decrease with Re, since the diffusion effect is suppressed with smaller Fr or bigger Re.

Chapter 7

Conclusion and future work

This thesis aims to investigate the transient behavior of the filling box flow resulted from the discharge of a fountain flow in a confined space. A series of 2D and 3D DNS runs were carried out using the commercial CFD package ANSYS Fluent 17.0, to simulate the behavior of the confined weak planar fountain and confined weak round fountain respectively. In addition, the high-speed camera and dyed flow visualization techniques were used in the experiments to benchmark the numerical results of confined weak round fountains and to study the behavior of confined intermediate and turbulent round fountains. Moreover these results were compared with the existing theories for gravity current and purely filling problems.

The general conclusions of this thesis are summarized briefly in § 7.1. In § 7.2, some suggestions for the future research on this topic are proposed.

7.1 Conclusion of the thesis

The major results of the work described in this thesis can be summarized as follows:

- The evolution of the flow behavior of a typical confined planar/round fountain is consist of five major development stages, *i.e.*, the formation of the fountain

flow, the intrusion flow, the wall fountain flow along the sidewall, the reversed flow from the sidewall to the fountain flow and the density stratification.

- Even the minimum confinement size ($\lambda = 10$) considered in this thesis is too large to influence the flow behavior when the fountain is formed. Hence the flow behavior of the confined planar/round fountain considered here in the fountain formation stage is same as the counterpart of the corresponding free fountain.

- A secondary intrusion flow is resulted from the impingement of the fountain downflow with the container bottom. The intrusion flow for the planar/round fountain can be treated as a planar/radial gravity current respectively, which may experience 'wall-jet', 'buoyancy-inertial' and 'buoyancy-viscosity' regimes in terms of the governing forces. The intrusion speed v_i increases with the increase of Re or the decrease of Fr. v_i can be approximately quantified by the scaling relations obtained by Chen [1] for gravity current. However, for the 'buoyancy-inertial' regime of planar fountains, a two-constant speed stage is observed and the influence of Re on v_i cannot be ignored, which is different from the previous studies. Similarly, for the 'wall-jet' regime and the 'buoyancy-inertial' regime of round fountains, the numerical results show that v_i is dependent on time, Fr and Re, instead of dependent of only time or Fr and time, as indicated by the scaling relations for radial gravity current. The modified correlations for these regimes are obtained with the results of this thesis.

- A noncontinuous secondary wall fountain flow is created after the intrusion flow impinges with the sidewall. The denser flow moves upward along the sidewall and penetrates to a finite height, then falls down under the influence of negative buoyancy. For a confined weak planar fountain, three mechanisms are identified for the behavior of the wall fountain behavior, *i.e.*, no falling, slumping down and rolling down. For the planar fountains with $0.1 \leq Fr \leq$

3.0, $Pr = 7$ and $\lambda = 20$, the wall fountain is found to slump down for $50 \leq Re \leq 100$ and to roll down for $200 \leq Re \leq 800$, but no falling is observed for $5 \leq Re \leq 20$. Additionally, the wall fountain changes from slumping down to rolling down when the confinement size is extended from $\lambda = 10$ to $\lambda \geq 15$. Similarly, for the confined weak round fountains, no falling is found for $5 \leq Re \leq 20$. The maximum penetration height of the wall fountain z_m is quantitatively scaled in terms of the governing parameters, where z_m is measured on the sidewall for the planar fountain but in the sidewall region for the round fountain. The results shows that z_m increases with the increase of Fr and λ for both planar and round fountains. However, the influence of Re and Pr on z_m for planar and round fountains follows different trends.

- Two dimensionless characteristic time-scales τ_w and τ_m are determined for the time instant when the intrusion impinges with the sidewall and the wall fountain reaches its maximum penetration height. It is found that τ_w and τ_m decrease with the increase of Re or the decrease of Fr for the confined weak planar/round fountains, except for the round fountains over the range of $2.0 \leq Fr$. The experimental results show that τ_w for confined intermediate and turbulent fountains remains unchanged for $Re \gtrsim 500$. While for $Re \approx 200$, τ_w has a significant decreases than that for $Re \gtrsim 500$, which is mainly because the laminar behavior of fountain flow for $Re \approx 200$ results in an earlier formation of the intrusion.

- The reversed flow is driven by the stagnation pressure from the sidewall, moving from the sidewall to the fountain flow. During this stage, the reversed flow interacts with the intrusion flow, the ambient fluid and the fountain flow, resulting in a two-layer structure. With the increase of Fr and Re, the interaction become more significant.

- A secondary stratification is formed in the confined space after a long run of the fountain. Convection, conduction, mixing and filling all contribute to

the evolution of the stratification. In the initial stages, the ambient fluid is entrained into the denser layer mainly by convection and mixing. During this stage, the bulk entrainment rate keeps increasing and then reaches a peaking point/stage. While after a quasi-steady stratification is formed, filling and thermal conduction dominate the flow behavior of the stratification. In this stage, the entrainment rate gradually decreases.

- The secondary flows, *e.g.*, the reversed flow and the stratification, in turn affect the behavior of the fountain flow. The interaction between the reversed flow and the fountain induces extra fluctuations in the penetration height of the fountain. The stratified structure around the fountain core reduces the local buoyancy flux, resulting in an increase in both the width and heights of the fountain flow. Additionally, the stratification also reduces the stability of the fountain structure, where a transfer from symmetric to asymmetric is observed.

- $Fr = 1.0$ and $Fr = 2.0$ are identified as the critical values to distinguish the influence of Fr on the behavior of the secondary flows which supports the current classification of the round fountain [2], while $Re = 200$ is determined as the critical number to divide the influence of Re, which is consistent with the existing results [30].

7.2 Future work

Important areas for further work are suggested by the results of this thesis:

- For the confined weak planar fountains, only two-dimensional numerical simulations results are obtained by assuming the flow behavior remains two-dimensional during the evolution. Moreover, the numerical results for planar

fountains are not benchmarked against experimental results due to the limitation of experimental apparatus. In the future work, 3D DNS and experiments should be carried out on confined planar fountains.

- 2D and 3D DNS in this thesis are only carried out for the confined planar/round fountains over a limited ranges of $0.1 \leq Fr \leq 3.0$ and $5 \leq Re \leq 800$. In the future numerical studies, these parameter ranges should be significantly expanded, covering a high Fr and Re, to explore the transient behavior of confined intermediate and forced turbulent fountains. Furthermore, considering the cost of computational source, appropriate turbulent models, *e.g.*, Large Eddy Simulations and advanced Reynolds Stress models can be used to simulate the flow behavior of the confined turbulent fountains.

- Without the assistance of the PIV system, the high-speed camera and video cameras can only record the bulk behavior projected on the sidewall in front. Thus the information inside the fluids cannot be obtained. Furthermore, the curvature of the cylindrical container also induces errors in the intrusion measurement. In the future work, the 2D and 3D PIV techniques should be conducted to get more detailed information of the confined fountains.

- This thesis focused on the evolution of the confined fountain flow, and the influence of the governing parameters on the secondary flows. But the influence of the secondary flows on the fountain flow is not investigated in detail. Future work can pay more attention on these aspects, *e.g.*, the change of the penetration height, the transfer of the fountain behavior from symmetric to asymmetric, *etc.*.

- The minimum confinement size in this project is $\lambda = 10$, which is still large enough to allows the fountain behaves as free fountain in the initial stages, which can be called as weakly confined condition. In the future work, smaller confinement can be used for the DNS and experimental study to investigate the behavior of a fountain in intermediately or highly confined space.

- The filling box flow in this thesis is resulted from discharging fountains in a confined space with a homogeneous ambient fluid. The future work can be extended to the case with a stratified environment.

- The bottom and sidewall for all the DNS runs considered in this thesis are set as no-slip insulated wall boundaries. In the future work, complex thermal boundary conditions can be applied, which is closer to the applications in reality.

Bibliography

[1] J-C Chen. *Studies on gravitational spreading currents*. PhD thesis, California Institute of Technology, 1980.

[2] GR Hunt and HC Burridge. Fountains in industry and nature. *Annual Review of Fluid Mechanics*, 47: 195–220, 2015.

[3] N Williamson, N Srinarayana, SW Armfield, GD McBain, and W Lin. Low-reynolds-number fountain behaviour. *Journal of Fluid Mechanics*, 608: 297–317, 2008.

[4] W Lin and SW Armfield. Direct simulation of weak axisymmetric fountains in a homogeneous fluid. *Journal of Fluid Mechanics*, 403: 67–88, 2000.

[5] WD Baines, AF Corriveau, and TJ Reedman. Turbulent fountains in a closed chamber. *Journal of Fluid Mechanics*, 255: 621–646, 1993.

[6] HC Burridge and GR Hunt. Entrainment by turbulent fountains. *Journal of Fluid Mechanics*, 790: 407–418, 2016.

[7] AB Shrinivas and GR Hunt. Unconfined turbulent entrainment across density interfaces. *Journal of Fluid Mechanics*, 757: 573–598, 2014.

[8] K Mehdi. *Conjugate natural convection boundary layers*. PhD thesis, James Cook University, 2018.

[9] IC ANSYS. Fluent theory guide, 2011.

[10] N Srinarayana, SW Armfield, and W Lin. Impinging plane fountains in a homogeneous fluid. *International Journal of Heat and Mass Transfer*, 52(11-12): 2614–2623, 2009.

[11] B Nathan. *Experimental study on fountain flows at intermediate Reynolds and Froude numbers*. Undergraduate thesis, James Cook University, 2018.

[12] G Carazzo and AM Jellinek. A new view of the dynamics, stability and longevity of volcanic clouds. *Earth and Planetary Science Letters*, 325: 39–51, 2012.

[13] E Kaminski, S Tait, and G Carazzo. Turbulent entrainment in jets with arbitrary buoyancy. *Journal of Fluid Mechanics*, 526: 361–376, 2005.

[14] G Carazzo, E Kaminski, and S Tait. On the dynamics of volcanic columns: A comparison of field data with a new model of negatively buoyant jets. *Journal of Volcanology and Geothermal Research*, 178(1): 94–103, 2008.

[15] A Neri, OT Esposti, G Macedonio, and D Gidaspow. Multiparticle simulation of collapsing volcanic columns and pyroclastic flow. *Journal of Geophysical Research: Solid Earth*, 108(B4), 2003.

[16] GF Lane-Serff, PF Linden, and M Hillel. Forced, angled plumes. *Journal of Hazardous Materials*, 33(1): 75–99, 1993.

[17] GA Kikkert, MJ Davidson, and RI Nokes. Inclined negatively buoyant discharges. *Journal of Hydraulic Engineering*, 133(5): 545–554, 2007.

[18] T Bleninger and GH Jirka. Modelling and environmentally sound management of brine discharges from desalination plants. *Desalination*, 221(1-3): 585–597, 2008.

[19] PN Papanicolaou and TJ Kokkalis. Vertical buoyancy preserving and non-preserving fountains, in a homogeneous calm ambient. *International Journal of Heat and Mass Transfer*, 51(15-16): 4109–4120, 2008.

[20] S He, Z Xu, and JD Jackson. An experimental investigation of buoyancy-opposed wall jet flow. *International Journal of Heat and Fluid Flow*, 23(4): 487–496, 2002.

[21] D Freire, S Kahan, C Cabeza, G Sarasúa, and AC Marti. The formation of coherent structures within turbulent fountains in stratified media. *European Journal of Mechanics-B/Fluids*, 50: 89–97, 2015.

[22] R Guarga, P Mastrángelo, G Scaglione, and E Supino. Evaluation of the sis: a new frost protection method applied in a citrus orchard. In *Proceedings of the 9th. Congress of the International Society of Citriculture*, 2000.

[23] D Frank and PF Linden. The effects of an opposing buoyancy force on the performance of an air curtain in the doorway of a building. *Energy and Buildings*, 96: 20–29, 2015.

[24] S Ferrari and G Querzoli. Mixing and re-entrainment in a negatively buoyant jet. *Journal of Hydraulic Research*, 48(5): 632–640, 2010.

[25] AF Alajmi, HZ Abou-Ziyan, and W El-Amer. Energy analysis of underfloor air distribution (ufad) system: An office building case study. *Energy Conversion and Management*, 73: 78–85, 2013.

[26] AF Alajmi and W El-Amer. Saving energy by using underfloor-air-distribution (ufad) system in commercial buildings. *Energy Conversion and Management*, 51(8): 1637–1642, 2010.

[27] BR Morton. Forced plumes. *Journal of Fluid mechanics*, 5(1): 151–163, 1959.

[28] JS Turner. Jets and plumes with negative or reversing buoyancy. *Journal of Fluid Mechanics*, 26(4): 779–792, 1966.

[29] LJ Bloomfield and RC Kerr. A theoretical model of a turbulent fountain. *Journal of Fluid Mechanics*, 424: 197–216, 2000.

[30] W Lin and SW Armfield. The reynolds and prandtl number dependence of weak fountains. *Computational Mechanics*, 31(5): 379–389, 2003.

[31] W Lin and SW Armfield. Very weak fountains in a homogeneous fluid. *Numerical Heat Transfer: Part A: Applications*, 38(4): 377–396, 2000.

[32] NB Kaye and GR Hunt. Weak fountains. *Journal of Fluid Mechanics*, 558: 319–328, 2006.

[33] GR Hunt and CJ Coffey. Characterising line fountains. *Journal of Fluid Mechanics*, 623: 317–327, 2009.

[34] LJ Bloomfield and RC Kerr. Inclined turbulent fountains. *Journal of Fluid Mechanics*, 451: 283–294, 2002.

[35] IG Papakonstantis, GC Christodoulou, and PN Papanicolaou. Inclined negatively buoyant jets 1: geometrical characteristics. *Journal of Hydraulic Research*, 49(1): 3–12, 2011.

[36] IG Papakonstantis, GC Christodoulou, and PN Papanicolaou. Inclined negatively buoyant jets 2: concentration measurements. *Journal of Hydraulic Research*, 49(1): 13–22, 2011.

[37] GC Christodoulou and IG Papakonstantis. Simplified estimates of trajectory of inclined negatively buoyant jets. *Environmental Hydraulics*, 1: 165–170, 2010.

[38] R Bashitialshaaer, M Larson, and KM Persson. An experimental investigation on inclined negatively buoyant jets. *Water*, 4(3): 720–738, 2012.

[39] CCK Lai and JHW Lee. Mixing of inclined dense jets in stationary ambient. *Journal of Hydro-environment Research*, 6(1): 9–28, 2012.

[40] P Cooper and PF Linden. Natural ventilation of an enclosure containing two buoyancy sources. *Journal of Fluid Mechanics*, 311: 153–176, 1996.

[41] QA Liu and PF Linden. The fluid dynamics of an underfloor air distribution system. *Journal of Fluid Mechanics*, 554: 323–341, 2006.

[42] H Mahmud, W Lin, W Gao, B Hill, SW Armfield, and Y He. Behavior of the interaction between twin transitional round fountains in a homogeneous fluid, part 1: Experimental study. *International Journal of Heat and Mass Transfer*, 86: 957–972, 2015.

[43] H Mahmud, W Lin, W Gao, SW Armfield, and Y He. Behavior of the interaction between twin transitional round fountains in a homogeneous fluid, part 2: Numerical study. *International Journal of Heat and Mass Transfer*, 86: 973–991, 2015.

[44] H Mahmud, W Lin, W Gao, SW Armfield, and Y He. Interaction behavior of triple transitional round fountains in a homogeneous fluid. *International Journal of Heat and Fluid Flow*, 62: 437–454, 2016.

[45] PJW Roberts and G Toms. Inclined dense jets in flowing current. *Journal of Hydraulic Engineering*, 113(3): 323–340, 1987.

[46] FJ Diez, LP Bernal, and GM Faeth. Plif and piv measurements of the self-preserving structure of steady round buoyant turbulent plumes in crossflow. *International Journal of Heat and Fluid Flow*, 26(6): 873–882, 2005.

[47] E Gungor and PJW Roberts. Experimental studies on vertical dense jets in a flowing current. *Journal of Hydraulic Engineering*, 135(11): 935–948, 2009.

[48] JK Ansong, A Anderson-Frey, and BR Sutherland. Turbulent fountains in one-and two-layer crossflows. *Journal of Fluid Mechanics*, 689: 254–278, 2011.

[49] PD Friedman and J Katz. Rise height for negatively buoyant fountains and depth of penetration for negatively buoyant jets impinging an interface. *Journal of Fluids Engineering*, 122(4): 779–782, 2000.

[50] PD Friedman. Oscillation in height of a negatively buoyant jet. *Journal of Fluids Engineering*, 128(4): 880–882, 2006.

[51] PD Friedman, VD Vadakoot, WJ Meyer, and S Carey. Instability threshold of a negatively buoyant fountain. *Experiments in Fluids*, 42(5): 751–759, 2007.

[52] P Philippe, C Raufaste, P Kurowski, and P Petitjeans. Penetration of a negatively buoyant jet in a miscible liquid. *Physics of Fluids*, 17(5): 053601, 2005.

[53] A Geyer, JC Phillips, M Mier-Torrecilla, SR Idelsohn, and E Oñate. Flow behaviour of negatively buoyant jets in immiscible ambient fluid. *Experiments in Fluids*, 52(1): 261–271, 2012.

[54] H Mahmud. *Behavior of multiple transitional round fountains interacting in homogeneous and stratified fluids*. PhD thesis, James Cook University, 2014.

[55] NB Kaye. Turbulent plumes in stratified environments: a review of recent work. *Atmosphere-ocean*, 46(4): 433–441, 2008.

[56] H Zhang and RE Baddour. Maximum penetration of vertical round dense jets at small and large froude numbers. *Journal of Hydraulic Engineering*, 124(5): 550–553, 1998.

[57] HC Burridge and GR Hunt. The rise heights of low-and high-froude-number turbulent axisymmetric fountains. *Journal of Fluid Mechanics*, 691: 392–416, 2012.

[58] N Srinarayana, N Williamson, SW Armfield, and W Lin. Line fountain behavior at low-reynolds number. *International Journal of Heat and Mass Transfer*, 53(9-10): 2065–2073, 2010.

[59] BR Morton, GI Taylor, and JS Turner. Turbulent gravitational convection from maintained and instantaneous sources. *Proc. R. Soc. Lond. A*, 234(1196): 1–23, 1956.

[60] G Abraham. Jets with negative buoyancy in homogeneous fluid. *Journal of Hydraulic Research*, 5(4): 235–248, 1967.

[61] TJ McDougall. Negatively buoyant vertical jets. *Tellus*, 33(3): 313–320, 1981.

[62] IH Campbell and JS Turner. Fountains in magma chambers. *Journal of Petrology*, 30(4): 885–923, 1989.

[63] T Mizushina, F Ogino, H Takeuchi, and H Ikawa. An experimental study of vertical turbulent jet with negative buoyancy. *Wärme-und Stoffübertragung*, 16(1): 15–21, 1982.

[64] WD Baines, JS Turner, and IH Campbell. Turbulent fountains in an open chamber. *Journal of Fluid Mechanics*, 212: 557–592, 1990.

[65] HC Burridge, A Mistry, and GR Hunt. The effect of source reynolds number on the rise height of a fountain. *Physics of Fluids*, 27(4): 047101, 2015.

[66] N Williamson, SW Armfield, and W Lin. Transition behaviour of weak turbulent fountains. *Journal of Fluid Mechanics*, 655: 306–326, 2010.

[67] BR Morton. On a momentum-mass flux diagram for turbulent jets, plumes and wakes. *Journal of Fluid Mechanics*, 10(1): 101–112, 1961.

[68] CG Johnson and AJ Hogg. Entraining gravity currents. *Journal of Fluid Mechanics*, 731: 477–508, 2013.

[69] A Ezzamel, P Salizzoni, and GR Hunt. Dynamical variability of axisymmetric buoyant plumes. *Journal of Fluid Mechanics*, 765: 576–611, 2015.

[70] LJ Bloomfield and RC Kerr. Turbulent fountains in a stratified fluid. *Journal of Fluid Mechanics*, 358: 335–356, 1998.

[71] G Carazzo, E Kaminski, and S Tait. The rise and fall of turbulent fountains: a new model for improved quantitative predictions. *Journal of Fluid Mechanics*, 657: 265–284, 2010.

[72] RW Cresswell and RT Szczepura. Experimental investigation into a turbulent jet with negative buoyancy. *Physics of Fluids A: Fluid Dynamics*, 5(11): 2865–2878, 1993.

[73] N Williamson, SW Armfield, and W Lin. Forced turbulent fountain flow behaviour. *Journal of Fluid Mechanics*, 671: 535–558, 2011.

[74] WD Baines. A technique for the direct measurement of volume flux of a plume. *Journal of Fluid Mechanics*, 132: 247–256, 1983.

[75] HC Burridge and GR Hunt. Scaling arguments for the fluxes in turbulent miscible fountains. *Journal of Fluid Mechanics*, 744: 273–285, 2014.

[76] WD Baines. Entrainment by a plume or jet at a density interface. *Journal of Fluid Mechanics*, 68(2): 309–320, 1975.

[77] M Kumagai. Turbulent buoyant convection from a source in a confined two-layered region. *Journal of Fluid Mechanics*, 147: 105–131, 1984.

[78] SSS Cardoso and AW Woods. Mixing by a turbulent plume in a confined stratified region. *Journal of Fluid Mechanics*, 250: 277–305, 1993.

[79] M Larson and L Jönsson. Mixing in a two-layer stably stratified fluid by a turbulent jet. *Journal of Hydraulic Research*, 32(2): 271–289, 1994.

[80] SS Shy. Mixing dynamics of jet interaction with a sharp density interface. *Experimental thermal and fluid science*, 10(3): 355–369, 1995.

[81] M Larson and L Jönsson. Efficiency of mixing by a turbulent jet in a stably stratified fluid. *Dynamics of Atmospheres and Oceans*, 24(1-4): 63–74, 1996.

[82] JS Turner. The influence of molecular diffusivity on turbulent entrainment across a density interface. *Journal of Fluid Mechanics*, 33(4): 639–656, 1968.

[83] CJ Coffey and GR Hunt. The unidirectional emptying box. *Journal of Fluid Mechanics*, 660: 456–474, 2010.

[84] YJP Lin and PF Linden. The entrainment due to a turbulent fountain at a density interface. *Journal of Fluid Mechanics*, 542: 25–52, 2005.

[85] AB Shrinivas. *Unconfined and confined turbulent plumes and jets in stratified environments*. PhD thesis, Imperial College London, 2014.

[86] MI Inam. *Behavior of transitional plane fountains in linearly-stratified environments*. PhD thesis, James Cook University, 2016.

[87] ALR Debugne and GR Hunt. A phenomenological model for fountain-top entrainment. *Journal of Fluid Mechanics*, 796: 195–210, 2016.

[88] AB Shrinivas and GR Hunt. Confined turbulent entrainment across density interfaces. *Journal of Fluid Mechanics*, 779: 116–143, 2015.

[89] L Guyonnaud, C Solliec, M Dufresne De Virel, and C Rey. Design of air curtains used for area confinement in tunnels. *Experiments in Fluids*, 28(4): 377–384, 2000.

[90] W Lin and SW Armfield. Direct simulation of weak laminar plane fountains in a homogeneous fluid. *International journal of heat and mass transfer*, 43(17): 3013–3026, 2000.

[91] N Srinarayana, SW Armfield, and W Lin. Behaviour of laminar plane fountains with a parabolic inlet velocity profile in a homogeneous fluid. *International Journal of Thermal Sciences*, 67: 87–95, 2013.

[92] N Srinarayana, GD McBain, SW Armfield, and W Lin. Height and stability of laminar plane fountains in a homogeneous fluid. *International Journal of Heat and Mass Transfer*, 51(19-20): 4717–4727, 2008.

[93] N Srinarayana, SW Armfield, and W Lin. Laminar plane fountains impinging on a ceiling with an opposing heat flux. *International Journal of Heat and Mass Transfer*, 52(19-20): 4545–4552, 2009.

[94] H Zhang and RE Baddour. Maximum vertical penetration of plane turbulent negatively buoyant jets. *Journal of Engineering Mechanics*, 123(10): 973–977, 1997.

[95] JS Turner. *Buoyancy effects in fluids*. Cambridge University Press, 1979.

[96] WD Baines and JS Turner. Turbulent buoyant convection from a source in a confined region. *Journal of Fluid mechanics*, 37(1): 51–80, 1969.

[97] NB Kaye and GR Hunt. Overturning in a filling box. *Journal of Fluid Mechanics*, 576: 297–323, 2007.

[98] SJ Barnett. *The dynamics of buoyant releases in confined spaces*. PhD thesis, University of Cambridge, 1992.

[99] Y Jaluria and K Kapoor. Wall and corner flows driven by a ceiling jet in an enclosure fire. *Combustion science and technology*, 86(1-6): 311–326, 1992.

[100] ALR Debugne and GR Hunt. The influence of spanwise confinement on round fountains. *Journal of Fluid Mechanics*, 845: 263–292, 2018.

[101] MC Lippert and AW Woods. Particle fountains in a confined environment. *Journal of Fluid Mechanics*, 855: 28–42, 2018.

[102] P Cooper and GR Hunt. Impinging axisymmetric turbulent fountains. *Physics of Fluids*, 19(11): 117101, 2007.

[103] CJ Lemckert. Spreading radius of fountains after impinging a free surface. In *15th Australian Fluid Mechanics Conference*, 2004.

[104] CY Ching, HJS Fernando, and Y Noh. Interaction of a negatively buoyant line plume with a density interface. *Dynamics of Atmospheres and Oceans*, 19(1-4): 367–388, 1993.

[105] JK Ansong, PJ Kyba, and BR Sutherland. Fountains impinging on a density interface. *Journal of Fluid Mechanics*, 595: 115–139, 2008.

[106] PF Crapper and WD Baines. Non boussinesq forced plumes. *Atmospheric Environment*, 11(5): 415–420, 1977.

[107] J Ai, AW Law, and SCM Yu. On boussinesq and non-boussinesq starting forced plumes. *Journal of Fluid Mechanics*, 558: 357–386, 2006.

[108] RE Baddour and H Zhang. Density effect on round turbulent hypersaline fountain. *Journal of Hydraulic Engineering*, 135(1): 57–59, 2009.

[109] F Moukalled, L Mangani, M Darwish, et al. The finite volume method in computational fluid dynamics. *An Advanced Introduction with OpenFOAM and Matlab*, 3–8, 2016.

[110] HK Versteeg and W Malalasekera. *An introduction to computional fluid dynamics: The finite volume method*. Pearson Education, 2007.

[111] JH Ferziger and M Peric. *Computational Methods for Fluid Dynamics*. Springer, 1999.

[112] ANSYS Fluent. Ansys fluent user's guide. *Ansys Inc*, 2011.

[113] N Didden and T Maxworthy. The viscous spreading of plane and axisymmetric gravity currents. *Journal of Fluid Mechanics*, 121: 27–42, 1982.